

TRANSPORT AND STABILITY ANALYSIS OF DILUTE MAGNETIZED  
ACCRETING FLOWS

Tanim Islam  
Hopewell, VA, United States

B.S., California Institute of Technology, 2000

A Dissertation Presented to the Graduate  
Faculty of the University of Virginia  
in Candidacy for the Degree of  
Doctor of Philosophy

Department of Astronomy

University of Virginia  
December 3, 2007

---

Roger Chevalier

---

Peter Arnold

---

Zhi-Yun Li

---

Jim Stone

---

Thesis Advisor: Steven Balbus

© Copyright by  
Tanim Shahriar Islam  
All Rights Reserved  
May 2008

## Abstract

Accretion, the process by which matter collects into a central object, is ubiquitous and often dynamically important for astrophysical objects on the scale of compact object disks ( $\sim 10^{10}$  cm) up to that of galactic clusters ( $\sim 10^{24}$  cm). In order for matter to accrete, it must lose angular momentum. The central issue in accretion theory is to explain the mechanism by which angular momentum is lost at rates sufficient to accord with observation, orders of magnitude beyond what may be accounted through collisional viscosity. For a wide class of astrophysical objects, characterized by collisional mean free paths far smaller than the system scale, the magnetorotational instability (MRI), first discovered in a restricted global form by Velikhov (1959); Chandrasekhar (1960), produces MHD turbulence and a level of angular momentum transport sufficient to account for observed rates of disk accretion (Balbus & Hawley 1991). However, in underluminous accretion flows in massive and supermassive central galactic black holes, the best studied example of which is Sagittarius A\* at the center of our Milky Way, the MRI is not the sole means of turbulent transport. These flows are characterized by the radiatively inefficient accretion of a hot, dilute (mildly collisional to highly collisionless), and optically thin plasma. In these plasmas, even an extremely weak magnetic field can lead, in addition to the MRI, to anisotropic heat fluxes and viscous stresses directed along field lines, resulting in new classes of instabilities. Furthermore, in these radiatively inefficient flows, the energy generated through gravitational infall must be transported through local thermal fluxes rather than locally dissipated as in highly collisional systems.

We propose a model to explain how hot, dilute accretion onto compact objects may then occur. We use both fluid and kinetic theory to examine the effects of other instabilities, the magnetothermal instability (Balbus 2001) and magnetoviscous instability (Balbus 2004b; Islam & Balbus 2005), that may operate within these flows.

A more elaborate kinetic theory must be applied for those dilute systems in which the collisional mean free path is larger than the system scale or larger than the wavelengths of the fastest growing instabilities. Our work demonstrates that these new modes may create sufficient angular momentum and thermal energy transport to account for the expected rates of accretion.

## Acknowledgements

I would like to thank my advisor, Professor Steven Balbus, for introducing me to the topic of dilute accretion and steering me in the right direction whenever I veered; I regret that I did not look to him for advice more frequently than I did. I would like to thank Dr. Lara Silvers, for keeping me sane while we were both enduring the French bureaucratic nightmare; Dr. Michel Pérault for assisting me, as much as was possible, with administrative issues; and the people of the Young Trendy Astronomers (YTA), for letting me get off some steam when nothing during the day, week, or month was going right. And finally, thank you to my parents, for helping to proofread my thesis, for making it clear and coherent. I could not have finished this thesis without your help.

I dedicate this thesis to you, my wife, Farzana Hoque, and to my parents, Drs. Shaheen and Quazi Islam.

# Table of Contents

<b>Abstract</b>	<b>iii</b>
<b>Acknowledgements</b>	<b>v</b>
<b>List of Figures</b>	<b>xii</b>
<b>List of Tables</b>	<b>xiii</b>
<b>1 Introduction</b>	<b>1</b>
1.1 Organization of the Thesis . . . . .	4
1.2 Nomenclature . . . . .	6
1.3 Classical Accretion as Applied to Compact Objects . . . . .	9
1.3.1 Eddington and Bondi Limits to Accretion . . . . .	10
1.3.2 Classical Accretion Disk Theory . . . . .	14
1.3.3 The Insufficiency of Hydrodynamics . . . . .	21
1.4 Evidence for Underluminous Accretion . . . . .	27
1.5 The Nature and Models of Radiatively Inefficient Accretion Flows . .	32
<b>2 The Stability of a Rotating MHD Plasma</b>	<b>37</b>
2.1 Adiabatic Instability in a Rotating MHD Medium . . . . .	38
2.2 The Magnetorotational Instability . . . . .	41

2.2.1	Linear Stability Analysis of the MRI . . . . .	42
2.2.2	Nonlinear MRI . . . . .	44
2.3	Anisotropic Viscous Stresses and Heat Fluxes in Dilute Plasmas . . .	51
2.4	Magnetothermal Instability (MTI) . . . . .	56
2.4.1	Linear Stability . . . . .	58
2.4.2	Nonlinear Behavior . . . . .	61
2.5	Magnetoviscous Instability (MVI) . . . . .	63
<b>3</b>	<b>Problem Setup</b>	<b>65</b>
3.1	Angular Momentum and Energy Balance . . . . .	66
3.1.1	Angular Momentum Balance . . . . .	67
3.1.2	Total Energy Balance . . . . .	68
<b>4</b>	<b>Fluid Treatment – the MVTI</b>	<b>71</b>
4.1	Dispersion Relation . . . . .	72
4.2	Growth Rate and Stability Characteristics . . . . .	78
4.3	Angular Momentum Flux And Heat Flux . . . . .	80
4.4	Finite Compressibility . . . . .	85
4.4.1	The Compressive MVTI Growth Rate . . . . .	93
4.4.2	Quadratic Fluxes for Compressive MVTI . . . . .	97
4.5	Summary of Results . . . . .	103
<b>5</b>	<b>Kinetic Treatment – the Collisionless MTI</b>	<b>104</b>
5.1	The Drift Kinetic Equation in Rotating Frame . . . . .	105
5.1.1	The Drift Kinetic Equation . . . . .	107
5.1.2	Moments of the Drift-Kinetic Equation . . . . .	112
5.1.3	Full Force Balance . . . . .	117
5.2	Perturbed Axisymmetric Distribution Function at the Midplane . . .	119

5.2.1	Dispersion Relations of the Collisionless MRI and MTI . . . .	121
5.2.2	Quadratic Fluxes of Collisionless MRI and MTI . . . . .	129
5.3	Finite Collisionality . . . . .	135
5.4	Summary of Results . . . . .	142
<b>6</b>	<b>Additional Physics: Electron and Off-Plane Dynamics</b>	<b>143</b>
6.1	Finite Ion and Electron Pressure Responses . . . . .	143
6.2	Off Plane Dynamics of the Plasma . . . . .	150
<b>7</b>	<b>Conclusions</b>	<b>160</b>
7.1	Summary of Results . . . . .	160
7.2	Numerical Simulations . . . . .	161
7.2.1	Landau Fluid Closures Appropriate to Collisionless MTI . . .	163
7.2.2	Pressure Anisotropy in Collisionless Plasmas . . . . .	167
7.3	Further Work . . . . .	175
<b>A</b>	<b>Variables</b>	<b>180</b>
<b>B</b>	<b>Plasma Equilibrium Disk</b>	<b>184</b>
<b>C</b>	<b>Full Perturbed Axisymmetric Distribution Function</b>	<b>193</b>
<b>D</b>	<b>Finite Ion and Electron Pressure Responses</b>	<b>197</b>
D.1	Fluid Treatment . . . . .	197
D.2	Kinetic Treatment . . . . .	200
<b>E</b>	<b>Off Plane Plasma Dynamics</b>	<b>202</b>
E.1	Fluid Treatment . . . . .	202
E.2	Kinetic Treatment . . . . .	206



# List of Figures

1.3.1 Artist's conception of an AGN . . . . .	10
1.3.2 Plot of wind-like and accretion Bondi solutions . . . . .	14
1.3.3 Physical model of a simple, classical accretion disk . . . . .	15
1.3.4 Classical accretion disk spectrum . . . . .	22
1.3.5 Textbook example of Taylor-Couette flow . . . . .	25
1.3.6 Princeton hydrodynamic stability experimental setup . . . . .	25
1.3.7 Demonstration of hydrodynamic stability in Taylor-Couette experiment	26
1.4.1 Census of AGNs within 400 million light years . . . . .	28
1.4.2 Chandra X Ray Image of Sagittarius A* . . . . .	30
1.5.1 Two-temperature nature of hot and dilute flows . . . . .	34
2.1.1 MHD modes in a Keplerian rotational profile . . . . .	40
2.2.1 Spring model of the MRI . . . . .	42
2.2.2 The MRI growth rate . . . . .	44
2.2.3 The MRI $W_{R\phi}$ . . . . .	45
2.2.4 Magnetic saturation in a local shearing box simulation . . . . .	47
2.2.5 Outward $W_{R\phi}$ in a local shearing box simulation . . . . .	48
2.2.6 Numerical stability of hydrodynamic shear . . . . .	49
2.2.7 Global MRI simulation . . . . .	51
2.2.8 Analytic model of a global MRI simulations . . . . .	52

2.2.9 Mass accretion and outflow rates in a global MRI simulation. . . . .	53
2.3.1 Faraday polarization due to internal magnetic field in Sag. A* . . . . .	55
2.4.1 Cartoon model of the magnetothermal instability . . . . .	58
2.4.2 Linear magnetothermal instability . . . . .	61
2.4.3 Development of isothermality due to magnetothermal instability . . . . .	62
2.4.4 Nonlinear development of the 3D magnetothermal instability . . . . .	63
2.5.1 Cartoon model of the magnetoviscous instability . . . . .	64
4.2.1 MVI-like limit of the incompressible MVTI . . . . .	80
4.2.2 MRI-like limit of the incompressible MVTI . . . . .	81
4.3.1 Heat flux for incompressible MVTI and large viscosity . . . . .	83
4.3.2 Angular momentum flux for incompressible MVTI and large viscosity . . . . .	84
4.3.3 Heat flux for incompressible MVTI and small viscosity . . . . .	85
4.3.4 Angular momentum flux for incompressible MVTI and small viscosity . . . . .	86
4.3.5 Angular momentum flux for MTI and rigid rotation profile . . . . .	87
4.4.1 Real part of the growth rate for the compressive MVTI . . . . .	93
4.4.2 Imaginary part of the growth rate for the compressive MVTI . . . . .	94
4.4.3 Real growth rate for compressive MVTI at fixed normalized viscosity . . . . .	95
4.4.4 Imaginary growth for compressive MVTI at fixed normalized viscosity . . . . .	96
4.4.5 Angular momentum flux for compressive MVTI and fixed viscosity . . . . .	99
4.4.6 Heat flux for compressive MVTI at fixed viscosity . . . . .	100
4.4.7 Angular momentum flux for compressive MVTI . . . . .	101
4.4.8 Heat flux for compressive MVTI . . . . .	102
5.2.1 Dispersion relation of the collisionless MRI . . . . .	124
5.2.2 Real growth rate for collisionless MTI . . . . .	125
5.2.3 Imaginary growth rate for collisionless MTI . . . . .	126

5.2.4 Real growth rate of collisionless MTI with varying $\beta$ . . . . .	127
5.2.5 Imaginary growth rate of collisionless MTI with varying $\beta$ . . . . .	128
5.2.6 Angular momentum flux for collisionless MTI . . . . .	132
5.2.7 Heat flux for collisionless MTI . . . . .	133
5.2.8 Angular momentum flux for collisionless MRI . . . . .	134
5.2.9 Angular momentum flux for collisionless MTI and zero shear . . . . .	135
5.3.1 Real and imaginary growth rates of the mildly collisional MTI . . . . .	141
6.1.1 Dispersion relation of the MVTI including finite ion thermal diffusivity	145
6.1.2 Collisionless MRI growth rate for various ion and electron temperatures	146
6.1.3 Real and imaginary parts of the growth rate of the collisionless MTI .	147
6.1.4 Collisionless MTI with finite electron temperature and various plasma $\beta$	149
6.2.1 Growth rate for fluid modes at $z/H = 0$ and three wavenumber slices	152
6.2.2 Growth rate for fluid modes at $z/H = 0$ and unstable wavenumbers .	153
6.2.3 Growth rate for fluid modes at $z/H = 0.5$ and three wavenumber slices	153
6.2.4 Growth rate for fluid modes at $z/H = 0.5$ and unstable wavenumbers	154
6.2.5 Growth rate for fluid modes at $z/H = 1$ and three wavenumber slices	154
6.2.6 Growth rate for fluid modes at $z/H = 1$ and all unstable wavenumbers	155
6.2.7 Collisionless offplane MRI for $k_Z v_{A0}/\Omega = 10^{-1}$ . . . . .	157
6.2.8 Collisionless offplane MRI for $k_Z v_{A0}/\Omega = 10^{-1/2}$ . . . . .	158
6.2.9 Collisionless offplane MRI for $k_Z v_{A0}/\Omega = 1$ . . . . .	159
7.2.1 Landau closure growth rate for collisionless MRI . . . . .	165
7.2.2 Landau closure imaginary growth rate for collisionless MTI . . . . .	166
7.2.3 Landau closure real growth rate for collisionless MTI . . . . .	167
7.2.4 Collisionless MRI with equilibrium pressure anisotropy . . . . .	172
7.2.5 Threshold anisotropy in solar wind due to gyrokinetic instabilities . .	174

7.3.1	Local evolution of total energy within MRI Simulation of Athena code	177
7.3.2	Spatiotemporal range of numerics and observations of black hole accretion	179
B.1	MHD equilibrium in a thin disk, mediated by electrostatic forces . . .	190
E.1	Offplane perpendicular pressure radial magnetic field response $\mathcal{A}_{R\perp}$ .	214
E.2	Offplane perpendicular pressure azimuthal magnetic field response $\mathcal{A}_{\phi\perp}$	215
E.3	Offplane parallel pressure radial magnetic field response $\mathcal{A}_{R\parallel}$ . . . .	216
E.4	Offplane parallel pressure azimuthal magnetic field response $\mathcal{A}_{\phi\parallel}$ . . .	217

# List of Tables

1.4.1 Accretion Flow and X-Ray Luminosities of Dim Galactic Black Holes	29
1.4.2 Dilute Nature of Dim Accreting Galactic Black Holes . . . . .	31
2.3.1 MHD Stability Criteria . . . . .	56
A.1 Table of Variables . . . . .	180
A.2 Table of Normalized and Simplified Variables . . . . .	182
A.3 Physical Parameters Associated With Black Hole Accretion . . . . .	183
E.1 Pressure Response Functions at Midplane For Various $\beta$ . . . . .	213

# Chapter 1

## Introduction

Accretion, the process by which matter collects onto a central object, may be incredibly efficient in converting gravitational energy into heat and radiation. Whereas nuclear fusion of hydrogen into heavier elements converts roughly 0.7% of mass into energy, accretion onto neutron stars or black holes may be as efficient as 15%. Active galactic nuclei (AGNs) and quasars derive their enormous power ( $10^{42} \text{ erg s}^{-1} \lesssim L < 10^{48} \text{ erg s}^{-1}$ ) from this high efficiency accretion onto massive ( $10^7 M_\odot < M < 10^9 M_\odot$ ) and supermassive ( $M > 10^9 M_\odot$ ) central galactic black holes, respectively (Lynden-Bell 1969).

Accretion typically occurs in astrophysical disks. Disks, from scales of a few thousand kilometers in the case of planetary rings to the scale of hundreds of kiloparsecs in the case of galaxies, are ubiquitous in our universe. These rotational plasmas and gases naturally arise from the fact that it is much easier for a system to lose energy rather than angular momentum, and also from the fact that centrifugal forces provide a steeper repulsive potential that can overcome gravitational attraction at sufficiently small radii.

Accretion can occur only if the angular momentum of the rotating gas is trans-

ported outwards, allowing matter to fall inwards. Fluid viscosity in a gas can provide a physical mechanism by which accretion can occur; however, most astrophysical disks are so large that collisional fluid viscous diffusion of angular momentum is ignorable. A central problem in astrophysics, therefore, is to explain how these rotational plasmas can transport angular momentum outwards, accreted matter inwards, and convert gravitational energy into radiation and thermal energy at rates consistent with the observed luminosity of accreting systems or with the expected lifetime of protostellar and protoplanetary systems.

Hydrodynamic turbulence, in light of the well-known result that fluid shear can become turbulent at a low enough viscosity, was proposed decades ago as a mechanism to drive sufficiently fast accretion to explain the luminosity of bright compact astrophysical objects. However, for disks in which the gravitational force originates from a central object, the angular speed of the plasma roughly follows a Keplerian rotation profile; strong epicycles associated with this angular speed profile result in hydrodynamic linear stability. Smooth profiles associated with rotationally supported, non-self-gravitating plasmas are then expected to be stable at all Reynolds numbers.

Velikhov (1959) and Chandrasekhar (1960) were the first to publish an interesting property of magnetized conducting fluids in a Taylor-Couette flow. A Taylor-Couette flow is one in which the fluid is confined between two concentric rotating cylinders. A schematic of a Taylor-Couette flow is given in Fig. (1.3.5). The fluid becomes unstable if angular speed, rather than angular momentum, decreases radially outwards. Balbus & Hawley (1991) applied this to astrophysical accretion flows. They noticed that Keplerian disks would be unstable to the magnetorotational instability (MRI). Numerical simulations showed that the MRI destabilizes a plasma and drives turbulence with the right (outwards) sign and magnitude of angular momentum flux causing astrophysical accretion (Balbus & Hawley 1998). A wide spectrum of local

and global simulations have demonstrated the efficacy of the MRI to drive accretion in a variety of different parameter regimes, in both fully ionized and low ionized systems.

For rotational flows in which the plasma or gas remains collisional, some form of classical accretion disk theory holds sway. Such disks are characterized by the following: their thermal speeds are much smaller than the orbital velocity, implying geometrically thin disks in which the disk height is much smaller than the radius; and the gas is maintained in virial equilibrium by radiative losses as it evolves. For compact objects there is strong evidence of Eddington-level luminosities for AGNs, quasars, and low-mass X-ray binaries (LMXB). In addition to lower-energy classical disks, accretion onto compact objects is characterized by radiation pressure domination in their inner regions.

However, within the past decade, there has been mounting X-ray observational evidence of hot, dilute, highly underluminous accretion onto central galactic black holes. These accretion plasmas are geometrically thick, optically thin, radiatively inefficient (only a small fraction of the energy generated through gravitational infall is radiated), and are at best only marginally collisional at the radius at which the accretion gas is gravitationally captured. Gas spectroscopic and stellar radial observations strongly imply the ubiquity of massive to supermassive central galactic black holes in spiral galaxies (Richstone et al. 1998). Hot underluminous accretion, rather than the extreme luminosity expected of AGNs and quasars, might therefore be the overwhelmingly common state of accretion onto compact objects. Analogues of the MRI, in which viscous rather than Lorentz forces lead to destabilizing torques (Balbus 2004b), as well as thermal instabilities that are driven by adverse temperature instead of entropy gradients (Balbus 2001), may also operate in these dilute plasmas. This motivates our research.



## 1.1 Organization of the Thesis

In §1, we discuss the geometry of an accretion disk and the algebraic nomenclature of equilibrium and perturbed quantities. We explain simple accretion models that constrain the mass inflow into these compact objects. We discuss classical disk accretion, characterized by efficient radiation within a virialized and geometrically thin disk, to demonstrate that angular momentum must be carried outward for accretion to occur. We demonstrate the insufficiency of hydrodynamics to produce turbulence in most accretion disks. We then discuss the observational evidence of highly underluminous (i.e., five orders of magnitude below what can be expected from efficient accretion) accretion black holes, for example in the center of our galaxy, and describe phenomenological models of underluminous accretion.

We begin in §2 with a physical model of the MRI and into a linear stability analysis. We continue with local numerical simulations of Keplerian disks, and discuss global simulations of nonradiative magnetized accretion flows unstable to the MRI. In §2.3, we discuss other instabilities, the magnetothermal instability (MTI) and magnetoviscous instability (MVI), that arise in dilute magnetized plasmas. Balbus (2001, 2004b) demonstrated that even magnetic fields too weak to provide significant Lorentz forces allow viscous stresses and heat fluxes along magnetic field lines to sharply destabilize the flow. We discuss the stability of systems that would be convectively stable by the classical Schwarzschild criterion but are destabilized by the MTI. We also show results of 3D (Parrish & Stone 2006) numerical simulations that confirm the linear analysis.

In §3 we focus on the equilibrium structure and the nature of accretion, driven by turbulence, of dilute magnetized accretion disks. We discuss the form of disk equilibrium to be used in further stability analysis and in future numerical simulations. A more detailed analysis of the local vertical profile of thin, weakly magnetized dilute

rotating disks is discussed in Appendix B. We derive expressions for energy and angular momentum carried by this turbulence, following a treatment described in Balbus (2004a) for radiatively inefficient accreting magnetized plasmas.

In §4 we discuss instabilities that arise when both viscous stresses and heat fluxes are directed along field lines. We demonstrate that the so-called magnetoviscous-thermal instability (MVTI) has the right properties to drive accretion in dilute flows. We also demonstrate that the effects of finite compressibility, which appear in the limit of finite ratio of magnetic to thermal pressure, does not qualitatively alter our results. We use a fluid theory approach to characterize the stability of these plasmas.

In §5 we recalculate the MVTI for the collisionless regime, which we denote as the collisionless MTI. We demonstrate that the collisionless MTI behaves qualitatively the same as the MVTI, with similar growth rates. We demonstrate that the collisionless MTI approaches the behavior of the MVTI at sufficiently high collisional frequencies, a property seen for the collisionless MRI and noted by Sharma et al. (2003). We also justify and consider simplifications by neglecting electron ion dynamics. In order to examine the behavior of the dilute plasma, we derive the collisionless Boltzmann equation appropriate for MHD stability analyses of dilute magnetized rotationally supported thin disks. This Boltzmann equation is referred to as the drift-kinetic equation (Kulsrud 1983, 2005). In Appendix C we express the perturbed drift-kinetic equation for axisymmetric modes, including noninertial forces in a rotating frame, equilibrium pressure and temperature gradients that drive the collisionless MTI, vertical equilibrium accelerations, separate ion and electron temperatures, and finite collisionality. This is useful for thesis research, as well as for further studies of MHD modes in dilute magnetized plasmas.

In §6 we show the modified MVTI (in the fluid plasma) and the collisionless MTI (in the collisionless plasma) when including the effects of both ion and electron tem-

perature, and by examining the behavior of the plasma away from the disk midplane. Since the plasma is dilute, ions and electrons are not explicitly thermally coupled even when the fluid approximation can describe their dynamics. Furthermore, we study the collisionless MTI away from the midplane due to the fact that electrons feel an acceleration larger than that of the ions by a factor of  $(m_p/m_e)^{1/2}$ . The effect of including both ion and electron dynamics for the MVTI and the collisionless MTI is discussed in Appendix D. The modifications to the collisionless MTI away from the disk midplane is discussed in Appendix E. We demonstrate that for astrophysical radiatively inefficient flows, in which ion temperatures are expected to be equal to or larger than electron temperatures, that a simplified one-temperature plasma is valid. Second, we show that the collisionless MTI and the MVTI are not substantially modified away from the midplane in low-magnetized plasmas.

Finally, in §7 we summarize our results and explain modifications to numerical codes to allow for nonlinear development of the collisionless MTI and MVTI. We discuss the form of heat fluxes that approximately model the collisionless or mildly collisional behavior of a plasma with equilibrium radial gradients of temperature and pressure. We discuss the effects of beyond-MHD physics that may ensure that the plasma viscous stress is kept from becoming too large. We suggest additional ideas to improve nonlinear MHD modeling of this important and predominant class of nonradiating flow, as well as additional physical effects that can be explored analytically.

## 1.2 Nomenclature

Our coordinate system for the rotating disk is a cylindrical system located about the central mass.  $R$  is the radial coordinate,  $\phi$  is the azimuthal angle, and  $z$  the vertical coordinate aligned along the axis of rotation.  $(\hat{\mathbf{R}}, \hat{\boldsymbol{\phi}}, \hat{\mathbf{z}})$  refer to unit vectors

in the radial, azimuthal, and vertical directions, respectively. For field variables of temperature  $T$ , pressure  $p$ , density  $\rho$ , electric and magnetic fields  $\mathbf{E}$  and  $\mathbf{B}$ , and heat flux  $\mathbf{q}$ , we use the following notation:

- Equilibrium value of, say density:  $\rho_0$ ,
- Perturbed density:  $\delta\rho$ ,
- Total density (equilibrium + perturbed):  $\rho = \rho_0 + \delta\rho$ .

For velocity, we use the following notation:

- Primary equilibrium flow velocity, which is azimuthal:  $\mathbf{V}_0 = R\Omega(R)\hat{\phi}$ , where  $\Omega(R)$  is the orbital angular velocity,
- Perturbed flow velocity:  $\delta\mathbf{u}$ ,
- Total flow velocity:  $\mathbf{V} = R\Omega(R)\hat{\phi} + \delta\mathbf{u}$ .

In our initial calculations we use a single fluid model of MHD for the plasma. The single-fluid MHD system of equations consists of mass continuity (Eq. [1.2.1]), force balance (Eq. [1.2.2]), energy balance (Eq. [1.2.3]), and magnetic induction (Eq. [1.2.4]).

$$\frac{\partial\rho}{\partial t} + \nabla \cdot (\rho\mathbf{V}) = 0, \quad (1.2.1)$$

$$\rho \left( \frac{\partial\mathbf{V}}{\partial t} + \mathbf{V} \cdot \nabla \mathbf{V} \right) = -\rho \nabla \Phi - \nabla \left( p + \frac{B^2}{8\pi} \right) + \frac{\mathbf{B} \cdot \nabla \mathbf{B}}{4\pi} - \nabla \cdot \boldsymbol{\sigma}, \quad (1.2.2)$$

$$\frac{3}{2}p \left( \frac{\partial}{\partial t} + \mathbf{V} \cdot \nabla \right) \ln p \rho^{-5/3} = \nabla \cdot \mathbf{q} - \boldsymbol{\sigma} : \nabla \mathbf{V}, \quad (1.2.3)$$

$$\frac{\partial\mathbf{B}}{\partial t} = \nabla \times (\mathbf{V} \times \mathbf{B}), \quad (1.2.4)$$

where  $\boldsymbol{\sigma}$  is the viscous stress tensor,  $\mathbf{q}$  is the heat flux, and  $\boldsymbol{\sigma} : \nabla \mathbf{V} = \sum_{ij} \sigma_{ij} \partial_i V_j$  is the viscous heating of the gas. If we transform to a frame comoving with the equilibrium

rotational flow,  $\mathbf{V}_0 = R\Omega(R, z)\hat{\phi}$ , Eqs. (1.2.1), (1.2.2), (1.2.3), and (1.2.4) reduce to the following:

$$\left(\frac{\partial}{\partial t} + \Omega\frac{\partial}{\partial\phi}\right)\rho + \mathbf{u} \cdot \nabla\rho + \rho(\nabla \cdot \mathbf{u}) = 0, \quad (1.2.5)$$

$$\begin{aligned} \rho \left( \left[ \frac{\partial}{\partial t} + \Omega\frac{\partial}{\partial\phi} \right] \mathbf{u} + \mathbf{u} \cdot \nabla\mathbf{u} + 2\Omega\hat{\mathbf{z}} \times \mathbf{u} + \Omega'Ru_R\hat{\phi} + R\frac{\partial\Omega}{\partial z}u_Z\hat{\mathbf{z}} \right) = \\ - \nabla \left( p + \frac{B^2}{8\pi} \right) + \frac{\mathbf{B} \cdot \nabla\mathbf{B}}{4\pi} - \nabla \cdot \boldsymbol{\sigma}, \end{aligned} \quad (1.2.6)$$

$$\frac{3}{2}p \left( \frac{\partial}{\partial t} + \Omega\frac{\partial}{\partial\phi} \right) \ln p\rho^{-5/3} + \frac{3}{2}p\mathbf{u} \cdot \nabla \ln p\rho^{-5/3} = \nabla \cdot \mathbf{q} - \boldsymbol{\sigma} : \nabla\mathbf{u}, \quad (1.2.7)$$

$$\begin{aligned} \left( \frac{\partial}{\partial t} + \Omega\frac{\partial}{\partial\phi} \right) \mathbf{B} + \mathbf{u} \cdot \nabla\mathbf{B} = -\mathbf{B}(\nabla \cdot \mathbf{u}) + \mathbf{B} \cdot \nabla\mathbf{u} + \Omega'RB_R\hat{\phi} + \\ R\frac{\partial\Omega}{\partial z}B_Z\hat{\phi}. \end{aligned} \quad (1.2.8)$$

We have allowed for the angular velocity to vary as height; however, the analysis of an equilibrium disk in Appendix B demonstrates that the orbital velocity is independent of  $z$ . Except where denoted, we take  $\Omega$  to be a function of  $R$  alone.

When we consider the dynamics of a dilute system, we use an electron-ion plasma. In these systems, the ions and electrons are only very weakly coupled collisionally, and therefore the pressure of both species may differ significantly. In an electron-ion plasma,  $p_i$  refers to ion pressure,  $p_e$  to electron pressure, and  $p_s$  to “species” pressure – either ion or electron. Furthermore, quantities such as equilibrium ion pressure will be denoted as  $p_{i0}$ . All tables are given in Appendix A. The list of variables used in the body of the thesis are enumerated in Table (A.1). The normalized and simplified variables are given in Table (A.2). Important physical parameters associated with massive and supermassive black hole accretion are given in Table (A.3).

Finally, we denote radial equilibrium gradients of density, temperature, and pressure as the following,

$$\frac{\partial \rho_0}{\partial R} \equiv \left. \frac{\partial \rho_0}{\partial R} \right|_{R,z=0}, \quad (1.2.9)$$

$$\frac{\partial T_0}{\partial R} \equiv \left. \frac{\partial T_0}{\partial R} \right|_{R,z=0}, \quad (1.2.10)$$

$$\frac{\partial p_0}{\partial R} \equiv \left. \frac{\partial p_0}{\partial R} \right|_{R,z=0}. \quad (1.2.11)$$

The variables  $T_0(R) \equiv T_0(R, z = 0)$ ,  $p_0(R) \equiv p_0(R, z = 0)$ , and  $n_0(R) = n_0(R, z = 0)$ . This compact notation is used in §3 - §7, and Appendices B and C.

### 1.3 Classical Accretion as Applied to Compact Objects

Here we describe simple models of accretion onto massive and supermassive black holes. The luminosity of these black holes can be estimated from their maximum accretion rate (Eddington), or the maximum rate due to gravitational capture of the ambient medium (Bondi rate). We describe the classical model of accretion onto compact objects (Pringle 1981; Frank et al. 2002). This classical model of accretion relates the rate of outward radial angular momentum flux to the luminosity and spectrum of accreting compact objects. However, this model does not describe the physical mechanism for outward angular momentum transport. One mechanism by which angular momentum can be transported outwards is through a collisional viscosity. However, in accretion disks we show that this mechanism is far too low to explain observed rates of accretion into compact objects.

In Fig. (1.3.1) we show an artist's depiction of the innermost regions of an AGN

or a quasar. The source of accretion matter for this black hole is either the ambient medium gravitationally captured by the black hole or winds from surrounding massive stars.



Fig. 1.3.1.— Artist's conception of the innermost region of an AGN, in which we have high mass rate disk-like accretion onto a supermassive black hole, This picture is taken from the [http://chandra.harvard.edu/photo/2006/j1655/j1655\\_ill\\_agn.jpg](http://chandra.harvard.edu/photo/2006/j1655/j1655_ill_agn.jpg)

### 1.3.1 Eddington and Bondi Limits to Accretion

The maximum luminosity of an object, known as the Eddington luminosity, occurs when radiation forces balance out gravitational forces. To estimate this luminosity, consider the simplest case of spherically symmetric accretion. The outward radiative force per particle is  $F\sigma_T/c$ , where  $F = L/(4\pi R^2)$  is the radiative flux,  $\sigma_T = 6.65 \times$

$10^{-25} \text{ cm}^{-2}$  is the Thomson scattering cross section, and  $R$  is the radial distance from the central object. The gravitational force per particle is  $GMm_p/R^2$ . The Eddington luminosity is given by,

$$L_{\text{edd}} = \frac{4\pi GMm_p c}{\sigma_T} \simeq 1.3 \times 10^{38} \left( \frac{M}{M_\odot} \right) \text{ erg s}^{-1}. \quad (1.3.1)$$

The Eddington accretion rate for 10% efficiency for matter to energy conversion is,

$$\dot{M}_{\text{edd}} = 2.3 \times 10^{-8} \left( \frac{M}{M_\odot} \right) M_\odot \text{ yr}^{-1}. \quad (1.3.2)$$

Quasars and AGNs have bolometric luminosities on the order of  $10^{42} - 10^{47} \text{ erg s}^{-1}$  (Richards et al. 2006). These luminosities are all consistent with Eddington accretion rates for massive ( $10^5 M_\odot \lesssim M < 10^7 M_\odot$ ) and supermassive ( $M \gtrsim 10^7 M_\odot$ ) black holes. Furthermore, such systems are, in their inner regions, dominated by radiation pressure. The photon bubble instability (Arons 1992; Gammie 1998) may allow for the advection of radiative energy through buoyant bubbles (Blaes & Socrates 2001; Begelman 2006a) and can allow for relatively long-term super-Eddington accretion rates (mass accretion rates larger than estimated in Eq. [1.3.2]) in ultra-luminous X-ray sources (Turner et al. 2005; Begelman 2006b). It may also be possible that most of the energy in optically thick, radiation pressure dominated plasmas could be advected into the black hole (Begelman 1978; Abramowicz et al. 1988), leading to super-Eddington accretion rates.

For central massive and supermassive black holes the primary mechanism for accretion in the outer regions is the gravitational capture of the ambient gas. Bondi (1952) first analyzed the result of spherical accretion of gas, with a specific polytropic equation of state, onto a central object. The general class of largely spherically symmetric and pressure-supported accretion or winds onto a central object is referred to



as Bondi flow. Many elaborations of Bondi flow can be found in the literature. Most explorations focus on either finite heating or cooling (Mestel 1954), finite thermal conductivity or viscosity (Johnson & Quataert 2007), or on partial rotational support (Proga & Begelman 2003). However, to within an order of magnitude one can estimate the Bondi mass accretion rate using dimensional analysis from the ambient gas density and temperature, and the central mass of the object. At the gravitational capture radius the escape velocity from the central object equals the local sound speed. The mass accretion rate can be estimated by assuming that matter, at the ambient density, flows inward through a sphere of the capture radius at the sound speed. The actual capture radius and Bondi mass accretion rate differ from these estimates by factors of order unity.

Consider one of the simplest types of Bondi flow: a simple ion-electron plasma in steady state with equal ion and electron temperatures  $T$ , an adiabatic equation of state  $p \propto \rho^\gamma$ , no fluid viscosity, and a spherically symmetric radial flow of matter. If  $\gamma > 1$ , Eqs. (1.2.1) and (1.2.2) can be reduced into the following forms,

$$4\pi r^2 \rho(r) u_r(r) = \dot{M}, \quad (1.3.3)$$

$$\frac{1}{2} u_r(r)^2 + \frac{\gamma}{\gamma-1} \theta_\infty \left( \frac{\rho}{\rho_\infty} \right)^{\gamma-1} - \frac{GM}{r} = \mathcal{B}, \quad (1.3.4)$$

where  $r$  is the spherical radial coordinate and  $u_r$  is the spherical radial flow velocity.  $\mathcal{B} = \frac{\gamma}{\gamma-1} \theta_\infty$  is the Bernoulli parameter,  $\theta_\infty = 2k_B T_\infty / m_p$  is the ambient isothermal sound speed squared, and  $T_\infty$  is the temperature at “infinity” (far from the gravitational influence of the central object). For isothermal flow, Eq. (1.3.4) is modified in the following manner:

$$\frac{1}{2} u_r(r)^2 + \theta_\infty \ln \left( \frac{\rho}{\rho_\infty} \right) - \frac{GM}{r} = 0 \quad (1.3.5)$$

At mass flow rates below the maximum accretion rate, Bondi flows are constrained to be inflowing solutions, everywhere with subsonic infall velocity. One can show that the maximum accretion rate associated with interaction of an object of mass  $M$  residing within a medium at  $\rho_\infty$  and  $\theta_\infty$ ,

$$\frac{\dot{M}_{\text{Bondi}}^2 \theta_\infty^3}{G^4 M^4 \pi^2 \rho_\infty^2} = \begin{cases} \gamma^{-3} \left( \frac{2}{5-3\gamma} \right)^{\frac{5-3\gamma}{\gamma-1}}, & 1 < \gamma \leq 5/3 \\ e^3. & \gamma = 1 \end{cases} \quad (1.3.6)$$

$\dot{M}_{\text{Bondi}}$  can be expressed in terms of physical parameters convenient for our area of interest. For a gas equation of state  $\gamma = 5/3$ .

$$\dot{M}_{\text{Bondi}} = 1.02 \times 10^{-4} \left( \frac{M}{10^7 M_\odot} \right)^2 \left( \frac{n_\infty}{100 \text{ cm}^{-3}} \right) \left( \frac{T_\infty}{10^7 \text{ K}} \right)^{-3/2} M_\odot \text{ yr}^{-1}. \quad (1.3.7)$$

A 10% matter-energy conversion efficiency gives Bondi accretion luminosities,

$$\begin{aligned} L_{\text{Bondi}} &= 0.1 \dot{M}_{\text{Bondi}} c^2 \\ &= 5.84 \times 10^{41} \left( \frac{M}{10^7 M_\odot} \right)^2 \left( \frac{n_\infty}{100 \text{ cm}^{-3}} \right) \left( \frac{T_\infty}{10^7 \text{ K}} \right)^{-3/2} \text{ erg s}^{-1}. \end{aligned} \quad (1.3.8)$$

Bondi flows in which the equation of state  $\gamma < 5/3$  become transonic at the maximal accretion rate  $\dot{M}_{\text{Bondi}}$ . The gas falls from infinity subsonically up to the sonic point, where the infall speed equals the local sound speed. Inside the sonic point, the gas flows in supersonically. However, for a  $\gamma = 5/3$  equation of state gas, this sonic point is located at the origin, therefore the flow at any allowable mass rate is subsonic. Another solution at maximum outflow rates is one of a transonic wind, in which the gas outflow velocity is subsonic inside the sonic point and supersonic outside it. Early models of the solar wind, for example, were fit to transonic Bondi outflow solutions (Parker 1958b). Plots of the Bondi flow Mach number as a function of the radius are

shown for a  $\gamma = 4/3$  plasma, in Fig. (1.3.2).

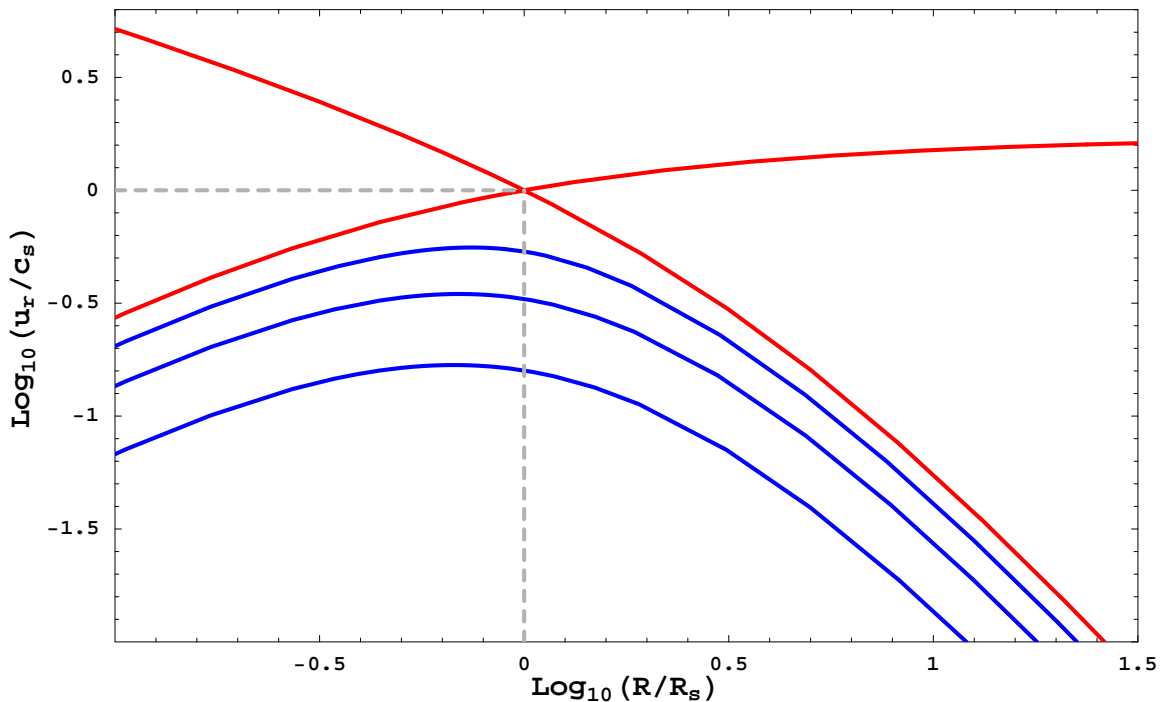


Fig. 1.3.2.— Plot of the Bondi Mach number (radial flow speed divided by sound speed  $c_s$ ) as a function of radius (normalized by gravitational capture radius) for physically allowable Bondi solutions. Lines in blue denote settling solutions, at accretion rates  $\dot{M} = \frac{3}{4}\dot{M}_{\text{Bondi}}$ ,  $\frac{1}{2}\dot{M}_{\text{Bondi}}$ , and  $\frac{1}{4}\dot{M}_{\text{Bondi}}$  moving down from the sonic point. The transonic inflow (subsonic outside a sonic point, supersonic inside) and transonic outflow (subsonic inside the sonic point, and supersonic outside) are shown in red.

### 1.3.2 Classical Accretion Disk Theory

In this section, we explain the salient physical features by which matter in a rotationally supported flow can accrete. We focus on classical accretion disk theory, which is characterized by the following major simplifications. One, the disk is geometrically thin, i.e. the disk height  $H$  is much smaller than the radius  $R$ . The gas thermal velocities are much smaller than orbital velocities, and therefore the gas follows an approximately Keplerian rotation profile,  $\Omega^2 \approx GM/R^3$ . Two, the gas is in virial equilibrium, which implies that at least half the energy generated through gravita-

tional infall of matter is radiated away in the accretion disk itself. This disk has an inner radius  $R_{\text{in}}$  and an outer radius  $R_{\text{out}}$ . For a neutron star or white dwarf,  $R_{\text{in}}$  may correspond to the surface of the star, while for a black hole it may correspond to its marginally stable orbit ( $R_{\text{in}} = 6GM/c^2$  for a Schwarzschild black hole) or perhaps even the event horizon (Krolik et al. 2005). A diagram of the mechanism of a classical accretion flow is shown in Fig. (1.3.3).

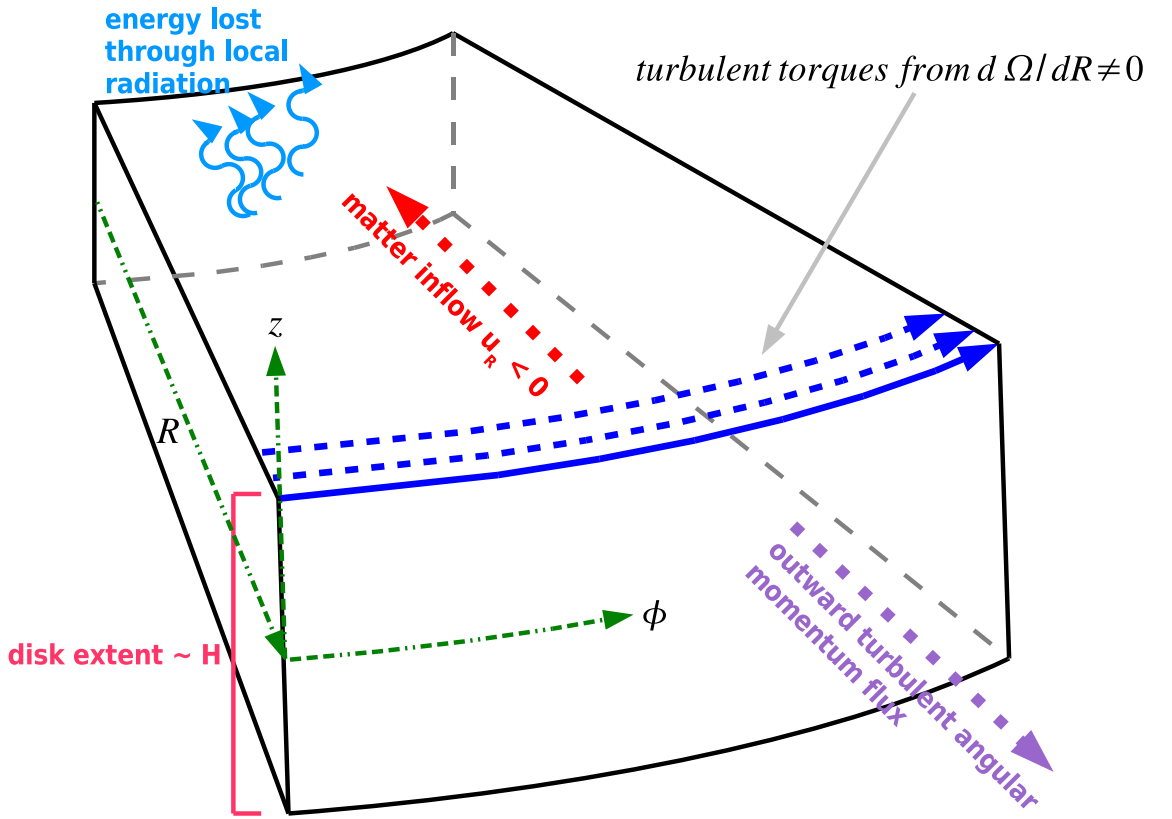


Fig. 1.3.3.— Classical accretion flows in a geometrically thin ( $H \ll R$ ) and optically thick disk. Turbulent torques arise via some physical mechanism due to nonrigid rotation,  $d \ln \Omega / d \ln R \neq 0$ . Turbulent torques transport angular momentum outwards, resulting in matter accretion. In classical disks, energy generated through accretion is locally radiated through the disk's vertical surfaces.

Note that for high mass rate accretion onto compact objects, the fluid has negligi-

ble viscosity over most of the spatial extent of the disk. By high mass accretion rates, we refer to infalling rates at either the Bondi or Eddington luminosities. Spectral models of emission from high mass accretion rate supermassive black holes suggest ion densities of the order  $10^9 - 10^{12} \text{ cm}^{-3}$  and ambient gas temperatures of the order of  $10^6 - 10^8 \text{ K}$  at the gas gravitational capture radius, of size  $10^{16} - 10^{18} \text{ cm}$ . Obviously, as one moves closer to the black hole, the plasma gets hotter and denser. The ion-ion and electron-electron collisional mean free paths are given by (Spitzer 1962),

$$\lambda_i = 1.5 \times 10^{13} \left( \frac{T}{10^4 \text{ K}} \right)^2 \left( \frac{n}{1 \text{ cm}^{-3}} \right)^{-1} \frac{1}{\ln \Lambda} \text{ cm}, \quad (1.3.9)$$

$$\lambda_e = 1.1 \times 10^{13} \left( \frac{T}{10^4 \text{ K}} \right)^2 \left( \frac{n}{1 \text{ cm}^{-3}} \right)^{-1} \frac{1}{\ln \Lambda} \text{ cm}. \quad (1.3.10)$$

Here  $\ln \Lambda \sim 20$  is the Coulomb logarithm,

$$\ln \Lambda = \ln \left( \frac{\lambda_{De}}{r_{\pi/2}} \right), \quad (1.3.11)$$

where  $\lambda_{De}$  is the Debye length (length scale over which electric fields are screened by the intervening plasma) and  $r_{\pi/2}$  is the ion impact parameter for a collision in which each particle has kinetic energy  $k_B T_i$ , and scatters by an angle  $\pi/2$ , in the center-of-mass frame. For the same ion and electron temperatures,  $\lambda_{De}$  and  $r_{\pi/2}$  can be expressed as,

$$\lambda_{De} = \sqrt{\frac{k_B T_i}{8\pi e^2 n_i}}, \quad (1.3.12)$$

$$r_{\pi/2} = \frac{e^2}{4k_B T_i}. \quad (1.3.13)$$

The Reynolds number  $\text{Re} = LV/\eta_\nu$  is the ratio of flow velocity to the collisional viscous velocity, where  $L$  and  $V$  are the system sizes and velocities, respectively. We

estimate  $L \sim R$  and the velocity as the isothermal sound speed. For these flows,  $\text{Re} = R/\lambda_i$  is on the order of  $10^7 - 10^{10}$ . Collisional viscosity is too small to explain the dynamics of accretion onto compact objects.

We now consider a simple model of classical accretion driven by hydrodynamic turbulence to demonstrate the presence of a turbulent torque that can transport angular momentum outwards, using arguments laid out in Balbus & Hawley (1998). We assume a disk that is steady and spatially smooth over time and length scales much larger than the turbulence. The fluctuation in fluid velocities  $(u_\phi, u_z)$ , magnetic field  $\mathbf{B}$ , and density  $\rho$  average to zero.

$$\langle \delta u_\phi \rangle_\rho = \langle \delta u_z \rangle_\rho = 0, \quad (1.3.14)$$

$$\langle \delta \mathbf{B} \rangle_\rho = \mathbf{0}, \quad (1.3.15)$$

$$\langle \delta \rho \rangle_\rho = 0.. \quad (1.3.16)$$

This average,  $\langle \rangle_\rho$ , is defined in the following manner:

$$\langle A \rangle_\rho = \frac{1}{2\pi\Sigma\Delta R\Delta T} \int_0^{\Delta T} \int_{R-\Delta R/2}^{R+\Delta R/2} \int_{\phi=0}^{2\pi} \int_{z=-\infty}^{\infty} A \rho \, dR' \, dz \, d\phi \, dt, \quad (1.3.17)$$

where,

$$\Sigma = \int_{z=-\infty}^{\infty} \rho \, dz. \quad (1.3.18)$$

This average is taken over a radial slice  $\Delta R$  much smaller than the disk radius but larger than the largest scale of the turbulence and a time scale  $\Delta T$  much longer than the turnover timescale of the turbulence. The radial velocity  $u_R$  consists of a fluctuating part  $\langle \delta u_R \rangle_\rho = 0$  and a nonzero mean mass flow. The mean flow velocity is far smaller than the root mean square turbulent velocity, i.e.,  $\langle u_R \rangle_\rho \ll \sqrt{|\langle \delta u_R \delta u_\phi \rangle_\rho|}$ .

We consider a system without collisional viscosity or thermal conductivity in steady state, but with a radiative flux that can cool the gas. Equations of mass continuity (Eq. [1.2.1]), force balance (Eq. [1.2.2]), and energy (Eq. [1.2.3]), then reduces to,

$$\nabla \cdot (\rho \mathbf{V}) = 0, \quad (1.3.19)$$

$$\rho \mathbf{V} \cdot \nabla \mathbf{V} = -\rho \nabla \Phi - \nabla \left( p + \frac{B^2}{8\pi} \right) + \frac{\mathbf{B} \cdot \nabla \mathbf{B}}{4\pi}, \quad (1.3.20)$$

$$\frac{3}{2} \rho \mathbf{V} \cdot \nabla \left( \frac{p}{\rho} \right) + p \nabla \cdot \mathbf{V} = -\nabla \cdot \mathbf{F}_{\text{rad}}. \quad (1.3.21)$$

where  $\mathbf{F}_{\text{rad}}$  is the radiative flux. We ignore radial pressure gradients in Eq. (1.3.20) since the disk is thin. In a thin disk, radial force balance results in a Keplerian rotation profile and vertical force balance results in a disk height on the order of  $H$ . The azimuthal component of Eq. (1.3.20), multiplied by  $R$ , can be written as,

$$\frac{1}{R} \frac{\partial}{\partial R} R^2 \left( \rho V_\phi V_R - \frac{B_R B_\phi}{4\pi} \right) = 0, \quad (1.3.22)$$

where  $R \left( \rho V_\phi V_R - \frac{B_R B_\phi}{4\pi} \right)$  is the total radial flux of angular momentum. It includes terms associated with angular momentum flux carried by the radial flow as well as angular momentum flux due to the hydromagnetic turbulence. If we take the scalar product of Eq. (1.3.20) with  $\mathbf{V}$  and add to Eq. (1.3.21) we then have the total energy balance equation:

$$\nabla \cdot \left( \mathbf{V} \left( \frac{1}{2} \rho v^2 + \rho \Phi \right) + \frac{\mathbf{B}}{4\pi} \times (\mathbf{V} \times \mathbf{B}) \right) = -\nabla \cdot \mathbf{F}_{\text{rad}}, \quad (1.3.23)$$

where we have ignored the enthalpy flux of a monotonic gas ( $5p\mathbf{V}/2$ ) due to the thinness of the disk.

For a thin disk, one may use lowest-order techniques to characterize the role that turbulence will play in transferring mass and angular momentum in an accretion disk. The turbulent flow speeds in a disk with subthermal magnetic fields will only reach the local sound speed due to the fast dissipation of supersonic turbulence through shocks. Because the turbulent flow speeds are much smaller than the orbital velocity, then to lowest order quadratic fluctuating fluid correlations of velocity and magnetic field can be used to characterize the accretion flow. It is the averaged quadratic correlations between radial and azimuthal velocities, and radial and azimuthal magnetic fields, that acts as an outward flux of angular momentum that allows accretion to occur.

First, consider mass flow. If we average Eq. (1.3.19) as described in Eq. (1.3.17), the mass accretion rate is related to the average radial flow:

$$\dot{M} = -2\pi R\Sigma \langle u_R \rangle_\rho. \quad (1.3.24)$$

Second, consider angular momentum balance. We use the boundary conditions that the radial flux of angular momentum is zero at  $R_{\text{in}}$ . If we take the average of Eq. (1.3.22), and use the mass flow relation in Eq. (1.3.24), we get,

$$\langle W_{R\phi} \rangle = \frac{\dot{M}\Omega}{2\pi\Sigma} \left[ 1 - (R_{\text{in}}/R)^{1/2} \right], \quad (1.3.25)$$

where  $W_{R\phi}$  is the  $R\phi$  component of the stress tensor, defined by,

$$\langle W_{R\phi} \rangle = \left\langle \delta u_R \delta u_\phi - \frac{\delta B_R \delta B_\phi}{4\pi\rho_0} \right\rangle_\rho. \quad (1.3.26)$$

$R\rho \langle W_{R\phi} \rangle$  is the angular momentum radial flux carried by the turbulence. This turbulence must yield  $\langle W_{R\phi} \rangle_\rho > 0$  in order for accretion to occur. Eqs. (1.3.24), (1.3.25), (1.3.26) and sonic turbulence imply mass flow velocities  $|\langle u_R \rangle_\rho| \sim \langle \delta u_R \delta u_\phi \rangle_\rho / (R\Omega)$ .



Third, expressions for mass and angular momentum flux are used to calculate the energy flux carried by the accretion flow. To lowest order, Eq. (1.3.23) can be written as,

$$\nabla \cdot \left( \rho u_R \hat{\mathbf{R}} \left[ \Phi + \frac{1}{2} R^2 \Omega^2 + R \Omega u_\phi \right] - R \Omega \frac{\delta B_R \delta B_\phi}{4\pi} \hat{\mathbf{R}} \right) = -\nabla \cdot \mathbf{F}_{\text{rad}}. \quad (1.3.27)$$

Using the Keplerian result  $\Phi = -R^2 \Omega^2$ , and averaging Eq. (1.3.23), we get,

$$\frac{1}{R} \frac{\partial}{\partial R} R \left( \frac{\dot{M} R \Omega^2}{4\pi} + \Sigma R \Omega \langle W_{R\phi} \rangle \right) = -\nabla \cdot \mathbf{F}_{\text{rad}}. \quad (1.3.28)$$

$\mathcal{F}_E$ , the energy flux carried by the accretion flow, is

$$\mathcal{F}_E = \frac{\dot{M} R \Omega^2}{4\pi} + \Sigma R \Omega \langle W_{R\phi} \rangle = \frac{3GM\dot{M}}{4\pi R^2} \left[ 1 - \frac{2}{3} (R_{\text{in}}/R)^{1/2} \right]. \quad (1.3.29)$$

In a radiatively efficient disk, the energy flux is radiated. The accretion luminosity is then given by:

$$\begin{aligned} L_{\text{acc}} &= 2\pi (R_{\text{in}} \mathcal{F}_E(R_{\text{in}}) - R \mathcal{F}_E(R_{\text{out}})) \\ &= \frac{GM\dot{M}}{2R_{\text{in}}} \left( 1 - 3 \frac{R_{\text{in}}}{R_{\text{out}}} + \frac{3}{2} \left( \frac{R_{\text{in}}}{R_{\text{out}}} \right)^{3/2} \right) \end{aligned} \quad (1.3.30)$$

If the outer edge of the disk  $R \gg R_{\text{in}}$ , then up to half the gravitational energy may be radiated away. The other half can either be accreted on the surface of a star or, in the case of black holes, lost as it passes through the event horizon. For a given  $\dot{M}$ , classical disk-like accretion onto a compact object can be extremely efficient. When  $\dot{M}$  is sufficiently large, the high luminosity of AGNs and quasars can be easily explained.

Classical accretion also has a characteristic spectrum. In an optically thick disk,

the energy generated through accretion is radiated through the outer disk surfaces as blackbody emission. This blackbody emission at a given radius  $R$  has temperature  $T_{\text{eff}}(R)$ , given by the relation below.

$$\begin{aligned} 2\sigma T_{\text{eff}}^4 &= \frac{1}{R} \frac{\partial}{\partial R} (R\mathcal{F}_E(R)), \\ T_{\text{eff}} &= \left( \frac{3GM\dot{M}}{8\pi R^3\sigma} \left( 1 - \sqrt{\frac{R_{\text{in}}}{R}} \right) \right)^{1/4} \end{aligned} \quad (1.3.31)$$

The factor of 2 arises because radiation escapes from both surfaces of the disk, and  $\sigma = 5.67 \times 10^{-5} \text{ erg cm}^{-2} \text{ s}^{-1} \text{ K}^{-4}$  is Stefan-Boltzmann's constant. For  $R \gg R_{\text{in}}$ , the temperature  $T_{\text{eff}}(R) = T_{\text{in}} (R/R_{\text{in}})^{-3/4}$ , where

$$T_{\text{in}} = \left( \frac{3GM\dot{M}}{8\pi R_{\text{in}}^3\sigma} \right)^{-1/4} \quad (1.3.32)$$

The blackbody spectral radiance  $B_\nu$  at  $T_{\text{eff}}$  is given by,

$$B_\nu(T_{\text{eff}}) \propto \frac{\nu^3}{e^{h\nu/(k_B T_{\text{eff}})} - 1}. \quad (1.3.33)$$

Where  $\nu$  is the frequency of emitted radiation. The emitted spectrum of the whole disk is,

$$S_\nu \propto \int_{R_{\text{in}}}^{R_{\text{out}}} B_\nu(T_{\text{eff}}(R)) 2\pi R dR \quad (1.3.34)$$

This spectrum is shown in Fig. (1.3.4).

### 1.3.3 The Insufficiency of Hydrodynamics

We have derived a theory of classical accretion but have not mentioned the form of  $W_{R\phi}$ . The study of a large class of rotationally supported astrophysical systems can

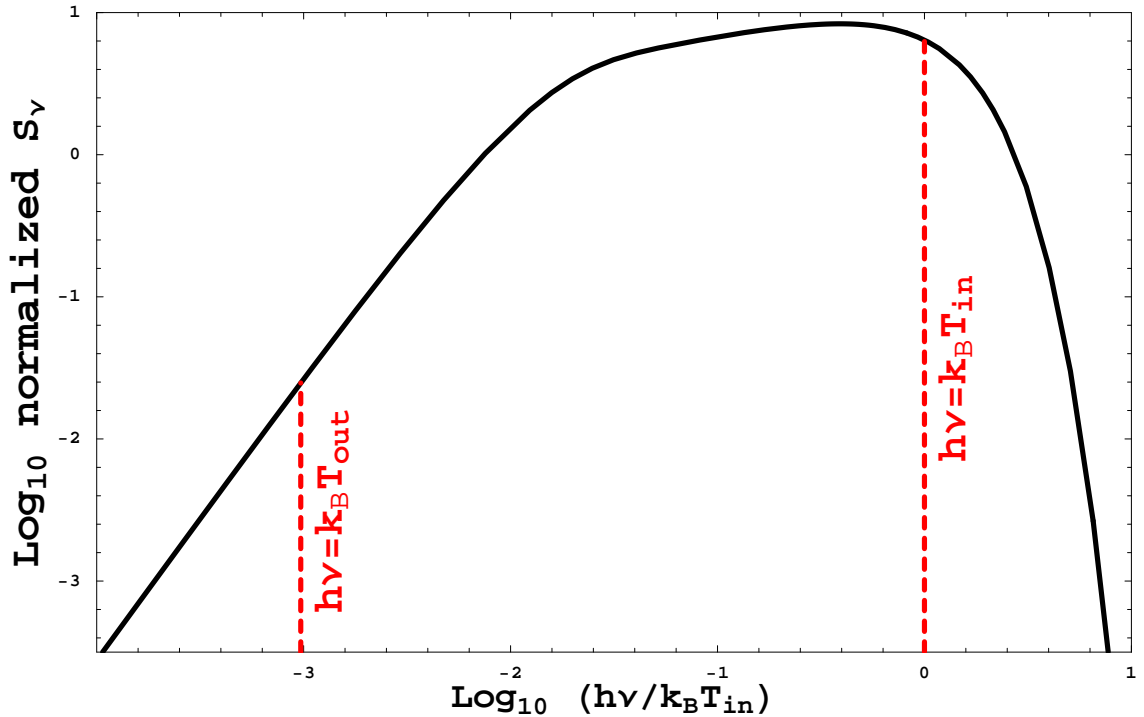


Fig. 1.3.4.— Emission spectrum from a classical accretion disk radiating as a local blackbody at each point, where the outer radius of the disk  $R_{\text{out}} = 1000R_{\text{in}}$ . The frequencies corresponding to emission at  $T_{\text{in}}$  (the temperature of the disk) and  $T_{\text{out}}$  (the temperature at the disk outer edge) are shown with arrows.

be reduced to the study of what physical processes can lead to a significant positive averaged  $\langle W_{R\phi} \rangle$  to drive accretion. For several decades, hydrodynamic turbulence was proposed as a promising mechanism to explain the necessary level of angular momentum transport that can power classical accretion flows or that can yield the relatively fast formation of stars from their protostellar disks. This appeared promising as flows became turbulent, for example, in rigid pipes at low Reynolds numbers of around  $\text{Re} \sim 10^3$  (Batchelor 1967). Furthermore, numerical simulations and experiment have demonstrated the existence of nonlinear hydrodynamic instability and turbulence of a Cartesian shear flow at small Reynolds number  $\sim 10^3$  (Orszag & Kells 1980; Drazin & Reid 1981; Bayly et al. 1988).

Although von Weizsäcker (1948) had proposed a mixing-length theory (analogous

to that of efficient thermal transport in convectively unstable flows) of disk turbulence, Shakura & Sunyaev (1973) proposed an ansatz of  $W_{R\phi}$  applicable to astrophysical accretion flows:

$$\langle W_{R\phi} \rangle = \alpha_{SS} \theta, \quad (1.3.35)$$

where  $\alpha_{SS}$  is some dimensionless parameter. This was justified by the fact that fast shock dissipation would constrain disk turbulence speed to be less than the sound speed  $c_s$ . An alternative ansatz is one in which there is an effective viscosity

$$\eta_{\nu,\text{eff}} = \alpha'_{SS} c_s H, \quad (1.3.36)$$

where  $\alpha'_{SS}$  and  $\alpha_{SS}$  differ by constants of order unity. Analytic or numerical models that employ this form of the effective viscosity or azimuthal tensor are referred to as  $\alpha$ -viscosity accretion models. The benefit of either closure, for a turbulent angular momentum flux or an effective turbulent viscosity, is that a relatively simple dynamical model of an accretion disk can be constructed. One may calculate from  $\dot{M}$  and  $\alpha_{SS}$  the disk mass, density, temperature, and height. In other words, one may calculate the mass accretion rate from the local structure of the disk and vice-versa.

Although hydrodynamic turbulence has for decades been deemed a plausible source for enhanced transport in disks, a Keplerian disk has specific angular momentum varies as  $R^{1/2}$  – increasing outwards. There exist strong stable epicycles that make the flow linearly stable to axisymmetric hydrodynamic perturbations, the so-called Rayleigh criterion. Numerical simulations have demonstrated hydrodynamic stability and dissipation of hydrodynamic turbulence at the limit of computationally accessible Reynolds numbers in local Keplerian rotating systems (Balbus et al. 1996; Hawley et al. 1998).

A recent careful laboratory experiment by Ji et al. (2006) has demonstrated that there is no linear or nonlinear hydrodynamic instability of a Taylor-Couette flow up to a Reynolds number of  $10^6$ . This Reynolds number is beyond the limit of numerical simulation (Lesur & Longaretti 2005) and approximately 20 times that previously achieved in the laboratory (Richard 2001). Ji et al. (2006) studied the stability properties of a Taylor-Couette flow of water or a water/glycerol mixture. A textbook example of a Taylor-Couette flow is shown in Fig. (1.3.5), and a diagram of the setup used in Ji et al. (2006) is shown in Fig. (1.3.6).  $\Omega_1$  and  $r_1$  are the inner cylinder's angular speed and radius, respectively, and  $\Omega_2$  and  $r_2$  are the angular speed and radius of the outer cylinder, respectively. Both cylinders rotate in the same sense, with  $\Omega_2 < \Omega_1$  but  $r_2^2\Omega_2 > r_1^2\Omega_1$ . This ensures an equilibrium rotation profile that is Rayleigh stable. In their setup, Ji et al. (2006) suppressed Ekman circulation by having the endcaps rotate differentially as well. For example, a cup of water takes a few seconds rather than minutes, from viscous diffusion of angular momentum, to lose its spin is due to an Ekman boundary layer at the cup's surface. They found that the angular momentum flux within this rotating system is zero to within experimental measurement. The results of Ji et al. (2006) are shown in Fig. (1.3.7). The Reynolds number of the flow was modified by changing the angular velocity of the inner and outer cylinders or by choosing different mixtures of water and glycerol. They measured a normalized averaged angular momentum flux  $\beta$  at the midplane of their apparatus, defined as,

$$\beta = \frac{\langle u_R u_\phi \rangle}{\langle u_\phi^2 \rangle q^2}, \quad (1.3.37)$$

where  $q = -\partial \ln \Omega / \partial \ln R$ .  $q = 3/2$  for a Keplerian flow, and  $1.2 \leq q \leq 1.9$  for their experimental setup. Although these results do not demonstrate that hydrodynamic

turbulence in Keplerian disks cannot transport angular momentum they appear to imply that the level of angular momentum transport is orders of magnitude smaller than that needed to explain astrophysical accretion.

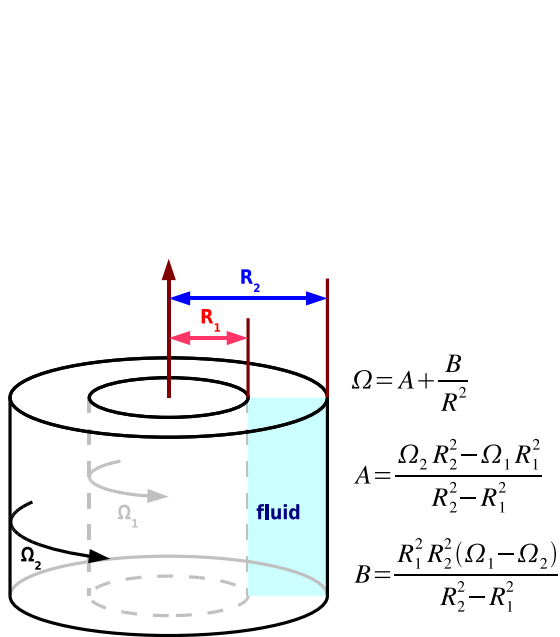


Fig. 1.3.5.— The textbook example of Taylor-Couette flow consists of an inviscid fluid spaced between two cylinders, of infinite vertical extent. Here the cylinders rotate in the same sense, with  $\Omega_2 < \Omega_1$ . As long as fluid specific angular momentum  $R^2\Omega$  increases outwards, the fluid is linearly stable.

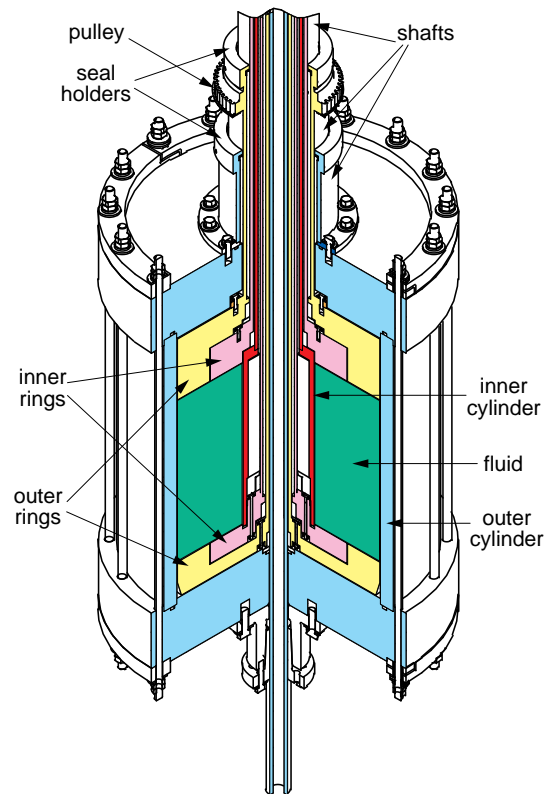


Fig. 1.3.6.— The Princeton experimental setup for a Taylor-Couette flow with water, glycerol, or a mixture of the two, taken from Ji et al. (2006). The inner and outer cylinders rotate in such a manner that the angular speed decreases outwards, but the angular momentum increases outwards. The endcaps also differentially rotate in order to frustrate Ekman circulation.

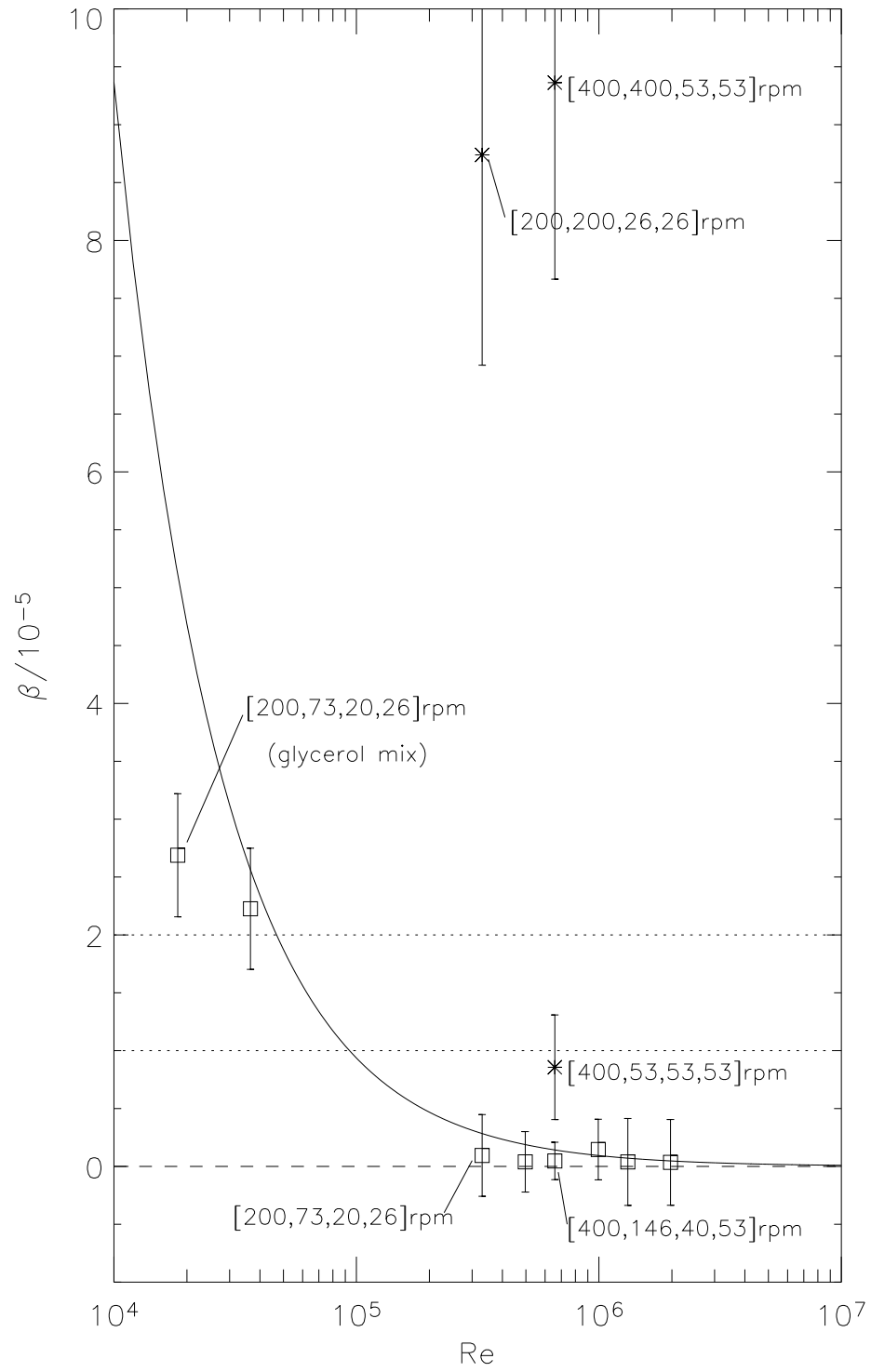


Fig. 1.3.7.— Normalized radial angular momentum flux in Ji et al. (2006) experiment. Angular momentum carried by the this flow was found to be zero to within experimental errors for the highest Reynolds number trials.

One must note that hydrodynamic instabilities can act on other rotationally supported systems to cause accretion. For self-gravitating systems such as galactic or dense protostellar disks, where the Jeans frequency  $\sqrt{G\rho} > \Omega$ , coherent spiral density waves develop (Toomre 1977) that can transport angular momentum and redistribute matter (Adams et al. 1989; Laughlin et al. 1997). A class of nonaxisymmetric instabilities within toroids, first studied by Papaloizou & Pringle (1984, 1985), and elucidated by Goldreich et al. (1986), is one in which waves on opposite sides of a corotation (CR) point can exchange energy with each other. One side of the CR with negative energy loses energy to the other side which has positive energy, hence the process runs away and destabilizes the torus. However, these instabilities require a hard wall or sharp torus edge on either side of the CR point – currently believed unlikely to occur in nature. They also require a rotation profile  $d \ln \Omega / d \ln R < -\sqrt{3}$ . For relatively slender disks in which the gravity is largely due to the central object, accretion does not occur due to hydrodynamic instabilities. Magnetic fields, however, can play a role in destabilizing even Keplerian flows. In §2 we describe the MRI, which has shown such promise in accretion physics.

## 1.4 Evidence for Underluminous Accretion

Although AGNs and quasars are some of the most powerful and most energetic compact objects in the universe, at recent epochs in the history of the universe ( $z < 1$ ) they are rare. Evidence from Very Large Baseline Interferometry (VLBI) measurements of water masers, from gas spectroscopy, and from stellar dynamics give strong evidence for the existence of massive and supermassive black holes in galaxies that possess a central bulge (see Richstone et al. (1998) for an exhaustive review on diagnostic tools for the detection of central galactic black holes). The bulge refers to the



central spherical gaseous and stellar component of a spiral galaxy. However, a very recent survey of AGNs has demonstrated that there exist  $\sim 200$  active black holes within 400 million light-years (see Fig. [1.4.1]). Within this 400 million light-year volume of space there exist  $\sim 10^4$  galaxies that possess a central bulge. Only a few percent of central galactic black holes at the current epoch are AGNs or quasars.

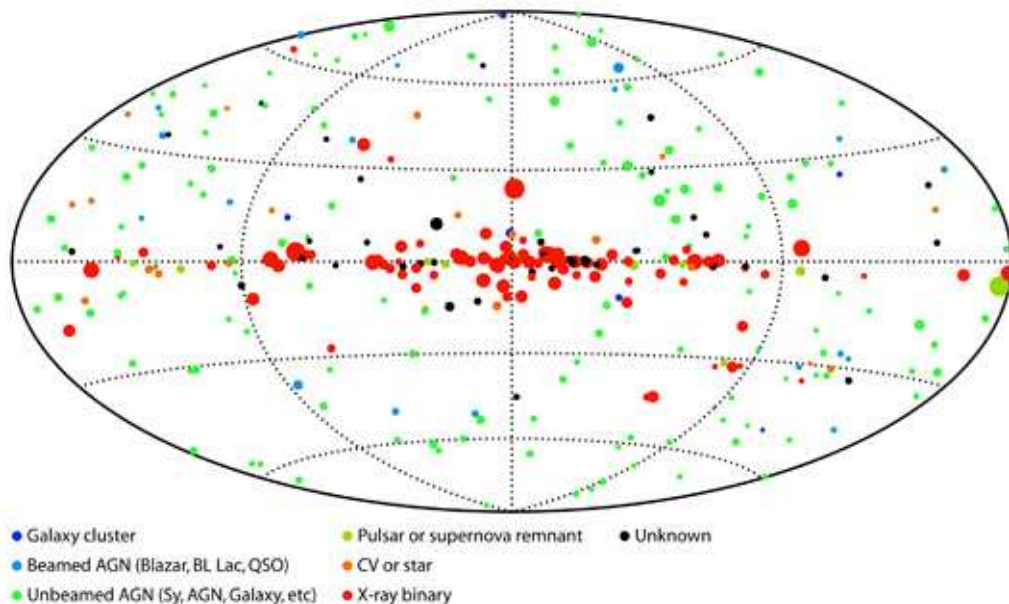


Fig. 1.4.1.— This all-sky map contains all active supermassive black holes out to a distance of 400 million light years from Earth. Scientists are convinced that no active black hole has gone uncoun-  
 counted. Shown here are all high-energy X-ray sources, which includes many star systems within our galaxy which are not part of the Swift black hole survey. The AGN are the light blue and green dots, largely "high" in the sky above and below the galactic plane. Figure and publication of results are taken from theNASA Website.

The Chandra space probe with its X-ray sensitivity and angular resolution of  $1''$  can resolve the inner structure of nearby underluminous galactic black holes to at least a few times the Bondi radius. In Table (1.4.1) we show results of measured emission from nearby galactic black holes, and compare to the expected luminosity from Bondi capture, assuming 10% conversion of matter to energy. Here we include

the Sagittarius A\* black hole at the center of our Milky Way galaxy, the best studied underluminous compact accretor to date. A false-color X-ray emission map of Sag. A\*, taken from Chandra, is shown in Fig. (1.4.2). The mass of the Sag. A\* black hole is far smaller, and its luminosity is far lower, than other nearby central galactic black holes. However, Sag. A\* is visible because it is 100 times closer than the next-nearest central galactic black hole. The measured bolometric emission from Sag. A\* is primarily in the far infrared and radio frequencies at a luminosity of  $L \sim 10^{36}$  erg s $^{-1}$ . This energy is only  $\sim 10^{-5}$  what would be expected from radiatively efficient Bondi accretion (Narayan 2002; Quataert 2003).

Table 1.4.1:: Accretion Flow and X-Ray Luminosities of  
Dim Galactic Black Holes

Galaxy	$d$ (Mpc)	$M_{\text{BH}}$ ( $\times 10^8 M_{\odot}$ )	$R_{\text{Bondi}}$ (arcsec)	$L_{\text{Bondi}}$ (erg s $^{-1}$ )	$L_X$ (erg s $^{-1}$ )
NGC 1399 <sup>1</sup>	20.5	10.6	0.36	$2.3 \times 10^{44}$	$\lesssim 9.7 \times 10^{38}$
NGC 4472 <sup>1</sup>	16.7	5.65	0.24	$4.5 \times 10^{43}$	$\lesssim 6.4 \times 10^{38}$
NGC 4636 <sup>1</sup>	15.0	0.791	0.049	$4.5 \times 10^{41}$	$\lesssim 2.7 \times 10^{38}$
M 82 <sup>2</sup>	18.4	30	2	$5 \times 10^{44}$	$\sim 7 \times 10^{40}$
Sag. A* <sup>3</sup>	$8.5 \times 10^{-3}$	0.026 <sup>4</sup>	2.2	$6 \times 10^{40}$	$2.2 \times 10^{33}$

Likewise, there is strong evidence of mildly collisional to collisionless plasma at the limits of resolution of Chandra. Using the ion-ion collisional mean free path as

---

<sup>1</sup>Taken from Loewenstein et al. (2001)

<sup>2</sup>Taken from Di Matteo et al. (2003)

<sup>3</sup>Taken from Baganoff et al. (2003)

<sup>4</sup>Mass measurement of Sag. A\* taken from Schödel et al. (2002); Ghez et al. (2003)

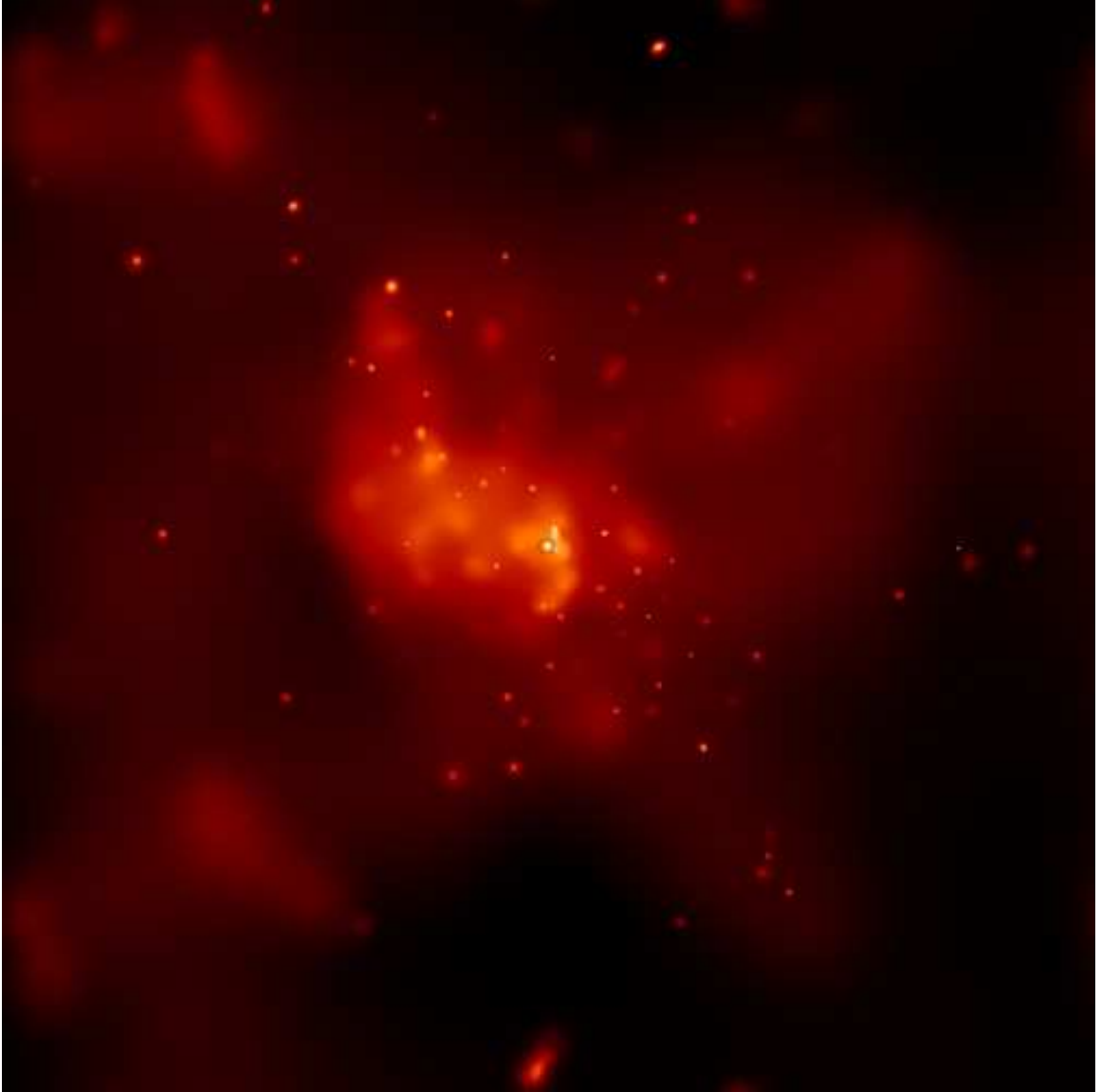


Fig. 1.4.2.— False color Chandra X ray image of 2-10 keV emission within 2 pc of the central galactic black hole Sagittarius A\*. The diffuse emission is attributed mainly to local shock heating and supernova heating, while point sources are associated with compact stellar emission. Image source is taken from the [http://chandra.harvard.edu/photo/2001/0204flare/0204flare\\_xray\\_circle.jpg](http://chandra.harvard.edu/photo/2001/0204flare/0204flare_xray_circle.jpg).

given in Eq. (1.3.9), the Bondi gravitational capture radius:

$$R_{\text{Bondi}} = \frac{GMm_p}{2k_B T}, \quad (1.4.1)$$

we calculate the mean free path of the ambient medium within  $1''$  from the central black hole as shown in Table (1.4.2). In our estimate the density and temperature of the ambient medium is kept constant down to the Bondi capture radius of the black hole. We have borrowed a table from Menou (2005), with Chandra data on the ambient electron number density  $n$  and temperature  $T$  within the inner  $1''$  of nearby underluminous massive and supermassive black hole accretors.

Table 1.4.2:: Dilute Nature of Dim Accreting Galactic  
Black Holes

Galaxy	$n (1'')$ ( $\text{cm}^{-3}$ )	$T (1'')$ ( $10^7 \text{ K}$ )	$R (1'')$ ( $\text{cm}$ )	$\lambda (1'') / R (1'')$	$\lambda (1'') / R_{\text{Bondi}}$
Sag. A <sup>*1</sup>	100	2.3	$1.3 \times 10^{17}$	0.4	0.4
NGC 1399 <sup>2</sup>	0.3	0.9	$3.1 \times 10^{20}$	0.009	0.02
NGC 4472 <sup>2</sup>	0.2	0.9	$2.5 \times 10^{20}$	0.016	0.07
NGC 4636 <sup>2</sup>	0.07	0.7	$2.2 \times 10^{20}$	0.032	0.6
M 82 <sup>3</sup>	0.17	0.9	$2.7 \times 10^{20}$	0.018	0.02
M 32 <sup>4</sup>	0.07	0.4	$1.2 \times 10^{19}$	0.2	1.3

Since the mean free path varies as  $n^{-1}T^2$ , for an adiabatic monatomic gas the mean free path is larger at smaller radii. For a relativistic gas, where  $T \propto n^{1/3}$ , the gas density must increase more steeply than  $R^{-3}$  in order for the plasma to become more collisional as one moves inwards. This requires that the infall velocity decreases faster than  $R$  for a steady inflow or wind. Such velocity profiles appear unlikely in extended astrophysical objects, for which the infall or outflow velocity increases

---

<sup>1</sup>Taken from Baganoff et al. (2003)

<sup>2</sup>Taken from Baganoff et al. (2003)

<sup>3</sup>Taken from Di Matteo et al. (2003)

<sup>4</sup>Taken from Ho et al. (2003)

inwards (for example, the solar wind). It is almost certain that the inner unresolved portions of these black holes become collisionless.

## 1.5 The Nature and Models of Radiatively Inefficient Accretion Flows

Underluminous accretion in black holes has been shown to be dilute as well as to have much lower luminosity than expected from gravitational capture of the ambient medium. Although it is likely that accretion occurs at rates far below the Bondi luminosity in these systems, the mildly collisional nature of the plasma also implies that the flows are radiatively inefficient. These flows are also sufficiently dilute that the bulk of their emission is optically thin. In these systems, the timescale over which energy is radiated is much longer than the infall timescale. The ion-electron energy coupling in this gas is so weak that the ions never cool, and remain at virial temperatures ( $T_i \sim 10^{12}$  K near the black hole event horizon). Electrons are efficient radiators. The time scale for electron radiation is much smaller than the timescale over which ions and electrons exchange energy, leading to much cooler electron temperatures  $T_e \sim 10^8 - 10^{10}$  K (Esin et al. 1997; Narayan et al. 1998; Quataert 2003).

We demonstrate the essential two-temperature nature of these hot and dilute plasmas in Fig. (1.5.1). Electrons are heated by the ions at a rate  $Q_{ie}$ , described by Stepney & Guilbert (1983), which balances out the relatively efficient electron radiative cooling  $Q_-$ . The radiative electron emission rate  $Q_-$  are from bremsstrahlung, synchrotron, synchrotron self-Compton (SSC), and inverse bremsstrahlung Compton (IBC). These radiation processes are described in some detail in Narayan et al. (1995) and references therein. We calculate the ratio of ion to electron temperature as a function of isothermal sound speed squared,  $\theta$ , and ion number density  $n_i$ . We

consider gas at a distance of ten Schwarzschild radii from the Sag. A\* black hole. We assume a density profile  $\rho \propto R^{-3/2}$ , which results in an optical depth to Compton scattering,

$$\tau_{es} = \sigma_T n_i \int_R^\infty (R/R')^{-3/2} dR' = 2\sigma_T R n_i, \quad (1.5.1)$$

The optical depth is important in characterizing the electron cooling due to SSC and IBC. We use<sup>1</sup>  $\beta = 200$ , to calculate synchrotron and SSC emission rates. We consider only those densities for which  $\tau_{es} < 1$ . We observe from our model that at relatively small densities but large normalized  $m_p \theta / k_B > 10^{10}$  K, the bulk of the thermal energy lies in the ions. Maximum electron temperatures are of the order of  $10^{10}$  K, only a few times the rest mass energy of the electron. The two-temperature nature of a hot and dilute plasma was first proposed by Shapiro et al. (1976) to explain hard X-ray spectrum of Cygnus X-1. However, it was demonstrated to be thermally unstable (Piran 1978). A thermally stable class of sub-Eddington solutions that also leads to two-temperature plasmas was studied in some detail by Ichimaru (1977) and Rees et al. (1982) in the context of the hot inner regions of AGNs. Self-similar models of underluminous accretion were investigated by Narayan & Yi (1994); Narayan et al. (1995); Narayan & Yi (1995). In such flows, known as advection dominated accretion flows (ADAFs), only a small fraction of the gravitational energy is radiated out by the electrons. Nearly all the energy is advected through the black hole.

The gas in an ADAF solution has positive Bernoulli parameter that increases at small radii, therefore a gram of gas near the black hole can unbound  $10^4$  grams of gas near the black hole's gravitational capture radius. This property of ADAFs led Blandford & Begelman (1999) to propose an advection-dominated inflow-outflow solution (ADIOS), in which the accretion rate due to an inflow decreases as a function

---

<sup>1</sup> $\beta = \theta/v_A^2$ , where  $v_A$  is the Alfvén speed. See Table (A.1).

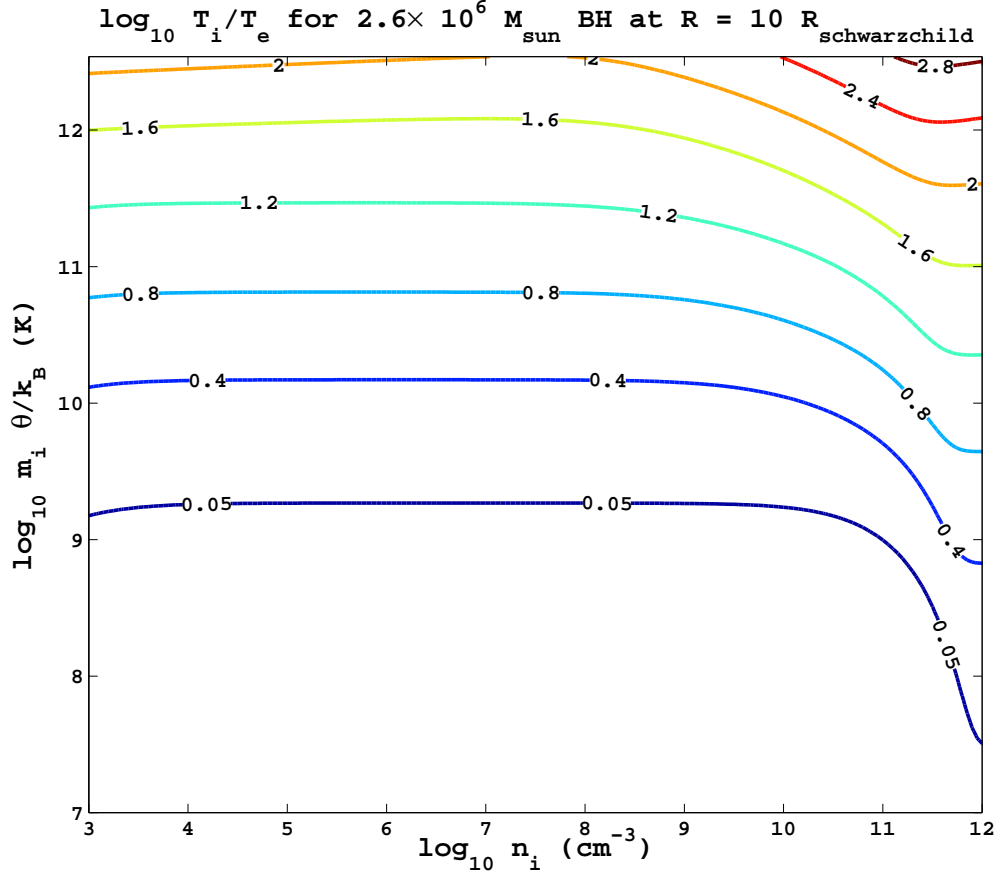


Fig. 1.5.1.— Contour plot of  $\log_{10} T_i/T_e$  at various  $\theta$  and  $n_i$  at  $R = 10R_{\text{schw}}$  for a  $2.6 \times 10^6 M_{\odot}$  black hole. The horizontal axis denotes ion density in  $\text{cm}^{-3}$  and the vertical axis is the average thermal energy per particle  $m_p \theta / k_B$  in Kelvins.

of radius. At large radii there is a relatively strong wind that carries out angular momentum and nearly balances a large mass inflow while near the black hole there is primarily a (small) mass inflow. Recent global MHD simulations (Hawley et al. 2001; Hawley & Balbus 2002; De Villiers & Hawley 2003) suggest, at large radii (approximately twenty times the inner radius), relatively large mass inflows are balanced by large mass outflows ( Fig. [2.2.9]).

A third class of analytic solutions is the convection-dominated accretion flow (CDAF). A variety of recent numerical simulations, incorporating a phenomenological

$\alpha$  viscosity (Igumenshchev & Abramowicz 1999) or an MRI turbulence (Igumenshchev et al. 2003), have suggested a model in which vigorous convection in an adverse entropy gradient disk stalls accretion by transporting angular momentum inwards. However, one reaches a quandary in that convection must be driven against decay by finite dissipation. In a disk, the only source of energy for convective motion is due to a  $W_{R\phi}$  that couples to the orbital angular velocity shear. If the convection suppresses the  $R\phi$  component of the stress tensor, it also chokes off the energy required to drive it. The essential inconsistency in having a convective turbulence in a disk that suppresses  $W_{R\phi}$ , and a confirmation that linear convective instability in an MRI-unstable magnetized disk is very inefficient in transporting angular momentum inwards (it actually transports angular momentum outwards), were discussed in Balbus & Hawley (2002).

Finally, Bondi solutions (Johnson & Quataert 2007) and self-similar inflow-outflow solutions (Menou 2005; Tanaka & Menou 2006) for dilute flows were constructed with a saturated heat flux by Cowie & McKee (1977):

$$\mathbf{q}_{\text{sat}} \simeq -5c_s p \nabla T / |\nabla T|. \quad (1.5.2)$$

These analytic treatments with large diffusive heat fluxes efficiently transport energy out from the hot inner regions and may yield accretion rates that are 1-3 orders of magnitude smaller than Bondi accretion.

These phenomenological models of dilute accretion either assume an  $\alpha$  closure in  $\langle W_{R\phi} \rangle$ , or a saturated conductivity that only points radially. Self-consistent preliminary numerical simulations of underluminous accretion have begun to show features, such as coronal envelopes and centrifugally evacuated funnels, whose basic features none of these models can predict. A class of numerical simulations (Hawley et al.



2001; Hawley & Balbus 2002; De Villiers & Hawley 2003) have also demonstrated that even nonradiative flows are largely Keplerian and have relatively slender disks (thermal energy  $\lesssim$  rotational kinetic energy). As a next step, a numerical code (Athena) that accurately accounts for the total energy generated through accretion has been developed (Gardiner & Stone 2005; Gardiner & Stone 2006). Local numerical simulations of differentially rotating systems have been performed using this new code (Simon 2007). Global simulations of these underluminous flows are currently being developed.

This thesis is an effort to construct more accurate physical models of accretion onto compact objects. We include anisotropic viscous stresses and thermal conductivity in the fluid limit and in the collisionless limit, which many numerical simulations of black hole accretion do not address. We demonstrate those instabilities that may operate in astrophysical hot and dilute accretion flows. In this thesis we also demonstrate additional sources of turbulent angular momentum flux and turbulent heat flux that may operate in dilute accretion flows. This is important, since flows the energy generated through gravitational infall in radiatively inefficient accretion flows cannot be radiated and must be advected or locally dissipated (Balbus 2004a).

## Chapter 2

# The Stability of a Rotating MHD Plasma

In dilute astrophysical plasmas, the collisional mean free path of a particle can exceed its Larmor radius. The thermal conductivity and viscosity of the plasma, in this case, can be dramatically altered. This causes outwardly decreasing orbital angular velocity or temperature gradients to become strongly destabilizing. Magnetic fields, even when highly subthermal, turn free energy gradients of ionized fluids into sources of instability. There are important astrophysical consequences of this condition. First, when temperature, rather than entropy, decreases upwards or outwards, dilute stratified plasmas become destabilized by the MTI (Balbus 2001). And second, large viscous stresses along magnetic field lines (MVI), rather than magnetic forces that tether fluid along field lines (MRI), destabilize the plasma. In both the MRI and MVI, when angular velocity, rather than angular momentum, decreases outwards, magnetized disks become turbulent.

To better understand the behavior of dilute magnetized plasmas, we first need to understand adiabatic modes. We begin with a discussion of the MRI, since this local

instability can destabilize even hydrodynamically stable Keplerian disks. We describe its linear behavior, and the main results of nonlinear local and global numerical simulations. We then justify our study of MHD instabilities in a dilute plasma, by showing that extremely weak fields can lead to anisotropic heat fluxes and viscous stresses. We then describe physical models of the MTI and the MVI.

## 2.1 Adiabatic Instability in a Rotating MHD Medium

In this section, we follow discussions as given in Balbus & Hawley (1998). Consider the stability of a simple, adiabatic, homogeneous differentially rotating fluid in an equilibrium magnetic field  $\mathbf{B}_0 = B_0 (\hat{\phi} \cos \chi + \hat{z} \sin \chi)$ . We consider eigenmodes varying as  $\exp(ik_Z z - i\omega t)$ , with wavenumber  $\mathbf{k} = k_Z \hat{z}$  and frequency  $\omega$ , in the WKB limit  $|k_Z R| \gg 1$ . We use the equations of continuity (Eq. [1.2.5]), force balance (Eq. [1.2.6]) without viscosity, and magnetic induction (Eq. [1.2.8]), all in a comoving frame. The system of equations to leading order in the fluctuating quantities are:

$$-i\omega \frac{\delta \rho}{\rho_0} + ik_Z \delta u_Z = 0 \quad (2.1.1)$$

$$-i\omega \delta u_R - 2\Omega \delta u_\phi = ik_Z v_A^2 \sin \chi \frac{\delta B_R}{B_0}, \quad (2.1.2)$$

$$-i\omega \delta u_\phi + (2\Omega + \Omega' R) \delta u_R = ik_Z v_A^2 \sin \chi \frac{\delta B_\phi}{B_0}, \quad (2.1.3)$$

$$-i\omega \delta u_Z = -ik_Z \left( \frac{\delta p}{\rho_0} + v_A^2 \cos \chi \frac{\delta B_\phi}{B_0} \right), \quad (2.1.4)$$

$$-i\omega \delta B_R = B_0 \sin \chi (ik_Z \delta u_R), \quad (2.1.5)$$

$$-i\omega \delta B_\phi - \Omega' R \delta B_R = -B_0 \cos \chi (ik_Z \delta u_Z) + B_0 \sin \chi (ik_Z \delta u_\phi), \quad (2.1.6)$$

$$\delta B_Z = 0, \quad (2.1.7)$$

$$\frac{\delta p}{p_0} = \frac{5}{3} \frac{\delta \rho}{\rho_0}. \quad (2.1.8)$$

We arrive at this polynomial equation in  $\omega$ ,

$$\begin{aligned} & (k_Z^2 v_A^2 \sin^2 \chi - \omega^2) (\omega^4 - k_Z^2 (c_s^2 + v_A^2) \omega^2 + k_Z^4 v_A^2 c_s^2 \sin^2 \chi) + \\ & \left( \kappa^2 \omega^4 - \omega^2 \left[ \kappa^2 k^2 (v_A^2 \cos^2 \chi + c_s^2) + k_Z^2 v_A^2 \sin^2 \chi \frac{d\Omega^2}{d \ln R} \right] \right) + \\ & k_Z^2 c_s^2 (k_Z^2 v_A^2 \sin^2 \chi) \frac{d\Omega^2}{d \ln R} = 0. \end{aligned} \quad (2.1.9)$$

The adiabatic sound speed  $c_s$  and the epicyclic frequency  $\kappa$  are given by,

$$\begin{aligned} c_s^2 &= \frac{5\theta}{3}, \\ \kappa^2 &= \frac{1}{R^3} \frac{d(R^4 \Omega^2)}{dR}. \end{aligned} \quad (2.1.10)$$

In the nonrotating limit  $\Omega \rightarrow 0$ , Eq. (2.1.9) reduces to,

$$(k_Z^2 v_A^2 \sin^2 \chi - \omega^2) (\omega^4 - k_Z^2 (c_s^2 + v_A^2) \omega^2 + k_Z^4 v_A^2 c_s^2 \sin^2 \chi) = 0. \quad (2.1.11)$$

One of the roots of Eq. (2.1.9) is given by,

$$\omega^2 = k_Z^2 v_A^2 \sin^2 \chi, \quad (2.1.12)$$

which corresponds to shear-Alfvén modes. These waves propagate along magnetic field lines with fluid and magnetic field perturbations perpendicular to the equilibrium field, similar to a plucked string with the magnetic tension providing the restoring force. In the limit of either  $v_A^2 \ll c_s^2$ ,  $c_s^2 \ll v_A^2$ , or  $\sin^2 \chi \ll 1$ , then to leading order the other two solutions correspond to the fast mode:

$$\omega_+^2 = k_Z^2 (c_s^2 + v_A^2), \quad (2.1.13)$$

and the slow mode:

$$\omega_-^2 = \frac{k_Z^2 v_A^2 c_s^2 \sin^2 \chi}{c_s^2 + v_A^2}. \quad (2.1.14)$$

In the weak magnetic field limit, where  $c_s^2/v_A^2 \rightarrow \infty$ , the slow and Alfvén modes become degenerate and the fast mode is identified with acoustic waves. An interesting effect occurs if we include rotation. In Fig. (2.1.1) we consider a Keplerian rotational profile, with  $\beta = 3$  and  $\chi = \pi/4$ . We observe how the normalized oscillation frequency  $\omega^2/(k_Z^2 v_A^2)$  of the three modes (fast, slow, and Alfvén) change with  $\Omega^2/(k_Z^2 v_A^2)$ . For  $\Omega^2 \geq k_Z^2 v_A^2/6$ , the slow mode becomes unstable. This is the essence of MHD turbulence in a differentially rotating medium.

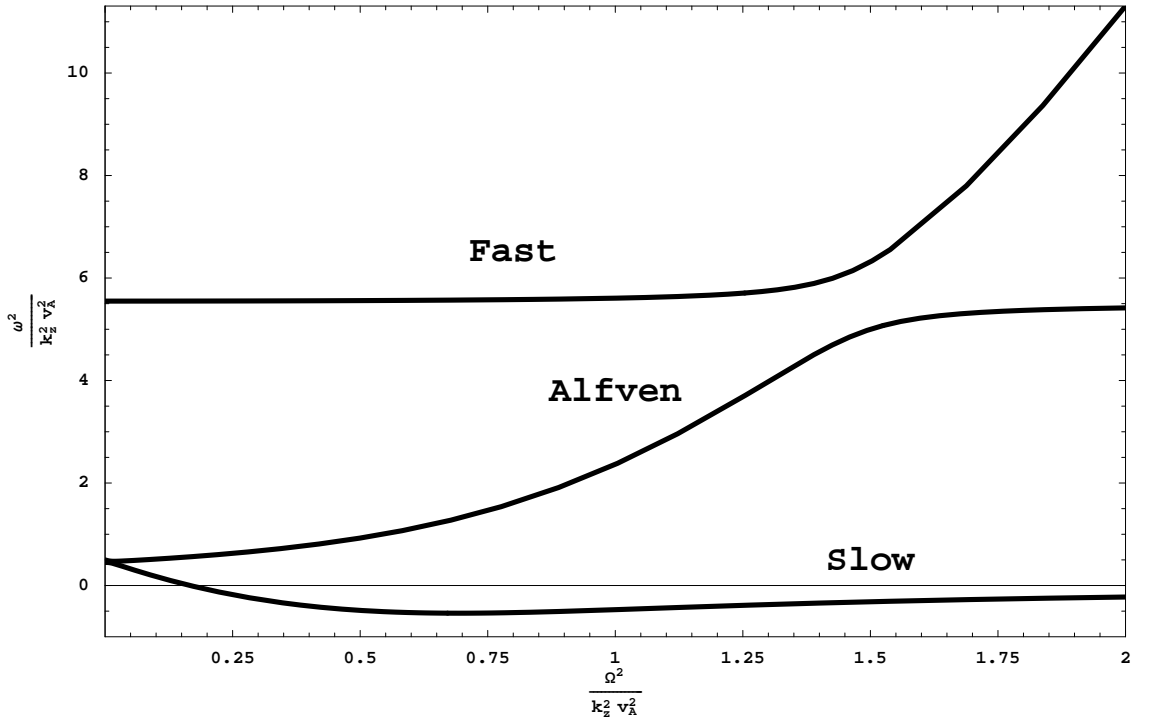


Fig. 2.1.1.— Normalized oscillation frequency  $\omega^2/(k_Z^2 v_A^2)$  versus  $\Omega^2/(k_Z^2 v_A^2)$  for the three modes of local oscillation in an adiabatic, homogeneous, rotating plasma with a Keplerian rotational profile.

## 2.2 The Magnetorotational Instability

Velikhov (1959) and Chandrasekhar (1960) studied the stability of a Taylor-Couette flow of a plasma within a magnetized medium, and found that it becomes unstable where the angular velocity, rather than the angular momentum, decreases outwards. Remarkably, a magnetic field of arbitrarily small strength was found to destabilize a Rayleigh stable flow. However, it was Balbus & Hawley (1991) who noted that this local instability could destabilize Keplerian disks and induce the right kind of turbulence that could drive accretion.

We can describe the MRI in the following manner: consider two points on a magnetic field line but radially separated. A small magnetic tension acts as a weak “spring” connecting these two points on the same field line. The outer point experiences a tension along its direction of motion, resulting in a torque which increases its angular momentum. The inner point experiences a tension opposite its direction of motion, resulting in a torque which decreases its angular momentum. For a Keplerian flow, the specific angular momentum increases with increasing radius. This implies that as a result of the torques arising from magnetic tension, the outer mass moves outwards while the inner mass moves inwards. Therefore, angular momentum is transferred from the inner object to the outer object. The spring is further stretched, the tension increases, and the points move further apart. The development of the MRI ceases if the oscillation frequency of this “spring” is of the order of the angular velocity; that is, if the “spring” is too rigid (many oscillations within an orbital period), the two masses will not spread apart and the system is stable. A cartoon demonstrating the MRI is shown in Fig. (2.2.1).

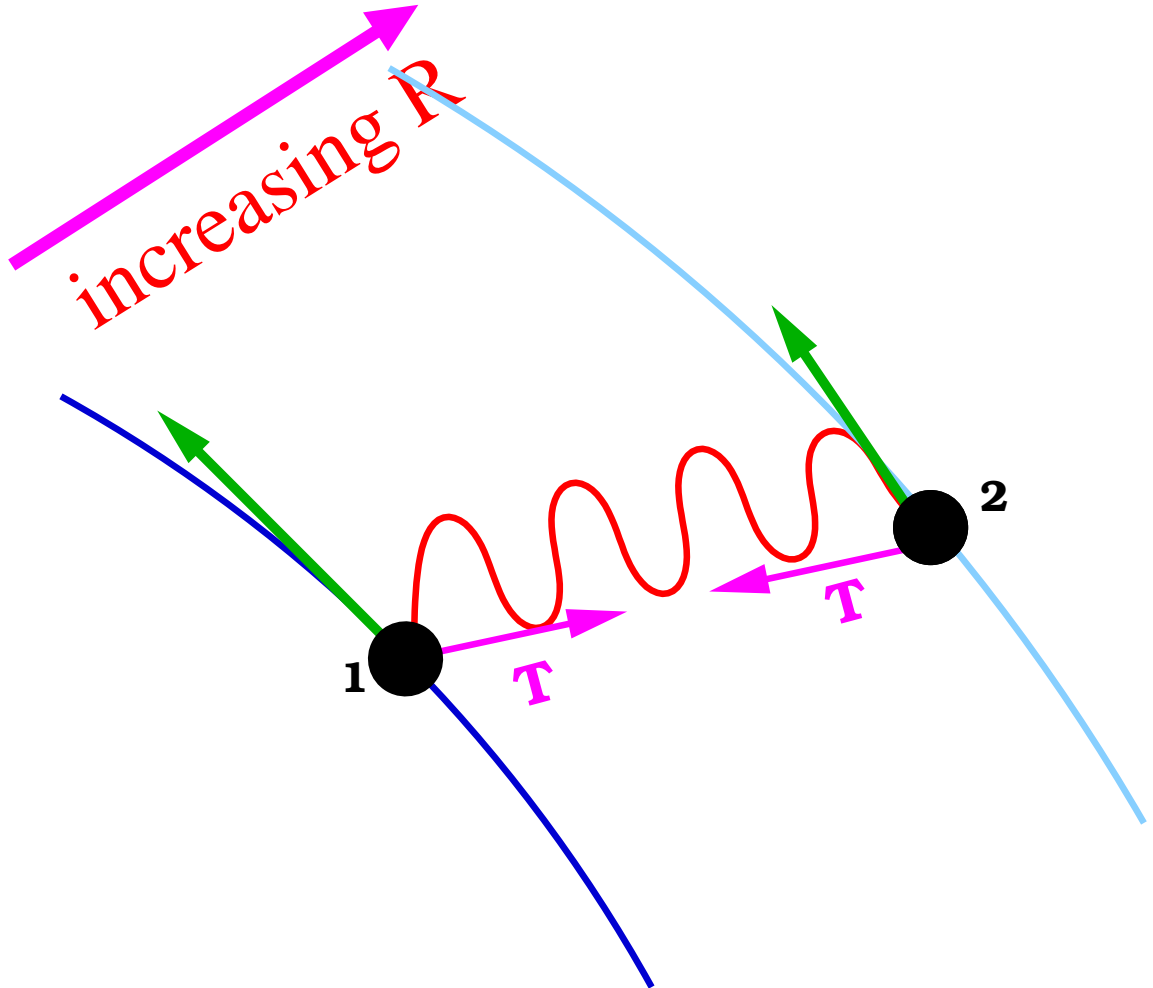


Fig. 2.2.1.— Spring model depiction of the MRI. Two masses are connected by a spring, with the gravitational force due to a central object (i.e., Keplerian rotation). Tension provides a torque that speeds up the outer mass and slows down the inner mass. Angular momentum is transferred outwards, the spring tension increases, and the process runs away.

### 2.2.1 Linear Stability Analysis of the MRI

The simplest description of the MRI is one with an equilibrium vertical magnetic field  $\mathbf{B}_0 = B_0 \hat{z}$ . Consider a Lagrangian fluid displacement  $\boldsymbol{\xi}$  with spatial variation  $\exp(ik_z z)$ , where  $\delta \mathbf{u} = d\boldsymbol{\xi}/dt$ . The frozen-in condition from Eq. (1.2.4) implies the form of the perturbed magnetic field,  $\delta \mathbf{B} = ik_z B_0 \boldsymbol{\xi}$ ,  $\delta B_z = 0$ , and  $\xi_z = 0$ . There is no magnetic compression,  $\mathbf{B}_0 \cdot \delta \mathbf{B} = 0$  and the flow is incompressible,  $\delta p = 0$ . The

magnetic tension is given by,

$$\frac{ikB}{4\pi\rho}\delta\mathbf{B} = -(\mathbf{k} \cdot \mathbf{v}_A)^2 \boldsymbol{\xi}. \quad (2.2.1)$$

In a frame corotating with the fluid, one can then show that radial and azimuthal force balance equations with Coriolis and tidal forces and magnetic tension are given by,

$$\frac{d^2\xi_R}{dt^2} + \frac{d\Omega^2}{d\ln R}\xi_R - 2\Omega\frac{d\xi_\phi}{dt} = -(\mathbf{k} \cdot \mathbf{v}_A)^2 \xi_R, \quad (2.2.2)$$

$$\frac{d^2\xi_\phi}{dt^2} + 2\Omega\frac{d\xi_R}{dt} = -(\mathbf{k} \cdot \mathbf{v}_A)^2 \xi_\phi. \quad (2.2.3)$$

If  $\boldsymbol{\xi} \propto \exp(\Gamma t)$ , we have the following dispersion relation:

$$\Gamma^4 + \Gamma^2 [\kappa^2 + 2(\mathbf{k} \cdot \mathbf{v}_A)^2] + (\mathbf{k} \cdot \mathbf{v}_A)^2 \left[ (\mathbf{k} \cdot \mathbf{v}_A)^2 + \frac{d\Omega^2}{d\ln R} \right] = 0, \quad (2.2.4)$$

For a Keplerian rotation profile, the maximum growth rate is  $\Gamma_{\max} = 3\Omega/4$  at wavenumber that satisfies the equation  $(\mathbf{k} \cdot \mathbf{v}_A)^2 = 15\Omega^2/16$ . Furthermore, magnetic tension quenches the MRI at wavenumbers satisfying  $(\mathbf{k} \cdot \mathbf{v}_A)^2 = 3\Omega^2$ . Over one orbital period, the fastest growing mode would lead to  $10^4$  amplification in modal energy. One can demonstrate that the modal  $R\phi$  component of the stress tensor is,

$$\begin{aligned} \langle W_{R\phi,k} \rangle &= \text{Re} \left( \Gamma^2 \xi_\phi \xi_R^* - \frac{\delta B_\phi^* \delta B_R}{4\pi\rho} \right) \\ &= |\xi_R|^2 \Gamma \Omega \frac{2\Omega^2 - \frac{1}{2}d\Omega^2/d\ln R - 4\Gamma^2}{\Gamma^2 + (\mathbf{k} \cdot \mathbf{v}_A)^2}. \end{aligned} \quad (2.2.5)$$

The normalized growth rate  $\Gamma/\Omega$  and normalized  $R\phi$  stress tensor component  $\langle W_{R\phi} \rangle / (|\xi_R|^2 \Omega^2)$  as a function of normalized wavenumber  $x = \mathbf{k} \cdot \mathbf{v}_A/\Omega$  are shown in Figs. (2.2.2) and (2.2.3), respectively. As shown in Fig. (2.2.3),  $W_{R\phi}$  is positive for the MRI, which



implies that the MRI not only destabilizes a plasma but can produce the right type of turbulence that can drive accretion.

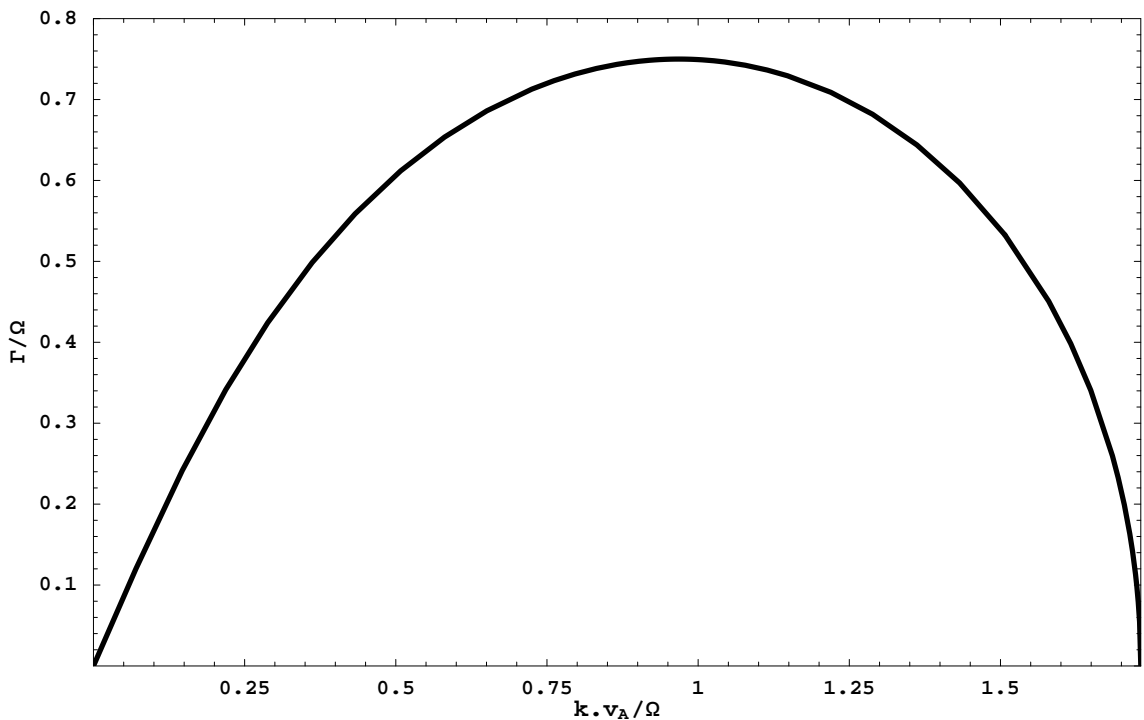


Fig. 2.2.2.— Normalized growth rate  $\Gamma/\Omega$  as a function of wavenumber  $\mathbf{k} \cdot \mathbf{v}_A/\Omega$ , for a Keplerian rotation profile and purely vertical wavenumber.

### 2.2.2 Nonlinear MRI

A variety of three-dimensional local simulations (Hawley et al. 1995, 1996) and global simulations (Hawley et al. 2001; Hawley & Balbus 2002; De Villiers & Hawley 2003) of magnetized accretion disks demonstrate the nonlinear development of the MRI and maintenance of a significant magnetic field, at maximum magnetic pressures of order of the initial gas pressure, against dissipation and diffusion. These simulations typically employ the ZEUS MHD algorithm (Stone & Norman 1992). These simulations also imply an average  $\alpha_{SS}$  in the range of  $10^{-3}$  to  $10^{-1}$ , consistent with astrophysical observations. Recall that  $\alpha_{SS}$  is a prescription (Shakura & Sunyaev 1973) relating

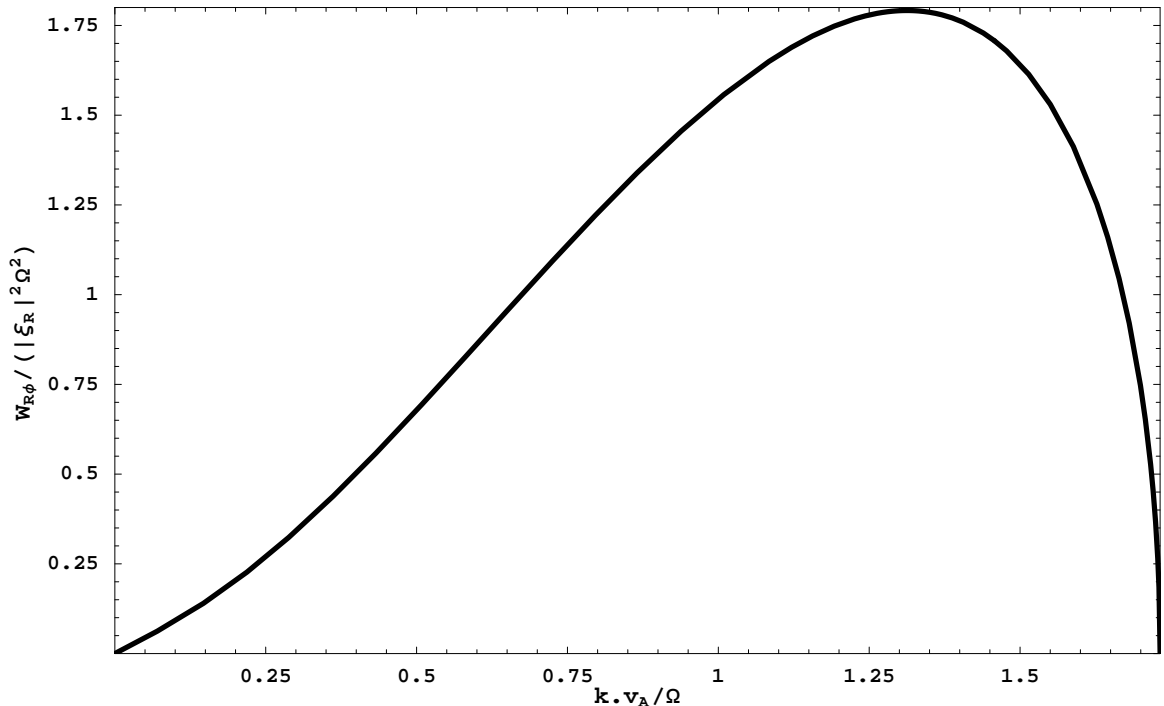


Fig. 2.2.3.— Normalized averaged  $R\phi$  component of the stress tensor, as a function of normalized wavenumber, for a Keplerian rotation profile and purely vertical wavenumber.

the angular momentum flux carried by turbulence to the pressure, and is defined as  $\langle T_{R\phi} \rangle = \alpha_{SS} p$  (see Eq. [1.3.35] in §1.3).

The nonlinear development of the MRI is robust to a variety of different physical systems, initial magnetic field configurations (Hawley et al. 1995), and to different numerical MHD algorithms (Brandenburg et al. 1995). Simulations of low and fully ionized plasmas have also demonstrated the nonlinear development and maintenance of the MRI when incorporating additional physics, such as: finite Hall effects (Wardle & Ng 1999; Sano & Stone 2002) or ambipolar diffusion (Hawley & Stone 1998) in low-ionized plasmas; finite self-gravity in massive disks (Fromang et al. 2004c,a,b); radiation pressure dominated systems (Turner et al. 2005; Begelman 2006b); and vertical stratification to explore the effects of magnetic buoyancy (Stone et al. 1996; Miller & Stone 2000) among others.

## Local Simulations

Local simulations of a rotating fluid consist of a coordinate system with at least relatively small radial extent,  $\Delta R \ll R$ , corotating with the fluid at a specific radius. This system transforms to a Cartesian coordinate system (where  $R$  is identified with  $x$ ,  $R\phi$  with  $y$ , and  $z$  unchanged) with noninertial Coriolis and tidal fluid forces and an azimuthal shear across the radial coordinate. For a Keplerian flow, the background shear velocity relative to the  $x = 0$  surface is  $u_y = -3x\Omega/2$ . To properly take into account differential azimuthal velocity across  $x$ , one employs a periodic shearing boundary condition in  $x$ . For a box with radial dimension  $L_X$ , azimuthal dimension  $L_Y$ , and vertical dimension  $L_Z$ , the boundary conditions for the excess azimuthal velocity  $u_y$  are,

$$u_y(x = 0, y, z) = u_y(x = L_X, y - qL_X\Omega t, z) + q\Omega L_X, \quad (2.2.6)$$

$$u_y(x, y = 0, z) = u_y(x, y = L_Y, z), \quad (2.2.7)$$

$$u_y(x, y, z = 0) = u_y(x, y, z = L_Z). \quad (2.2.8)$$

Boundary conditions for all other fluid quantities  $f$  are,

$$f(x = 0, y, z) = f(x = L_X, y - qL_X\Omega t, z), \quad (2.2.9)$$

$$f(x, y = 0, z) = f(x, y = L_Y, z), \quad (2.2.10)$$

$$f(x, y, z = 0) = f(x, y, z = L_Z), \quad (2.2.11)$$

where  $q = -d \ln \Omega / d \ln R$ . This treatment has been applied to local studies of other differentially rotating systems, such as the galactic disk (Goldreich & Lynden-Bell 1965; Julian & Toomre 1966) and planetary rings (Wisdom & Tremaine 1988).

Local numerical simulations of the MRI demonstrate the maintenance of a fluc-

tuating magnetic field against rather strong numerical dissipation and diffusion, and fluctuating velocity and magnetic field correlations resulting in a net outward angular momentum flux. In Figs. (2.2.4) and (2.2.5), taken from Hawley et al. (1996), we show these effects.

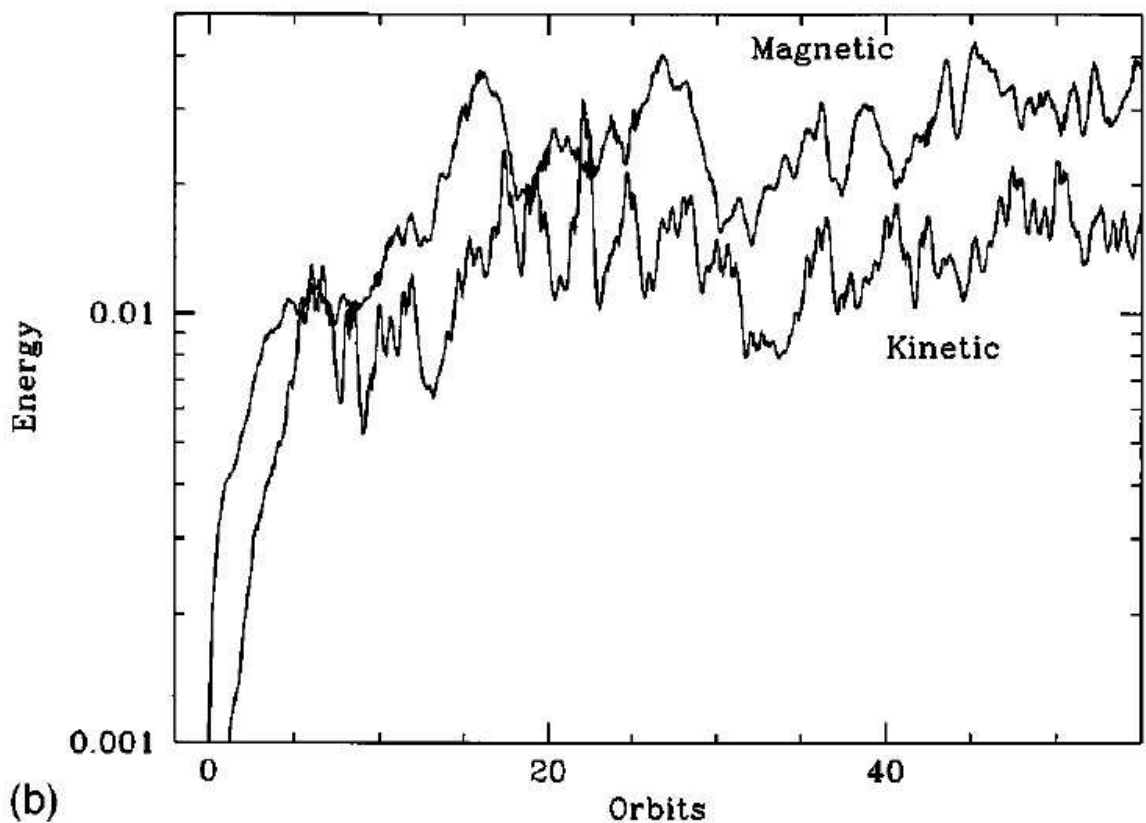


Fig. 2.2.4.— Saturation of magnetic and gas pressure fluctuations in a long-term shearing box simulation of a magnetized disk. The magnetic and gas pressures normalized by the initial gas pressure are plotted as a function of time in units of orbital periods. This figure is taken from Hawley et al. (1996).

Furthermore, Balbus et al. (1996) performed purely hydrodynamic 3D simulations of a local Keplerian shearing box with size  $L$  and coarse numerical resolution of  $31^3$ . They demonstrate that only systems in which the angular momentum decreases outwards,  $\kappa^2/\Omega^2 < 0$ , sustain and increase kinetic fluctuations against numerical dissipation at these resolutions. This result is consistent with the fact that equilibrium

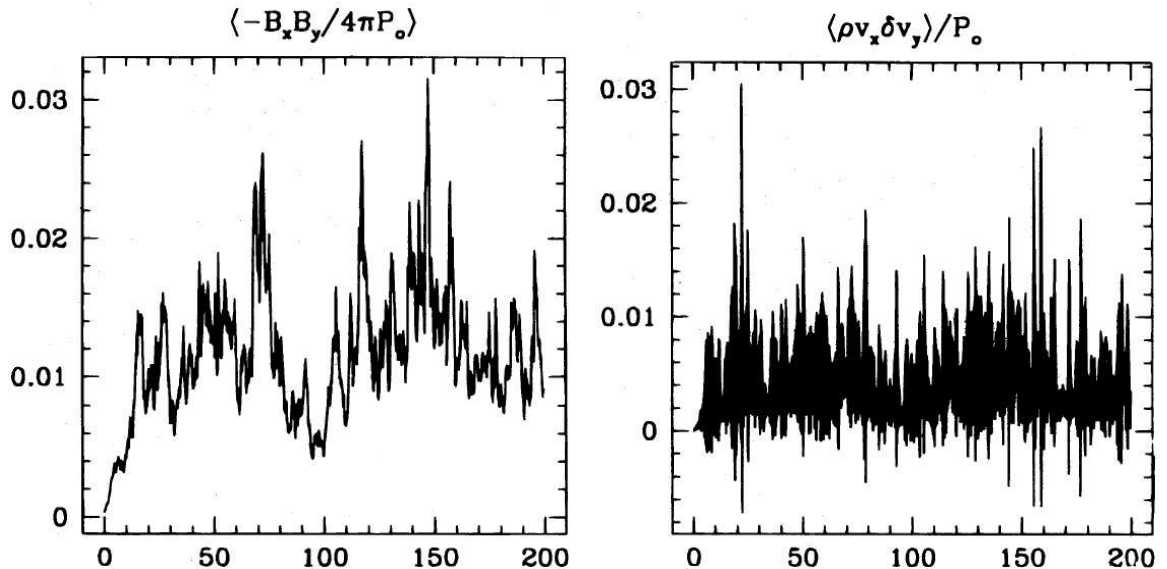


Fig. 2.2.5.— On the left is the evolution of the magnetic contribution, and on the right the kinetic contribution, to the box-averaged  $\langle \rho W_{R\phi} \rangle$  normalized by the initial gas pressure, for a long-period shearing box simulation. One can observe a net outwards flux of angular momentum associated with the nonlinear development of the MRI. The time is in units of orbital period. These figures are taken from Hawley et al. (1996).

rotating flows in which angular momentum decreases radially outwards are hydrodynamically unstable. In addition, the well-known nonlinear instability of a purely Cartesian shear layer (i.e., no Coriolis force associated with a rotating system) has been demonstrated in this simulation. These results imply that a hydrodynamic Keplerian disk will remain stable and unable to efficiently transport angular momentum outwards, even at arbitrarily small viscosities. The results of the simulations of Balbus et al. (1996) are shown in Fig. (2.2.6). A series of recent numerical hydrodynamic simulations of local sheared rotating boxes, at far higher Reynolds numbers of up to  $10^5$ , also confirm these results for hydrodynamic flows (Lesur & Longaretti 2005).

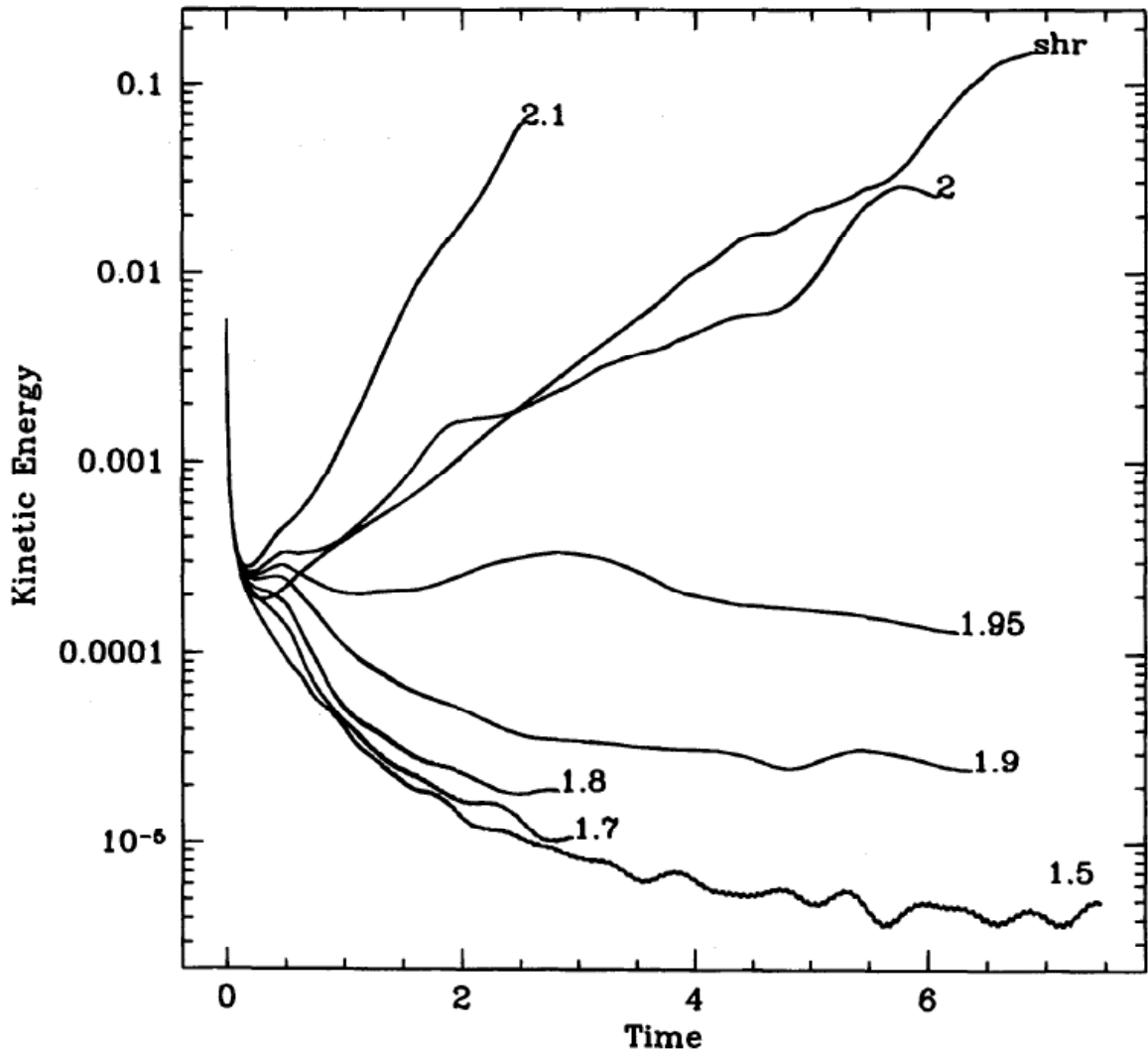


Fig. 2.2.6.— The box-averaged kinetic energy, normalized in units of  $L^2\Omega^2$ , as a function of normalized time  $t\Omega$ , in a Keplerian shearing cube of size  $L$ . The line labeled “shr” refers to a pure shearing box. Only those simulations in which there is pure shear or in which  $q > 2$  demonstrate kinetic turbulence sustained against numerical dissipation. This figure is taken from Balbus et al. (1996).

### Global Simulations

The most promising global simulations are performed with radiatively inefficient plasmas in order to extract as much computational efficiency as possible. In these astrophysical systems, the disk height is not orders of magnitude smaller than the disk radius, in contrast to classical accretion disks. The simplest MHD algorithms

that can treat this problem do not include the effects of radiative pressure or radiative transfer. As a result, nonradiative flows in the inner regions of black holes provide a good candidate for the first treatments of the global MRI. Hawley et al. (2001); Hawley & Balbus (2002) demonstrate that constant-angular momentum tori, marginally stable under the Rayleigh criterion, evolve via the MRI into relatively slender disks of rotating plasma with the following four main properties. First, the orbital speed is larger than the thermal speed; consequently, these disks are relatively slender and the orbital flow is approximately Keplerian. Second, the disk has a roughly fixed opening angle (the ratio of disk height to radius is relatively constant). Third, there are outflowing coronal regions, in which the magnetic pressure is larger than the gas pressure, above and below the disk. Fourth, a funnel region about the rotation axis is evacuated of matter due to a centrifugal barrier. These features are demonstrated in Figs. (2.2.7). An analytic model developed by Balbus (2005) demonstrates the gross features of these simulations. An isodensity, or isobaric or isoenergy, plot of this analytic flow model is taken from Balbus (2005) and shown in Fig. (2.2.8).

These simulations have generally been shown to result in relatively small rates of mass accretion as well as outflowing winds as shown in Fig. (2.2.9). The mass-averaged accretion and outflow velocities  $\langle |u_R| \rangle_\rho$  are much smaller than the orbital velocity or what may be expected from pressure-supported flows. This feature of preliminary global MRI simulations appears to be relatively robust, and is seen in a variety of different numerical simulations, e.g., Hawley (2001); Igumenshchev et al. (2003); De Villiers & Hawley (2003).

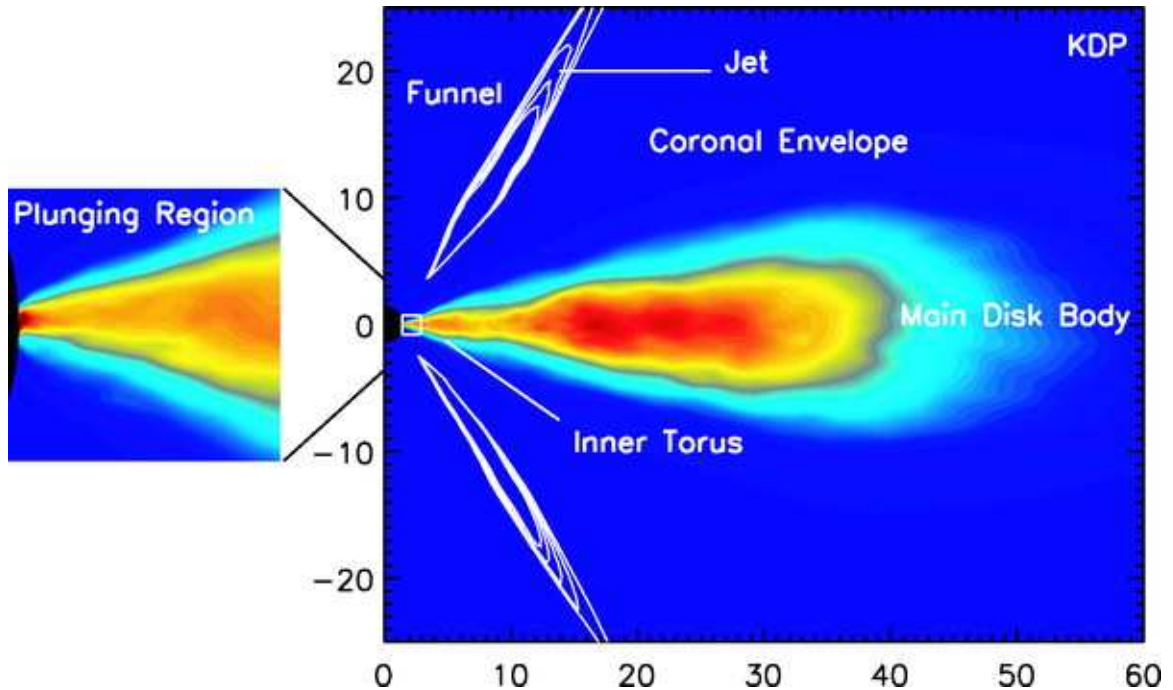


Fig. 2.2.7.— Azimuthally averaged density of a long time snapshot of a global MRI simulation of accretion onto a black hole, taken at 10 orbital time periods at the outer radius of the simulation box,  $R = 100$  Schwarzschild radii. One observes the salient features of this simulation: a relatively slender disk (thermal velocities  $\lesssim$  orbital velocities), implying Keplerian rotation profiles in the disk bulk; an outlying coronal region of dilute, magnetic pressure dominated plasma; and a funnel outflow at a finite opening angle (the jet is outlined by contours of positive radial momentum). The figure is taken from De Villiers et al. (2003).

## 2.3 Anisotropic Viscous Stresses and Heat Fluxes in Dilute Plasmas

Another class of magnetized instabilities can occur in dilute plasmas. Even in weak fields, in which the Lorentz forces are negligible, a magnetic field fundamentally changes the stability properties of a plasma. In a gas viscous stresses and heat fluxes are isotropic and generally stabilizing. However, in a magnetized plasma these transport processes are constrained to move along field lines and may become destabilizing.



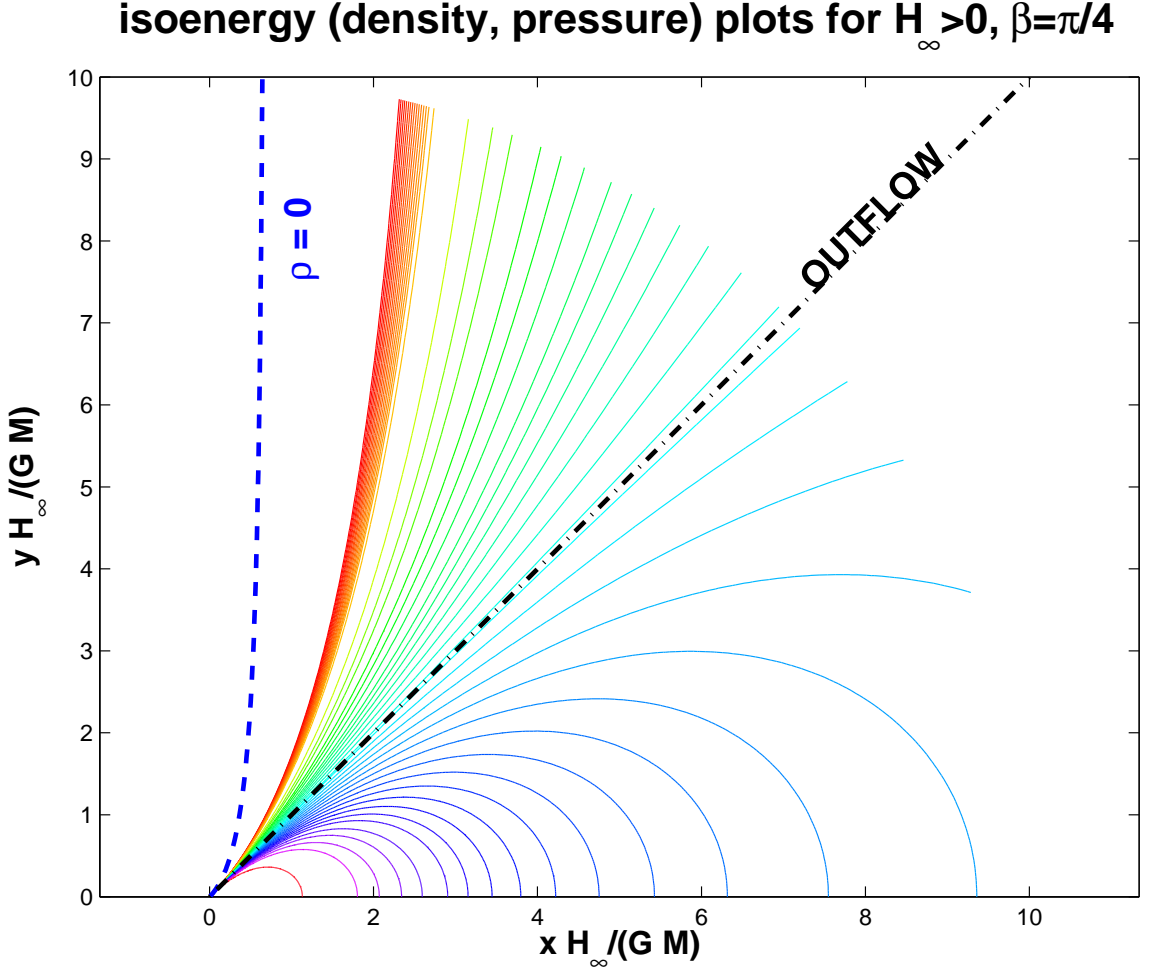


Fig. 2.2.8.— Isobaric, or isodensity or isoenergy, contours for an adiabatic disk in which  $\Omega$  is 0.84 of its Keplerian value. This corresponds to a disk opening angle  $\beta = 45^\circ$ , separated by the line marked **OUTFLOW**. Above **OUTFLOW**, the contours are open and become very packed near the  $\rho = 0$  line about the axis.  $\mathcal{H}_\infty$  refers to the gas enthalpy at infinity. This description is taken from Balbus (2005).

For mildly collisional or collisionless systems, viscosity and thermal conductivity may have dynamical time scale consequences, while collisional momentum transfer effects, such as electrical resistivity, may become dynamically unimportant. If the ion collisional mean free path is smaller than the ion gyroradius, then heat fluxes and viscous stresses are constrained to follow magnetic field lines. This property of dilute magnetized plasmas was noted by Chew et al. (1956) and formalized, in

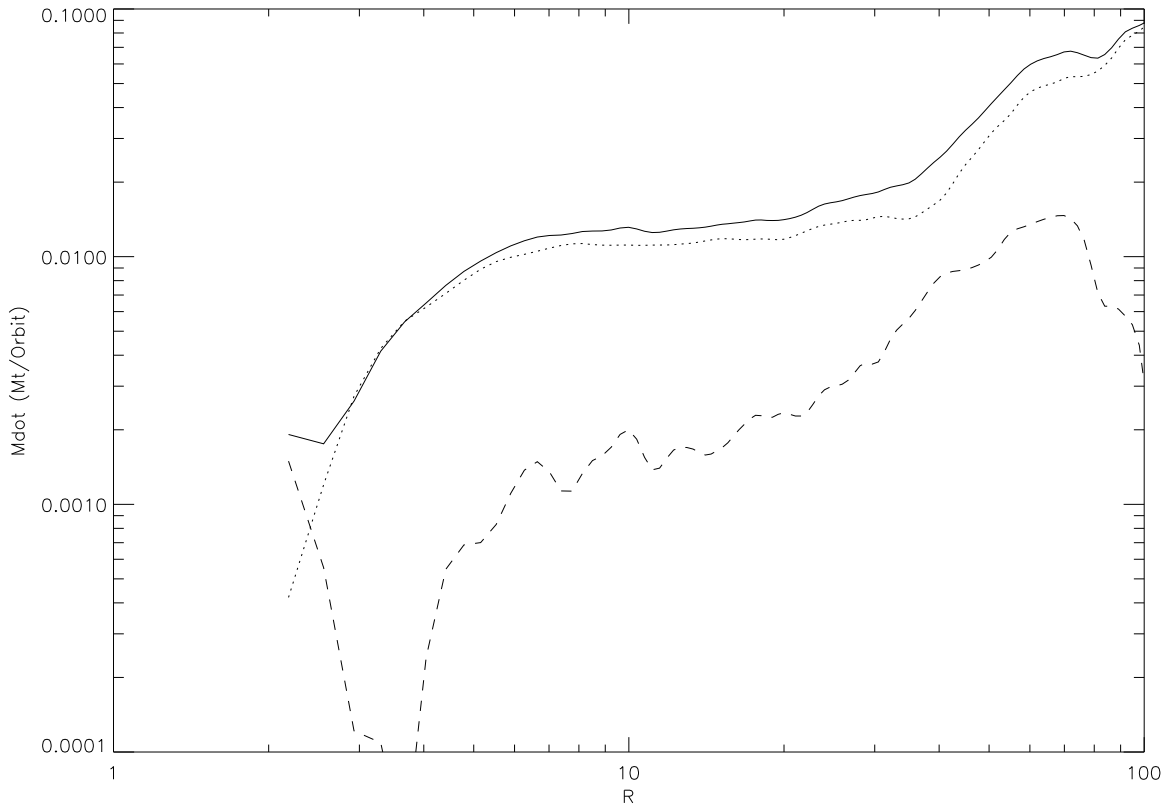


Fig. 2.2.9.— Time averaged mass accretion and outflow rates in initial global simulations of the MRI (Hawley et al. 2001). The unit of accretion rate is the mass of the initial torus divided by the orbital period at the radius where the initial torus had its maximal pressure. The mass accretion rate is normalized in these units. The solid line is the inflow rate, the dashed line is the outflow rate, and the dotted line is the net accretion rate. The mass accretion and outflow rates decreases with decreasing radius down to the marginally stable orbit.

expressions for anisotropic viscosity, thermal conductivity, electrical resistivity and other collisional transport phenomena, by Braginskii (1965).

The ion and electron gyroradii, in astrophysical units, are given by,

$$r_{Li} = 9.5 \times 10^7 \left( \frac{B}{1 \mu\text{G}} \right)^{-1} \left( \frac{T}{10^4 \text{ K}} \right)^{1/2} \text{ cm}, \quad (2.3.1)$$

$$r_{Le} = 2.2 \times 10^6 \left( \frac{B}{1 \mu\text{G}} \right)^{-1} \left( \frac{T}{10^4 \text{ K}} \right)^{1/2} \text{ cm}. \quad (2.3.2)$$

From Eqs. (1.3.9) and (2.3.1), the estimated threshold magnetic field strength at

which the ion mean free path is smaller than the ion Larmor radius,

$$B \gtrsim 6.33 \times 10^{-12} \left( \frac{T}{10^4 \text{ K}} \right)^{-3/2} \left( \frac{n}{1 \text{ cm}^{-3}} \right) \text{ G.} \quad (2.3.3)$$

Furthermore, from Eqs. (1.3.10) and (2.3.2), the threshold magnetic field at which the electron mean free path is smaller than the electron Larmor radius is smaller than the magnetic field strength for ion transport effects, given in Eq. (2.3.3), by a factor of roughly  $(2m_i/m_e)^{-1/2}$ ,

$$B \gtrsim 1.05 \times 10^{-13} \left( \frac{T}{10^4 \text{ K}} \right)^{-3/2} \left( \frac{n}{1 \text{ cm}^{-3}} \right) \text{ G.} \quad (2.3.4)$$

Faraday polarization observed in the emission of Sag. A\* at millimeter wavelengths (Aitken et al. 2000; Bower et al. 2003; Marrone et al. 2006), at frequencies for which Faraday polarization due to the intervening interstellar medium is negligible, implies magnetic fields well in excess of Eq. (2.3.3). The observations of Bower et al. (2003) is shown in Fig. (2.3.1).

In a plasma in which ion and electron temperatures are of the same order, the viscous stress is carried by the ions and the heat flux is carried by the electrons. For dilute plasma fluids, the smallness of the electron gyroradius relative to the ion mean free path results in a heat flux  $\mathbf{q}$  along the magnetic field line represented by,

$$\mathbf{q} = q\mathbf{b}. \quad (2.3.5)$$

We require a viscous stress tensor that is traceless, symmetric, rotationally invariant and results in viscous stress directed only along the direction of the magnetic field. The stress must also be physical, since viscosity transports momentum from regions of higher to lower momentum density. The viscous stress tensor that fulfills these

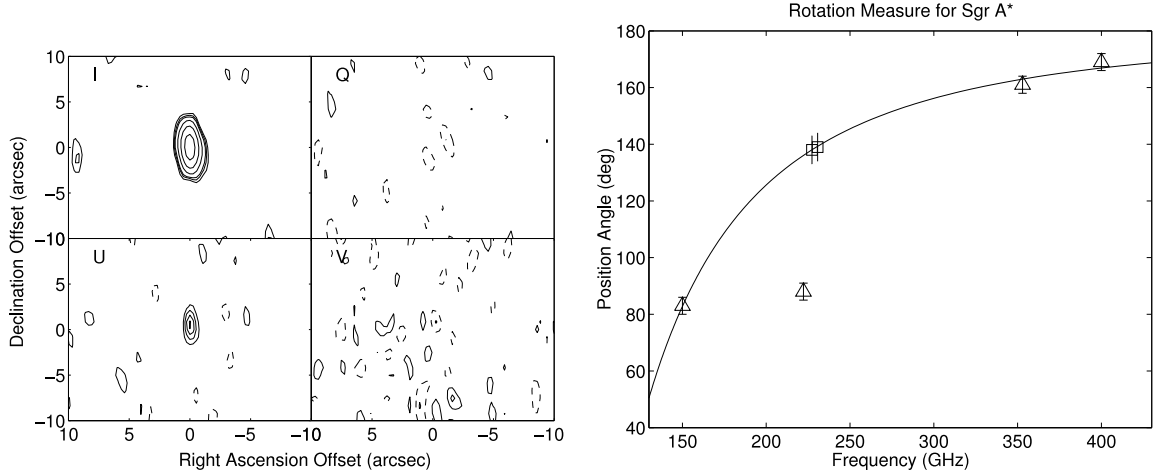


Fig. 2.3.1.— Evidence of internal magnetic field in Sag. A\* from Faraday polarization at high radio frequencies. On the left is the unresolved 1'' millimeter and far infrared radio emission from the Sag. A\* sources. On the right is difference between left and right circularly polarized radiation from Sag. A\* as a function of frequency; the best-fit rotation measure  $RM = 4.3 \pm 0.1 \times 10^5 \text{ rad m}^{-2}$ . This plot is taken from Bower et al. (2003).

properties is,

$$\sigma = \sigma_{\mathbf{b}\mathbf{b}} \left( \mathbf{b}\mathbf{b} - \frac{1}{3}\mathbb{I} \right), \quad (2.3.6)$$

where  $\sigma_{\mathbf{b}\mathbf{b}}$  is the magnitude of the viscous stress (or pressure), specifically  $\sigma_{\mathbf{b}\mathbf{b}} = -3\mathbf{n} \cdot \boldsymbol{\sigma} \cdot \mathbf{n}$ , where  $\mathbf{n} \cdot \mathbf{b} = 0$  and  $\mathbf{n}^2 = 1$ . If the mean free path is smaller than the system scale or the size of the turbulence, then fluid expressions for the viscous stress and heat flux can be derived (Braginskii 1965):

$$\sigma_{\mathbf{b}\mathbf{b}} = -3\eta_\nu \left( \mathbf{b} \cdot \nabla \mathbf{V} \cdot \mathbf{b} - \frac{1}{3} \nabla \cdot \mathbf{V} \right), \quad (2.3.7)$$

$$q = -\eta_\kappa (nk_B \mathbf{b} \cdot \nabla T_e). \quad (2.3.8)$$

In the collisionless limit, the magnitude of  $\sigma_{\mathbf{b}\mathbf{b}}$  and  $q$  depend on the specific physical process that may drive transport and may not necessarily be diffusive in nature.

Tab. (2.3.1), summarizes the role that magnetic fields in collisional or dilute plasmas may play in transporting energy or angular momentum via MHD instabilities in non self-gravitating magnetized plasmas. The columns describe the plasma initial state, and the rows denote the particular MHD turbulent transport phenomenon. Entries within the grid correspond to stability criteria for either angular momentum or energy transport. The entry on convective stability in a magnetized, collisional plasma (row **energy transfer**) is described in Balbus (1995) and is not discussed here. In §2.4 and §2.5 we describe the two important MHD instabilities relevant to dilute magnetized plasmas.

Table 2.3.1: MHD Stability Criteria

	<b>nonmagnetized</b>	<b>magnetized, collisional</b>	<b>magnetized, dilute</b>
<b>angular momentum transfer</b>	angular momentum ( $R^2\Omega$ ) increases outwards	angular velocity $\Omega$ increases outwards	angular velocity $\Omega$ increases outwards
<b>energy transfer</b>	entropy $\ln p_0\rho_0^{-5/3}$ increases upward	entropy $\ln p_0\rho_0^{-5/3}$ increases upward	temperature $T_0$ increases upward

## 2.4 Magnetothermal Instability (MTI)

The magnetothermal instability destabilizes equilibrium systems in which the temperature, rather than entropy, decreases outwards or upwards. The simplest case is an equilibrium box in which magnetic field lines lie along isotherms. The gravitational acceleration points downwards, with the bottom being hot and the top being cold. Parrish & Stone (2005) performed a two-dimensional numerical simulation, and Parrish & Stone (2006) performed a three-dimensional numerical simulation, of this equilibrium box to demonstrate the nonlinear development of the MTI into bulk isothermal layers across the direction of heat flux. Now we perturb the magnetic field

lines so that some component of field line lies in layers that are hotter and cooler than the equilibrium layer. High thermal conductivity along magnetic field lines ensures efficient heat flow from the hotter fluid element at the bottom to the colder fluid element at the top. Force balance yields pressure equilibrium at each thermal layer. For the component of magnetic field line in the cooler (upper) region, the plasma along the field becomes hotter and less dense than the ambient medium, so that buoyancy forces push the fluid element upward. For the component of magnetic field line in the hotter (lower) region, the plasma along the field line becomes cooler and more dense than the ambient medium, so that buoyancy forces push the fluid element downwards. The magnetic field lines stretch out further, leading to larger heat fluxes along the direction of thermal gradient, causing the process to run away. This is demonstrated in Fig. (2.4.1). The stability condition for this box is,

$$-\frac{1}{\rho_0} \nabla p_0 \cdot \nabla T_0 \geq 0. \quad (2.4.1)$$

If we include the effects of rotation, the stability criterion is modified in the following manner (Balbus 2001):

$$-\frac{1}{\rho_0} \nabla p_0 \cdot \nabla \ln T_0 + \frac{\partial \Omega^2}{\partial \ln R} \geq 0. \quad (2.4.2)$$

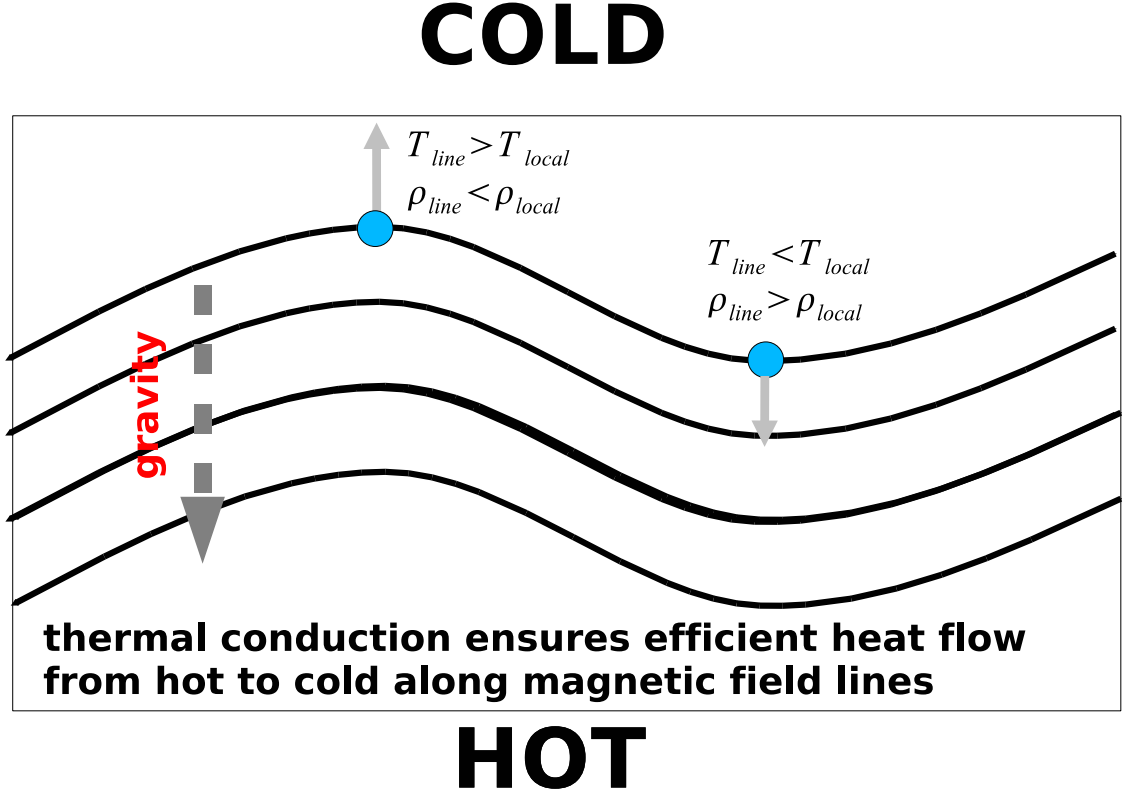


Fig. 2.4.1.— Depiction of the method by which the magnetothermal instability operates. Fast thermal conductivity along magnetic field lines result in heat flow from hotter to colder regions along the deformed field. Pressure balance results in the component of fluid along the field line in the upper region to be lighter than the ambient medium. Similarly, the fluid element in the lower region is heavier than the ambient medium. This leads to a runaway process as buoyant forces stretch the field lines further, leading to larger heat fluxes along the direction of equilibrium temperature gradient.

### 2.4.1 Linear Stability

Here we consider the linear stability of a convectively stable, dilute magnetized equilibrium box. The mean free path along magnetic field lines is smaller than the size of the box, therefore the form of the heat flux  $q$  is given by Eq. (2.3.8). Gravity points downwards,  $\mathbf{g} = -g\hat{\mathbf{z}}$ . Therefore  $\partial \ln p_0 / \partial z < 0$ . Isotherms and isobars are on surfaces of constant  $z$ . The equilibrium magnetic field  $\mathbf{B}_0 = B_0 \hat{\mathbf{R}}$ , so that  $\mathbf{B}_0 \cdot \nabla T_0 = 0$ . The fluid is at rest, i.e.,  $\mathbf{V}_0 = \mathbf{0}$ . The MHD internal energy equation Eq. (1.2.3),

becomes,

$$\frac{3}{2}p\frac{d}{dt}\ln p\rho^{-5/3} = \nabla \cdot (\rho\eta_\kappa \mathbf{b}\mathbf{b} \cdot \nabla \theta). \quad (2.4.3)$$

We look at modes of the form  $\delta a \propto \exp(\Gamma t + ik_R R)$ . The perturbed MHD equations are then given by,

$$\Gamma \frac{\delta \rho}{\rho_0} + ik_R \delta u_R + \delta u_Z \frac{\partial \ln \rho_0}{\partial z} = 0, \quad (2.4.4)$$

$$\Gamma \delta u_R = -ik_R \theta_0 \frac{\delta p}{p_0}, \quad (2.4.5)$$

$$\Gamma \delta u_\phi = \frac{ik_R B_0 \delta B_\phi}{4\pi \rho_0}, \quad (2.4.6)$$

$$\Gamma \delta u_Z = \frac{ik_R B_0 \delta B_Z}{4\pi \rho_0} + \frac{\delta \rho}{\rho_0} \theta_0 \frac{\partial \ln p_0}{\partial z}, \quad (2.4.7)$$

$$\Gamma \left( \frac{3}{2} \frac{\delta p}{p_0} - \frac{5}{2} \frac{\delta \rho}{\rho_0} \right) + \frac{3}{2} \delta u_Z \frac{\partial \ln p_0 \rho_0^{-5/3}}{\partial z} = -\eta_\kappa k_R^2 \frac{\delta \theta}{\theta_0} + ik_R \eta_\kappa \delta b_Z \frac{\partial \ln T_0}{\partial z}, \quad (2.4.8)$$

$$\Gamma \delta B_\phi = ik_R B_0 \delta u_\phi, \quad (2.4.9)$$

$$\Gamma \delta B_Z = ik_R B_0 \delta u_Z. \quad (2.4.10)$$

One mode corresponds to a shear-Alfvén wave, only  $\delta u_\phi$  and  $\delta B_\phi$  are nonzero, and  $\Gamma^2 = -k_R^2 v_A^2$ . Other modes satisfy the following dispersion relation:

$$\begin{aligned} & \left( \Gamma + \frac{2}{5} \eta_\kappa k_R^2 \right) (\Gamma^2 + k_R^2 v_A^2) - \\ & \theta_0 \frac{\partial \ln p_0}{\partial z} \left( \frac{2}{5} \eta_\kappa k_R^2 \frac{\partial \ln T_0}{\partial z} + \frac{3}{5} \Gamma \frac{\partial \ln p_0 \rho_0^{-5/3}}{\partial z} \right) + \\ & \frac{\Gamma^2}{k_R^2 \theta_0} \left( \frac{3}{5} \Gamma + \frac{2}{5} \eta_\kappa k_R^2 \right) \left( \theta_0 \left[ \frac{\partial \ln p_0}{\partial z} \right]^2 + \Gamma^2 + k_R^2 v_A^2 \right) = 0. \end{aligned} \quad (2.4.11)$$



We consider simplifications to elucidate the plasma behavior. In the Boussinesq limit, where  $\beta \gg 1$ , Eq. (2.4.11) becomes:

$$\begin{aligned} & (\Gamma^2 + k_R^2 v_A^2) \left( \Gamma + \frac{2}{5} \eta_\kappa k_R^2 \right) = \\ & \theta_0 \frac{\partial \ln p_0}{\partial z} \left( \frac{2}{5} \eta_\kappa k_R^2 \frac{\partial \ln T_0}{\partial z} + \frac{3}{5} \Gamma \frac{\partial \ln p_0 \rho_0^{-5/3}}{\partial z} \right) \end{aligned} \quad (2.4.12)$$

In the limit of large thermal diffusivity,  $\eta_\kappa k_R^2 \gg \Gamma$ , the growth rate of unstable modes follows from Eq. (2.4.11),

$$\Gamma^2 = \theta_0 \frac{\partial \ln p_0}{\partial z} \frac{\partial \ln T_0}{\partial z} - k_R^2 v_A^2. \quad (2.4.13)$$

If  $\partial \ln T_0 / \partial z < 0$ , then  $\Gamma^2 > 0$  for arbitrarily small wavenumbers in the Boussinesq limit. This is the essence of the MTI. Furthermore, if the thermal diffusivity goes to zero, we reproduce the criterion for convective instability within a magnetized medium. The modes are unstable if the entropy decreases upwards,  $\partial \ln p_0 \rho_0^{-5/3} / \partial z < 0$ . The dispersion relation becomes,

$$\Gamma^2 \approx \frac{3}{5} \theta_0 \left( \frac{\partial \ln p_0}{\partial z} \right) \left( \frac{\partial \ln p_0 \rho_0^{-5/3}}{\partial z} \right) - k_R^2 v_A^2 \quad (2.4.14)$$

We define natural units of growth rate  $\Gamma_0$  and wavenumber  $k_{R0}$  for the MTI in this box as,

$$\Gamma_0 = \sqrt{\theta_0 \left( \frac{\partial \ln p_0}{\partial z} \right) \left( \frac{\partial \ln T_0}{\partial z} \right)}, \quad (2.4.15)$$

$$k_{R0} = \sqrt{\beta \left( \frac{\partial \ln p_0}{\partial z} \right) \left( \frac{\partial \ln T_0}{\partial z} \right)}. \quad (2.4.16)$$

In Fig. (2.4.2) we show solutions to the full dispersion relation of the MTI, given by Eq. (2.4.11). We plot the normalized growth rate  $\Gamma/\Gamma_0$  as a function of normalized radial wavenumber  $k_R/k_{R0}$  for various normalized thermal diffusivities  $\eta_\kappa \Gamma_0/v_A^2 \geq 1$ . We take  $\beta = 100$  and choose  $\partial \ln p_0/\partial z = 4\partial \ln T_0/\partial z < 0$ . This ensures convective stability,  $\partial \ln p_0 \rho_0^{-5/3}/\partial z = -\partial \ln T_0/\partial z > 0$ .

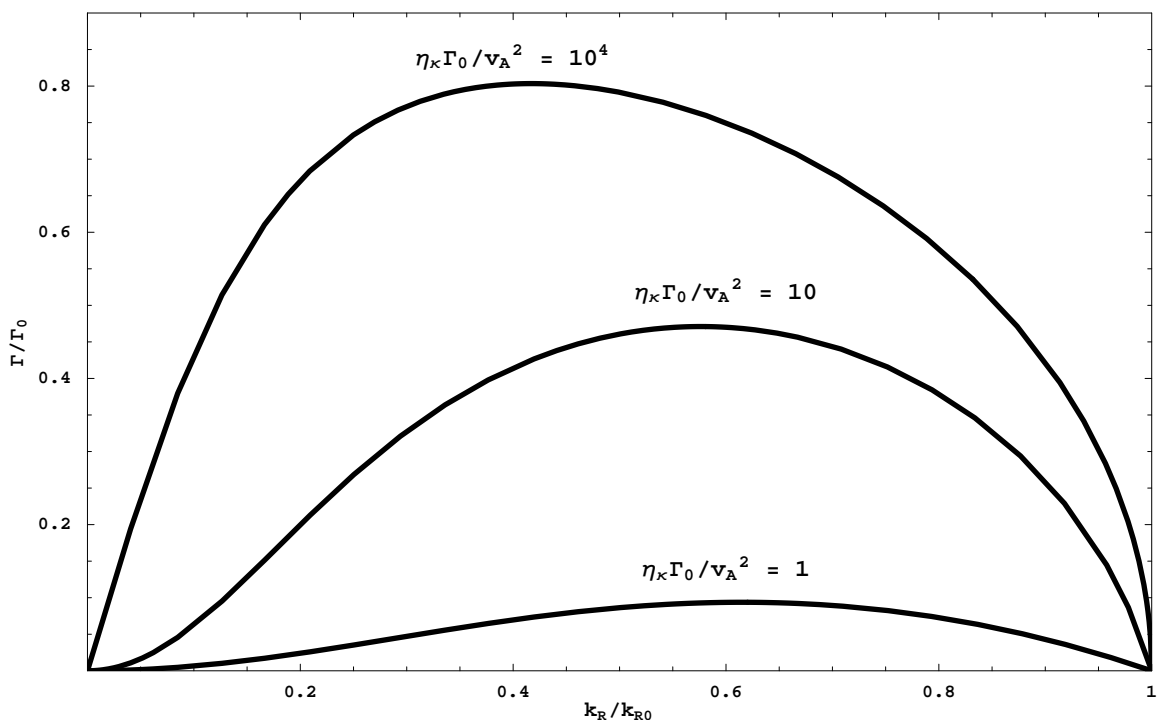


Fig. 2.4.2.— Normalized growth rate of the MTI as a function of normalized wavenumber for plasma  $\beta = 100$  and various values of normalized thermal diffusivity, under the condition of convective stability

## 2.4.2 Nonlinear Behavior

Numerical simulations have demonstrated the nonlinear development of the MTI in a three dimensional convectively stable Cartesian box that is hot at the bottom and cold on top (Parrish & Stone 2006). The top and bottom regions are stabilized to the MTI, via isotropic thermal diffusivities larger than the anisotropic thermal

diffusivity, in order to remove the effects of simulation boundary layers on the MTI. The middle layer has a largely anisotropic thermal diffusivity and is linearly unstable to the MTI. The initial condition is a temperature profile linear with height in the unstable middle layer and magnetic fields that lie along isotherms. The plasma in this box develops into a steady state with a bulk isothermal layer, shown in Fig. (2.4.3). The magnetic field is sustained, via fluid motion driven by the boundary conditions, against numerical resistivity. This is shown in Fig. (2.4.4).

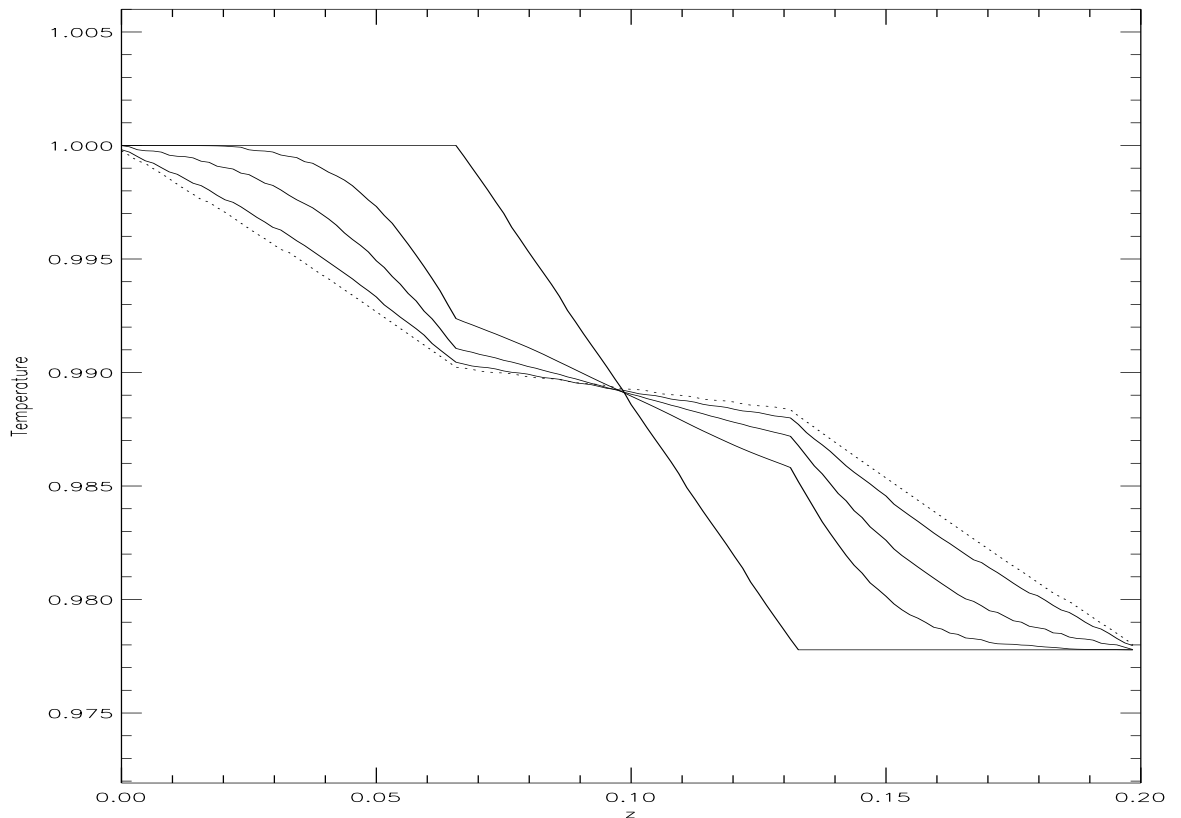


Fig. 2.4.3.— Plot of the horizontally averaged temperature, as a function of box height, for various times in the three-dimensional simulation. This plot is taken from Parrish & Stone (2006). Over a period of a few dynamic timescales an isothermal layer develops.

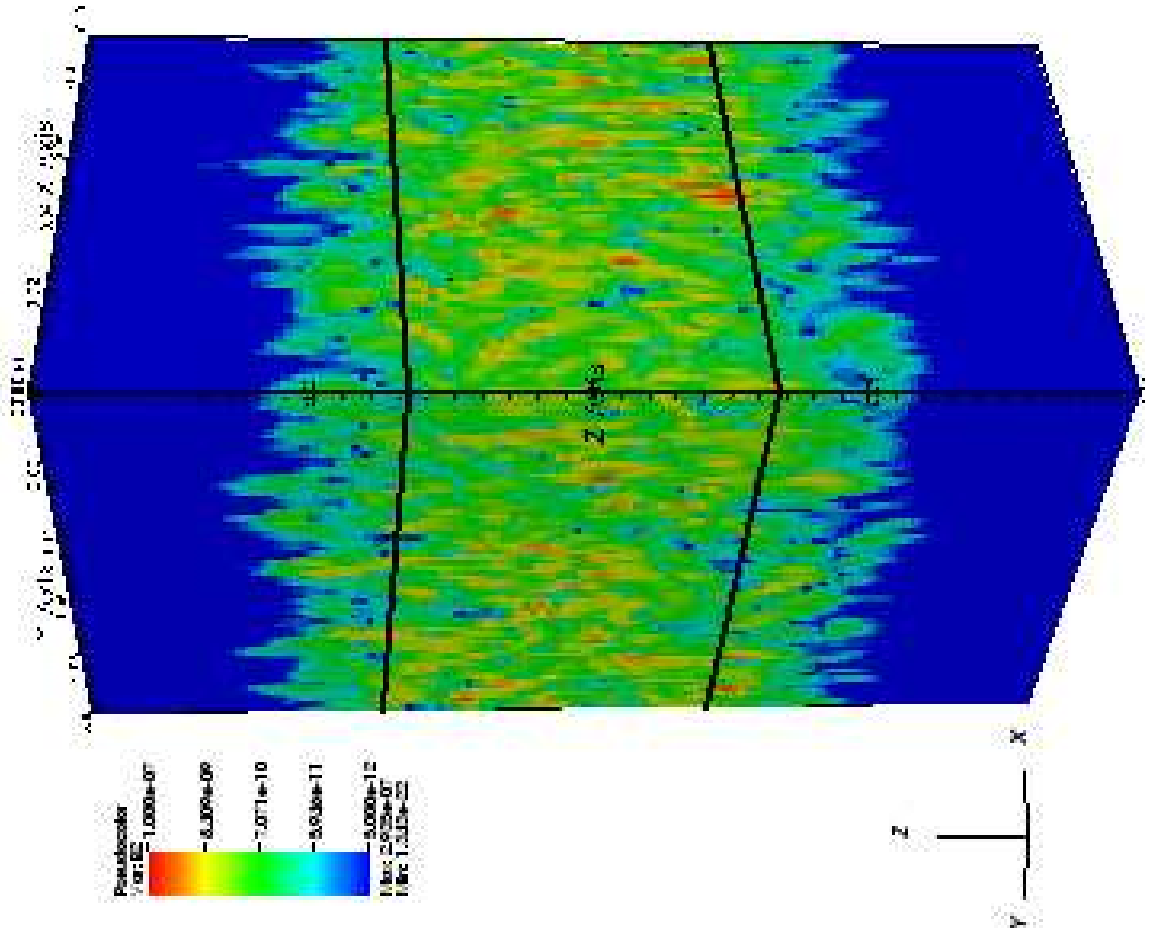


Fig. 2.4.4.— The magnetic energy density at late times in a convectively stable three-dimensional box. This plot is taken from Parrish & Stone (2006). Gravity points to the right ( $-z$  direction) in this box. Temperature gradients point to the left.

## 2.5 Magnetoviscous Instability (MVI)

The MVI is an instability when torques arising from magnetic field-directed viscous stresses, rather than Lorentz forces as in the MRI, may destabilize a rotating plasma. Consider, from Eq. (2.3.6), a type of fluid stress directed along magnetic field lines. This stress disappears in a rigidly rotating disk, but in the presence of angular velocity shear it will result in torques. Consider two points connected by a magnetic field line. This field line is perturbed slightly so that there exists some component of magnetic

field along the radial direction. One point is located at  $R > R_0$ , while the other is located at  $R < R_0$ , where  $R_0$  is the equilibrium radius. Strong viscous stresses, along the field line, transfer angular velocity from the inner point to the outer point. The outer point rotates faster than the ambient medium, and is pushed outwards. The inner point rotates slower than the ambient medium, and is pushed inwards. As these points are further separated, they experience even stronger forces pushing them apart, and the process runs away. This is shown in Fig. (2.5.1). The first discussion

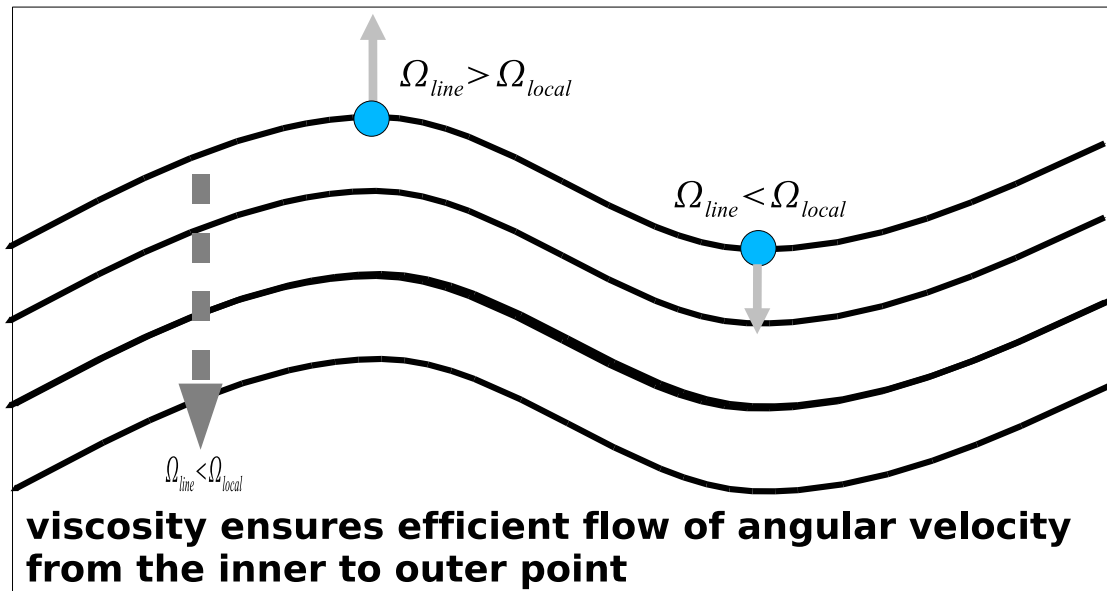


Fig. 2.5.1.— Depiction of the magnetoviscous instability. Viscosity ensures the efficient transport of angular velocity from the inner point to the outer point.

of the magnetoviscous instability in a Keplerian disks was given by Balbus (2004b), and its collisionless limit, which has been denoted as the collisionless MRI, was first explored by Quataert et al. (2002).

## Chapter 3

### Problem Setup

In this chapter, we discuss the nature of accretion within a dilute, magnetized rotating plasma. To set up the background for the stability analysis we use the following three preliminaries. First, we consider a local patch of a thin dilute magnetized disk. This plasma has local radial gradients of temperature and pressure such that the system is Schwarzschild stable,  $\partial \ln p_0 \rho_0^{-5/3} / \partial \ln R > 0$ , and has a nonradial magnetic field in the disk midplane. For arbitrarily thin disk,  $H^2/R^2 \rightarrow 0$  or equivalently  $\theta_0/(R^2\Omega^2) \rightarrow 0$ , the disk has the following properties: 1) the temperature is locally constant along field lines, hence isothermal in  $z$ ; 2) the magnetic field is nonradial and constant; and 3) the angular velocity is constant along field lines, hence constant in height. The local patch of the disk has a gaussian profile of pressure and density in height. The equilibrium magnetic field is,

$$\mathbf{B}_0 = B_0 \left( \hat{\phi} \cos \chi + \hat{z} \sin \chi \right). \quad (3.0.1)$$

Second, we derive expressions for angular momentum and energy flux carried by the turbulence within a dilute radiatively inefficient accretion flow. Finally, we explore

only the fastest-growing, axisymmetric, local instabilities, of the form,

$$\delta a \propto \exp(\Gamma t + ik_R R + ik_Z z), \quad (3.0.2)$$

where  $\delta a$  is some perturbed field variable. The details of our derivation of a local disk vertical profile is discussed in Appendix B. We demonstrate expressions for the angular momentum flux and energy flux carried in the linear stages of these instabilities. Terms associated with finite viscosity and thermal conductivity appear in expressions for angular momentum and thermal energy flux.

### 3.1 Angular Momentum and Energy Balance

As described in §1.3.2, a necessary condition for accretion flow within a disk requires that fluctuations due to turbulence or waves must have  $\langle W_{R\phi} \rangle > 0$ . This leads to a characteristic accretion power through  $R\phi$  stress,  $-\rho \langle W_{R\phi} \rangle d\Omega/d \ln R$ . In a classical accretion disk this energy is locally thermalized and radiated away. In a dilute and radiatively inefficient disk this energy cannot be radiated; hence, it must either remain as heat, or be actively transported outwards. This suggests that we must solve the equations of angular momentum balance and total energy balance for a dilute nonradiating flow, in order to extract the form of  $W_{R\phi}$  and heat flux. We employ MHD equations in a rotating frame, Eqs. (1.2.5) - (1.2.8), and in a nonrotating frame, Eqs. (1.2.1) - (1.2.4). We follow the vocabulary and formalism of Balbus & Hawley (1998) for classical accretion disks and continued in Balbus (2004a) for radiatively inefficient flows. We consider fluctuating fluid parameters whose behavior is described in §1.3.2. We study a thin disk; since we suppose velocity fluctuations are at best of order  $\theta_0^{1/2} \ll R\Omega(R)$ . Since the fluid fluctuations are relatively small, then quadratic correlations of fluctuating parameters dominate in expressions for heat and angular

momentum fluxes.

### 3.1.1 Angular Momentum Balance

We employ the method of angular momentum balance in an accretion disk described in Balbus et al. (1994); Balbus & Hawley (1998) and in §1.3. The angular momentum density  $\mathcal{L}_z$  is given by,

$$\mathcal{L}_z = \rho R V_\phi \quad (3.1.1)$$

If we multiply the azimuthal component of Eq. (1.2.2) by  $R$  we then have the following equation,

$$\frac{\partial \mathcal{L}_z}{\partial t} + \nabla \cdot \left( R \left[ \rho V_\phi \mathbf{V} - \frac{B_\phi \mathbf{B}}{4\pi} + \left( p + \frac{B^2}{8\pi} \right) \hat{\phi} + \boldsymbol{\sigma} \cdot \hat{\phi} \right] \right) = 0. \quad (3.1.2)$$

We take Eq. (3.1.2) and apply the velocity decomposition given in §1.2. We average that resulting equation according to the prescription of Eq. (1.3.17). We derive the form of the averaged angular momentum balance equation,

$$\frac{\partial \langle \mathcal{L}_z \rangle}{\partial t} + \frac{1}{R} \frac{\partial}{\partial R} (R^2 \langle T_{R\phi} \rangle + R^3 \Omega \langle \rho u_R \rangle) = 0, \quad (3.1.3)$$

where  $\langle T_{R\phi} \rangle = \rho \langle W_{R\phi} \rangle$  and is defined by,

$$\langle T_{R\phi} \rangle = \left\langle \rho \delta u_R \delta u_\phi - \frac{\delta B_R \delta B_\phi}{4\pi} + \delta \sigma_{\mathbf{b}\mathbf{b}} \delta b_R \cos \chi \right\rangle_\rho. \quad (3.1.4)$$

In Eq. (3.1.4), we have used the equilibrium magnetic field given in Eq. (3.0.1) and the viscous stress tensor given in Eq. (2.3.6).



### 3.1.2 Total Energy Balance

To derive the energy balance equation, we first dot the MHD comoving force balance equation, Eq. (1.2.6), with  $\mathbf{u}$ , and use Eq. (2.3.6), for the form of the viscous stress tensor,

$$\begin{aligned} \mathbf{u} \cdot \left( \frac{\partial}{\partial t} + \Omega \frac{\partial}{\partial \phi} \right) (\rho \mathbf{u}) + \mathbf{u} \cdot \nabla p + u_i \partial_j (\rho u_i u_j) + \\ u_i \partial_j \left( \sigma_{\mathbf{b}\mathbf{b}} \left[ b_i b_j - \frac{1}{3} \delta_{ij} \right] \right) + \Omega' R \rho u_R u_\phi + R \frac{\partial \Omega}{\partial z} \rho u_z u_\phi = \\ \frac{\rho}{\rho_0} \mathbf{u} \cdot \nabla p_0 - \mathbf{u} \cdot \frac{(\nabla \times \mathbf{B}) \times \mathbf{B}}{4\pi} \end{aligned} \quad (3.1.5)$$

Next, we dot the MHD comoving induction equation, Eq. (1.2.8), with  $\mathbf{B}$  to get the magnetic energy equation,

$$\begin{aligned} \left( \frac{\partial}{\partial t} + \Omega \frac{\partial}{\partial \phi} \right) \frac{B^2}{8\pi} = -\mathbf{u} \cdot \nabla \left( \frac{B^2}{8\pi} \right) - \frac{B^2}{4\pi} \nabla \cdot \mathbf{u} + \frac{B^2}{4\pi} \mathbf{b} \cdot \nabla \mathbf{u} \cdot \mathbf{b} + \\ \Omega' R \frac{B_R B_\phi}{4\pi} + \frac{\partial \Omega}{\partial z} R \frac{B_z B_\phi}{4\pi}. \end{aligned} \quad (3.1.6)$$

Using Eq. (2.3.6) for the viscous stress tensor and Eq. (2.3.5) for the heat flux, the MHD comoving internal energy equation, Eq. (1.2.7), becomes,

$$\begin{aligned} \frac{3}{2} \left( \frac{\partial}{\partial t} + \Omega \frac{\partial}{\partial \phi} \right) p + \nabla \cdot \left( \frac{3}{2} p \mathbf{u} \right) + p \nabla \cdot \mathbf{u} = -\nabla \cdot (q \mathbf{b}) - \\ \sigma_{\mathbf{b}\mathbf{b}} \left( \mathbf{b} \cdot \nabla \mathbf{u} \cdot \mathbf{b} + R \mathbf{b} \cdot \nabla \Omega b_\phi - \frac{1}{3} \nabla \cdot \mathbf{u} \right). \end{aligned} \quad (3.1.7)$$

We add Eqs. (3.1.5), (3.1.6), and (3.1.7), to arrive at the total energy equation:

$$\begin{aligned}
& \left( \frac{\partial}{\partial t} + \Omega \frac{\partial}{\partial \phi} \right) \left( \frac{1}{2} \rho u^2 + \frac{3}{2} p + \frac{B^2}{8\pi} \right) + \\
& \nabla \cdot \left( \mathbf{u} \left[ \frac{1}{2} \rho u^2 + \frac{5}{2} p \right] + \frac{\mathbf{B} \times (\mathbf{u} \times \mathbf{B})}{4\pi} + \sigma_{\mathbf{b}\mathbf{b}} \left( \mathbf{b} (\mathbf{u} \cdot \mathbf{b}) - \frac{1}{3} \mathbf{u} \right) \right) - \\
& \rho \mathbf{u} \cdot \frac{1}{\rho_0} \nabla p_0 = - \frac{\partial \Omega}{\partial \ln R} \left( \rho u_R u_\phi - \frac{B_R B_\phi}{4\pi} + \boldsymbol{\sigma}_{R\phi} \right) - \\
& R \frac{\partial \Omega}{\partial z} \left( \rho u_z u_\phi - \frac{B_z B_\phi}{4\pi} + \boldsymbol{\sigma}_{z\phi} \right). \tag{3.1.8}
\end{aligned}$$

Applying the prescription for the average as given by Eq. (1.3.17) to Eq. (3.1.8), we arrive at the formula for the averaged total energy balance equation,

$$\frac{\partial}{\partial t} \langle \mathcal{E} \rangle + \frac{1}{R} \frac{\partial}{\partial R} R \langle F_{ER} \rangle - \langle \rho u_R \rangle \frac{1}{\rho_0} \frac{\partial p_0}{\partial R} = - \frac{\partial \Omega}{\partial \ln R} \langle T_{R\phi} \rangle, \tag{3.1.9}$$

where,

$$\langle \mathcal{E} \rangle = \left\langle \frac{1}{2} \rho u^2 + \frac{3}{2} p + \frac{B^2}{8\pi} \right\rangle_\rho, \tag{3.1.10}$$

$$\langle F_{ER} \rangle = \frac{5}{2} \rho_0 \langle \delta u_R \delta \theta \rangle_\rho + \langle \delta q \delta b_R \rangle_\rho - \frac{1}{3} \langle \delta \sigma_{\mathbf{b}\mathbf{b}} \delta u_R \rangle_\rho. \tag{3.1.11}$$

In Eq. (3.1.9) we have ignored the flux of gas kinetic energy since it appears as a cubic correlation in fluctuating quantities, and the Poynting flux  $\mathbf{B} \times (\mathbf{u} \times \mathbf{B}) / (4\pi)$  since it is subdominant to the terms in the energy flux. In steady state, the energy generated through the coupling of fluctuations to the radial angular velocity gradient is carried out by the quadratic correlation of turbulent heat flux,  $\langle F_{ER} \rangle$ .

We need to estimate the angular momentum flux and heat flux carried by unstable modes, to demonstrate that these modes allow accretion to occur. This requires expressions for quadratic correlations in the unstable modes. We consider a cylindrical annulus with radial extent  $\Delta R$  and infinite vertical extent. We assume that in this

annulus, the unstable modes have characteristic radial wavelength much smaller than  $\Delta R$  and vertical wavelength much smaller than  $H$ . It is relatively easy to show that the magnitude of the quadratic correlations of spatially varying modal quantities  $A$  and  $B$

$$\langle AB \rangle_{\mathbf{k}} \equiv \text{Re} (A_{\mathbf{k}} B_{\mathbf{k}}^*), \quad (3.1.12)$$

$$\langle A \hat{\mathbf{e}} \cdot \nabla B \rangle \equiv \text{Im} (A_{\mathbf{k}} (\hat{\mathbf{e}} \cdot \mathbf{k}) B_{\mathbf{k}}^*). \quad (3.1.13)$$

## Chapter 4

# Fluid Treatment – the MVTI

In this chapter we describe stability of a rotating plasma with radial gradients of temperature and pressure using a fluid treatment. The formal regime of validity of the fluid treatment is that  $\lambda_i \lesssim R$ . This bound on  $\lambda_i$  breaks down in the innermost regions of black hole accretion flows, for example in Sag. A\* (Quataert 2004) or in other underluminous objects. However, our fluid approximation is expected to be well-satisfied within the outermost regions of this flow. The viscous stress  $\sigma_{\mathbf{bb}}$ , and the heat flux  $q$ , are given by Eqs. (2.3.7) and (2.3.8), respectively. In the outer regions of hot dilute magnetized accretion flows, the fluid approximation is valid and ion and electron temperatures are equal. Here the (electron) thermal diffusion coefficient is larger than the (ion) viscous diffusion coefficient by a factor of order  $(m_i/m_e)^{1/2}$ .

We analyze unstable modes in the Boussinesq limit, characterized by incompressible perturbations. We calculate the dispersion relation of an idealized plasma where both ions and electrons have the same temperature  $T$ . The temperature and pressure decrease radially outwards such that the plasma is Schwarzschild stable. We show that the linear stability behavior of this plasma reduces to that of the MRI, the MVI (Balbus 2004b; Islam & Balbus 2005), and MTI in specific limiting cases. We also

demonstrate that the quadratic heat fluxes and quadratic angular momentum fluxes associated with the MVTI are of the right sense and magnitude to drive accretion in radiatively inefficient astrophysical plasmas.

In §4.1 we derive the MVTI dispersion relation and show its limiting cases. In §4.2 we discuss the main features of the MVTI dispersion relation. In §4.3 we derive bulk fluxes for the modes of the MVTI, showing that turbulence driven by this MHD instability can drive accretion in radiatively inefficient flows. These modes, where the phase velocities smaller than that of the sound speed  $\theta_0^{1/2}$ , are almost incompressible. We show in §4.4 that for plasmas with finite compressibility, in a weak magnetic field,  $\beta \gg 1$ , there is very little change in the the growth rate and quadratic fluxes of angular momentum and heat.

## 4.1 Dispersion Relation

Assume small perturbations about the equilibrium, in which the viscous stress tensor and heat flux are zero. We look at axisymmetric modes of the form given by Eq. (3.0.2), for a plasma with nonradial magnetic field  $\mathbf{B}_0 = B_0 (\hat{\phi} \cos \chi + \hat{z} \sin \chi)$ . The perturbed viscous stress and heat flux magnitude are given by,

$$\delta \boldsymbol{\sigma} = -3\rho_0 \eta_\nu \left( \mathbf{b}_0 \mathbf{b}_0 - \frac{1}{3} \mathbb{I} \right) (i (\mathbf{k} \cdot \mathbf{b}_0) (\mathbf{b}_0 \cdot \delta \mathbf{u}) + \Omega' R \delta \bar{B}_R \cos \chi), \quad (4.1.1)$$

$$\delta q = -\eta_\kappa p_0 \delta \bar{B}_R \frac{\partial \ln T_0}{\partial R} - \eta_\kappa p_0 (i \mathbf{k} \cdot \mathbf{b}_0) \frac{\delta T}{T_0}, \quad (4.1.2)$$

where  $\delta\bar{\mathbf{B}} = \delta\mathbf{B}/B_0$ . The perturbed comoving induction equation, Eq. (1.2.8), can be written as,

$$\begin{aligned}\Gamma\delta\bar{B}_R &= ik_Z \sin\chi \delta u_R, \\ \Gamma\delta\bar{B}_\phi &= ik_Z \sin\chi \delta u_\phi + \Omega' R \delta\bar{B}_R, \\ \Gamma\delta\bar{B}_Z &= ik_Z \sin\chi \delta u_Z,\end{aligned}\tag{4.1.3}$$

where  $\Omega' = d\Omega/dR$ . The nonzero components of the perturbed viscous stress tensor are,

$$\delta\sigma_{\phi\phi} = \delta\sigma_{ZZ} = \left(\cos^2\chi - \frac{1}{3}\right) \delta\sigma_{\mathbf{b}\mathbf{b}},\tag{4.1.4}$$

$$\delta\sigma_{RR} = -\frac{1}{3}\delta\sigma_{\mathbf{b}\mathbf{b}},\tag{4.1.5}$$

$$\delta\sigma_{Z\phi} = \delta\sigma_{\phi Z} = (\sin\chi \cos\chi) \delta\sigma_{\mathbf{b}\mathbf{b}}.\tag{4.1.6}$$

If we substitute Eq. (4.1.3) into Eq. (4.1.1), we get,

$$\delta\sigma_{\mathbf{b}\mathbf{b}} = -3\rho_0\eta_\nu\Gamma\left(\delta\bar{B}_\phi \cos\chi - \frac{k_R}{k_Z}\delta\bar{B}_R \sin\chi\right).\tag{4.1.7}$$

The perturbed comoving energy balance equation, Eq. (1.2.7), can be written as,

$$\begin{aligned}\Gamma\left(\frac{\delta p}{p_0} - \frac{5}{3}\delta\bar{\rho}\right) + \delta u_R \frac{\partial \ln p_0 \rho_0^{-5/3}}{\partial R} = \\ \frac{2}{3}\eta_\kappa\left(ik_Z \sin\chi\left(\delta\bar{B}_R \frac{\partial \ln T_0}{\partial R}\right) - k_Z^2 \sin^2\chi \frac{\delta T}{T_0}\right) + \frac{2}{3}p_0^{-1}\delta\boldsymbol{\sigma} : \nabla\left(R\Omega\hat{\boldsymbol{\phi}}\right),\end{aligned}\tag{4.1.8}$$

where  $\delta\bar{\rho} = \delta\rho/\rho_0$ . For the perturbed viscous stress tensor given by Eqs. (4.1.4) - (4.1.6),  $\delta\boldsymbol{\sigma} : \nabla\left(R\Omega\hat{\boldsymbol{\phi}}\right) = 0$ . For incompressible perturbations,  $\delta p/p_0 \ll \delta\rho/\rho_0$ ,

Eq. (4.1.8) can be solved for the perturbed density,

$$\delta\bar{\rho} = \frac{3}{5} \times \frac{\delta u_R \partial \ln p_0 \rho_0^{-5/3} / \partial R - \frac{2}{3} i \eta_\kappa k_Z \sin \chi \delta \bar{B}_R \partial \ln T_0 / \partial R}{\Gamma + \frac{2}{5} \eta_\kappa k_Z^2 \sin^2 \chi}. \quad (4.1.9)$$

The perturbed form of the comoving force balance equation, Eq. (1.2.6), can be written as,

$$\begin{aligned} \frac{\partial \delta \mathbf{u}}{\partial t} + 2\Omega \hat{\mathbf{z}} \times \delta \mathbf{u} + \Omega' R \hat{\phi} = -\frac{1}{\rho_0} \nabla \left( \delta p + \frac{\mathbf{b}_0 \cdot \delta \mathbf{B}}{4\pi} \right) + \frac{\mathbf{b}_0 \cdot \nabla \delta \mathbf{B}}{4\pi \rho_0} - \\ \rho_0^{-1} \nabla \cdot \delta \boldsymbol{\sigma} + \delta \bar{\rho} \theta_0 \frac{\partial \ln p_0}{\partial R} \hat{\mathbf{R}}, \end{aligned} \quad (4.1.10)$$

whose components are,

$$\begin{aligned} \Gamma \delta u_R - 2\Omega \delta u_\phi = -ik_R \left( \frac{\delta p}{\rho_0} + \frac{B_0 \cos \chi \delta B_\phi + B_0 \sin \chi \delta B_Z}{4\pi \rho_0} \right) + \\ \frac{ik_Z B_0 \sin \chi}{4\pi \rho_0} \delta B_R + ik_R \rho_0^{-1} \delta \sigma_{RR} + ik_Z \rho_0^{-1} \delta \sigma_{zR} + \delta \bar{\rho} \theta_0 \frac{\partial \ln p_0}{\partial R}, \end{aligned} \quad (4.1.11)$$

$$\begin{aligned} \Gamma \delta u_\phi + (2\Omega + \Omega' R) \delta u_R = \frac{ik_Z B_0 \sin \chi}{4\pi \rho_0} \delta B_\phi + ik_R \rho_0^{-1} \delta \sigma_{\phi R} + \\ ik_Z \rho_0^{-1} \delta \sigma_{\phi z}, \end{aligned} \quad (4.1.12)$$

$$\begin{aligned} \Gamma \delta u_Z = -ik_Z \left( \frac{\delta p}{\rho_0} + \frac{B_0 \cos \chi \delta B_\phi + B_0 \sin \chi \delta B_Z}{4\pi \rho_0} \right) + \\ \frac{ik_Z B_0 \sin \chi}{4\pi \rho_0} \delta B_Z + ik_R \rho_0^{-1} \delta \sigma_{ZR} + ik_Z \rho_0^{-1} \delta \sigma_{ZZ}. \end{aligned} \quad (4.1.13)$$

Eq. (4.1.13) can be rearranged into,

$$\begin{aligned} \frac{\delta p}{\rho_0} + v_A^2 \cos \chi \delta \bar{B}_\phi = \eta_\nu \Gamma (3 \sin^2 \chi - 1) \left( \delta \bar{B}_\phi \cos \chi - \frac{k_R}{k_Z} \delta \bar{B}_R \sin \chi \right) - \\ \frac{ik_R}{k_Z^2} \Gamma \delta u_R. \end{aligned} \quad (4.1.14)$$

Using Eq. (4.1.3) and Eqs. (4.1.11), (4.1.12), and (4.1.14), we can express radial and azimuthal force balance equations in terms of  $\delta\bar{B}_R$  and  $\delta\bar{B}_\phi$ :

$$\begin{aligned} & \left(1 + \frac{k_R^2}{k_Z^2}\right) \Gamma^2 \delta\bar{B}_R - 2\Omega \left(\Gamma \delta\bar{B}_\phi - \Omega' R \delta\bar{B}_R\right) = \\ & 3\eta_\nu \Gamma k_R k_Z \sin^3 \chi \left(\delta\bar{B}_\phi \cos \chi - \frac{k_R}{k_Z} \delta\bar{B}_R \sin \chi\right) - \end{aligned} \quad (4.1.15)$$

$$\begin{aligned} & (k_R^2 + k_Z^2) v_A^2 \sin^2 \chi \delta\bar{B}_R + \\ & \frac{3}{5} \theta_0 \left(\frac{\partial \ln p_0}{\partial R}\right) \frac{\Gamma \partial \ln p_0 \rho_0^{-5/3} / \partial R + \frac{2}{3} \eta_\kappa k_Z^2 \sin^2 \chi \partial \ln T_0 / \partial R}{\Gamma + \frac{2}{5} \eta_\kappa k_Z^2 \sin^2 \chi} \delta\bar{B}_R, \\ & \Gamma^2 \delta\bar{B}_\phi + 2\Omega \Gamma \delta\bar{B}_R = -3\eta_\nu \Gamma k_Z^2 \sin^2 \chi \cos \chi \left(\delta\bar{B}_\phi \cos \chi - \frac{k_R}{k_Z} \delta\bar{B}_R \sin \chi\right) - \\ & k_Z^2 v_A^2 \sin^2 \chi \delta\bar{B}_\phi. \end{aligned} \quad (4.1.16)$$

Eqs. (4.1.15) and (4.1.16) can be solved for the dispersion relation for the incompressible MVTI,

$$\begin{aligned} & \left(\frac{k^2}{k_Z^2} \Gamma^2 + \frac{d\Omega^2}{d \ln R} + 3\eta_\nu k_R^2 \Gamma \sin^4 \chi + k^2 v_A^2 \sin^2 \chi - \right. \\ & \left. \frac{3}{5} \theta_0 \left(\frac{\partial \ln p_0}{\partial R}\right) \frac{\Gamma \partial \ln p_0 \rho_0^{-5/3} / \partial R + \frac{2}{3} \eta_\kappa k_Z^2 \sin^2 \chi \partial \ln T_0 / \partial R}{\Gamma + \frac{2}{5} \eta_\kappa k_Z^2 \sin^2 \chi}\right) \times \\ & (\Gamma^2 + k_Z^2 v_A^2 \sin^2 \chi + 3\eta_\nu k_Z^2 \Gamma \sin^2 \chi \cos^2 \chi) + \\ & \Gamma^2 (4\Omega^2 - 9\eta_\nu^2 k_R^2 k_Z^2 \sin^6 \chi \cos^2 \chi) = 0, \end{aligned} \quad (4.1.17)$$

where  $k^2 = k_R^2 + k_Z^2$ . If electrons and ions have the same temperature, the Prandtl number is given by Braginskii (1965),

$$\text{Pr} \equiv \eta_\nu / \eta_\kappa \approx \frac{0.96}{3.2} \left(\frac{2m_e}{m_i}\right)^{1/2} \approx 1/101. \quad (4.1.18)$$



We employ normalizations of fluid variables as given in Tab. (A.2). One can write Eq. (4.1.17) as,

$$\begin{aligned}
& \left( \frac{\hat{k}^2}{\hat{k}_Z^2} \gamma^2 + 2 \frac{d \ln \Omega}{d \ln R} + 3 \hat{\eta}_\nu \hat{k}_R^2 \gamma \sin^4 \chi + \hat{k}^2 \sin^2 \chi - \right. \\
& \left. \frac{3}{5} \alpha_P \frac{\alpha_S \gamma + \frac{2}{3} \alpha_T \text{Pr}^{-1} \hat{\eta}_\nu \hat{k}_Z^2 \sin^2 \chi}{\gamma + \frac{2}{5} \text{Pr}^{-1} \hat{\eta}_\nu \hat{k}_Z^2 \sin^2 \chi} \right) \times \\
& \left( \gamma^2 + \hat{k}_Z^2 \sin^2 \chi + 3 \hat{\eta}_\nu \hat{k}_Z^2 \gamma \sin^2 \chi \cos^2 \chi \right) + \\
& \gamma^2 \left( 4 - 9 \hat{\eta}_\nu^2 \hat{k}_R^2 \hat{k}_Z^2 \sin^6 \chi \cos^2 \chi \right) = 0,
\end{aligned} \tag{4.1.19}$$

where  $\hat{k}^2 = k^2 v_A^2 / \Omega^2$ ,  $\alpha_S = -H \frac{\partial \ln p_0 \rho_0^{-5/3}}{\partial R}$ ,  $\alpha_P = -H \frac{\partial \ln p_0}{\partial R}$ , and  $\alpha_T = -H \frac{\partial \ln T_0}{\partial R}$ .

We now consider the form of Eq. (4.1.19) under the following limiting conditions. First, if the transport coefficient and equilibrium gradients go to zero, the dispersion relation reduces to that of the MRI,

$$\left( \frac{\hat{k}^2}{\hat{k}_Z^2} \gamma^2 + 2 \frac{d \ln \Omega}{d \ln R} + \hat{k}^2 \sin^2 \chi \right) \left( \gamma^2 + \hat{k}_Z^2 \sin^2 \chi \right) + 4 \gamma^2 = 0. \tag{4.1.20}$$

Second, if the equilibrium gradients are zero and the viscosity is nonzero, we reproduce the MVI dispersion relation (Islam & Balbus 2005),

$$\begin{aligned}
& \left( \frac{\hat{k}^2}{\hat{k}_Z^2} \gamma^2 + 2 \frac{d \ln \Omega}{d \ln R} + 3 \hat{\eta}_\nu \hat{k}_R^2 \gamma \sin^4 \chi + \hat{k}^2 \sin^2 \chi \right) \times \\
& \left( \gamma^2 + \hat{k}_Z^2 \sin^2 \chi + 3 \hat{\eta}_\nu \hat{k}_Z^2 \gamma \sin^2 \chi \cos^2 \chi \right) + \\
& \gamma^2 \left( 4 - 9 \hat{\eta}_\nu^2 \hat{k}_R^2 \hat{k}_Z^2 \sin^6 \chi \cos^2 \chi \right) = 0.
\end{aligned} \tag{4.1.21}$$

Third, in the limit of no viscosity but finite thermal conductivity, we reproduce the

MTI in a differentially rotating plasma (Balbus 2001),

$$\left( \frac{\hat{k}^2}{\hat{k}_Z^2} \gamma^2 + 2 \frac{d \ln \Omega}{d \ln R} + \hat{k}^2 \sin^2 \chi - \frac{3}{5} \alpha_P \frac{\alpha_S \gamma + \frac{2}{3} \alpha_T \text{Pr}^{-1} \hat{\eta}_\nu \hat{k}_Z^2 \sin^2 \chi}{\gamma + \frac{2}{5} \text{Pr}^{-1} \hat{\eta}_\nu \hat{k}_Z^2 \sin^2 \chi} \right) \times \quad (4.1.22)$$

$$\left( \gamma^2 + \hat{k}_Z^2 \sin^2 \chi \right) + 4\gamma^2 = 0.$$

Finally, in the limit of zero thermal conductivity and zero viscosity, but finite equilibrium gradients, we reproduce the dispersion relation for convectively unstable modes in a rotating magnetized plasma (Balbus 1995),

$$\left( \frac{\hat{k}^2}{\hat{k}_Z^2} \gamma^2 + 2 \frac{d \ln \Omega}{d \ln R} + \hat{k}^2 \sin^2 \chi - \frac{3}{5} \alpha_P \alpha_S \right) \left( \gamma^2 + \hat{k}_Z^2 \sin^2 \chi \right) + \quad (4.1.23)$$

$$4\gamma^2 = 0.$$

To better understand the stability of this dilute weakly magnetized plasma, consider the limit of Eq. (4.1.19) for which the viscosity becomes dynamically important,  $\eta_\nu \Omega / v_A^2 > 1$ . First, the viscous force dominates so that we reproduce a dispersion relation similar to the MVI. The fastest growing wavenumbers are those for which  $\eta_\nu k^2 \sim \Omega$ . In the MRI, the growth rate reaches a maximum of order  $\Omega$  at wavenumbers  $k \sim \Omega / v_A$ . For the MVI, the growth rate reaches a maximum at wavenumbers  $k \sim (\Omega / \eta_\nu)^{1/2} \ll \Omega / v_A$ .

Second, in the limit of dynamically important viscosity, the density response simplifies. We always have  $\text{Pr} < 1$ , therefore  $\delta \bar{\rho}$  as given by Eq. (4.1.9) can be approximated as,

$$\delta \bar{\rho} \approx -\frac{\delta u_R}{\Gamma} \left( \frac{\partial \ln T_0}{\partial R} \right), \quad (4.1.24)$$

and the following approximation occurs in Eq. (4.1.19),

$$\frac{3}{5}\alpha_P \frac{\alpha_S\gamma + \frac{2}{3}\alpha_T\text{Pr}^{-1}\hat{\eta}_\nu\hat{k}_Z^2\sin^2\chi}{\gamma + \frac{2}{5}\text{Pr}^{-1}\hat{\eta}_\nu\hat{k}_Z^2\sin^2\chi} \rightarrow \alpha_P\alpha_T. \quad (4.1.25)$$

Furthermore,  $\eta_\kappa \gg \eta_\nu$ , so that the range of applicability of thermal effects is significantly larger than that of viscous transport. That is, one can satisfy the condition of dynamically important thermal conductivity, as given in Eqs. (4.1.24) and (4.1.25), even when  $\eta_\nu\Omega/v_A^2 < 1$ .

We can express the regime of dynamically important viscous diffusion in terms of physical parameters appropriate to our astrophysical problem. The viscous diffusivity and Alfvén velocity in dimensional units are given by,

$$\eta_\nu = 1.4 \times 10^{19} \left( \frac{T}{10^4 \text{ K}} \right)^{5/2} \left( \frac{n}{1 \text{ cm}^{-3}} \right)^{-1} \frac{1}{\ln \Lambda} \text{ cm}^2 \text{ s}^{-1}, \quad (4.1.26)$$

$$v_A = 2.2 \times 10^5 \left( \frac{B}{1 \text{ } \mu\text{G}} \right) \left( \frac{n}{1 \text{ cm}^{-3}} \right)^{-1/2} \text{ cm s}^{-1}. \quad (4.1.27)$$

Recall that  $\Lambda$  is the roughly the ratio of the Debye length to the  $\pi/2$  impact parameter or the DeBroglie wavelength, whichever is larger. Therefore the orbital angular velocity must be,

$$\Omega \gtrsim 3.5 \times 10^{-9} \left( \frac{B}{1 \text{ } \mu\text{ G}} \right)^2 \left( \frac{T}{10^4 \text{ K}} \right)^{-5/2} (\ln \Lambda) \text{ s}^{-1}, \quad (4.1.28)$$

in order for the viscosity to be dynamically important.

## 4.2 Growth Rate and Stability Characteristics

Here we consider two equilibrium configurations that illustrate the MVTI dispersion relation. We only consider a physical pressure profile,  $\alpha_P = 10$ . We also consider a

Schwarzschild stable flow, with  $H\partial \ln P \rho^{-5/3}/\partial R > 0$  or  $\alpha_S < 0$ . This implies,

$$0 < \alpha_T \leq \frac{2}{5}\alpha_P, \quad (4.2.1)$$

so that  $\alpha_T \leq 4$ . We focus our analysis on purely vertical wavenumbers,  $k_R/k_Z = 0$ . Then Eq. (4.1.19) reduces to the following quintic polynomial, where  $x = (\mathbf{k} \cdot \mathbf{v}_A)/\Omega = \hat{k}_Z \sin \chi$ :

$$\begin{aligned} & \left( \left[ \gamma^2 + 2 \frac{d \ln \Omega}{d \ln R} + x^2 \right] \left[ \gamma + \frac{2}{5} \text{Pr}^{-1} \hat{\eta}_\nu x^2 \right] - \frac{3}{5} \alpha_P \left[ \alpha_S \gamma + \frac{2}{3} \alpha_T \text{Pr}^{-1} \hat{\eta}_\nu x^2 \right] \right) \times \\ & (\gamma^2 + x^2 + 3 \hat{\eta}_\nu \gamma x^2 \cos^2 \chi) + 4 \gamma^2 \left( \gamma + \frac{2}{5} \text{Pr}^{-1} \hat{\eta}_\nu x^2 \right) = 0. \end{aligned} \quad (4.2.2)$$

In Fig. (4.2.1), we consider both viscous diffusivity and thermal conductivity to be dynamically significant. Dispersion relations match the salient characteristic of the MVI, where the growth rate approaches a maximum at wavenumbers  $k \sim (\Omega/\eta_\nu)^{1/2} \ll \Omega/v_A$ . For  $\alpha_P = 0$  and  $\alpha_T = 0$ , the MVTI dispersion relation reduces to that of the MVI. In Fig. (4.2.2), we consider only the thermal conductivity to be dynamically important. The dispersion relations are similar to the MTI in a rotating frame. For  $\alpha_T > 0$ , the growth rate and range of wavenumber of the instability are increased. This is shown in Figs. (4.2.1) and (4.2.2). We expect that equilibrium scale heights of temperature, pressure, and entropy are of order the radius  $R$ . Therefore, in order to have significant magnetoviscous and magnetothermal effects one requires that  $\alpha_T$ ,  $\alpha_P$ , and  $\alpha_S$  be of order unity. Only relatively thick disks,  $H \lesssim R$ , are expected to be significantly susceptible to these classes of instability.

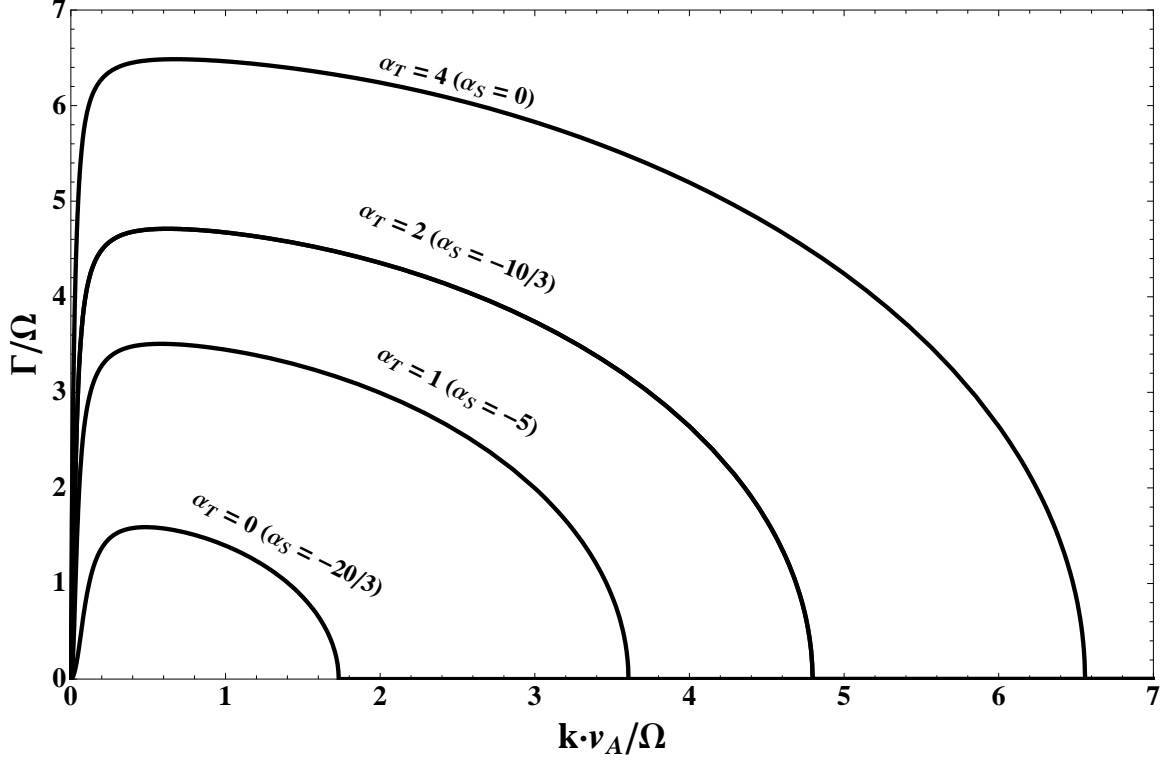


Fig. 4.2.1.— Plot of the growth rate as a function of wavenumber for various  $\alpha_T$  for a Keplerian rotation profile and  $\eta_\nu \Omega / v_A^2 = 10^2$ .

### 4.3 Angular Momentum Flux And Heat Flux

Here we calculate the quadratic  $R\phi$  component of the stress tensor  $T_{R\phi}$  and radial heat flux  $F_{ER}$  associated with the incompressible MVTI, using expressions derived in §3.1. Eqs. (3.1.4) and (3.1.11) can be rewritten as expressions for modal  $\langle T_{R\phi} \rangle$  and  $\langle F_{ER} \rangle$ , respectively,

$$\langle T_{R\phi} \rangle = \rho_0 \text{Re} \left( \delta u_\phi \delta u_R^* - v_A^2 \delta \bar{B}_\phi \delta B_R^* + \delta \sigma_{\mathbf{bb}} \delta \bar{B}_R^* \cos \chi \right), \quad (4.3.1)$$

$$\langle F_{ER} \rangle = \text{Re} \left( \frac{5}{2} \rho_0 \delta \theta \delta u_R^* + \delta q \delta \bar{B}_R^* - \frac{1}{3} \delta \sigma_{\mathbf{bb}} \delta u_R^* \right). \quad (4.3.2)$$

We express all eigenmodal fluctuations, such as  $\delta \bar{B}_R$ , in terms of the radial Lagrangian displacement  $\xi_R = \Gamma^{-1} \delta u_R$ .

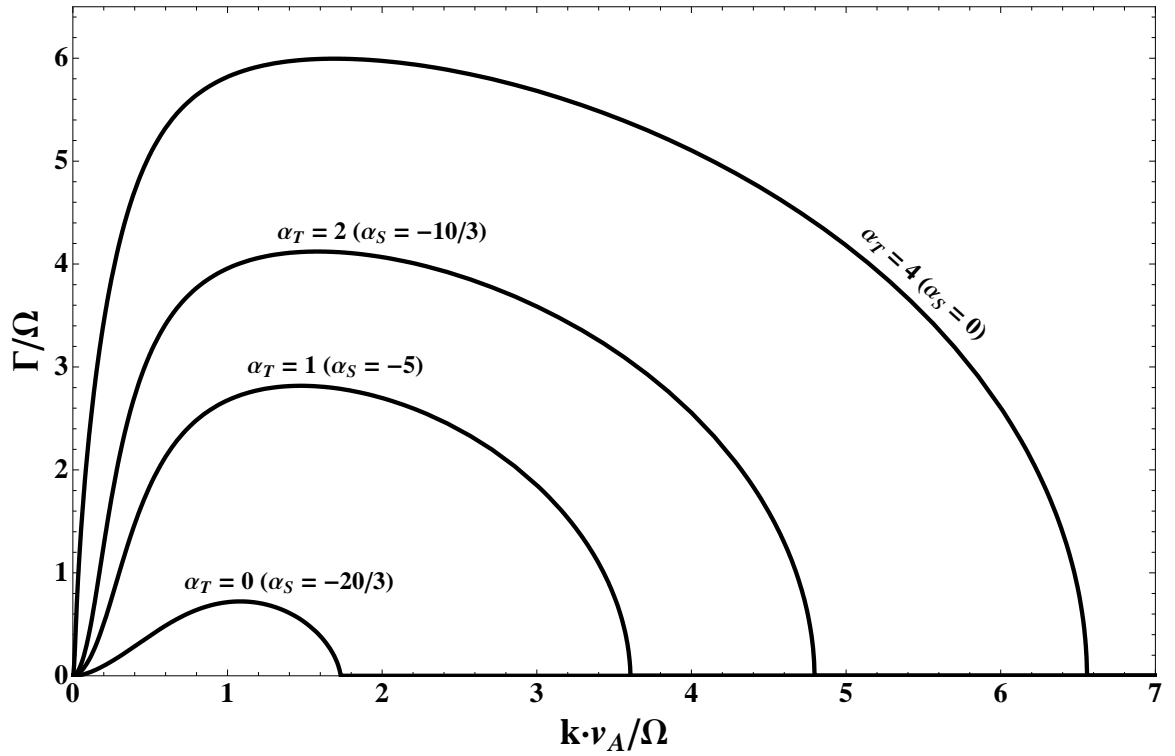


Fig. 4.2.2.— Plot of the dispersion relation for various  $\alpha_T$  for a Keplerian rotation profile and a small viscous diffusion coefficient  $\eta_\nu \Omega / v_A^2 = 1$ .

The following are the modal perturbed velocities, magnetic fields, density, tem-

perature, viscous stress, and heat flux. We consider nonradial modes,

$$\begin{aligned}
\delta u_R &= \gamma \Omega \xi_R \\
\delta u_\phi &= - \left( \frac{2\gamma^2}{\gamma^2 + x^2 + 3\hat{\eta}_\nu x^2 \gamma \cos^2 \chi} + \frac{d \ln \Omega}{d \ln R} \right) \Omega \xi_R \\
\delta \bar{B}_R &= ix \left( \Omega \xi_R v_A^{-1} \right) \\
\delta \bar{B}_\phi &= -ix \frac{2\gamma}{\gamma^2 + x^2 + 3\hat{\eta}_\nu x^2 \gamma \cos^2 \chi} \left( \Omega \xi_R v_A^{-1} \right) \\
\delta \rho &= -\frac{3}{5} \times \frac{\gamma \alpha_S + \frac{2}{3} \text{Pr}^{-1} \hat{\eta}_\nu x^2 \alpha_T}{\gamma + \frac{2}{5} \text{Pr}^{-1} \hat{\eta}_\nu x^2} \left( \rho H^{-1} \xi_R \right), \\
\delta \theta / \theta_0 &= \frac{3}{5} \times \frac{\gamma \alpha_S + \frac{2}{3} \text{Pr}^{-1} \hat{\eta}_\nu x^2 \alpha_T}{\gamma + \frac{2}{5} \text{Pr}^{-1} \hat{\eta}_\nu x^2} \left( \rho H^{-1} \xi_R \right), \\
\delta \sigma_{\mathbf{bb}} &= \frac{6ix\gamma^2 \hat{\eta}_\nu \cos \chi}{\gamma^2 + x^2 + 3\hat{\eta}_\nu x^2 \gamma \cos^2 \chi} \left( \rho_0 \Omega v_A \xi_R \right), \\
\delta q &= \frac{2}{5} \times \frac{\text{Pr}^{-1} \hat{\eta}_\nu \gamma \alpha_P}{\gamma + \frac{2}{5} \text{Pr}^{-1} \hat{\eta}_\nu x^2} \left( p_0 \Omega v_A H^{-1} \xi_R \right)
\end{aligned} \tag{4.3.3}$$

If we substitute Eq. (4.3.3) into Eq. (4.3.1), we get,

$$\langle T_{R\phi} \rangle = \gamma \left( 2 - \frac{d \ln \Omega}{d \ln R} - \frac{4\gamma^2}{\gamma^2 + x^2 + 3\hat{\eta}_\nu x^2 \gamma \cos^2 \chi} \right) \rho_0 \Omega^2 |\xi_R|^2. \tag{4.3.4}$$

If we substitute Eq. (4.3.3) into Eq. (4.3.2), we get,

$$\langle F_{ER} \rangle = \left( \frac{3}{2} \gamma \frac{\gamma \alpha_S + \frac{2}{3} \hat{\eta}_\nu \text{Pr}^{-1} x^2 \alpha_T}{\gamma + \frac{2}{5} \hat{\eta}_\nu \text{Pr}^{-1} x^2} \right) p_0 \Omega |\xi_R|^2 H^{-1}. \tag{4.3.5}$$

In all the plots of quadratic flux, we keep  $\alpha_P = 10$ , choose physical  $\alpha_T > 0$  for which the flow is Schwarzschild stable, and use the Prandtl number  $\text{Pr} = 1/101$ . Figs. (4.3.1) and (4.3.2) are plots of normalized heat flux  $\langle F_{ER} \rangle$  and angular momentum flux  $\langle T_{R\phi} \rangle$ , respectively, for MVI-like dispersion modes ( $\eta_\nu \Omega / v_A^2 = 10^2$ ). Figs. (4.3.3) and (4.3.4) are plots of normalized heat flux  $\langle F_{ER} \rangle$  and angular momentum flux  $\langle T_{R\phi} \rangle$ , respectively, for MRI-like modes ( $\eta_\nu \Omega / v_A^2 = 1$ ). From Figs. (4.3.1) and (4.3.3),

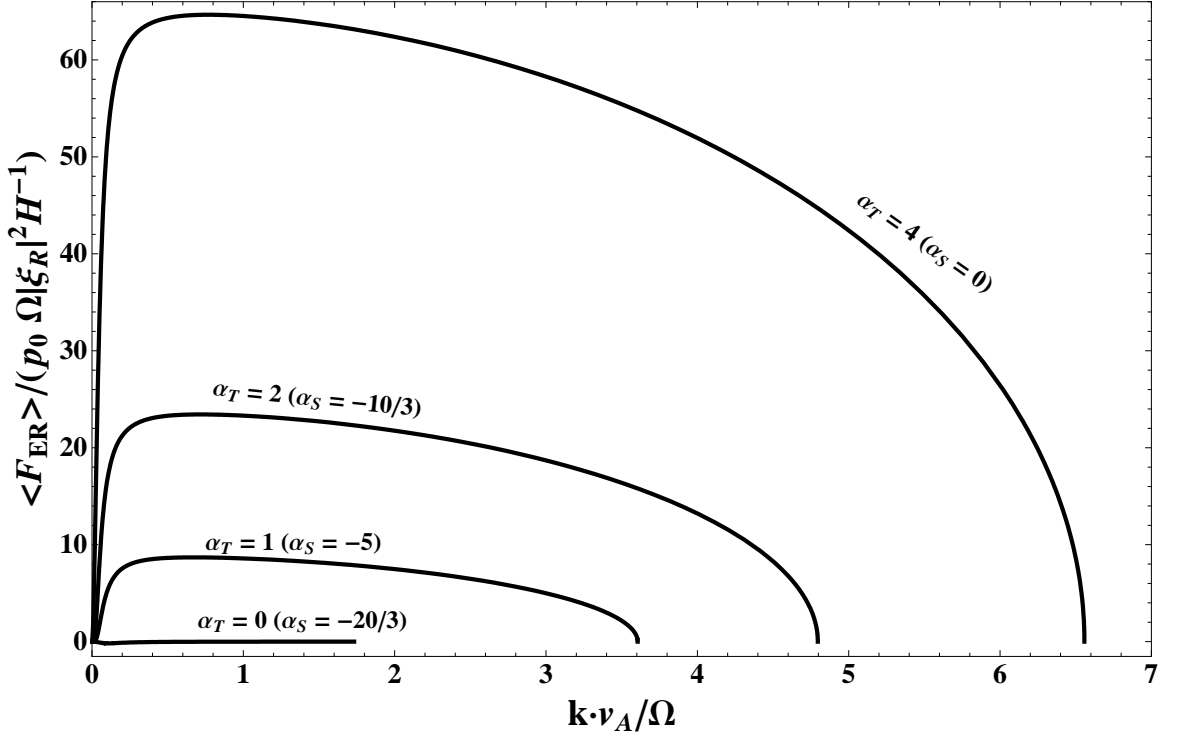


Fig. 4.3.1.— Normalized radial flux of thermal energy for a Keplerian rotational profile and  $\eta_\nu \Omega / v_A^2 = 10^2$ .

we observe that the quadratic heat flux is outward and dynamically significant, with  $\langle F_{ER} \rangle \gtrsim \langle T_{R\phi} \rangle \theta_0^{1/2}$ , in the limit of large ( $\eta_\nu \Omega / v_A^2 \gg 1$ ) and moderate ( $\eta_\nu \Omega / v_A^2 \sim 1$ ) viscosities. This implies that the nonlinear MVTI can play an important role in transporting out the energy, generated via the coupling of  $\langle T_{R\phi} \rangle$  with rotational shear, in nonradiative accreting flows. From Figs. (4.3.2) and (4.3.4), we observe that the flux of angular momentum for these modes can be either inwards or outwards.

Surprisingly, the MTI in a rigidly rotating plasma can also transport angular momentum inwards or outwards. We can rederive the dispersion relation and angular momentum flux for the MTI in a rotating plasma by setting  $\text{Pr}^{-1} = \eta_\kappa / \eta_\nu$ , while letting  $\eta_\nu \rightarrow 0$ . The normalized dispersion relation, Eq. (4.2.2), and angular momentum



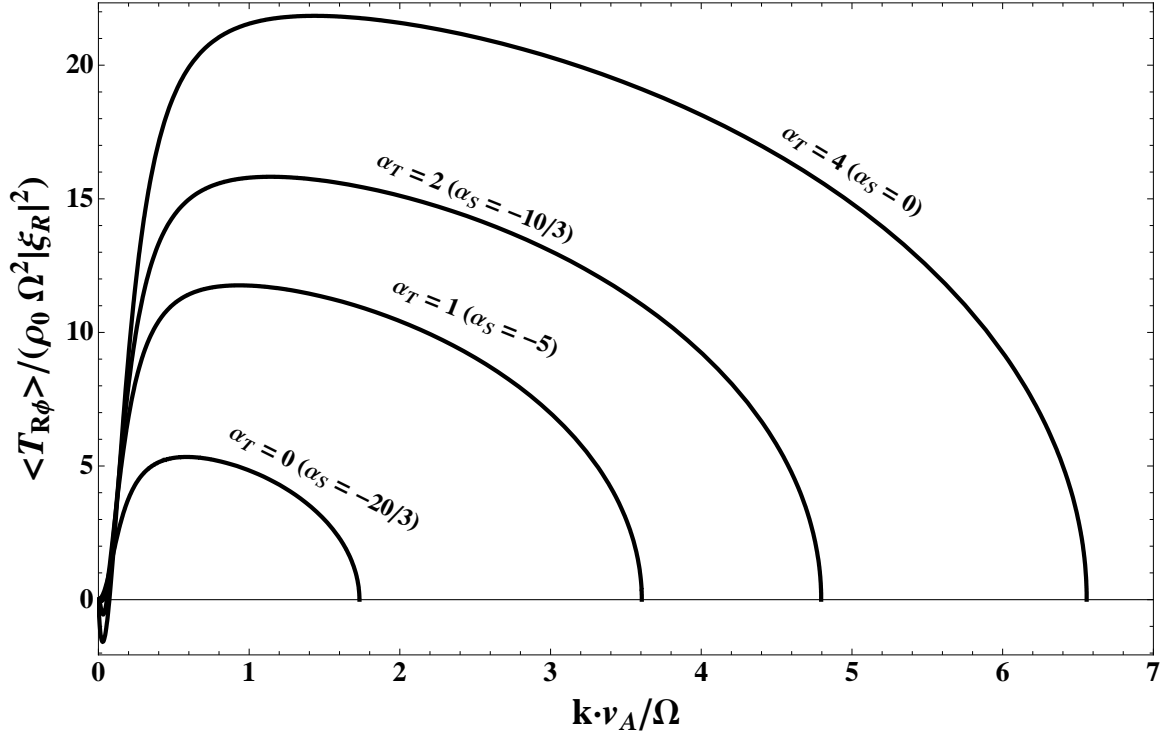


Fig. 4.3.2.— Normalized angular momentum flux for a Keplerian rotational profile and  $\eta_\nu \Omega / v_A^2 = 10^2$ .

flux, Eq. (4.3.4), are given by,

$$\left( \left[ \gamma^2 + 2 \frac{d \ln \Omega}{d \ln R} + x^2 \right] \left[ \gamma + \frac{2}{5} \hat{\eta}_\kappa x^2 \right] - \frac{3}{5} \alpha_P \left[ \alpha_S \gamma + \frac{2}{3} \alpha_T \hat{\eta}_\kappa x^2 \right] \right) (\gamma^2 + x^2) + 4\gamma^2 \left( \gamma + \frac{2}{5} \hat{\eta}_\kappa x^2 \right) = 0, \quad (4.3.6)$$

$$\langle T_{R\phi} \rangle = \gamma \frac{x^2 (2 - d \ln \Omega / d \ln R) - \gamma^2 (2 + d \ln \Omega / d \ln R)}{\gamma^2 + x^2} \rho_0 \Omega^2 |\xi_R|^2. \quad (4.3.7)$$

Fig. (4.3.5) demonstrates that in a rigidly rotating plasma  $\Omega' R = 0$ , the magnetothermal instability can transport angular momentum either inwards or outwards, depending on wavenumber. As the system approaches marginal convective stability  $\alpha_S \rightarrow 0$  from isothermality ( $\alpha_T = 0$ ), the range of wavenumbers for which the stress is outwards decreases. However, in the absence of rotational shear no energy can be extracted from the flow (see Eq. [3.1.9]).

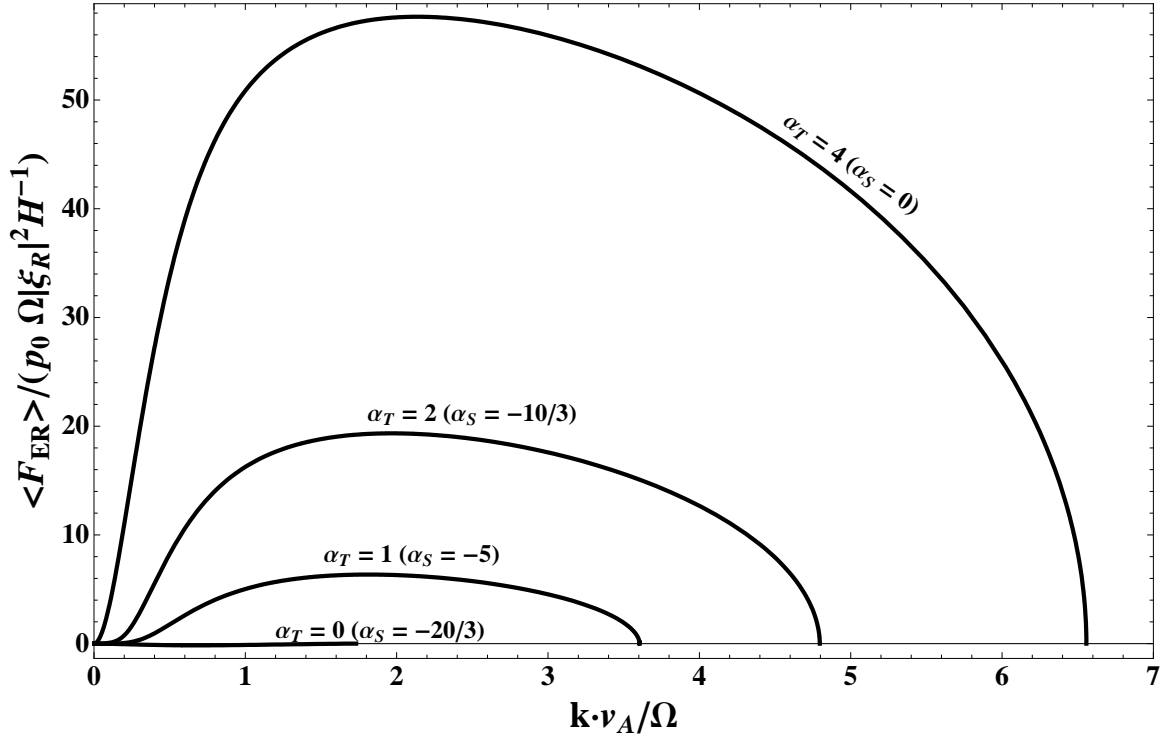


Fig. 4.3.3.— Normalized radial flux of thermal energy for a Keplerian rotational profile and  $\eta_\nu \Omega / v_A^2 = 1$ .

## 4.4 Finite Compressibility

Physical effects associated with finite plasma compressibility appear when we consider the effects of large but finite plasma  $\beta$ . These MHD modes, whose phase velocities are of order  $v_A$ , become more compressible as  $v_A \rightarrow \theta_0^{1/2}$ . Therefore, for plasmas with weak magnetic fields,  $\beta \gg 1$ , the growth rates and quadratic fluxes differ little from their Boussinesq limit approximations.

The normalized viscous diffusivity  $\eta_\nu \Omega / \theta_0 \sim \Omega / \nu_i$ . If the wavelength of the fastest growing modes, of order  $v_A / \Omega$ , is smaller than the mean free path,  $\lambda_i \sim \theta_0^{1/2} / \nu_i$ , then the fluid approximation breaks down. Therefore, if  $\nu_i \gtrsim \Omega \beta^{1/2}$  or equivalently if  $\hat{\eta}_\nu \lesssim \beta^{1/2}$ , then the plasma can be described by a fluid approximation.

Here we calculate the dispersion relation with finite compressibility. From Eq. (2.3.7),

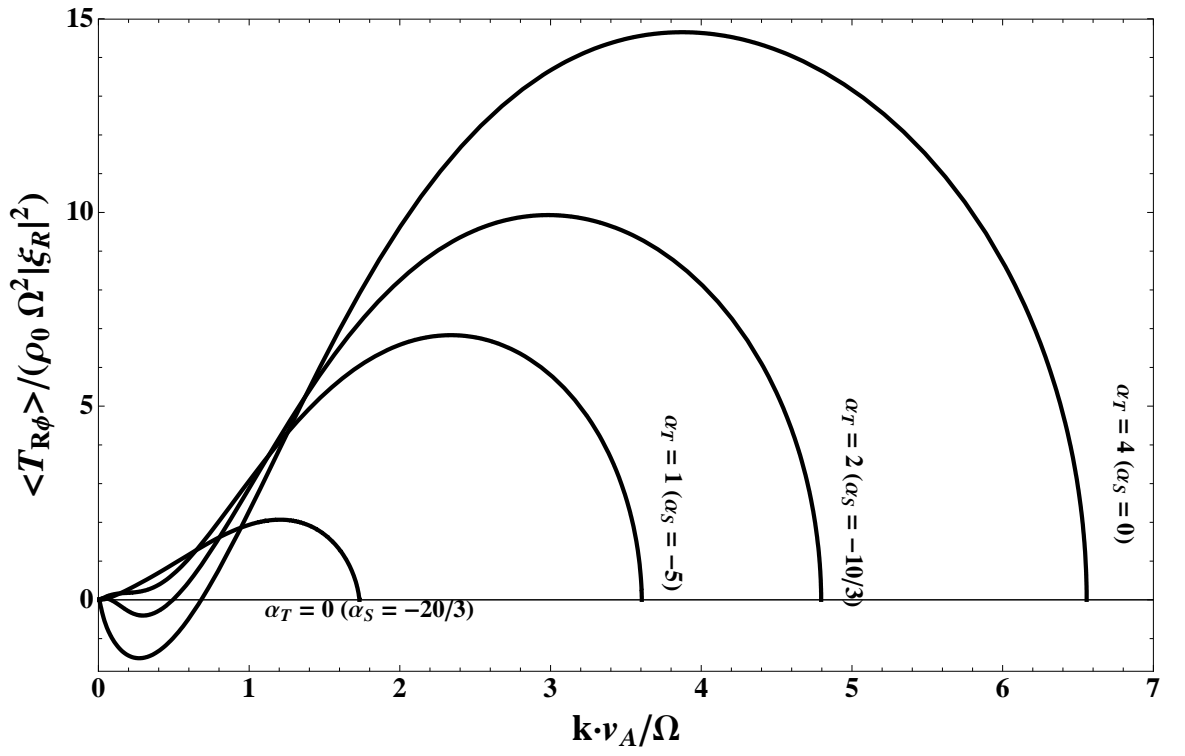


Fig. 4.3.4.— Normalized azimuthal momentum radial flux for a Keplerian rotational profile and  $\eta_\nu \Omega / v_A^2 = 1$ .

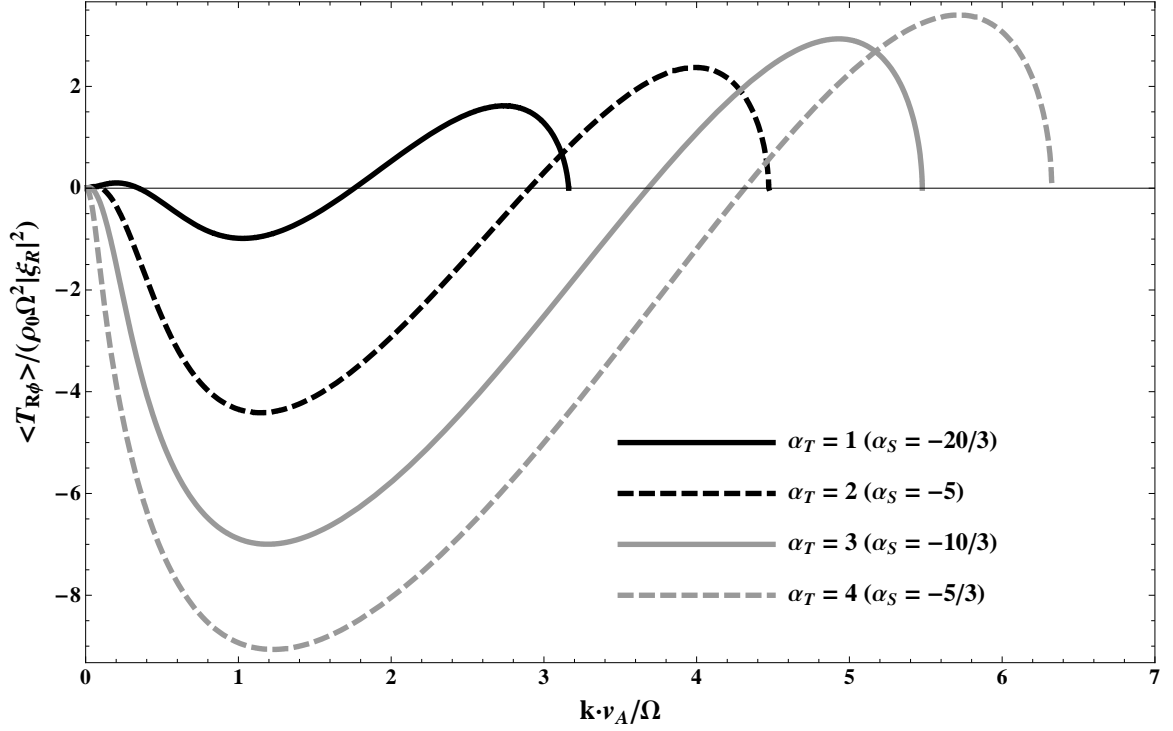


Fig. 4.3.5.— Normalized angular momentum flux  $T_{R\phi} / (\rho_0 \Omega^2 |\xi_R|^2)$  for a rigid rotation profile ( $\Omega' R = 0$ ) for the MTI in a rotating disk (see Eq. [4.3.6]). There is a much larger range of wavenumbers for which the angular momentum angular momentum flux is inwards, than shown in Fig. (4.3.4).

the perturbed form of the fluid viscous stress  $\delta\sigma_{\mathbf{b}\mathbf{b}}$  with compressibility becomes,

$$\delta\sigma_{\mathbf{b}\mathbf{b}} = -3\rho_0\eta_\nu \left( i(\mathbf{k} \cdot \mathbf{b}_0)(\mathbf{b}_0 \cdot \delta\mathbf{u}) + \Omega' R \delta\bar{B}_R \cos \chi - \frac{1}{3}(\nabla \cdot \delta\mathbf{u}) \right). \quad (4.4.1)$$

The perturbed induction equations, Eq. (1.2.8), can be written as,

$$\begin{aligned} \Gamma \delta\bar{B}_R &= ik_Z \sin \chi \delta u_R, \\ \Gamma \delta\bar{B}_\phi &= -\cos \chi (\nabla \cdot \delta\mathbf{u}) + ik_Z \sin \chi \delta u_\phi + \Omega' R \delta\bar{B}_R, \\ \Gamma \delta\bar{B}_Z &= -\sin \chi (\nabla \cdot \delta\mathbf{u}) + ik_Z \sin \chi \delta u_z. \end{aligned} \quad (4.4.2)$$

The MHD continuity equation, Eq. (1.2.5), can be written as,

$$\nabla \cdot \delta \mathbf{u} = -\Gamma \delta \bar{\rho} - \delta u_R \frac{\partial \ln \rho_0}{\partial R}, \quad (4.4.3)$$

From Eq. (4.4.3), the perturbed vertical velocity  $\delta u_Z$  is given by,

$$\delta u_Z = -\frac{k_R}{k_Z} \delta u_R - \frac{\Gamma}{ik_Z} \delta \bar{\rho} - \frac{\delta u_R}{ik_Z} \frac{\partial \ln \rho_0}{\partial R}. \quad (4.4.4)$$

If we substitute Eqs. (4.4.2) and (4.4.3) into Eq. (4.4.1),  $\delta \sigma_{\mathbf{b}\mathbf{b}}$  can be represented as,

$$\begin{aligned} \delta \sigma_{\mathbf{b}\mathbf{b}} = & -3\rho_0 \eta_\nu \Gamma \left( \delta \bar{B}_\phi \cos \chi - \frac{k_R}{k_Z} \delta \bar{B}_R \sin \chi - \frac{2}{3} \delta \bar{\rho} - \right. \\ & \left. \frac{2\delta \bar{B}_R}{3ik_Z \sin \chi} \frac{\partial \ln \rho_0}{\partial R} \right). \end{aligned} \quad (4.4.5)$$

If we substitute Eq. (4.4.5) into the MHD comoving force balance equations, Eq. (1.2.5), we are left with,

$$\begin{aligned} \Gamma \delta u_R - 2\Omega \delta u_\phi = & -ik_R \left( \frac{\delta p}{\rho_0} + v_A^2 \left[ \delta \bar{B}_\phi \cos \chi - \frac{k_R}{k_Z} \delta \bar{B}_R \sin \chi \right] + \right. \\ & \left. \eta_\nu \Gamma \left[ \delta \bar{B}_\phi \cos \chi - \frac{k_R}{k_Z} \delta \bar{B}_R \sin \chi - \frac{2}{3} \delta \bar{\rho} - \frac{2\delta \bar{B}_R}{3ik_Z \sin \chi} \frac{\partial \ln \rho_0}{\partial R} \right] \right) + \end{aligned} \quad (4.4.6)$$

$$\begin{aligned} & ik_Z v_A^2 \delta \bar{B}_R \sin \chi + \delta \bar{\rho} \theta_0 \frac{\partial \ln p_0}{\partial R} \\ \Gamma \delta u_\phi + (2\Omega + \Omega' R) \Gamma \delta u_R = & 3ik_Z \eta_\nu \sin \chi \cos \chi \left( \delta \bar{B}_\phi \cos \chi - \right. \\ & \left. \frac{k_R}{k_Z} \delta \bar{B}_R \sin \chi - \frac{2}{3} \delta \bar{\rho} - \frac{2\delta \bar{B}_R}{ik_Z \sin \chi} \frac{\partial \ln \rho_0}{\partial R} \right) + ik_Z v_A^2 \delta \bar{B}_\phi \sin \chi \end{aligned} \quad (4.4.7)$$

$$\begin{aligned} \Gamma \delta u_z = & -ik_Z \left( \frac{\delta p}{\rho_0} + v_A^2 \left[ \delta \bar{B}_\phi \cos \chi - \frac{k_R}{k_Z} \delta \bar{B}_R \sin \chi \right] \right) + \\ & ik_Z \eta_\nu \Gamma (3 \sin^2 \chi - 1) \left( \delta \bar{B}_\phi \cos \chi - \frac{k_R}{k_Z} \delta \bar{B}_R \sin \chi - \frac{2}{3} \delta \bar{\rho} - \right. \\ & \left. \frac{2\delta \bar{B}_R}{3ik_Z \sin \chi} \frac{\partial \ln \rho_0}{\partial R} \right) - ik_R v_A^2 \delta \bar{B}_R \sin \chi \end{aligned} \quad (4.4.8)$$

The perturbed form of the MHD comoving internal energy balance equation, Eq. (4.1.8), with finite pressure perturbations, yields the equation for  $\delta\bar{\rho}$  as,

$$\delta\bar{\rho} = \frac{3}{5} \times \frac{\delta u_R \partial \ln p_0 \rho_0^{-5/3} / \partial R - \frac{2}{3} i \eta_\kappa k_Z \sin \chi \delta \bar{B}_R \partial \ln T_0 / \partial R}{\Gamma + \frac{2}{5} \eta_\kappa k_Z^2 \sin^2 \chi} + \frac{3\delta p}{5p_0} \times \frac{\Gamma + \frac{2}{3} \eta_\kappa k_Z^2 \sin^2 \chi}{\Gamma + \frac{2}{5} \eta_\kappa k_Z^2 \sin^2 \chi} \quad (4.4.9)$$

If we substitute Eq. (4.4.4) into Eq. (4.4.8) we have an expression for the perturbed pressure,

$$\begin{aligned} \frac{\delta p}{\rho_0} + v_A^2 \left( \delta \bar{B}_\phi \cos \chi - \frac{k_R}{k_Z} \delta \bar{B}_R \sin \chi \right) &= \eta_\nu \Gamma (3 \sin^2 \chi - 1) (\delta \bar{B}_\phi \cos \chi - \\ &\frac{k_R}{k_Z} \delta \bar{B}_R \sin \chi - \frac{2}{3} \delta \bar{\rho} - \frac{2 \delta \bar{B}_R}{3 i k_Z \sin \chi} \frac{\partial \ln \rho_0}{\partial R}) - \frac{k_R}{k_Z} v_A^2 \delta \bar{B}_R \sin \chi - \\ &\frac{\Gamma}{i k_Z} \left( -\frac{k_R}{k_Z} \delta u_R - \frac{\Gamma}{i k_Z} \delta \bar{\rho} - \frac{\delta u_R}{i k_Z} \frac{\partial \ln \rho_0}{\partial R} \right). \end{aligned} \quad (4.4.10)$$

If we substitute the radial component of Eq. (4.4.2) into Eq. (4.4.10), the perturbed pressure can be written as,

$$\begin{aligned} \frac{\delta p}{p_0} &= -\delta \bar{B}_R \left( \frac{\eta_\nu \Gamma}{\theta_0} [3 \sin^2 \chi - 1] \left[ \frac{k_R}{k_Z} \sin \chi + \frac{2}{3 i k_Z \sin \chi} \frac{\partial \ln \rho_0}{\partial R} \right] + \right. \\ &\frac{\Gamma^2}{k_Z^2 \theta_0 \sin \chi} \left[ \frac{k_R}{k_Z} + \frac{1}{i k_Z} \frac{\partial \ln \rho_0}{\partial R} \right] \Bigg) + \\ &\delta \bar{B}_\phi \left( \frac{\eta_\nu \Gamma}{\theta_0} [3 \sin^2 \chi - 1] - \beta^{-1} \right) \cos \chi + \delta \bar{\rho} \left( \frac{\Gamma^2}{k_Z^2 \theta_0} - \frac{2 \eta_\nu \Gamma}{3 \theta_0} [3 \sin^2 \chi - 1] \right) \end{aligned} \quad (4.4.11)$$

Eqs. (4.4.9) and (4.4.11) can be combined to yield an equation for  $\delta\bar{\rho}$  in terms of  $\delta\bar{B}_R$

and  $\delta\bar{B}_\phi$ ,

$$\begin{aligned}
\delta\bar{\rho} = & \frac{3\delta\bar{B}_R}{5ik_Z \sin \chi} \times \frac{\Gamma \frac{\partial \ln p_0 \rho_0^{-5/3}}{\partial R} + \frac{2}{3}\eta_\kappa k_Z^2 \sin^2 \chi \frac{\partial \ln T_0}{\partial R}}{\left(\Gamma + \frac{2}{5}\eta_\kappa k_Z^2 \sin^2 \chi\right) \left(1 - \frac{3\Gamma^2}{5k_Z^2 \theta_0} + \frac{2\eta_\nu \Gamma}{5\theta_0} [3 \sin^2 \chi - 1]\right)} - \\
& \frac{3}{5}\delta\bar{B}_R \left( \frac{\eta_\nu \Gamma}{\theta_0} [3 \sin^2 \chi - 1] \left[ \frac{k_R}{k_Z} \sin \chi + \frac{2}{3ik_Z \sin \chi} \frac{\partial \ln \rho_0}{\partial R} \right] + \frac{\Gamma^2}{k_Z^2 \theta_0 \sin \chi} \right. \\
& \left. \left[ \frac{k_R}{k_Z} + \frac{1}{ik_Z} \frac{\partial \ln \rho_0}{\partial R} \right] \right) \frac{\Gamma + \frac{2}{3}\eta_\kappa k_Z^2 \sin^2 \chi}{\left(\Gamma + \frac{2}{5}\eta_\kappa k_Z^2 \sin^2 \chi\right) \left(1 - \frac{3\Gamma^2}{5k_Z^2 \theta_0} + \frac{2\eta_\nu \Gamma}{5\theta_0} [3 \sin^2 \chi - 1]\right)} + \\
& \frac{3}{5}\delta\bar{B}_\phi \frac{(\Gamma + \frac{2}{3}\eta_\kappa k_Z^2 \sin^2 \chi) \left( \frac{\eta_\nu \Gamma}{\theta_0} [3 \sin^2 \chi - 1] - \beta^{-1} \right) \cos \chi}{\left(\Gamma + \frac{2}{5}\eta_\kappa k_Z^2 \sin^2 \chi\right) \left(1 - \frac{3\Gamma^2}{5k_Z^2 \theta_0} + \frac{2\eta_\nu \Gamma}{5\theta_0} [3 \sin^2 \chi - 1]\right)}. \quad (4.4.12)
\end{aligned}$$

If we substitute Eqs. (4.4.2) and (4.4.11) into Eq. (4.4.6), then,

$$\begin{aligned}
& \Gamma^2 \left( 1 + \frac{k_R^2}{k_Z^2} \right) \delta\bar{B}_R - 2\Omega \left( \Gamma \delta\bar{B}_\phi - \Omega' R \delta\bar{B}_R - \frac{2}{3}\Gamma \delta\bar{\rho} - \frac{2\Gamma}{3ik_Z \sin \chi} \frac{\partial \ln \rho_0}{\partial R} \delta\bar{B}_R \right) = \\
& 3\eta_\nu k_R k_Z \Gamma \sin^3 \chi \left( \delta\bar{B}_\phi \cos \chi - \frac{k_R}{k_Z} \delta\bar{B}_R \sin \chi - \frac{2}{3}\delta\bar{\rho} - \right. \\
& \left. \frac{2}{3ik_Z \sin \chi} \frac{\partial \ln \rho_0}{\partial R} \delta\bar{B}_R \right) - (k_R^2 + k_Z^2) v_A^2 \sin^2 \chi \delta\bar{B}_R + \\
& \delta\bar{\rho} \left( ik_Z \sin \chi \theta_0 \frac{\partial \ln p_0}{\partial R} \right). \quad (4.4.13)
\end{aligned}$$

If we substitute Eq. (4.4.2) into Eq. (4.4.7) then,

$$\begin{aligned}
& \Gamma^2 \left( \delta\bar{B}_\phi - \frac{2}{3}\delta\bar{\rho} - \frac{2}{3ik_Z \sin \chi} \frac{\partial \ln \rho_0}{\partial R} \right) + 2\Omega \Gamma \delta\bar{B}_R = \\
& - 3\eta_\nu k_Z^2 \Gamma \sin^2 \chi \cos \chi \left( \delta\bar{B}_\phi \cos \chi - \frac{k_R}{k_Z} \delta\bar{B}_R \sin \chi - \right. \\
& \left. \frac{2}{3}\delta\bar{\rho} - \frac{2}{3ik_Z \sin \chi} \frac{\partial \ln \rho_0}{\partial R} \right) - k_Z^2 v_A^2 \sin^2 \chi \delta\bar{B}_\phi. \quad (4.4.14)
\end{aligned}$$

Eqs. (4.4.12) - (4.4.14) are a set of eigenvector equations,

$$\begin{pmatrix} A_{RR} & A_{R\phi} & A_{R\bar{\rho}} \\ A_{\phi R} & A_{\phi\phi} & A_{\phi\bar{\rho}} \end{pmatrix} \begin{pmatrix} 1 & 0 \\ 0 & 1 \\ C_{\bar{\rho}R} & C_{\bar{\rho}\phi} \end{pmatrix} \begin{pmatrix} \delta\bar{B}_R \\ \delta\bar{B}_\phi \end{pmatrix} = \begin{pmatrix} 0 \\ 0 \end{pmatrix}. \quad (4.4.15)$$

The solution for the normalized growth rate  $\gamma$  can be found by solving the following eigenvalue equation,

$$\begin{vmatrix} A_{RR} + A_{R\bar{\rho}}C_{\bar{\rho}R} & A_{R\phi} + A_{R\bar{\rho}}C_{\bar{\rho}\phi} \\ A_{\phi R} + A_{\phi\bar{\rho}}C_{\bar{\rho}R} & A_{\phi\phi} + A_{\phi\bar{\rho}}C_{\bar{\rho}\phi} \end{vmatrix} = 0. \quad (4.4.16)$$

We use normalizations given in Tab. (A.2) for the components of the  $A$  and  $C$  matrices, given in Eqs. (4.4.15) and (4.4.16). We use expressions for radial and azimuthal force balance in terms of  $\delta\bar{B}_R$  and  $\delta\bar{B}_\phi$ , given by Eqs. (4.4.13) and (4.4.14), respectively. We use the expression for the perturbed density  $\delta\bar{\rho}$  in terms of  $\delta\bar{B}_R$  and  $\delta\bar{B}_\phi$ ,



given in Eq. (4.4.12). Components of the  $A$  and  $C$  matrices are calculated as,

$$\begin{aligned}
A_{RR} &= \gamma^2 \left( 1 + \frac{\hat{k}_R^2}{\hat{k}_Z^2} \right) + \left( \hat{k}_R^2 + \hat{k}_Z^2 \right) \sin^2 \chi + 2 \frac{d \ln \Omega}{d \ln R} - \\
&\quad \frac{2\gamma}{i\hat{k}_Z \sin \chi} (\alpha_P - \alpha_T) \beta^{-1/2} + 3\hat{\eta}_\nu \hat{k}_R^2 \gamma \sin^4 \chi + \\
&\quad 2i\hat{\eta}_\nu \hat{k}_R \gamma \sin^2 \chi (\alpha_P - \alpha_T) \beta^{-1/2}, \\
A_{R\phi} &= -\gamma \left( 2 + 3\hat{\eta}_\nu \hat{k}_R \hat{k}_Z \sin^3 \chi \cos \chi \right), \\
A_{R\bar{\rho}} &= \frac{2}{3} \gamma \left( 2 + 3\hat{\eta}_\nu \hat{k}_R \hat{k}_Z \sin^3 \chi \right) + i\hat{k}_Z \sin \chi \alpha_P \beta^{1/2}, \\
A_{\phi R} &= \gamma \left( 2 - 3\hat{\eta}_\nu \hat{k}_R \hat{k}_Z \sin^3 \chi \cos \chi \right) + \frac{2\gamma^2}{3i\hat{k}_Z \sin \chi} (\alpha_P - \alpha_T) \beta^{-1/2} - \\
&\quad 2i\hat{\eta}_\nu \hat{k}_Z \gamma \sin \chi \cos \chi (\alpha_P - \alpha_T) \beta^{-1/2}, \\
A_{\phi\phi} &= \gamma^2 + \hat{k}_Z^2 \sin^2 \chi + 3\hat{\eta}_\nu \hat{k}_Z^2 \gamma \sin^2 \chi \cos^2 \chi, \\
A_{\phi\bar{\rho}} &= -\frac{2}{3} \gamma \left( \gamma + 3\hat{\eta}_\nu \hat{k}_Z^2 \sin^2 \chi \cos \chi \right),
\end{aligned} \tag{4.4.17}$$

and,

$$\begin{aligned}
C_{\bar{\rho}R} &= - \frac{3 \left( \gamma \alpha_S + \frac{2}{3} \text{Pr}^{-1} \hat{\eta}_\nu \hat{k}_Z^2 \sin^2 \chi \alpha_T \right) \beta^{-1/2}}{5i\hat{k}_Z \sin \chi \left( \gamma + \frac{2}{5} \text{Pr}^{-1} \hat{\eta}_\nu \hat{k}_Z^2 \sin^2 \chi \right) \left( 1 - \frac{3\gamma^2}{5\hat{k}_Z^2} \beta^{-1} + \frac{2}{5} \hat{\eta}_\nu \gamma \beta^{-1} [3 \sin^2 \chi - 1] \right)} - \\
&\quad \frac{3}{5} \beta^{-1} \left( \hat{\eta}_\nu \gamma [3 \sin^2 \chi - 1] \left[ \frac{\hat{k}_R}{\hat{k}_Z} \sin \chi - \frac{2}{3i\hat{k}_Z \sin \chi} (\alpha_P - \alpha_T) \beta^{-1/2} \right] + \right. \\
&\quad \left. \frac{\gamma^2}{\hat{k}_Z^2} \left[ \frac{\hat{k}_R}{\hat{k}_Z} - \frac{1}{i\hat{k}_Z} (\alpha_P - \alpha_T) \beta^{-1/2} \right] \right) \times \\
&\quad \frac{\gamma + \frac{2}{3} \text{Pr}^{-1} \hat{\eta}_\nu \hat{k}_Z^2 \sin^2 \chi}{\left( \gamma + \frac{2}{5} \text{Pr}^{-1} \hat{\eta}_\nu \hat{k}_Z^2 \sin^2 \chi \right) \left( 1 - \frac{3\gamma^2}{5\hat{k}_Z^2} \beta^{-1} + \frac{2}{5} \hat{\eta}_\nu \gamma \beta^{-1} [3 \sin^2 \chi - 1] \right)}, \\
C_{\bar{\rho}\phi} &= \frac{3 \left( \gamma + \frac{2}{3} \text{Pr}^{-1} \hat{\eta}_\nu \hat{k}_Z^2 \sin^2 \chi \right) (\hat{\eta}_\nu \gamma [3 \sin^2 \chi - 1] - 1) \beta^{-1} \cos \chi}{5 \left( \gamma + \frac{2}{5} \text{Pr}^{-1} \hat{\eta}_\nu \hat{k}_Z^2 \sin^2 \chi \right) \left( 1 - \frac{3\gamma^2}{5\hat{k}_Z^2} \beta^{-1} + \frac{2}{5} \hat{\eta}_\nu \gamma \beta^{-1} (3 \sin^2 \chi - 1) \right)}.
\end{aligned} \tag{4.4.18}$$

In the limit  $\beta \rightarrow \infty$ , the full compressive dispersion relation, Eq. (4.4.16), reduces to

Eq. (4.1.19).

#### 4.4.1 The Compressive MVTI Growth Rate

To observe how the MVTI changes as only the magnetic field strength increases, we vary  $\beta$  but keep  $\alpha_P$ ,  $\alpha_T$ ,  $\eta_\nu$ , and  $\eta_\kappa$  constant. We set  $\alpha_P = 5$ ,  $\alpha_T = 1$  (thus ensuring a Schwarzschild stable disk),  $\chi = \pi/4$ , use a Keplerian rotation profile, and set  $\eta_\nu\Omega/\theta_0 = 10^{-3}$ . We plot the real and imaginary parts of the normalized growth rate  $\Gamma/\Omega$  as a function of normalized nonradial wavenumber  $k_Z v_A/\Omega$  for various  $\beta$  in Figs. (4.4.1) and (4.4.2), respectively. Collisional theory applies where  $\beta \lesssim (\eta_\nu\Omega/\theta_0)^{-2} = 10^6$ . For  $\beta > 10^3$  the viscosity becomes dynamically important and we have MVI-like modes. For  $1 < \beta < 10^3$ , we reproduce the MRI-like modes.

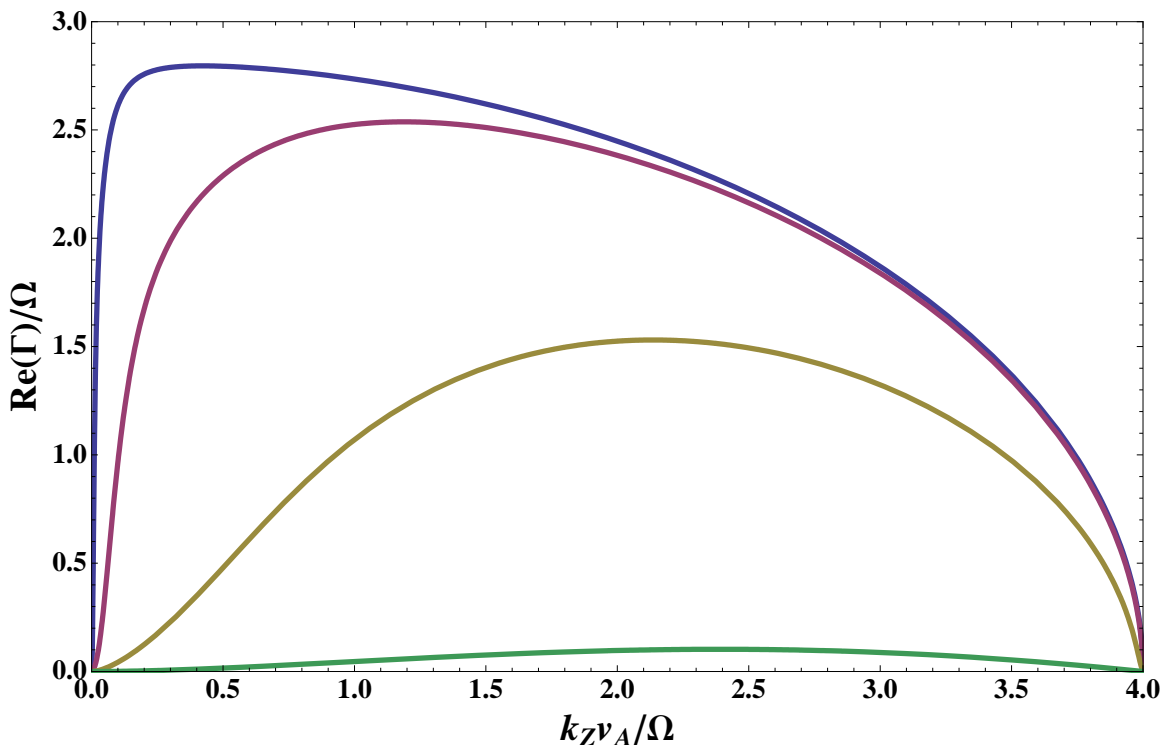


Fig. 4.4.1.— Real part of the growth rate for the MVTI as a function of normalized vertical wavenumber for various  $\beta \lesssim 10^6$  and  $\eta_\nu\Omega/\theta_0 = 10^{-3}$ . The top line is  $\beta = 10^6$ , the second line is  $\beta = 10^4$ , the third line is  $\beta = 10^2$ , and the bottom line is  $\beta = 1$ .

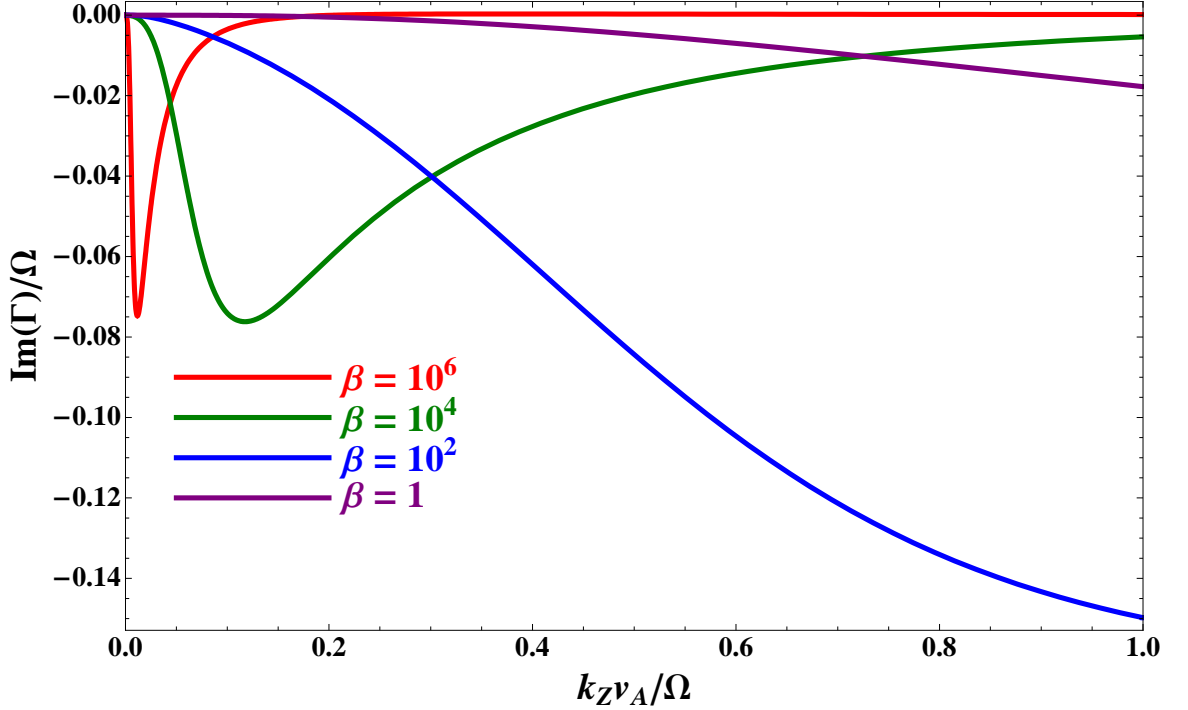


Fig. 4.4.2.— Imaginary part of the growth rate for the MVTI as a function of normalized vertical wavenumber for various  $\beta \lesssim 10^6$  and  $\eta_\nu \Omega / \theta_0 = 10^{-3}$ .

To observe MVI-like modes of varying degrees of compressibility, we fix the normalized viscosity  $\hat{\eta}_\nu = 10$  but vary  $\beta$ . This corresponds to a physical system in which  $\nu_i \propto \beta$ . We set  $\alpha_P = 5$ ,  $\alpha_T = 1$ ,  $\chi = \pi/4$ , and use a Keplerian rotational profile. For the fluid approximation to apply, we require that  $\beta \geq 10^2$ . We plot the growth rate as a function of normalized nonradial wavenumber  $k_Z v_A / \Omega$  for various  $\beta \geq 10^2$ . The real and imaginary parts of the growth rate as a function of vertical wavenumber are shown in Figs. (4.4.3) and (4.4.4), respectively. The modes become more incompressible as  $\beta$  increases. As  $\beta \rightarrow \infty$ , we see the following results: first, the imaginary part of the growth rate goes to zero (see Fig. [4.4.4]); and second, the real part of the growth rate approaches the value as given in Eq. (4.1.19) (see Fig. [4.4.3]).

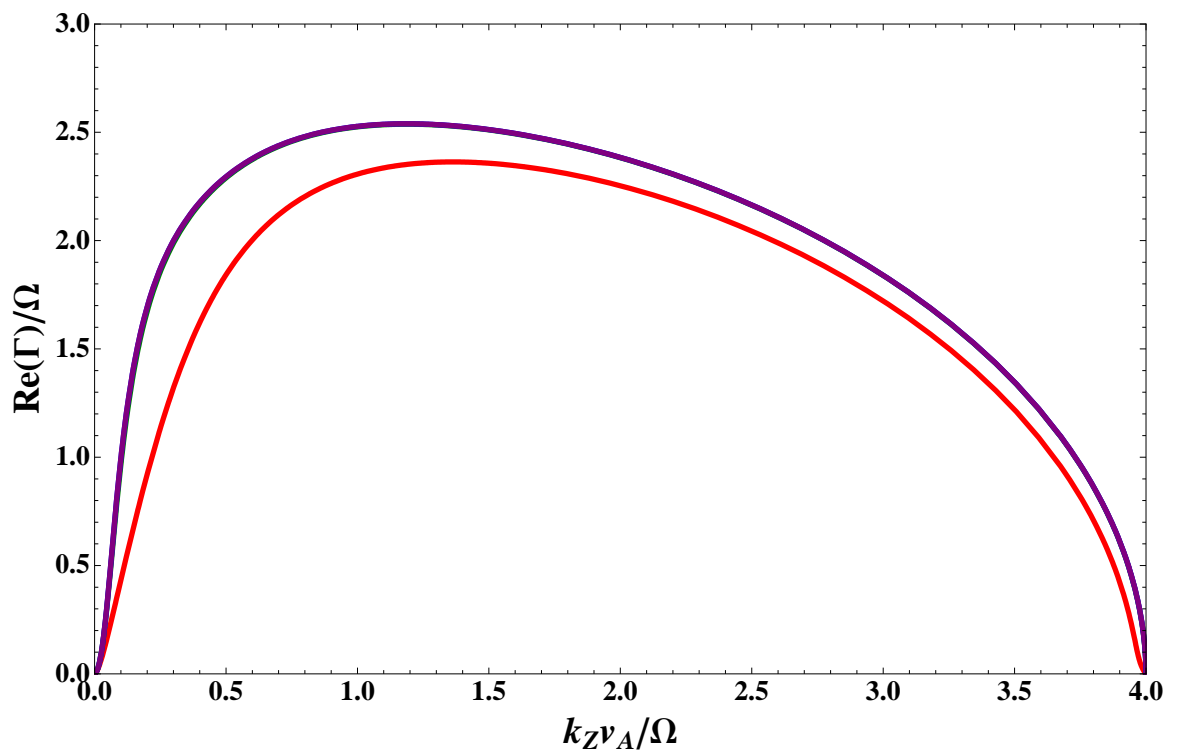


Fig. 4.4.3.— Real part of the growth rate as a function of vertical wavenumber for the compressive MVTI with fixed viscous diffusivity  $\eta_\nu \Omega / v_A^2 = 10$ , for various  $\beta \geq 10^2$ . The line in red denotes the dispersion relation for  $\beta = 10^2$ . The line in purple denotes the dispersion relations for  $\beta = 10^4$ ,  $10^6$ , and  $10^8$ , which coincide at the resolution of this graph.

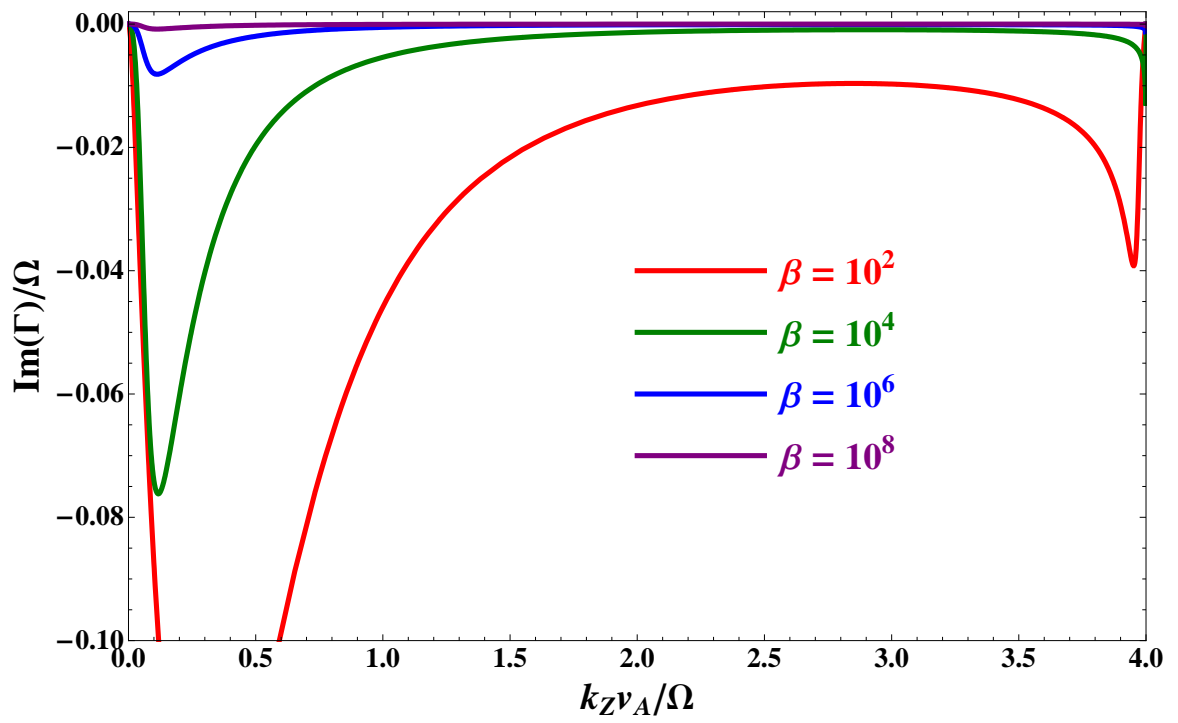


Fig. 4.4.4.— Imaginary part of the growth rate as a function of vertical wavenumber for the compressive MVTI with fixed viscous diffusivity  $\eta_\nu \Omega / v_A^2 = 10$ , for various  $\beta \geq 10^2$ . As  $\beta \rightarrow \infty$ ,  $\text{Im}(\Gamma) / \Omega \rightarrow 0$  at all unstable wavenumbers.

#### 4.4.2 Quadratic Fluxes for Compressive MVTI

To calculate the quadratic fluxes of angular momentum and energy for the compressive MVTI, we use the modal forms of  $\langle T_{R\phi} \rangle$  and  $\langle F_{ER} \rangle$ , given in Eqs. (4.3.1) and (4.3.2), respectively. The term  $-\frac{1}{3}\text{Re}(\delta\sigma_{\mathbf{bb}}\delta u_R^*) = 0$  in  $\langle F_{ER} \rangle$  in the incompressible limit, but is nonzero if we include finite compressibility. We calculate expressions for perturbed modal fluid quantities in terms of  $\xi_R$ .

The radial component of Eq. (4.4.2) can yield,

$$\delta\bar{B}_R = i\hat{k}_Z \sin\chi \left(\Omega v_A^{-1}\xi_R\right). \quad (4.4.19)$$

If we substitute Eq. (4.4.19) into Eq. (4.4.15), we get,

$$\delta\bar{B}_\phi = -\frac{A_{\phi R} + A_{\phi\bar{\rho}}C_{\bar{\rho}R}}{A_{\phi\phi} + A_{\phi\bar{\rho}}C_{\bar{\rho}\phi}} i\hat{k}_Z \sin\chi \left(\Omega v_A^{-1}\xi_R\right). \quad (4.4.20)$$

$\delta\bar{\rho}$  can be found from Eqs. (4.4.18), (4.4.19), and (4.4.20),

$$\delta\bar{\rho} = \left(A_{\bar{\rho}R} - A_{\bar{\rho}\phi} \frac{A_{\phi R} + A_{\phi\bar{\rho}}C_{\bar{\rho}R}}{A_{\phi\phi} + A_{\phi\bar{\rho}}C_{\bar{\rho}\phi}}\right) i\hat{k}_Z \sin\chi \left(\Omega v_A^{-1}\xi_R\right). \quad (4.4.21)$$

If we substitute expressions for  $\delta\bar{B}_R$ ,  $\delta\bar{B}_\phi$ , and  $\delta\bar{\rho}$  as given by Eqs. (4.4.19) - (4.4.21), then the azimuthal component of Eq. (4.4.2) can be solved for  $\delta u_\phi$ ,

$$\begin{aligned} \delta u_\phi = & \left( \gamma \left[ \frac{\alpha_P - \alpha_T}{i\hat{k}_Z \beta^{1/2} \sin\chi} + \right. \right. \\ & \left. \left. (C_{\bar{\rho}\phi} - 1) \frac{A_{\phi R} + A_{\phi\bar{\rho}}C_{\bar{\rho}R}}{A_{\phi\phi} + A_{\phi\bar{\rho}}C_{\bar{\rho}\phi}} - C_{\bar{\rho}R} \right] - \frac{d\ln\Omega}{d\ln R} \right) \Omega \xi_R. \end{aligned} \quad (4.4.22)$$

If we substitute Eqs. (4.4.19) - (4.4.21) into Eq. (4.4.11), then,

$$\frac{\delta p}{p_0} = \mathcal{A}_p i\hat{k}_Z \sin\chi \left(\Omega v_A^{-1}\xi_R\right), \quad (4.4.23)$$

where,

$$\begin{aligned} \mathcal{A}_p = & -\beta^{-1} \left( \hat{\eta}_\nu \gamma (3 \sin^2 \chi - 1) \left( \frac{\hat{k}_R}{\hat{k}_Z} \sin \chi - \frac{2(\alpha_P - \alpha_T)}{3i\hat{k}_Z \sin \chi \beta^{1/2}} \right) + \right. \\ & \left. \frac{\gamma^2}{\hat{k}_Z^2 \sin \chi} \left[ \frac{\hat{k}_R}{\hat{k}_Z} - \frac{\alpha_P - \alpha_T}{i\hat{k}_Z \beta^{1/2}} \right] + C_{\bar{\rho}R} \left[ \frac{\gamma^2}{\hat{k}_Z^2} - \frac{2\hat{\eta}_\nu \gamma}{3} (3 \sin^2 \chi - 1) \right] \right) - \\ & \frac{A_{\phi R} + A_{\phi \bar{\rho}} C_{\bar{\rho}R}}{A_{\phi \phi} + A_{\phi \bar{\rho}} C_{\bar{\rho} \phi}} (\hat{\eta}_\nu \gamma (3 \sin^2 \chi - 1) - 1 + \\ & \left. C_{\bar{\rho} \phi} \left[ \frac{\gamma^2}{\hat{k}_Z^2} - \frac{2\hat{\eta}_\nu \gamma}{3} (3 \sin^2 \chi - 1) \right] \right) \beta^{-1}. \end{aligned} \quad (4.4.24)$$

The perturbed temperature is given by,

$$\delta\theta = \theta_0 \left( \frac{\delta p}{p_0} - \delta\bar{\rho} \right). \quad (4.4.25)$$

If we substitute Eqs. (4.4.19) - (4.4.21) into Eq. (4.4.5), then  $\delta\sigma_{\mathbf{bb}}$  can be represented by,

$$\begin{aligned} \delta\sigma_{\mathbf{bb}} = & 3\rho_0 \hat{\eta}_\nu \gamma (\Omega v_A \xi_R) \left( i\hat{k}_R \sin^2 \chi - \frac{2(\alpha_P - \alpha_T)}{3\beta^{1/2}} + \right. \\ & \left. \frac{A_{\phi R} + A_{\phi \bar{\rho}} C_{\bar{\rho}R}}{A_{\phi \phi} + A_{\phi \bar{\rho}} C_{\bar{\rho} \phi}} \left[ i\hat{k}_Z \sin \chi \cos \chi - \frac{2}{3} C_{\bar{\rho} \phi} \right] + \frac{2}{3} C_{\bar{\rho}R} \right). \end{aligned} \quad (4.4.26)$$

The perturbed heat flux  $\delta q$  can be expressed as,

$$\delta q = \hat{\eta}_\kappa p_0 v_A \left( i\hat{k}_Z \sin \chi \alpha_T H^{-1} \xi_R - i\hat{k}_Z \sin \chi \frac{\delta\theta}{\theta_0} \right). \quad (4.4.27)$$

We plot normalized angular momentum flux, in Fig. (4.4.5), and heat flux, in Fig. (4.4.6), as functions of nonradial wavenumber for a Keplerian rotation profile,  $\chi = \pi/4$ ,  $\alpha_P = 5$ ,  $\alpha_T = 1$ , and viscous diffusivity  $\eta_\nu \Omega / \theta_0 = 10^{-3}$ , for various  $\beta \leq 10^6$ . In Eq. (4.3.2), the dominant term in  $\langle F_{ER} \rangle$ ,  $\text{Re}(\delta q \delta \bar{B}_R^*) \propto \beta^{1/2}$ . Therefore the quadratic heat flux  $\langle F_{ER} \rangle \propto \beta^{1/2}$  when the viscous diffusivity and gas pressure are kept constant

but the magnetic field strength varies. At fixed viscous diffusivity the quadratic heat flux due to the MVTI becomes stronger as the magnetic field becomes weaker. In Fig. (4.4.6), we plot  $\langle F_{ER} \rangle$  normalized in units of  $p_0 \Omega^2 |\xi|_R^2 v_A^{-1}$ . The normalization of the flux in Fig. (4.4.6) has magnitude  $\beta^{1/2}$  times  $p_0 \Omega |\xi|_R^2 H^{-1}$ , the normalization of heat fluxes in Figs. (4.3.1) and (4.3.3).

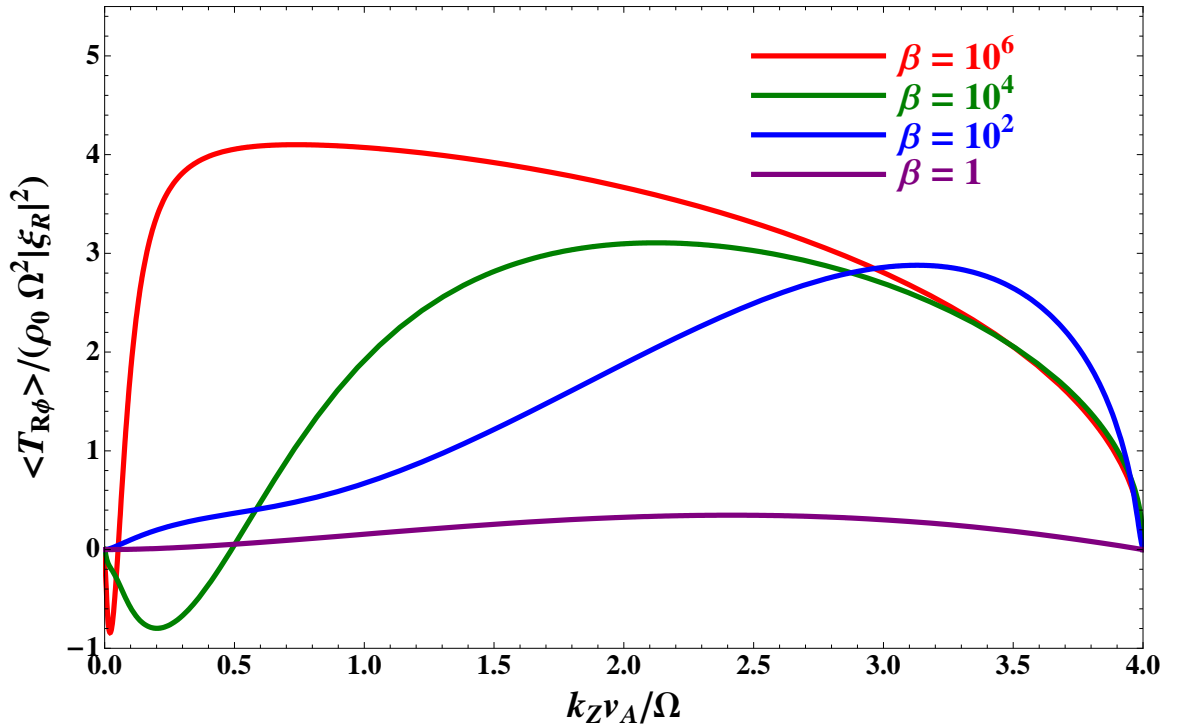


Fig. 4.4.5.— Normalized modal angular momentum flux as a function of vertical wavenumber  $k_Z v_A / \Omega$  for  $\eta_\nu \Omega / \theta_0 = 10^{-3}$  and  $\beta \leq 10^6$ .



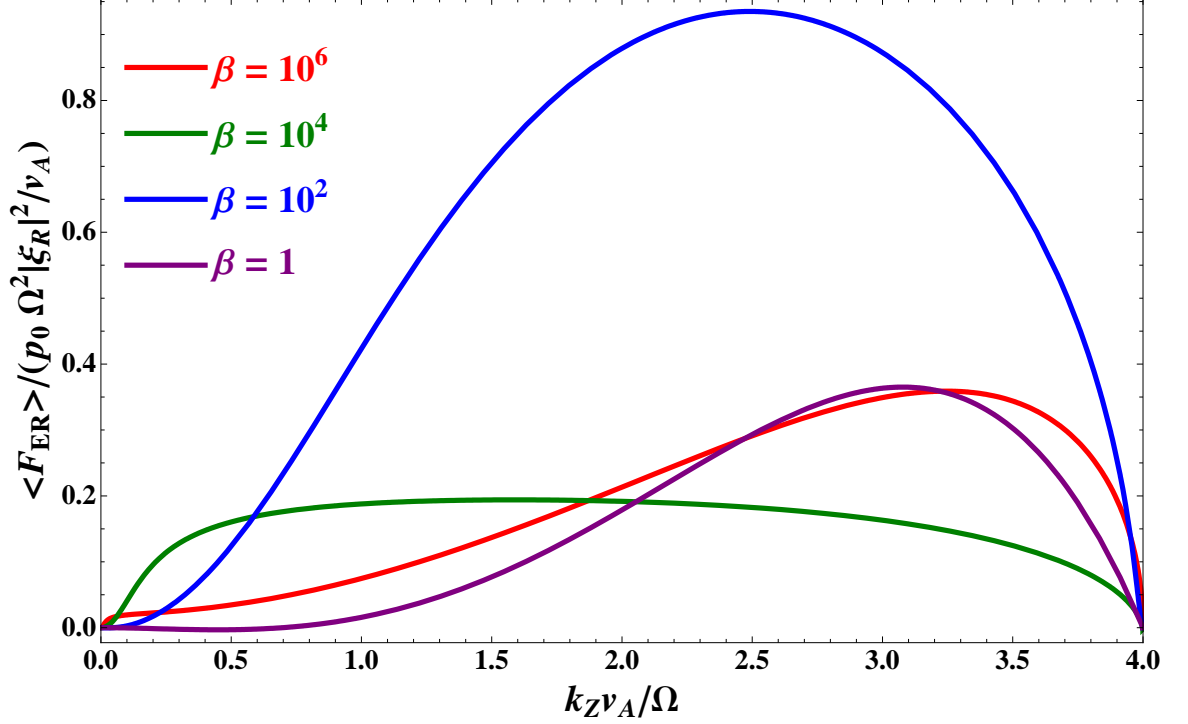


Fig. 4.4.6.— Normalized modal heat flux as a function of vertical wavenumber  $k_Z v_A / \Omega$  for  $\eta_\nu \Omega / \theta_0 = 10^{-3}$  and  $\beta \leq 10^6$ .

In Figs. (4.4.7) and (4.4.8) we plot normalized angular momentum flux and normalized heat flux as a function of nonradial wavenumber, respectively. We take a Keplerian rotation profile,  $\chi = \pi/4$ ,  $\alpha_P = 5$ ,  $\alpha_T = 1$ , and  $\eta_\nu \Omega / v_A^2 = 10$ , for various  $\beta \geq 10^2$ . At fixed normalized viscous diffusivity, as  $\beta$  increases we recover the incompressible limits of  $\langle F_{ER} \rangle$  and  $\langle T_{R\phi} \rangle$ , as given by Eqs. (4.3.5) and (4.3.4), respectively.

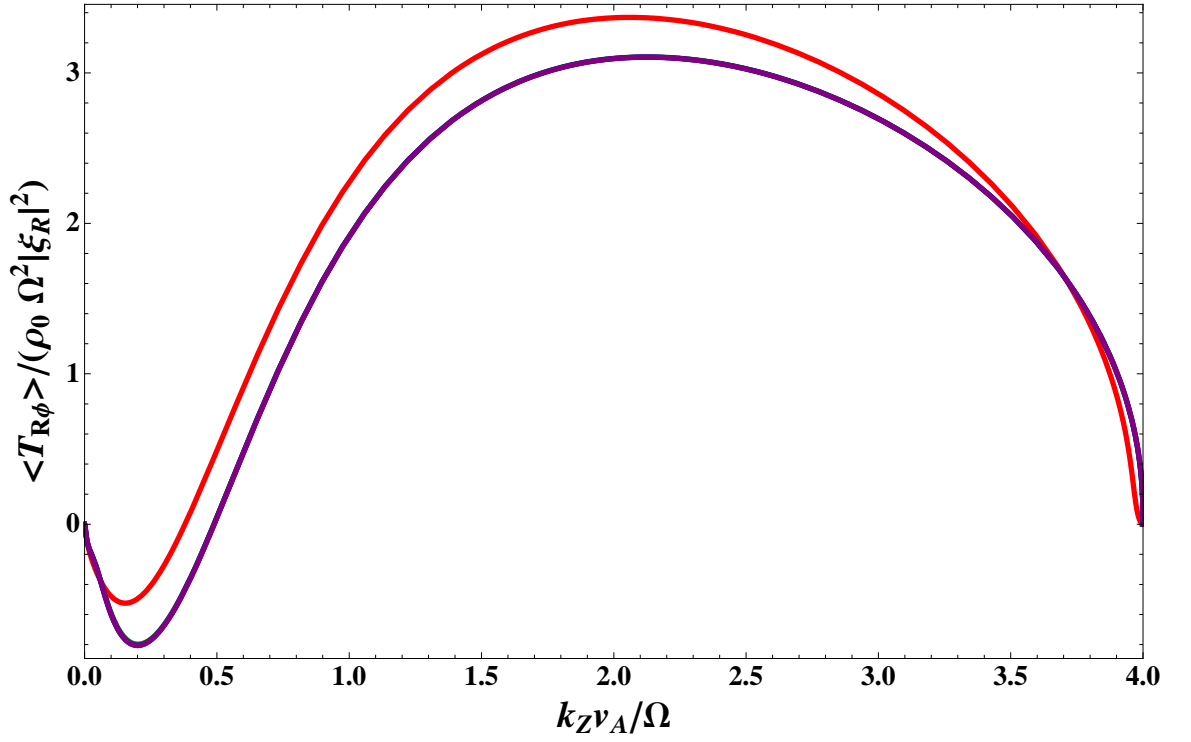


Fig. 4.4.7.— Normalized modal angular momentum flux as a function of vertical wavenumber  $k_Z v_A / \Omega$  for  $\eta_\nu \Omega / v_A^2 = 10$  and various  $\beta \geq 10^2$ . The red line corresponds to  $\beta = 10^2$ . Lines corresponding to  $\beta = 10^4$ ,  $\beta = 10^6$ , and  $\beta = 10^8$  coincide at the resolution of this graph and are denoted by the purple line.

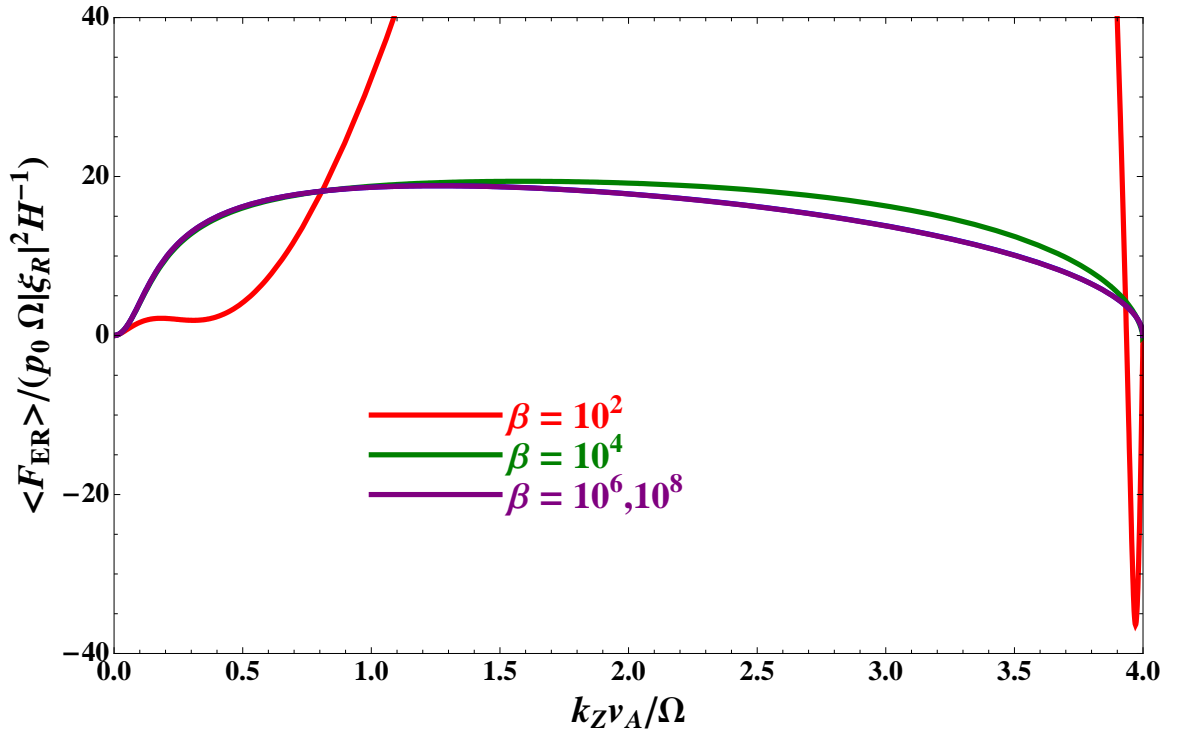


Fig. 4.4.8.— Normalized modal heat flux as a function of vertical wavenumber  $k_Z v_A / \Omega$  for  $\eta_\nu \Omega / v_A^2 = 10$  and  $\beta \geq 10^2$ . Heat flux is especially large for  $\beta = 10^2$ . Lines corresponding to  $\beta = 10^6$  and  $\beta = 10^8$ , coincide at the resolution of this graph.

## 4.5 Summary of Results

We have demonstrated several important properties of the MVTI. First, we find that both slender and thick disks with sufficiently large thermal diffusion coefficients are susceptible to the MVTI. Second, outwardly decreasing temperature profiles increase the range of unstable wavenumbers and growth rate of unstable modes for the MRI-like instability and the MVI-like instability. Third, collisional viscosity and thermal conductivity in dilute plasmas contribute significantly to quadratic modal fluxes of angular momentum and heat in the MVTI. The MVTI can transport angular momentum either outwards or inwards even when there is no orbital angular velocity shear. Finally, we demonstrate that the MVTI become more compressible as  $\beta$  decreases while the normalized viscous diffusivity  $\eta_\nu \Omega / v_A^2$  stays constant.

# Chapter 5

## Kinetic Treatment – the Collisionless MTI

In this chapter we formulate a model of the collisionless MTI, which is the analogue of the MVTI in the absence of collisions. Kulsrud’s drift-kinetic approximation to the Boltzmann equation (Kulsrud 1983, 2005) is well suited for collisionless or mildly collisional MHD plasma equilibrium and dynamics. Dynamics only along magnetic field lines, MHD conditions of quasineutrality and zero equilibrium current, and conservation of magnetic moment are the features of the lowest order particle distribution function. In these dilute plasmas, interspecies momentum and energy transfer processes such as temperature equilibration or electric resistivity, that cannot be modeled through the Kulsrud formalism, are not physically relevant to our problem of interest. Such effects may be modelled by a distribution function expansion in collisional frequency, or by applying a more accurate collisional operator (Braginskii 1965; Chang & Callen 1992).

The drift-kinetic equation has been used in treatments of accretion in dilute rotating astrophysical plasmas (Quataert et al. 2002; Sharma et al. 2003). We derive a

drift-kinetic equation for rotating plasmas, with a simplified collision operator, BGK (Bhatnager et al. 1954), that reproduces the qualitative form of viscous and thermal transport in magnetized plasmas in the limit of high collisionality (Snyder et al. 1997). The organization of this chapter is as follows. In §5.1, we derive the drift-kinetic equation in a rotating frame in which the sound speed is subdominant to the orbital speed. We derive velocity moments that reduce to the fluid equations. In §5.2 we consider the stability of hot dilute rotating plasmas to the collisionless MRI and MTI as well as demonstrate the form of outward quadratic angular momentum and heat fluxes. In §5.3 we consider finite collisionality. We demonstrate that for collisional frequencies large enough such that the ion mean free path is longer than the wavelength of the fastest growing modes (of order  $v_A/\Omega$ ), we reproduce the Braginskii fluid viscosity and thermal conductivity. Finally, in §5.4 we summarize our results.

## 5.1 The Drift Kinetic Equation in Rotating Frame

Let us consider the form of the electric field and the equilibrium force balance equation in a dilute magnetized rotating disk. The structure of a thin dilute magnetized disk is described in some detail in Appendix B. Electric fields constrain the electrons and ions to have the same velocity and number density. The electric field is given by Eq. (B.5), where  $\mathbf{E}_{\text{ES}} = E_{R,\text{ES}}\hat{\mathbf{R}} + E_{Z,\text{ES}}\hat{\mathbf{z}}$  is the electrostatic field that ensures quasineutrality.  $E_{\parallel}$  is the component of the electric field parallel to the magnetic field, and in equilibrium  $E_{\parallel 0} = 0$ . The ion and electron equilibrium radial and vertical force balance equations are given by Eqs. (B.25) - (B.28). For a mildly collisional or collisionless plasma, the slowest and largest scale plasma dynamics may be described by dilute MHD. This is valid if we consider the following hierarchy of scales:  $1/T < \omega_{pi} \ll \Omega_{ci}$ ,  $1/L < \omega_{pi}/c \ll \rho_i$ , where  $\omega_{pi}/c$  is the inverse ion

inertial depth, and  $L$  and  $T$  are the shortest length and fastest time scales associated with this system. Particle motion along magnetic fields is unconstrained. In the purely collisionless case a valid equilibrium is one in which pressures parallel and perpendicular to the magnetic field may not necessarily be equal. We consider a plasma equilibrium such that pressures parallel and perpendicular to the magnetic field are equal.

The Boltzmann equation governing the dynamics of a particle species  $s$  is,

$$\frac{\partial f_s}{\partial t} + \mathbf{U} \cdot \nabla f_s + \frac{Z_s e}{m_s} \left( \mathbf{E} + \frac{1}{c} \mathbf{U} \times \mathbf{B} \right) \cdot \frac{\partial f_s}{\partial \mathbf{U}} + \frac{\mathbf{F}_s}{m_s} \cdot \frac{\partial f_s}{\partial \mathbf{U}} = C[f_s]. \quad (5.1.1)$$

Here  $f_s$  is the distribution function,  $C[f_s]$  is a collision operator acting on  $f_s$ ,  $\mathbf{F}_s$  is the force acting on a particle, and  $m_s$  and  $Z_s$  are the mass and charge of a particle.

In a dilute magnetized plasma, a natural ordering of the particle distribution function is in powers of  $(\Omega_s T)^{-1} \ll 1$ , where  $\Omega_s = Z_s e B / (m_s c)$  is the cyclotron frequency. The particle distribution function  $f_s$  can be expanded as,

$$f_s = f_s^0 + f_s^1 + \dots \quad (5.1.2)$$

The first to employ this formalism was Chew et al. (1956), who studied the adiabatic response of magnetized plasmas. However, the adiabatic approximation is relevant only to modes with phase velocities much faster than the sound speed. This is not the case for these MHD modes in a weakly-magnetized plasma. From Eq. (1.2.4) we get the simplified induction equation,

$$\Gamma \delta \bar{\mathbf{B}} = i k_{\parallel} \delta \mathbf{u} + (R \delta \bar{\mathbf{B}} \cdot \nabla \Omega) \hat{\phi} - \mathbf{b}_0 (i \mathbf{k} \cdot \delta \mathbf{u}) \quad (5.1.3)$$

In §5.1.1 we derive evolution equations for the zeroth-order distribution function for

each species. In §5.1.2 and §5.1.3 we derive the fluid equations for this plasma from the drift-kinetic equation.

### 5.1.1 The Drift Kinetic Equation

To derive the drift-kinetic equation in a rotating frame from the Boltzmann equation, Eq. (5.1.1), it is convenient to use a set of gyromotion variables centered about the equilibrium flow. The particle velocity can then be represented as,

$$\mathbf{U} = R\Omega(R)\hat{\boldsymbol{\phi}} + \mathbf{u}_\perp + v_\parallel \mathbf{b} + \sqrt{2\mu B} (\hat{\mathbf{x}}_\perp \cos \psi + \hat{\mathbf{y}}_\perp \sin \psi), \quad (5.1.4)$$

where  $v_\parallel$  is the particle velocity parallel to the magnetic field,  $\mu$  is the magnetic moment,  $\hat{\mathbf{x}}_\perp$  and  $\hat{\mathbf{y}}_\perp$  are mutually orthogonal vectors perpendicular to the magnetic field, and  $\psi$  is the gyroangle.  $\mathbf{u}_\perp$  is the the bulk flow velocity perpendicular to the magnetic field in an MHD fluid. Thus, the gyromotion-centered variables are,

$$v_\parallel = \mathbf{U} \cdot \mathbf{b} - R\Omega b_\phi, \quad (5.1.5)$$

$$\mu = \frac{\left( \mathbf{U} - R\Omega\hat{\boldsymbol{\phi}} + R\Omega b_\phi \mathbf{b} - \mathbf{b} (\mathbf{U} \cdot \mathbf{b}) - \mathbf{u}_\perp \right)^2}{2B}, \quad (5.1.6)$$

$$\tan \psi = \frac{\hat{\mathbf{y}}_\perp \cdot (\mathbf{U} - R\Omega\hat{\boldsymbol{\phi}} - \mathbf{u}_\perp)}{\hat{\mathbf{x}}_\perp \cdot (\mathbf{U} - R\Omega\hat{\boldsymbol{\phi}} - \mathbf{u}_\perp)}, \quad (5.1.7)$$

The Jacobian transformations with respect to  $\mathbf{U}$  are,

$$\frac{\partial v_\parallel}{\partial \mathbf{U}} = \mathbf{b}, \quad (5.1.8)$$

$$\frac{\partial \mu}{\partial \mathbf{U}} = \sqrt{\frac{2\mu}{B}} (\hat{\mathbf{x}}_\perp \cos \psi + \hat{\mathbf{y}}_\perp \sin \psi), \quad (5.1.9)$$

$$\frac{\partial \psi}{\partial \mathbf{U}} = -\frac{\hat{\mathbf{y}}_\perp \cos \psi - \hat{\mathbf{x}}_\perp \sin \psi}{\sqrt{2\mu B}}, \quad (5.1.10)$$



If we employ the electric field (Eq. [B.5]), equilibrium force balance equations for ions and electrons (Eqs. [B.25] - [B.28]), and the velocity transformation (Eq. [5.1.4]), the total acceleration of a particle of species  $s$  is given by, retaining terms only to order  $z^2$  in the force balance equation,

$$\begin{aligned} \frac{Z_s e}{m_s} \left( \mathbf{E} + \frac{1}{c} \mathbf{U} \times \mathbf{B} \right) - \left( \Omega_K^2 R \left( 1 - \frac{3z^2}{2R^2} \right) \hat{\mathbf{R}} + \Omega_K^2 z \hat{\mathbf{z}} \right) = \\ \frac{Z_s e}{m_s} \left( E_{\parallel} \mathbf{b} + \delta \mathbf{E}_{\text{ES}} + \frac{1}{c} B \sqrt{2\mu B} (\hat{\mathbf{x}}_{\perp} \cos \psi + \hat{\mathbf{y}}_{\perp} \sin \psi) \times \mathbf{b} \right) + \\ \left( \frac{1}{m_s n_{s0}} \nabla p_{s0} - \Omega^2 R \hat{\mathbf{R}} \right) \end{aligned} \quad (5.1.11)$$

where  $\delta \mathbf{E}_{\text{ES}} = \mathbf{E}_{\text{ES}} - \mathbf{E}_{\text{ES},0}$ . To lowest order in  $\Omega_s T$ , the Boltzmann equation is,

$$\Omega_s \left( \sqrt{2\mu B} (\hat{\mathbf{x}}_{\perp} \cos \psi + \hat{\mathbf{y}}_{\perp} \sin \psi) \times \mathbf{b} \right) \cdot \frac{\partial f_s^0}{\partial \mathbf{U}} = 0. \quad (5.1.12)$$

Using the velocity Jacobian transformations given by Eqs. (5.1.8) - (5.1.10), Eq. (5.1.12) reduces to,

$$\Omega_s \frac{\partial f_s^0}{\partial \psi} = 0. \quad (5.1.13)$$

Hence  $f_s^0 \equiv f_s^0(v_{\parallel}, \mu)$ , i.e., the particle distribution function is only a function of the parallel velocity and magnitude of the perpendicular velocity about the equilibrium flow. As a consequence, the pressure tensor is  $\mathbb{P} = p_{\parallel} \mathbf{b}\mathbf{b} + p_{\perp} (\mathbb{I} - \mathbf{b}\mathbf{b})$ .

Using the equilibrium force balance equation, Eqs. (B.25) - (B.28), the velocity transformation, Eq. (5.1.4), and the zeroth-order distribution function, Eq. (5.1.13),

the next order in the Boltzmann equation is,

$$\begin{aligned} & \frac{\partial f_s^0}{\partial t} + \left( R\Omega\hat{\phi} + \mathbf{u}_\perp + v_\parallel \mathbf{b} + \sqrt{2\mu B} (\hat{\mathbf{x}}_\perp \cos \psi + \hat{\mathbf{y}}_\perp \sin \psi) \right) \cdot \nabla f_s^0 + \\ & \left( \frac{Z_s e}{m_s} E_\parallel \mathbf{b} + \frac{1}{m_s n_{s0}} \nabla p_{s0} - \Omega^2 R \hat{\mathbf{R}} + \frac{Z_s e}{m_s} \delta \mathbf{E}_{\text{ES}} \right) \cdot \\ & \left( \mathbf{b} \frac{\partial f_s^0}{\partial v_\parallel} + \sqrt{\frac{2\mu}{B}} (\hat{\mathbf{x}}_\perp \cos \psi + \hat{\mathbf{y}}_\perp \sin \psi) \frac{\partial f_s^0}{\partial \mu} \right) = C[f_s^0], \end{aligned} \quad (5.1.14)$$

Terms with  $\Omega_s \partial f_s^1 / \partial \psi$  are nonconstant functions of  $\psi$  and so cannot contribute to expressions for  $f_s^0$ . The simplest way to keep terms constant in gyrophase angle is to average Eq. (5.1.14) over  $\psi$ . The Jacobians of velocity with respect to time are,

$$\frac{\partial v_\parallel}{\partial t} = \left( \mathbf{u}_\perp + \sqrt{2\mu B} (\hat{\mathbf{x}}_\perp \cos \psi + \hat{\mathbf{y}}_\perp \sin \psi) \right) \cdot \frac{\partial \mathbf{b}}{\partial t}, \quad (5.1.15)$$

$$\frac{\partial \mu}{\partial t} = -\sqrt{\frac{2\mu}{B}} (\hat{\mathbf{x}}_\perp \cos \psi + \hat{\mathbf{y}}_\perp \sin \psi) \cdot \left( \frac{\partial \mathbf{b}}{\partial t} v_\parallel + \frac{\partial \mathbf{u}_\perp}{\partial t} \right) - \frac{\mu}{B} \frac{\partial B}{\partial t}, \quad (5.1.16)$$

and the Jacobians of velocity with respect to position are,

$$\nabla v_\parallel = \nabla \mathbf{b} \cdot \left( \sqrt{2\mu B} (\hat{\mathbf{x}}_\perp \cos \psi + \hat{\mathbf{y}}_\perp \sin \psi) + \mathbf{u}_\perp \right) - \mathbf{b} \cdot \nabla (R\Omega\hat{\phi}), \quad (5.1.17)$$

$$\nabla \mu = -\sqrt{\frac{2\mu}{B}} (\hat{\mathbf{x}}_\perp \cos \psi + \hat{\mathbf{y}}_\perp \sin \psi) \cdot \left( v_\parallel \nabla \mathbf{b} + \nabla \mathbf{u}_\perp + \nabla (R\Omega\hat{\phi}) \right) \quad (5.1.18)$$

We need not compute the derivatives  $\partial \psi / \partial t$  and  $\nabla \psi$  since  $f_s^0$  is independent of  $\psi$ . Thus,  $\partial f_s^0 / \partial t \rightarrow \partial f_s^0 / \partial t + (\partial f_s^0 / \partial v_\parallel) \partial v_\parallel / \partial t + (\partial f_s^0 / \partial \mu) \partial \mu / \partial t$  and  $\nabla f_s^0 \rightarrow \nabla f_s^0 +$

$\nabla v_{\parallel} (\partial f_s^0 / \partial v_{\parallel}) + \nabla \mu (\partial f_s^0 / \partial \mu)$ . The gyroaveraged Eq. (5.1.14) reduces to,

$$\begin{aligned}
& \frac{\partial f_s^0}{\partial t} + \left( R\Omega \hat{\phi} + \mathbf{u}_{\perp} + v_{\parallel} \mathbf{b} \right) \cdot \nabla f_s^0 + \\
& \frac{\partial f_s^0}{\partial v_{\parallel}} \left( \mathbf{u}_{\perp} \cdot \frac{\partial \mathbf{b}}{\partial t} + \left( R\Omega \hat{\phi} + \mathbf{u}_{\perp} + v_{\parallel} \mathbf{b} \right) \cdot \left( \nabla \mathbf{b} \cdot \mathbf{u}_{\perp} - \mathbf{b} \cdot \nabla \left( R\Omega \hat{\phi} \right) \right) \right) + \\
& \frac{\partial f_s^0}{\partial v_{\parallel}} 2\mu B \langle (\hat{\mathbf{x}}_{\perp} \cos \psi + \hat{\mathbf{y}}_{\perp} \sin \psi) (\hat{\mathbf{x}}_{\perp} \cos \psi + \hat{\mathbf{y}}_{\perp} \sin \psi) : \nabla \mathbf{b} \rangle_{\psi} - \\
& \frac{\partial f_s^0}{\partial \mu} \left( \frac{\mu}{B} \frac{\partial B}{\partial t} \right) - 2\mu \frac{\partial f_s^0}{\partial \mu} \langle (\hat{\mathbf{x}}_{\perp} \cos \psi + \hat{\mathbf{y}}_{\perp} \sin \psi) \\
& (\hat{\mathbf{x}}_{\perp} \cos \psi + \hat{\mathbf{y}}_{\perp} \sin \psi) : \left( v_{\parallel} \nabla \mathbf{b} + \nabla \mathbf{u}_{\perp} + \nabla \left( R\Omega \hat{\phi} \right) \right) \rangle_{\psi} + \\
& \left( \frac{Z_s e}{m_s} E_{\parallel} + \frac{1}{m_s n_{s0}} \mathbf{b} \cdot \nabla p_{s0} - \Omega^2 R b_R \right) \frac{\partial f_s^0}{\partial v_{\parallel}} = \langle C [f_s^0] \rangle_{\psi}
\end{aligned} \tag{5.1.19}$$

The term  $\delta \mathbf{E}_{\text{ES}} \cdot \mathbf{b}$  is absorbed into  $E_{\parallel}$ , and the gyroaveraged quantity  $\langle F \rangle_{\psi} = \frac{1}{2\pi} \int_0^{2\pi} F d\psi$ . From Eq. (1.2.8), the evolution of the magnetic field magnitude  $B = \mathbf{B} \cdot \mathbf{b}$  is given by,

$$\begin{aligned}
& \frac{1}{B} \left( \frac{\partial}{\partial t} + \Omega \frac{\partial}{\partial \phi} \right) B = -\frac{\mathbf{u} \cdot \nabla B}{B} - \nabla \cdot \mathbf{u} + \mathbf{b} \cdot \nabla \mathbf{u} \cdot \mathbf{b} + \\
& R b_{\phi} \mathbf{b} \cdot \nabla \Omega.
\end{aligned} \tag{5.1.20}$$

The gyroaveraged tensor is,

$$\langle (\hat{\mathbf{x}}_{\perp} \cos \psi + \hat{\mathbf{y}}_{\perp} \sin \psi) (\hat{\mathbf{x}}_{\perp} \cos \psi + \hat{\mathbf{y}}_{\perp} \sin \psi) \rangle_{\psi} = \frac{1}{2} (\mathbb{I} - \mathbf{b}\mathbf{b}). \tag{5.1.21}$$

We use a simplified form of the collision operator (Bhatnager et al. 1954) that can qualitatively reproduce the collisional form of the viscous stress and conductive heat

flux:

$$\begin{aligned}
C \langle f_s^0 \rangle &= \nu_s (f_s^0 - \langle f_s \rangle), \\
\langle f_s \rangle &= \frac{n}{(2\pi k_B T_s / m_s)^{3/2}} \exp \left( -\frac{m_s (v_{\parallel} - u_{\parallel})^2}{2k_B T_s} - \frac{m_s \mu B}{k_B T_s} \right), \quad (5.1.22) \\
T_s &= T_{s\parallel}/3 + 2T_{s\perp}/3,
\end{aligned}$$

where  $T_{s\parallel}$  and  $T_{s\perp}$  are defined as  $nk_B T_{s\parallel} = p_{s\parallel}$  and  $nk_B T_{s\perp} = p_{s\perp}$ , and  $\nu_s$  is the collision frequency of species  $s$ . After some algebra, using Eqs. (5.1.20) - (5.1.22), we obtain the drift-kinetic equation in covariant form:

$$\begin{aligned}
&\left( \frac{\partial}{\partial t} + \Omega \frac{\partial}{\partial \phi} \right) (f_s^0 B) + \nabla \cdot ([v_{\parallel} \mathbf{b} + \mathbf{u}_{\perp}] f_s^0 B) + \\
&\frac{\partial}{\partial v_{\parallel}} \left( f_s^0 B \left[ \frac{Z_s e}{m_s} E_{\parallel} + \frac{1}{n_{s0} m_s} \mathbf{b} \cdot \nabla p_{s0} \right] \right) + \\
&\frac{\partial}{\partial v_{\parallel}} \left( f_s^0 B \left[ -\mathbf{b} \cdot \left( \left[ \frac{\partial}{\partial t} + \Omega \frac{\partial}{\partial \phi} \right] \mathbf{u}_{\perp} + [v_{\parallel} \mathbf{b} + \mathbf{u}_{\perp}] \cdot \nabla \mathbf{u}_{\perp} \right) + \right. \quad (5.1.23) \\
&\left. \mu B \nabla \cdot \mathbf{b} + 2\Omega \hat{\mathbf{z}} \cdot (\mathbf{b} \times \mathbf{u}) - b_{\phi} R (\mathbf{u}_{\perp} + v_{\parallel} \mathbf{b}) \cdot \nabla \Omega \right] ) = \\
&- \nu_s (f_s^0 B - \langle f_s \rangle B),
\end{aligned}$$

Additional terms appear in the formulation of Eq. (5.1.23) that do not appear in the normal drift-kinetic equation (Kulsrud 1983, 2005). It includes terms associated with noninertial rotational accelerations along the magnetic field,  $2\Omega \hat{\mathbf{z}} \cdot (\mathbf{b} \times \mathbf{u}) - b_{\phi} R (\mathbf{u}_{\perp} + v_{\parallel} \mathbf{b}) \cdot \nabla \Omega$ , and pressure forces along the magnetic field,  $1/(\rho_0 m_s) \mathbf{b} \cdot \nabla p_{s0}$ . An equilibrium particle distribution function of Eq. (5.1.23) is,

$$f_{s0}^0 = \frac{\rho_0(R, z)}{(2\pi k_B T_{s0}(R)/m_s)^{3/2}} \exp \left( -\frac{m_s v_{\parallel}^2}{2k_B T_{s0}(R)} - \frac{m_s \mu B}{k_B T_{s0}(R)} \right). \quad (5.1.24)$$

The density profile, as described in §3, is  $\rho_0(R, z) = \rho_0(R) \exp(-z^2/(2H^2))$ .

### 5.1.2 Moments of the Drift-Kinetic Equation

We take moments of the drift-kinetic equation in order to reproduce MHD equations for continuity, force balance, internal energy, and heat flux. We consider moments up to third order in velocity of Eq. (5.1.23), using the formalism of Snyder et al. (1997). We note that the velocity volume element is  $d^3\mathbf{U} = B d\mu dv_{\parallel} d\psi$ . For a function  $F$  independent of  $\psi$ ,  $\int F d^3\mathbf{U} = 2\pi \int F B d\mu dv_{\parallel}$ . The following are the nonzero moments used in deriving fluid evolution equations from the drift-kinetic equation:

$$\begin{aligned}
n_s &= 2\pi \int f_s^0 B d\mu dv_{\parallel}, \\
n_s u_{\parallel} &= 2\pi \int f_s^0 v_{\parallel} (B d\mu dv_{\parallel}), \\
p_{s\parallel} &= 2\pi \int m_s (v_{\parallel} - u_{\parallel})^2 f_s^0 (B d\mu dv_{\parallel}), \\
p_{s\perp} &= 2\pi \int m_s \mu B f_s^0 (B d\mu dv_{\parallel}), \\
q_{s\parallel} &= 2\pi \int m_s (v_{\parallel} - u_{\parallel})^3 f_s^0 (B d\mu dv_{\parallel}), \\
q_{s\perp} &= 2\pi \int m_s (v_{\parallel} - u_{\parallel}) \mu B f_s^0 (B d\mu dv_{\parallel}), \\
r_{s\parallel} &= 2\pi \int m_s (v_{\parallel} - u_{\parallel})^4 f_s^0 (B d\mu dv_{\parallel}), \\
r_{s\times} &= 2\pi \int m_s (v_{\parallel} - u_{\parallel})^2 \mu B f_s^0 (B d\mu dv_{\parallel}), \\
r_{s\perp} &= 2\pi \int m_s \mu^2 B^2 f_s^0 (B d\mu dv_{\parallel}).
\end{aligned} \tag{5.1.25}$$

The moments of the collision operator are,

$$\begin{aligned}
2\pi \int m_s C[f_s^0] B d\mu dv_{\parallel} &= 0, \\
2\pi \int m_s v_{\parallel} C[f_s^0] B d\mu dv_{\parallel} &= 0, \\
2\pi \int m_s (v_{\parallel} - u_{\parallel})^2 C[f_s^0] B d\mu dv_{\parallel} &= -\frac{2}{3} \nu_s (p_{s\parallel} - p_{s\perp}), \\
2\pi \int m_s \mu B C[f_s^0] B d\mu dv_{\parallel} &= -\frac{1}{3} \nu_s (p_{s\perp} - p_{s\parallel}), \\
2\pi \int m_s (v_{\parallel} - u_{\parallel})^3 C[f_s^0] B d\mu dv_{\parallel} &= -\nu_s q_{s\parallel}, \\
2\pi \int m_s \mu B (v_{\parallel} - u_{\parallel}) C[f_s^0] B d\mu dv_{\parallel} &= -\nu_s q_{s\perp}.
\end{aligned} \tag{5.1.26}$$

If we take appropriate moments of Eq. (5.1.23) with moments of the collision operator, Eq. (5.1.26), we have the fluid equations for continuity, parallel force balance, parallel

and perpendicular pressures, and heat fluxes:

$$\left(\frac{\partial}{\partial t} + \Omega \frac{\partial}{\partial \phi}\right) n_s + \nabla \cdot (n_s \mathbf{u}) = 0, \quad (5.1.27)$$

$$\begin{aligned} & \left(\frac{\partial}{\partial t} + \Omega \frac{\partial}{\partial \phi}\right) v_{\parallel} + \mathbf{u} \cdot \nabla v_{\parallel} + \frac{1}{n_s m_s} \nabla \cdot (p_{s\parallel} \mathbf{b}) - \frac{p_{s\perp}}{n_s m_s} \nabla \cdot \mathbf{b} - \\ & 2\Omega \hat{\mathbf{z}} \cdot (\mathbf{b} \times \mathbf{u}) + R b_{\phi} \mathbf{u} \cdot \nabla \Omega + \mathbf{b} \cdot \left( \left[ \frac{\partial}{\partial t} + \Omega \frac{\partial}{\partial \phi} \right] \mathbf{u}_{\perp} + \mathbf{u} \cdot \nabla \mathbf{u}_{\perp} \right) - \end{aligned} \quad (5.1.28)$$

$$\begin{aligned} & \frac{Z_s e}{m_s} E_{\parallel} - \frac{1}{\rho_0 m_s} \mathbf{b} \cdot \nabla p_{s0} = 0, \\ & \left(\frac{\partial}{\partial t} + \Omega \frac{\partial}{\partial \phi}\right) p_{s\parallel} + \nabla \cdot (p_{s\parallel} \mathbf{u}) + \nabla \cdot (q_{s\parallel} \mathbf{b}) + \end{aligned} \quad (5.1.29)$$

$$\begin{aligned} & 2p_{s\parallel} (\mathbf{b} \cdot \nabla \mathbf{u} \cdot \mathbf{b} + R b_{\phi} \mathbf{b} \cdot \nabla \Omega) - 2q_{s\perp} \nabla \cdot \mathbf{b} = -\frac{2}{3} (p_{s\parallel} - p_{s\perp}), \\ & \left(\frac{\partial}{\partial t} + \Omega \frac{\partial}{\partial \phi}\right) p_{s\perp} + p_{s\perp} (\nabla \cdot \mathbf{u} - \mathbf{b} \cdot \nabla \mathbf{u} \cdot \mathbf{b} - R b_{\phi} \mathbf{b} \cdot \nabla \Omega) + \end{aligned} \quad (5.1.30)$$

$$\nabla \cdot (p_{s\perp} \mathbf{u}) + \nabla \cdot (q_{s\perp} \mathbf{b}) + q_{s\perp} \nabla \cdot \mathbf{b} = -\frac{1}{3} (p_{s\perp} - p_{s\parallel}),$$

$$\begin{aligned} & \left(\frac{\partial}{\partial t} + \Omega \frac{\partial}{\partial \phi}\right) q_{s\parallel} + \nabla \cdot (q_{s\parallel} \mathbf{u}) + \nabla \cdot (\mathbf{b} r_{s\parallel}) + \\ & 3 \left( \frac{p_{s\parallel} [p_{s\parallel} - p_{s\perp}]}{n_s m_s} - r_{s\times} \right) \nabla \cdot \mathbf{b} - \frac{3p_{s\parallel}}{n_s m_s} \mathbf{b} \cdot \nabla p_{s\parallel} + \end{aligned} \quad (5.1.31)$$

$$\begin{aligned} & 3q_{s\parallel} (\mathbf{b} \cdot \nabla \mathbf{u} \cdot \mathbf{b} + R b_{\phi} \mathbf{b} \cdot \nabla \Omega) = -\nu_s q_{s\parallel} \\ & \left(\frac{\partial}{\partial t} + \Omega \frac{\partial}{\partial \phi}\right) q_{s\perp} + \nabla \cdot (q_{s\perp} \mathbf{u}) + \nabla \cdot (r_{s\times} \mathbf{b}) + \\ & \left( \frac{p_{s\perp} [p_{s\perp} - p_{s\parallel}]}{n_s m_s} + r_{s\times} - r_{s\perp} \right) \nabla \cdot \mathbf{b} - \frac{p_{s\perp}}{n_s m_s} \mathbf{b} \cdot \nabla p_{s\parallel} + \end{aligned} \quad (5.1.32)$$

$$q_{s\perp} \nabla \cdot \mathbf{u} = -\nu_s q_{s\perp}.$$

We make the following substitutions for pressures and heat fluxes,

$$\begin{aligned}
p_s &= \frac{1}{3} (p_{s\parallel} + 2p_{s\perp}), \\
p_{sv} &= p_{s\parallel} - p_{s\perp}, \\
q_s &= q_{s\parallel}/2 + q_{s\perp}, \\
q_{sv} &= q_{s\parallel} - q_{s\perp}.
\end{aligned} \tag{5.1.33}$$

We rearrange Eqs. (5.1.29) and (5.1.30) into,

$$\begin{aligned}
&\frac{3}{2} \left( \frac{\partial}{\partial t} + \Omega \frac{\partial}{\partial \phi} + \mathbf{u} \cdot \nabla \right) p_s + \frac{5}{2} p_s \nabla \cdot \mathbf{u} = -\nabla \cdot (q_s \mathbf{b}) - \\
&p_{sv} \left( \mathbf{b} \cdot \nabla \mathbf{u} \cdot \mathbf{b} - \frac{1}{3} \nabla \cdot \mathbf{u} + R b_\phi \mathbf{b} \cdot \nabla \Omega \right)
\end{aligned} \tag{5.1.34}$$

$$\begin{aligned}
&\left( \frac{\partial}{\partial t} + \Omega \frac{\partial}{\partial \phi} + \mathbf{u} \cdot \nabla + \frac{4}{3} \nabla \cdot \mathbf{u} + [\mathbf{b} \cdot \nabla \mathbf{u} \cdot \mathbf{b} + R b_\phi \mathbf{b} \cdot \nabla \Omega] + \nu_s \right) p_{sv} = \\
&- 3p_s \left( \mathbf{b} \cdot \nabla \mathbf{u} \cdot \mathbf{b} + R b_\phi \mathbf{b} \cdot \nabla \Omega - \frac{1}{3} \nabla \cdot \mathbf{u} \right) - \nabla \cdot (q_{sv} \mathbf{b}) + \\
&(2q_s - q_{sv}) \nabla \cdot \mathbf{b}
\end{aligned} \tag{5.1.35}$$

If we substitute in Eqs. (5.1.20) and (5.1.27), we rearrange Eqs. (5.1.34) and (5.1.35) into the following forms (Chew et al. 1956),

$$\begin{aligned}
&\rho B \left( \frac{\partial}{\partial t} + \Omega \frac{\partial}{\partial \phi} \right) \left( \frac{p_{s\perp}}{\rho B} \right) + \rho B \mathbf{u} \cdot \nabla \left( \frac{p_{s\perp}}{\rho B} \right) = -\nabla \cdot (q_{s\perp} \mathbf{b}) - \\
&q_{s\perp} \nabla \cdot \mathbf{b} - \frac{1}{3} \nu_s (p_{s\perp} - p_{s\parallel}),
\end{aligned} \tag{5.1.36}$$

$$\begin{aligned}
&\frac{\rho^3}{B^2} \left( \frac{\partial}{\partial t} + \Omega \frac{\partial}{\partial \phi} \right) \left( \frac{p_{s\parallel} B^2}{\rho^3} \right) + \frac{\rho^3}{B^2} \mathbf{u} \cdot \nabla \left( \frac{p_{s\parallel} B^2}{\rho^3} \right) = -\nabla \cdot (q_{s\parallel} \mathbf{b}) - \\
&2q_{s\perp} \nabla \cdot \mathbf{b} - \frac{2}{3} \nu_s (p_{s\parallel} - p_{s\perp}).
\end{aligned} \tag{5.1.37}$$



Using Eqs. (5.1.20) and (5.1.27), Eqs. (5.1.31) and (5.1.32) can be written as,

$$\begin{aligned} & \left( \frac{d}{dt} + \frac{5}{3} \nabla \cdot \mathbf{u} + \mathbf{b} \cdot \nabla \mathbf{u} \cdot \mathbf{b} + R b_\phi \mathbf{b} \cdot \nabla \Omega + \nu_s \right) q_s + \\ & \left( \mathbf{b} \cdot \nabla \mathbf{u} \cdot \mathbf{b} - \frac{1}{3} \nabla \cdot \mathbf{u} + R b_\phi \mathbf{b} \cdot \nabla \Omega \right) q_{sv} = \\ & - \nabla \cdot \left( \mathbf{b} \left[ \frac{1}{2} r_{s\parallel} + r_{s\times} \right] \right) + \left( \frac{1}{2} r_{s\times} + r_{s\perp} \right) \nabla \cdot \mathbf{b} + \end{aligned} \quad (5.1.38)$$

$$\begin{aligned} & \frac{5p_s}{2n_s m_s} \mathbf{b} \cdot \nabla p_s + \frac{5p_s}{3n_s m_s} \mathbf{b} \cdot \nabla p_{sv} + \frac{5p_{sv}}{3n_s m_s} \mathbf{b} \cdot \nabla \left( p_s + \frac{2}{3} p_{sv} \right) - \\ & \frac{(p_s + \frac{8}{3} p_{sv}) p_{sv}}{2n_s m_s} \nabla \cdot \mathbf{b}, \\ & \left( \frac{\partial}{\partial t} + \Omega \frac{\partial}{\partial \phi} + 2\mathbf{b} \cdot \nabla \mathbf{u} \cdot \mathbf{b} + 2R b_\phi \mathbf{b} \cdot \nabla \Omega + \frac{1}{3} \nabla \cdot \mathbf{u} + \nu_s \right) q_{sv} + \\ & 2 \left( \mathbf{b} \cdot \nabla \mathbf{u} \cdot \mathbf{b} + R b_\phi \mathbf{b} \cdot \nabla \Omega - \frac{1}{3} \nabla \cdot \mathbf{u} \right) q_s = - \nabla \cdot (q_{sv} \mathbf{u}) - \\ & \nabla \cdot (\mathbf{b} [r_{s\parallel} - r_{s\times}]) + (4r_{s\times} - r_{s\perp}) \nabla \cdot \mathbf{b} + \frac{2p_s}{n_s m_s} \mathbf{b} \cdot \nabla p_s + \\ & \frac{7p_{sv}}{3n_s m_s} \mathbf{b} \cdot \nabla \left( p_s + \frac{2}{3} p_{sv} \right). \end{aligned} \quad (5.1.39)$$

For sufficiently high collisionality, we can consider a subsidiary fluid ordering of the plasma distribution function,

$$f_s^0 = \frac{n_s}{(2\pi k_B T_s / m_s)^{3/2}} \exp \left( -\frac{m_s v_\parallel^2 + 2m_s \mu B}{2k_B T_s} \right) + \delta_1 f_s^0 + \dots \quad (5.1.40)$$

where  $T_{s\parallel} \approx T_{s\perp} = T_s$ .  $\delta_1 f_s^0$  refers to deviations of the zeroth-order distribution function from Maxwellian of order  $\nu_s^{-1}$ . Then, to lowest order in  $\nu_s^{-1}$ , the fourth-order moments of the distribution function are then given by,

$$r_{s\parallel} = 3n k_B T_s \frac{k_B T_s}{m_s}, \quad (5.1.41)$$

$$r_{s\times} = n k_B T_s \frac{k_B T_s}{m_s}, \quad (5.1.42)$$

$$r_{s\perp} = 2n k_B T_s \frac{k_B T_s}{m_s}. \quad (5.1.43)$$

From Eqs. (5.1.35), (5.1.38), and (5.1.39), if we substitute Eqs. (5.1.41) - (5.1.43), then to lowest order in  $\nu_s^{-1}$ , the viscous pressure  $p_{sv}$  and heat fluxes  $q_s$  and  $q_{sv}$  are given by,

$$p_{sv} \approx -\frac{3p_s}{\nu_s} \left( \mathbf{b} \cdot \nabla \mathbf{u} \cdot \mathbf{b} + Rb_\phi \mathbf{b} \cdot \nabla \Omega - \frac{1}{3} \nabla \cdot \mathbf{u} \right), \quad (5.1.44)$$

$$q_s \approx -\frac{5nk_B T_s}{2m_s \nu_s} \mathbf{b} \cdot \nabla (k_B T_s), \quad (5.1.45)$$

$$q_{sv} \approx -\frac{2nk_B T_s}{m_s \nu_s} \mathbf{b} \cdot \nabla (k_B T_s), \quad (5.1.46)$$

These differ from the expressions for the viscous pressure and thermal conductivity given in Braginskii (1965) by factors of order unity.

### 5.1.3 Full Force Balance

We note that Eq. (5.1.23) only describes force balance parallel to the magnetic field, Eq. (5.1.28). In order to describe total force balance, we consider Eq. (5.1.1) with the excess electric field defined as,

$$\Delta \mathbf{E} = E_\parallel \mathbf{b} + \delta \mathbf{E}_{\text{ES}}, \quad (5.1.47)$$

where  $\delta \mathbf{E}_{\text{ES}} = \mathbf{E}_{\text{ES}} - \mathbf{E}_{0,\text{ES}}$ . To first order in the distribution function we have,

$$\begin{aligned} \frac{\partial f_s^0}{\partial t} + \mathbf{U} \cdot \nabla f_s^0 + \left( \frac{Z_s e}{m_s} \Delta \mathbf{E} - \Omega^2 R + \frac{1}{m_s n_{s0}} \mathbf{b} \cdot \nabla p_{s0} \right) \cdot \frac{\partial f_s^0}{\partial \mathbf{U}} + \\ \frac{Z_s e}{m_s} \left( -\frac{1}{c} \mathbf{u} \times \mathbf{B} - \frac{1}{c} R \Omega \hat{\phi} \times \mathbf{B} + \frac{1}{c} \mathbf{v} \times \mathbf{B} \right) \cdot \frac{\partial f_s^1}{\partial \mathbf{U}} = C[f_s^0]. \end{aligned} \quad (5.1.48)$$

Using the velocity transformation,

$$\mathbf{U} = \mathbf{v} + R \Omega \hat{\phi} + \mathbf{u}, \quad (5.1.49)$$

we reduce Eq. (5.1.48) to,

$$\begin{aligned} & \left( \frac{\partial}{\partial t} + \Omega \frac{\partial}{\partial \phi} \right) f_s^0 + \mathbf{u} \cdot \nabla f_s^0 + \mathbf{v} \cdot \nabla f_s^0 + \frac{Z_s e}{m_s c} (\mathbf{v} \times \mathbf{B}) \cdot \frac{\partial f_s^1}{\partial \mathbf{v}} - \\ & \frac{\partial f_s^0}{\partial \mathbf{v}} \cdot \left( \frac{\partial \mathbf{u}}{\partial t} + (R\Omega \hat{\phi} + \mathbf{v} + \mathbf{u}) \cdot \nabla (R\Omega \hat{\phi} + \mathbf{u}) - \right. \\ & \left. \frac{Z_s e}{m_s} \Delta \mathbf{E} + \Omega^2 R \hat{\mathbf{R}} + \frac{1}{m_s n_{s0}} \nabla p_{s0} \right) = 0, \end{aligned} \quad (5.1.50)$$

where we use moments of the distribution function in terms of  $\mathbf{v}$ , given by,

$$\begin{aligned} & \int f_s^0 d^3 \mathbf{v} = n_s, \\ & \int f_s^0 \mathbf{v} d^3 \mathbf{v} = \mathbf{0}, \\ & m_s \int f_s^0 \mathbf{v} \mathbf{v} d^3 \mathbf{v} = \mathbb{P}_s = p_{s\perp} \mathbb{I} + (p_{s\parallel} - p_{s\perp}) \mathbf{b} \mathbf{b}. \end{aligned} \quad (5.1.51)$$

Taking the moment of Eq. (5.1.50) with respect to  $\mathbf{v}$ , and using moments given by Eq. (5.1.51), we arrive at the comoving species force balance equation:

$$\begin{aligned} & m_s n_s \left( \left[ \frac{\partial}{\partial t} + \Omega \frac{\partial}{\partial \phi} \right] \mathbf{u} + \mathbf{u} \cdot \nabla \mathbf{u} - 2\Omega \mathbf{u} \times \hat{\mathbf{z}} + R \mathbf{u} \cdot \nabla \Omega \hat{\phi} \right) + \nabla \cdot \mathbb{P}_s = \\ & \frac{1}{c} \left( Z_s e \int f_s^1 \mathbf{v} d^3 \mathbf{v} \right) \times \mathbf{B} - \frac{1}{c} (\mathbf{u} \times \mathbf{B}) \left( \int Z_s e \int f_s^1 d^3 \mathbf{v} \right) + \\ & Z_s e n_s \Delta \mathbf{E} + \frac{n_s}{n_{s0}} \nabla p_{s0}. \end{aligned} \quad (5.1.52)$$

Currents and charges appear at first order in the distribution function,

$$\mathbf{J} = e \int (f_i^1 - f_e^1) \mathbf{v} d^3 \mathbf{v}, \quad (5.1.53)$$

$$\rho_q = e \int (f_i^1 - f_e^1) d^3 \mathbf{v}. \quad (5.1.54)$$

If we add Eq. (5.1.52) for ions and electrons, and substitute in Eqs. (5.1.53) and (5.1.54), we derive the MHD force balance equation in the local rotating frame,

Eq. (1.2.6). Dotting Eq. (1.2.6) with  $\mathbf{b}$  yields the force balance equation parallel to the magnetic field, Eq. (5.1.28). We ignore the contribution  $\rho_q \mathbf{u}$  in the above equation since our plasma is nonrelativistic – specifically the Alfvén speed is smaller than the speed of light.

## 5.2 Perturbed Axisymmetric Distribution Function at the Midplane

Consider an equilibrium particle distribution given by Eq. (5.1.24). Assume equal scale heights of radial ion and electron temperature gradients, so that  $\partial \ln T_{i0}/\partial R = \partial \ln T_{e0}/\partial R = \partial \ln T_0/\partial R$ . For small perturbations of the particle distribution function and of the electromagnetic field, at the disk midplane Eq. (5.1.23) reduces to,

$$\delta f_i = \frac{m_p v_{\parallel}}{k_B T_{i0}} \left( \frac{-ik_{\parallel} \mu \delta B + e \delta E_{\parallel}/m_p}{\Gamma + ik_{\parallel} v_{\parallel}} - \frac{(2\Omega + \Omega' R) \Gamma \cos \chi \delta \bar{B}_R + ik_{\parallel} v_{\parallel} \Omega' R \cos \chi \delta \bar{B}_R}{ik_{\parallel} (\Gamma + ik_{\parallel} v_{\parallel})} \right) f_{i0}^0 - \quad (5.2.1)$$

$$\frac{f_{i0}^0 \delta \bar{B}_R}{ik_{\parallel}} \left( \frac{\partial \ln \rho_0}{\partial R} - \frac{3}{2} \frac{\partial \ln T_0}{\partial R} + \left( \frac{m_p \mu B_0}{k_B T_{i0}} + \frac{m_p v_{\parallel}^2}{2k_B T_{i0}} \right) \frac{\partial \ln T_0}{\partial R} \right) + \frac{\delta \bar{B}_R v_{\parallel} \partial \ln p_0 / \partial R}{\Gamma + ik_{\parallel} v_{\parallel}} f_{i0}^0,$$

$$\delta f_e = \frac{m_e v_{\parallel}}{k_B T_{e0}} \left( \frac{-ik_{\parallel} \mu \delta B - e \delta E_{\parallel}/m_e}{\Gamma + ik_{\parallel} v_{\parallel}} - \frac{(2\Omega + \Omega' R) \Gamma \cos \chi \delta \bar{B}_R + ik_{\parallel} v_{\parallel} \Omega' R \cos \chi \delta \bar{B}_R}{ik_{\parallel} (\Gamma + ik_{\parallel} v_{\parallel})} \right) f_{e0}^0 - \quad (5.2.2)$$

$$\frac{f_{e0}^0 \delta \bar{B}_R}{ik_{\parallel}} \left( \frac{\partial \ln \rho_0}{\partial R} - \frac{3}{2} \frac{\partial \ln T_0}{\partial R} + \left( \frac{m_e \mu B_0}{k_B T_{e0}} + \frac{m_e v_{\parallel}^2}{2k_B T_{e0}} \right) \frac{\partial \ln T_0}{\partial R} \right) + \frac{\delta \bar{B}_R v_{\parallel} \partial \ln p_0 / \partial R}{\Gamma + ik_{\parallel} v_{\parallel}} f_{e0}^0.$$

Terms with  $\Omega$  arise due to the fact that the plasma is rotating. Terms with equilibrium gradients of temperature, density, or pressure may drive convective and free energy gradient instabilities.  $\delta E_{\parallel}$  is the electric field that ensures quasineutrality, i.e.  $n_i = n_e = n$ . In the limit  $T_{i0} \geq T_{e0}$ , the electric field  $\delta E_{\parallel}$  and electron quantities (such as  $\delta p_{e\perp}$  and  $\delta p_{e\parallel}$ ) become unimportant in the plasma dynamics. This is the simplification employed by Quataert et al. (2002) and Sharma et al. (2003). In Appendix D.2 we see that the resulting dispersion relation calculated with equal ion and electron temperatures is not significantly different from that where the ions are orders of magnitude hotter than the electrons.

Using the induction equation (Eq. [5.1.3]) and the continuity equation (Eq. [5.1.27]), the total force balance equation, Eq. (1.2.6), becomes,

$$\begin{aligned} & \gamma^2 \delta \bar{\mathbf{B}} - \gamma^2 \mathbf{b}_0 \left( \delta \bar{\rho} - \frac{\alpha_P - \alpha_T}{ix\beta^{1/2}} \delta \bar{B}_R \right) + 2 \frac{d \ln \Omega}{d \ln R} \delta \bar{B}_R \hat{\mathbf{R}} + \\ & 2\gamma \cos \chi \left( \delta \bar{\rho} - \frac{\alpha_P - \alpha_T}{ix\beta^{1/2}} \delta \bar{B}_R \right) \hat{\mathbf{R}} + 2\gamma \hat{\mathbf{z}} \times \delta \bar{\mathbf{B}} = \hat{\mathbf{k}} x \beta \frac{\delta p_{\perp}}{p_0} + \quad (5.2.3) \\ & x^2 \beta \frac{\delta p_{\parallel} - \delta p_{\perp}}{p_0} \mathbf{b}_0 - ix\beta^{1/2} \alpha_P \delta \bar{\rho} \hat{\mathbf{R}} - x^2 \delta \bar{\mathbf{B}} + \hat{\mathbf{k}} x \frac{\delta B}{B_0}, \end{aligned}$$

where  $\delta B/B_0 = \delta \bar{B}_{\phi} \cos \chi - (k_R/k_Z) \delta \bar{B}_R \sin \chi$ ,  $\delta p_{\parallel} = \delta p_{i\parallel} + \delta p_{e\parallel}$ , and  $\delta p_{\perp} = \delta p_{i\perp} + \delta p_{e\perp}$ . Contributions due to  $\delta \bar{\rho} - (\alpha_P - \alpha_T) / (ix\beta^{1/2}) \delta \bar{B}_R$  arise from finite plasma compressibility. The eigenvalue problem consists of three equations: one for radial force balance, one for azimuthal force balance, and one for force balance along the

equilibrium magnetic field. These are,

$$\begin{aligned} & \left( \gamma^2 + x^2 \left[ 1 + \frac{k_R^2}{k_Z^2} \right] + 2 \frac{d \ln \Omega}{d \ln R} - 2\gamma \cos \chi \frac{\alpha_P - \alpha_T}{ix\beta^{1/2}} \right) \delta \bar{B}_R - \\ & \left( 2\gamma + x^2 \frac{\cos \chi}{\sin \chi} \frac{k_R}{k_Z} \right) \delta \bar{B}_\phi + \delta \bar{\rho} (2\gamma \cos \chi + ix\beta^{1/2} \alpha_P) = \frac{k_R}{k_Z \sin \chi} x^2 \beta \frac{\delta p_\perp}{p_0}, \end{aligned} \quad (5.2.4)$$

$$\begin{aligned} & \left( \gamma^2 \cos \chi \frac{\alpha_P - \alpha_T}{ix\beta^{1/2}} + 2\gamma \right) \delta \bar{B}_R + (\gamma^2 + x^2) \delta \bar{B}_\phi - \gamma^2 \cos \chi \delta \bar{\rho} = \\ & x^2 \cos \chi \beta \frac{\delta p_\parallel - \delta p_\perp}{p_0}, \end{aligned} \quad (5.2.5)$$

$$\begin{aligned} & \delta \bar{B}_R \left( \gamma^2 \frac{\alpha_P - \alpha_T}{ix\beta^{1/2}} - \gamma^2 \frac{k_R}{k_Z} \sin \chi + 2\gamma \cos \chi \right) + \gamma^2 \cos \chi \delta \bar{B}_\phi - \\ & \gamma^2 \delta \bar{\rho} = x^2 \beta \frac{\delta p_\parallel}{p_0}, \end{aligned} \quad (5.2.6)$$

where  $\delta p_\perp$  and  $\delta p_\parallel$  are linear functions of  $\delta \bar{B}_R$ ,  $\delta \bar{B}_\phi$ , and  $\delta \bar{\rho}$ . We work in the limit of small electron thermal energies, hence  $\theta_0 \rightarrow v_i$  and  $\delta E_\parallel \rightarrow 0$ , where, from Tab. (A.1),  $v_i = \sqrt{k_B T_{i0}/m_p}$  is the ion isothermal sound speed. For the treatment of the collisionless rotational MTI, we choose a Schwarzschild stable stratified medium, in which  $\alpha_S \leq 0$  or equivalently  $\alpha_T \leq \frac{2}{5} \alpha_P$ .

### 5.2.1 Dispersion Relations of the Collisionless MRI and MTI

In this section we derive the dispersion relations of the collisionless MRI (Quataert et al. 2002) and the collisionless MTI. Its dispersion relation in the fluid limit has been studied by Balbus (2001). We demonstrate the salient feature of these dispersion relations, namely collisionless damping of long wavelength modes along the magnetic field lines,  $k_\parallel < \Omega/v_i$ .

From Eq. (5.2.1),  $\delta p_\perp$ ,  $\delta p_\parallel$ , and  $\delta \bar{\rho}$  are given by,

$$\begin{aligned} \frac{\delta p_\perp}{p_{i0}} = & 2 \frac{\delta B}{B_0} + 2\pi (p_{i0})^{-1} \int \delta f_i^0 \mu B^2 d\mu dv_\parallel = \frac{\delta \bar{B}_R}{ik_\parallel} \left( \frac{\partial \ln p_0}{\partial R} \right) \times \\ & (R(i\zeta_i) - 1) - \frac{2\delta B}{B} (R(i\zeta_i) - 1) + \frac{2\Omega\Gamma}{k_\parallel^2 v_i^2} \delta \bar{B}_R \cos \chi R(i\zeta_i), \end{aligned} \quad (5.2.7)$$

$$\begin{aligned} \frac{\delta p_\parallel}{p_{i0}} = & - \frac{2\delta \bar{B}_R}{ik_\parallel} \left( \frac{\partial \ln p_0}{\partial R} \right) \zeta_i^2 R(i\zeta_i) + \frac{2\delta B}{B} \zeta_i^2 R(i\zeta_i) + \\ & \frac{2\Omega\Gamma}{k_\parallel^2 v_i^2} \delta \bar{B}_R \cos \chi (1 - 2\zeta_i^2 R(i\zeta_i)), \end{aligned} \quad (5.2.8)$$

$$\begin{aligned} \delta \bar{\rho} = & - \frac{\delta B}{B_0} (R(i\zeta_i) - 1) + \frac{\delta \bar{B}_R}{ik_\parallel} \left( \frac{\partial \ln p_0}{\partial R} \right) R(i\zeta_i) - \\ & \frac{\delta \bar{B}_R}{ik_\parallel} \left( \frac{\partial \ln \rho_0}{\partial R} \right) + \frac{2\Omega\Gamma}{k_\parallel^2 v_i^2} \delta \bar{B}_R \cos \chi R(i\zeta_i). \end{aligned} \quad (5.2.9)$$

There are terms associated with rotation (terms proportional to  $\Omega$  and  $\Omega'R$ ) and finite equilibrium gradients in density and temperature. The phase velocity normalized to the ion isothermal sound speed is  $\zeta_i = \Gamma / (k_\parallel v_i \sqrt{2})$ . The plasma response function  $R(\zeta)$  is defined as,

$$R(\zeta) = \frac{1}{\sqrt{\pi}} \int_{-\infty}^{\infty} \frac{x e^{-x^2}}{x - \zeta} dx, \quad (5.2.10)$$

By substituting the rotational term  $2\Omega\Gamma / (k_\parallel^2 v_i^2)$  for  $\delta \bar{\rho}$ , we rearrange Eqs. (5.2.7) - (5.2.9) into the following expressions for  $\delta p_\perp$  and  $\delta p_\parallel$ ,

$$\frac{\delta p_\perp}{p_{i0}} = \delta \bar{\rho} - \frac{\delta B}{B_0} (R(i\zeta_i) - 1) + \frac{\delta \bar{B}_R}{ik_\parallel} \left( \frac{\partial \ln \rho_0}{\partial R} - \frac{\partial \ln p_0}{\partial R} \right), \quad (5.2.11)$$

$$\begin{aligned} \frac{\delta p_\parallel}{p_{i0}} = & \left( \frac{1 - 2\zeta_i^2 R(i\zeta_i)}{R(i\zeta_i)} \right) \delta \bar{\rho} - \left( \frac{1 - [1 + 2\zeta_i^2] R(i\zeta_i)}{R(i\zeta_i)} \right) \frac{\delta B}{B_0} + \\ & \frac{\delta \bar{B}_R}{ik_\parallel} \left( \frac{1 - 2\zeta_i^2 R(i\zeta_i)}{R(i\zeta_i)} \times \frac{\partial \ln \rho_0}{\partial R} - \frac{\partial \ln p_0}{\partial R} \right). \end{aligned} \quad (5.2.12)$$

In the limit  $|\zeta_i| \gg 1$ ,

$$R(i\zeta_i) = \frac{1}{2\zeta_i^2} - \frac{3}{4\zeta_i^4} + \frac{15}{8\zeta_i^6} + \mathcal{O}(1/\zeta_i^8). \quad (5.2.13)$$

In this limit, the pressure responses reduce to the double-adiabatic limit (Chew et al. 1956) with equilibrium pressure gradients,

$$\frac{\delta p_{\parallel}}{p_{i0}} \rightarrow \frac{\delta B}{B_0} + \delta \bar{\rho} - \xi_R \frac{\partial \ln T_0}{\partial R}, \quad (5.2.14)$$

$$\frac{\delta p_{\perp}}{p_{i0}} \rightarrow 3\delta \bar{\rho} - 2\frac{\delta B}{B_0} + \xi_R \left( 3\frac{\partial \ln \rho_0}{\partial R} - \frac{\partial \ln p_0}{\partial R} \right). \quad (5.2.15)$$

In the limit  $|\zeta_i| \ll 1$ ,

$$R(i\zeta_i) = 1 - \zeta_i \sqrt{\pi} + \mathcal{O}(\zeta_i^2). \quad (5.2.16)$$

The phase velocity of the collisionless MRI and MTI modes  $\sim v_i$ , i.e.  $|\zeta_i| \sim 1$ . These perturbations are not adiabatic and the slow wave limit,  $|\zeta_i| \ll 1$ , holds for most unstable wavenumbers. The expressions for perturbed pressures up to first order in  $\zeta_i$  are,

$$\frac{\delta p_{\parallel}}{p_{i0}} \rightarrow \delta \bar{\rho} + \sqrt{\pi} \zeta_i \frac{\delta B}{B_0} - \xi_R \frac{\partial \ln T_0}{\partial R}, \quad (5.2.17)$$

$$\frac{\delta p_{\perp}}{p_{i0}} \rightarrow \delta \bar{\rho} - \sqrt{\pi} \zeta_i \frac{\delta B}{B_0} + \xi_R \left( 3\frac{\partial \ln \rho_0}{\partial R} - \frac{\partial \ln p_0}{\partial R} \right). \quad (5.2.18)$$

Dispersion relations for the collisionless MRI and MTI are shown in Figs. (5.2.1) - (5.2.3), The primary feature of the plasma response via the MRI and MTI is collisionless damping of long wavelength modes  $k_{\parallel} < \Omega/v_i$ . This feature has been noted in previous studies of the collisionless MRI (Quataert et al. 2002; Sharma et al. 2003). This damping has the effect of suppressing pressure variations at small wavenum-



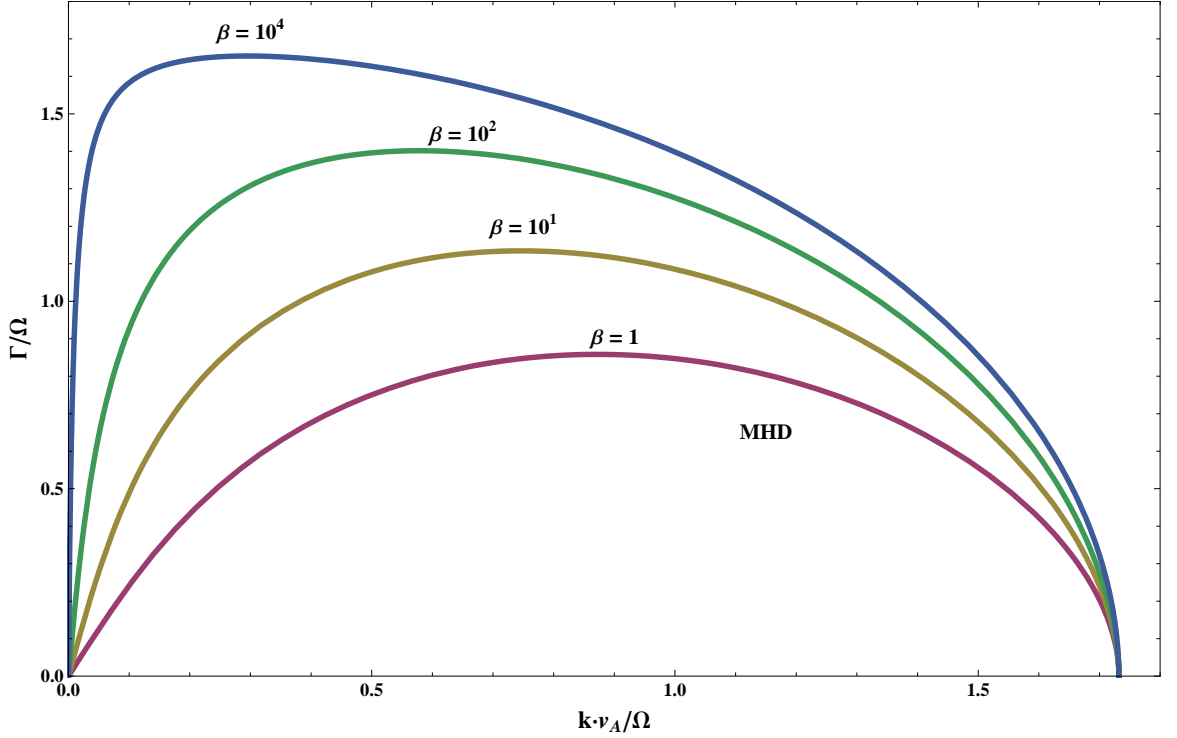


Fig. 5.2.1.— The growth rate for nonradial wavenumbers for the collisionless MRI, with a Keplerian-like rotation profile,  $\chi = \pi/4$ , and varying  $\beta$ . We see a turnover where the phase velocity of the wave becomes sonic at wavenumbers  $k_{\parallel}v_i \simeq \Omega$ .

bers. Therefore, as the plasma  $\beta \rightarrow 1$ , the anisotropic pressure becomes dynamically unimportant,  $|\delta p_{\parallel} - \delta p_{\perp}| \ll \delta p_{\parallel}$ , and we reproduce purely MHD phenomena without collisionless viscous or thermal transport. Also, as  $\beta \rightarrow 1$  the effects of finite compressibility become dynamically important. In Figs. (5.2.4) and (5.2.5) we see that the collisionless MTI approaches the compressible MHD limit as  $\beta \rightarrow 1$ . We take a Keplerian profile,  $\alpha_P = 5$ ,  $\alpha_T = 2$ , and  $\chi = \pi/4$ . The real part of the growth rate, in Fig. (5.2.4), is suppressed as  $\beta \rightarrow 1$ . The imaginary part of the growth rate, in Fig. (5.2.5), becomes more compressible as  $\beta \rightarrow 1$ .

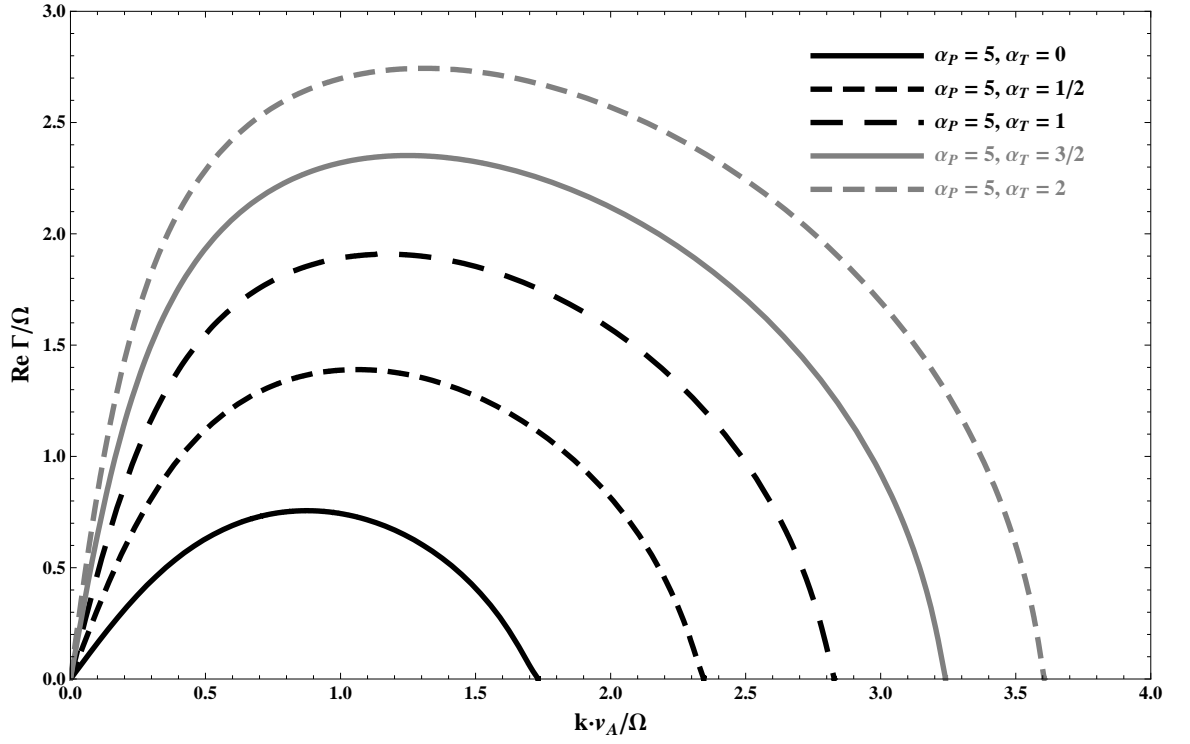


Fig. 5.2.2.— The real part of the growth rate for nonradial wavenumbers, with a Keplerian-like rotation profile,  $\beta = 10^2$ ,  $\chi = \pi/4$ , and various equilibrium gradients of pressure and temperature. We set  $\alpha_P = 5$  and vary  $\alpha_T \leq 2$ .

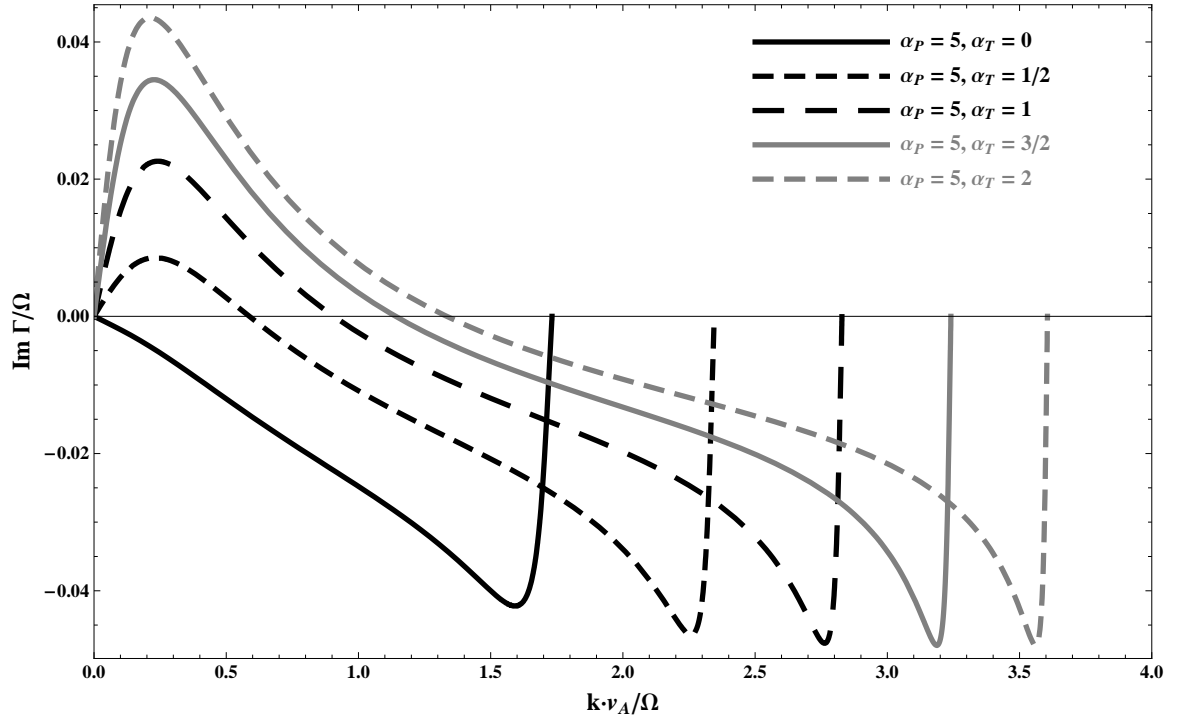


Fig. 5.2.3.— The imaginary part of the growth rate for nonradial wavenumbers, with a Keplerian-like rotation profile,  $\beta = 10^2$ ,  $\chi = \pi/4$ , and various equilibrium gradients of pressure and temperature. We set  $\alpha_P = 5$  and vary  $\alpha_T \leq 2$ .

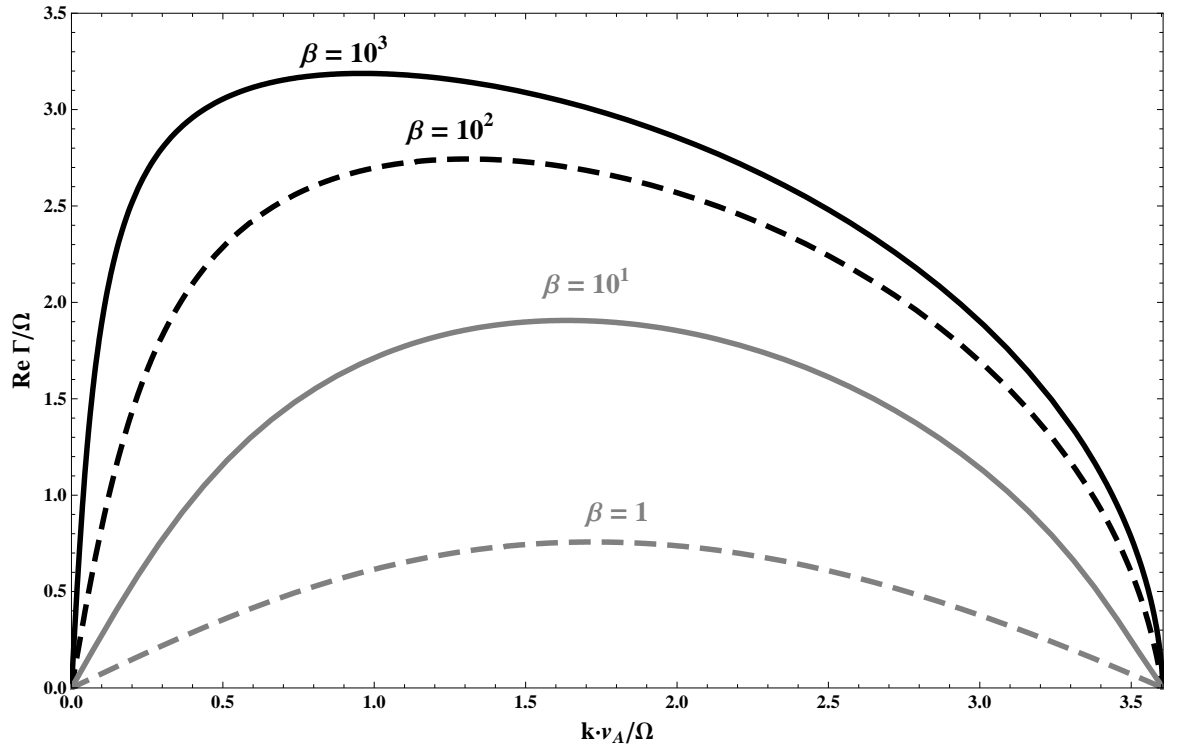


Fig. 5.2.4.— The real component of the growth rate for various  $\beta$ ,  $\chi = \pi/4$ , and a marginally Schwarzschild stable Keplerian-like rotating flow. For large  $\beta$  we reproduce MRI-like modes.

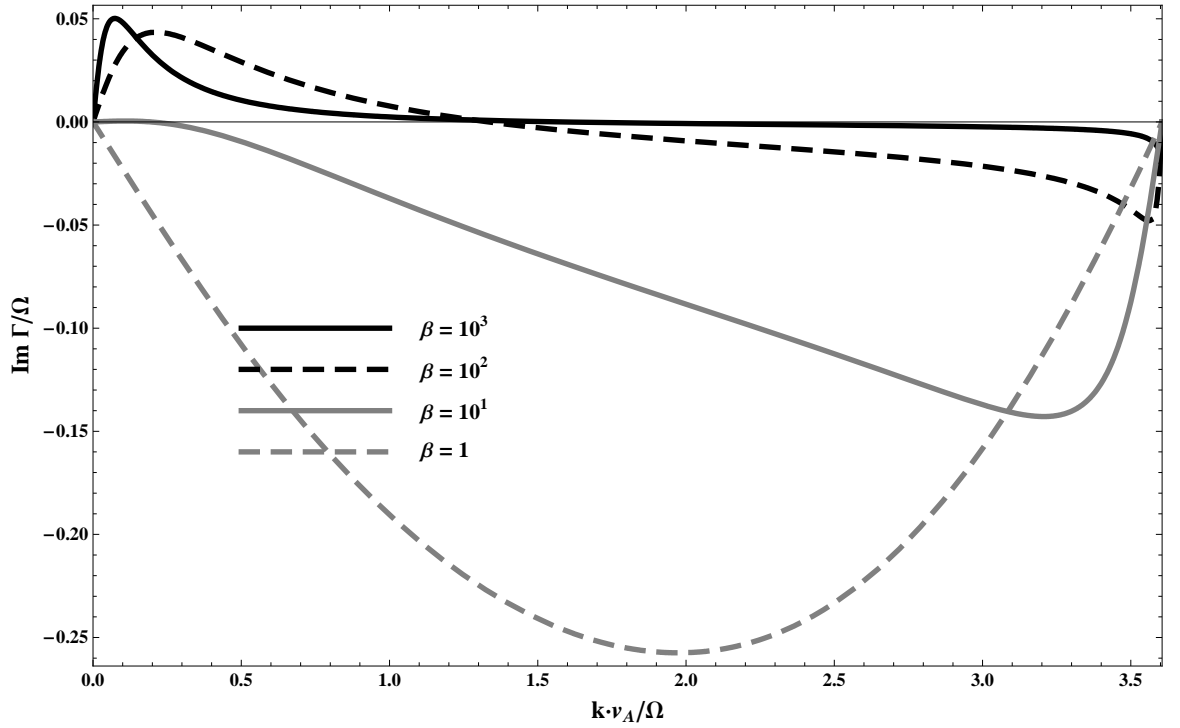


Fig. 5.2.5.— The imaginary component of the growth rate for various  $\beta$ ,  $\chi = \pi/4$ , and a marginally Schwarzschild stable Keplerian-like rotating flow. For large  $\beta$  the imaginary component reaches a maximum at those wavenumbers at which the growth rate of the instability saturates. As  $\beta \rightarrow 1$ , the imaginary component of the growth rate increases in magnitude.

Dispersion relations for the collisionless MRI and MTI are similar to their fluid counterparts, the MVI and the MVTI, respectively.

### 5.2.2 Quadratic Fluxes of Collisionless MRI and MTI

Here, we determine the normalized quadratic heat and angular momentum flux associated with a given collisionless MRI or MTI mode of purely vertical wavenumber  $k_Z$ . We express these fluxes in terms of  $\xi_R$ . Expressions for  $\langle F_{ER} \rangle$  and  $\langle T_{R\phi} \rangle$  for axisymmetric modes are given by,

$$\langle T_{R\phi} \rangle = \text{Re} \left( \rho_0 \delta u_R^* \delta u_\phi - v_A^2 \delta \bar{B}_R^* \delta \bar{B}_\phi + \cos \chi \delta \bar{B}_R^* \delta p_v \right), \quad (5.2.19)$$

$$\langle F_{ER} \rangle = \text{Re} \left( \frac{5}{2} \delta u_R^* \delta \theta - \delta q \delta \bar{B}_R^* - \frac{1}{3} \delta p_v \delta \bar{B}_R^* \right). \quad (5.2.20)$$

These expressions for quadratic fluxes due to collisionless modes are obtained from their fluid counterparts, Eqs. (4.3.1) and (4.3.2), by replacing  $\delta \sigma_{\mathbf{b}\mathbf{b}}$  with  $\delta p_v$ .

From Eq. (5.2.1) and the moment equations, Eq. (5.1.25), we have,

$$\delta u_{\parallel}/v_i = -i\zeta_i \sqrt{2} R (i\zeta_i) \left( \frac{\delta B}{B_0} - \frac{2\Omega\Gamma}{k_{\parallel}^2 v_i^2} \delta \bar{B}_R \cos \chi + \frac{i\delta \bar{B}_R}{k_{\parallel}} \left( \frac{\partial \ln p_0}{\partial R} \right) \right) + \quad (5.2.21)$$

$$\frac{i\delta \bar{B}_R}{k_{\parallel}} \cos \chi \Omega' R,$$

$$\delta q_{\parallel}/(p_{i0} v_i) = -3\delta u_{\parallel}/v_i + \frac{2\pi m_p}{p_{i0} v_i} \int v_{\parallel}^3 \delta f_i^0 B d\mu dv_{\parallel} = \left( i\zeta_i \sqrt{2} \left( \frac{\delta B}{B_0} \right) - \frac{\delta \bar{B}_R}{k_{\parallel}} \left( \frac{\partial \ln p_0}{\partial R} \right) \zeta_i \sqrt{2} - \frac{\Omega \zeta_i^2}{k_{\parallel} v_i} i\delta \bar{B}_R \cos \chi \right) \times \quad (5.2.22)$$

$$([2\zeta_i^2 + 3] R (i\zeta_i) - 1),$$

$$\delta q_{\perp}/(p_{i0} v_i) = -\delta u_{\parallel}/v_i + \frac{2\pi m_p}{p_{i0} v_i} \int v_{\parallel} \mu B^2 \delta f_i^0 d\mu dv_{\parallel} = -i\zeta_i \sqrt{2} \left( \frac{\delta B}{B_0} \right) R (i\zeta_i). \quad (5.2.23)$$

We substitute variables for pressure and heat flux, given in Eq. (5.1.33). We use expressions for the perturbed pressures, given in Eqs. (5.2.7) and (5.2.8), and heat fluxes, given in Eqs. (5.2.22) and (5.2.23).  $\delta\bar{\rho}$  and  $\delta\bar{B}_\phi$  are described in the eigenvalue equations (Eqs. [5.2.4] - [5.2.6]).  $\langle T_{R\phi} \rangle$  is normalized in units of  $\rho_0\Omega^2 |\xi_R|^2$ , and  $\langle F_{ER} \rangle$  is normalized in terms of  $p_0\Omega H^{-1} |\xi_R|^2$ . The modal expressions for  $\delta u_R$ ,  $\delta\bar{B}_R$ ,  $\delta\bar{B}_\phi$ , and  $\delta u_\phi$  in terms of  $\xi_R$  are,

$$\delta u_R = \gamma (\Omega \xi_R), \quad (5.2.24)$$

$$\delta\bar{B}_R = ix \left( \frac{\Omega}{v_A} \xi_R \right), \quad (5.2.25)$$

$$\delta\bar{B}_\phi = -ix \left( \frac{\Omega}{v_A} \xi_R \right) \times \frac{2\gamma \left( \sin^2 \chi + R \left( \frac{i\gamma}{x\sqrt{2\beta}} \cos^2 \chi \right) \right) - ix\beta^{1/2}\alpha_P \cos \chi \left[ R \left( \frac{i\gamma}{x\sqrt{2\beta}} \right) - 1 \right]}{\gamma^2 \left( \sin^2 \chi + R \left( \frac{i\gamma}{x\sqrt{2\beta}} \right) \cos^2 \chi \right) + x^2 - 2x^2\beta \cos^2 \chi \left[ \left( 1 + \frac{\gamma^2}{2x^2\beta} \right) R \left( \frac{i\gamma}{x\sqrt{2\beta}} \right) - 1 \right]} \quad (5.2.26)$$

$$\delta u_\phi = \frac{\gamma}{ix} v_A \delta\bar{B}_\phi \left( \sin^2 \chi + R \left( \frac{i\gamma}{x\sqrt{2\beta}} \right) \cos^2 \chi \right) + \Omega \xi_R \times \left( \left| \frac{d \ln \Omega}{d \ln R} \right| - \cos \chi \left[ \frac{2\gamma^2}{x^2\beta} \cos \chi + i\alpha_P \frac{\gamma}{x\beta^{1/2}} \right] R \left( \frac{i\gamma}{x\sqrt{2\beta}} \right) \right). \quad (5.2.27)$$

Using Eq. (5.1.33), and expressions for the perturbed heat fluxes as given in Eqs. (5.2.22)

and (5.2.23), we have expressions for  $\delta p_v$ ,  $\delta\theta$ , and  $\delta q$ :

$$\begin{aligned} \delta p_v = & (p_{i0} H^{-1} \xi_R) \left( \left[ \frac{\gamma^2}{x^2 \beta} - 1 \right] R \left( \frac{i\gamma}{x\sqrt{2\beta}} \right) + 1 \right) + \\ & 2 \left( p_{i0} \delta \bar{B}_\phi \cos \chi - i\beta^{-1} \frac{\gamma}{x} p_{i0} \xi_R \frac{\Omega}{v_A} \right) \left( \left[ 1 + \frac{\gamma^2}{2x^2 \beta} \right] R \left( \frac{i\gamma}{x\sqrt{2\beta}} \right) - 1 \right), \end{aligned} \quad (5.2.28)$$

$$\begin{aligned} \frac{\delta\theta}{\theta_0} = & \frac{\delta p}{p_{i0}} - \delta\bar{\rho} = (\xi_R H^{-1}) \left( \alpha_T + \alpha_P \left( \left[ \frac{5}{3} + \frac{\gamma^2}{3x^2 \beta} \right] R \left( \frac{i\gamma}{x\sqrt{2\beta}} \right) - \frac{5}{3} \right) \right) + \\ & \frac{1}{3} \delta \bar{B}_\phi \cos \chi \left( \left[ \frac{\gamma^2}{2x^2 \beta} - 1 \right] R \left( \frac{i\gamma}{x\sqrt{2\beta}} \right) + 1 \right) - \\ & \frac{2}{3} i\beta^{-1} \frac{\gamma}{x} \cos \chi \left( \frac{\Omega}{v_A} \xi_R \right) \left( \left[ 1 + \frac{\gamma^2}{x^2 \beta} \right] R \left( \frac{i\gamma}{x\sqrt{2\beta}} \right) - 1 \right), \end{aligned} \quad (5.2.29)$$

$$\begin{aligned} \delta q = & (p_{i0} \Omega \xi_R) \cos \chi \left( i\alpha_P \frac{\gamma}{x\beta^{1/2}} + \frac{2\gamma^2}{x^2 \beta} \right) \left( \left[ \frac{3}{2} + \frac{\gamma^2}{2x^2 \beta} \right] R \left( \frac{i\gamma}{x\sqrt{2\beta}} \right) - \frac{1}{2} \right) + \\ & i (p_{i0} v_i \delta \bar{B}_\phi) \frac{\gamma}{2x\beta^{1/2}} \cos \chi \left( \left[ 1 + \frac{\gamma^2}{x^2 \beta} \right] R \left( \frac{i\gamma}{x\sqrt{2\beta}} \right) - 1 \right), \end{aligned} \quad (5.2.30)$$

Figs. (5.2.6) and (5.2.7) are plots of normalized  $\langle T_{R\phi} \rangle$  and  $\langle F_{ER} \rangle$  for the collisionless MTI for different  $\alpha_T \leq \frac{2}{5} \alpha_P$ .



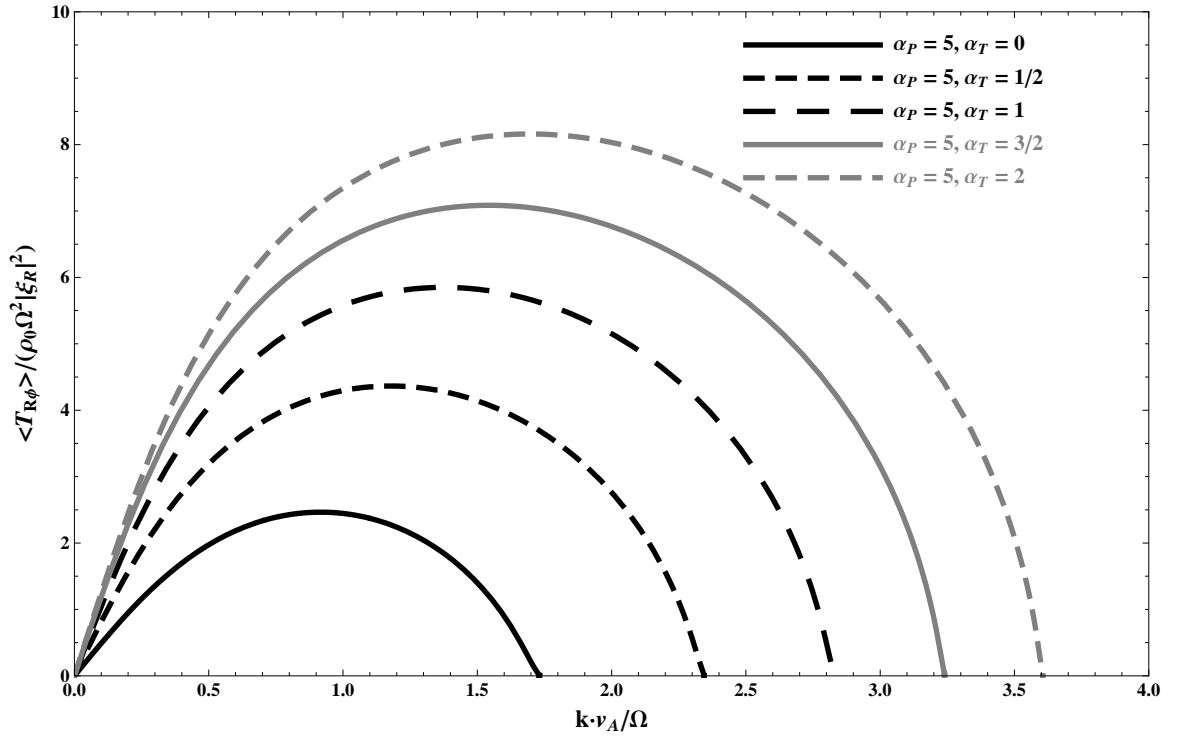


Fig. 5.2.6.— Normalized  $\langle T_{R\phi} \rangle$  for the collisionless MTI, for a Keplerian-like rotation profile,  $\beta = 10^2$ ,  $\chi = \pi/4$ ,  $\alpha_P = 5$ , and  $\alpha_T \leq 2$ .

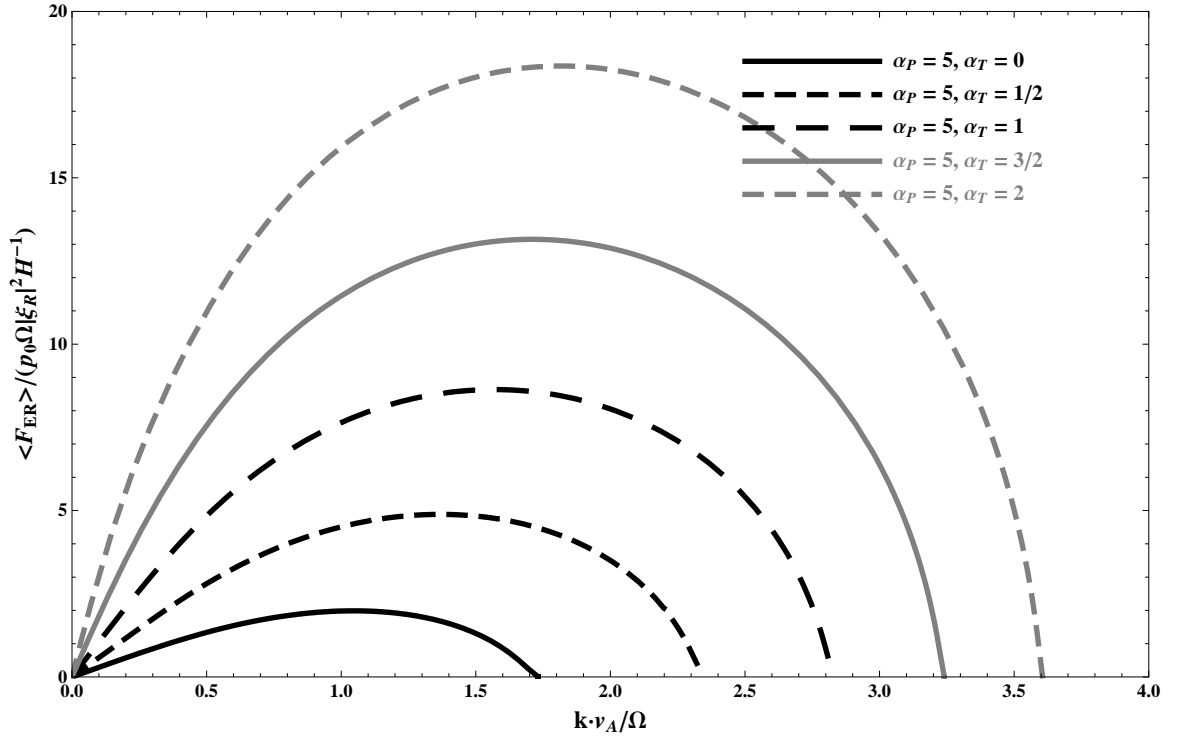


Fig. 5.2.7.— Normalized  $\langle F_{ER} \rangle$  for the collisionless MTI, for a Keplerian-like rotation profile,  $\beta = 10^2$ , and  $\chi = \pi/4$ , for various Schwarzschild stable equilibrium profiles with  $\alpha_P = 5$  and  $\alpha_T \leq 2$ .

Fig. (5.2.8) is a plot of the normalized quadratic angular momentum flux for the collisionless MRI for various  $\beta \geq 1$ . There is no equilibrium radial gradient of temperature or density, and the growth rate is real. For a purely unstable mode the temperature and viscous pressure perturbations are out of phase with the perturbed radial velocity, and the perturbed heat flux is out of phase with the perturbed radial magnetic field. Therefore, the heat flux for the collisionless MRI is zero.

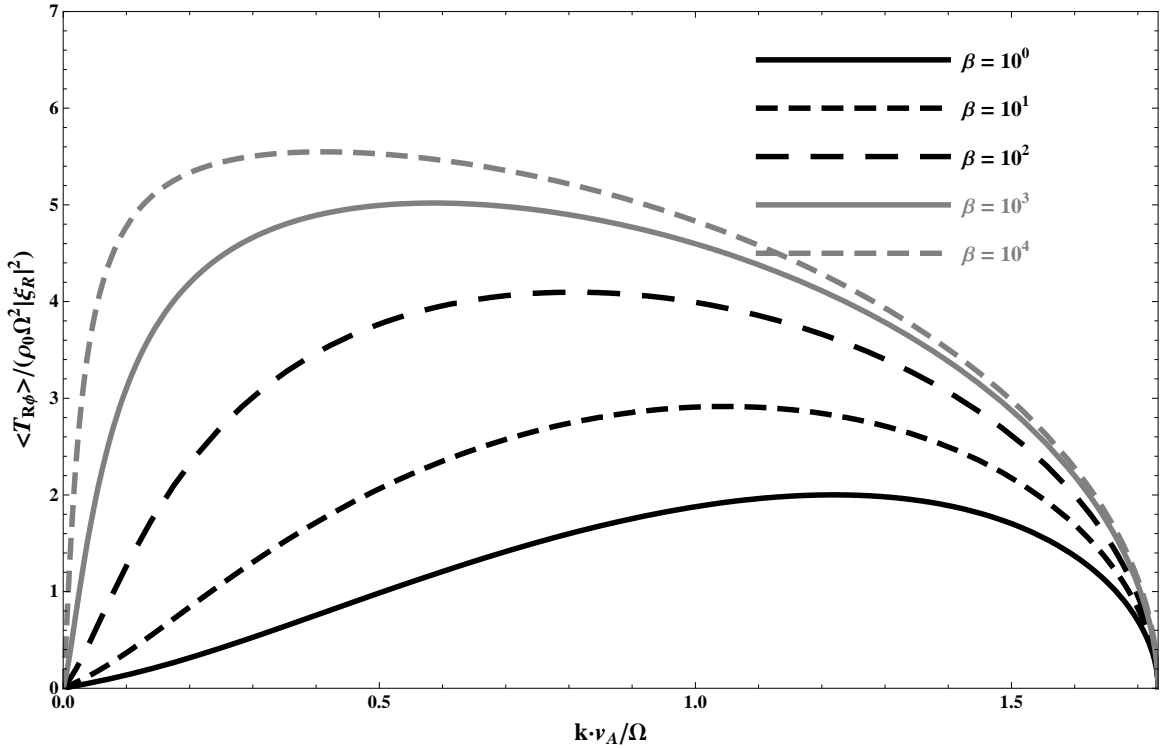


Fig. 5.2.8.— Normalized quadratic angular momentum flux for the collisionless MRI, for a Keplerian-like rotation profile,  $1 \leq \beta \leq 10^4$ , and  $\chi = \pi/4$ .

The collisionless MTI produces outward heat and angular momentum flux that can drive accretion in radiatively inefficient rotating plasmas. Furthermore, even in the absence of rotational shear  $\Omega'R = 0$  the effects of a heat flux can also transport angular momentum outwards, which is demonstrated in Fig. (5.2.9). The same qualitative behavior is seen for the MVTI in a rigidly rotating plasma, demonstrated in Fig. (4.3.5).

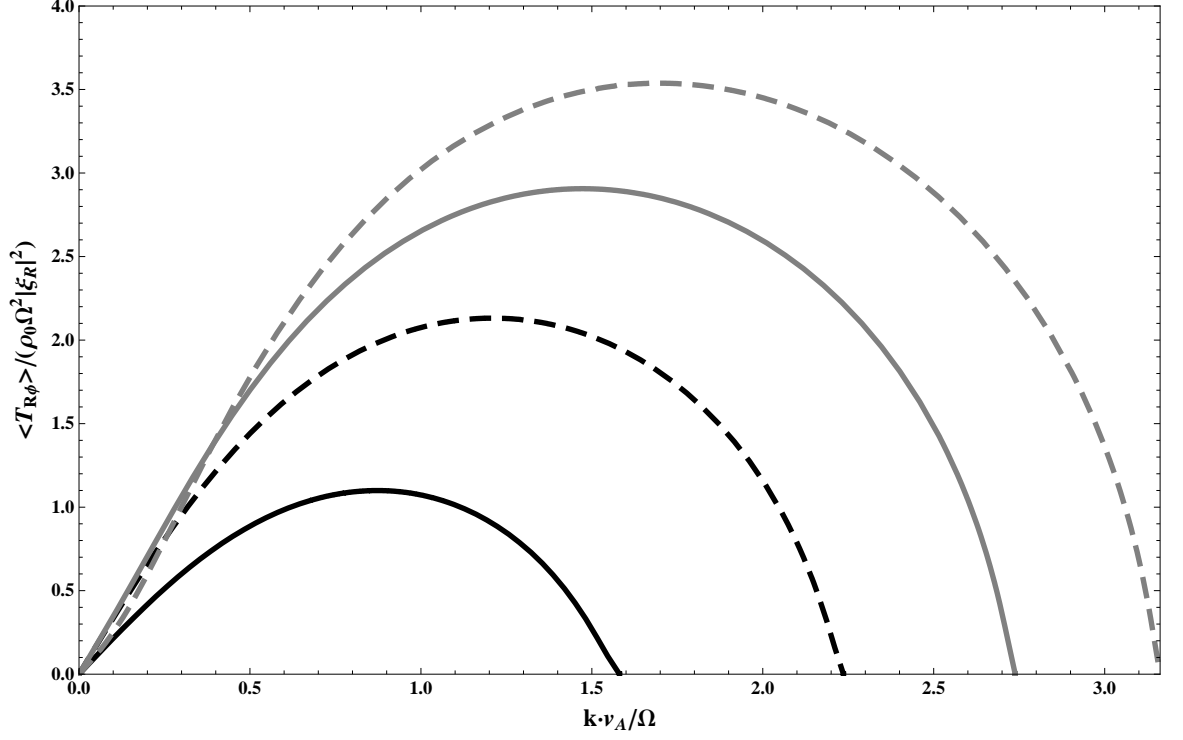


Fig. 5.2.9.— The normalized quadratic angular momentum flux for the collisionless MTI and zero rotational shear. Plasma  $\beta = 10^2$  and  $\alpha_P = 5$ . The innermost curve has  $\alpha_T = 1/2$ , the next curve has  $\alpha_T = 1$ , the third has  $\alpha_T = 3/2$ , and the outermost curve has  $\alpha_T = 2$ .

### 5.3 Finite Collisionality

We now consider the perturbed distribution functions with finite collisionality. From Eq. (5.1.22), the perturbed collisional operator is,

$$\delta C(f_s^0) = \nu_s (\delta f_s - \delta \langle f_s^0 \rangle), \quad (5.3.1)$$

where,

$$\delta \langle f_s^0 \rangle = f_{s0}^0 \left( \frac{\delta n_s}{n_{s0}} - \frac{\delta T_{s\parallel}/2 + \delta T_{s\perp}}{T_{s0}} + \left[ \frac{m_s \mu B_0}{k_B T_{s0}} + \frac{m_s v_{\parallel}^2}{2k_B T_{s0}} \right] \times \right. \\ \left. \left[ \frac{\delta T_{s\parallel}/3 + 2\delta T_{s\perp}/3}{T_{s0}} \right] - \frac{m_s \mu \delta B}{k_B T_{s0}} + \frac{m_s v_{\parallel} \delta u_{\parallel}}{k_B T_{s0}} \right). \quad (5.3.2)$$

If we use Eq. (5.3.2), then Eq. (5.1.23) yields expressions for the perturbed ion and electron particle distribution functions:

$$\begin{aligned} \delta f_i = & \frac{m_p v_{\parallel}}{k_B T_{i0}} \left( \frac{-ik_{\parallel} \mu \delta B + e \delta E_{\parallel} / m_p + \delta \bar{B}_R v_i^2 \partial \ln p_{i0} / \partial R}{\Gamma + ik_{\parallel} v_{\parallel} + \nu_i} - \right. \\ & \left. \frac{(2\Omega + \Omega' R) \Gamma \cos \chi \delta \bar{B}_R}{ik_{\parallel} (\Gamma + ik_{\parallel} v_{\parallel} + \nu_i)} \right) f_{i0}^0 + \\ & f_{i0}^0 \frac{\nu_i}{\Gamma + ik_{\parallel} v_{\parallel} + \nu_i} \left( \delta \bar{\rho} - \frac{\delta T_{i\parallel} / 2 + \delta T_{i\perp}}{T_{i0}} + \left[ \frac{m_p \mu B_0}{k_B T_{i0}} + \frac{m_p v_{\parallel}^2}{2k_B T_{i0}} \right] \times \right. \end{aligned} \quad (5.3.3)$$

$$\begin{aligned} & \left[ \frac{\delta T_{i\parallel} / 3 + 2\delta T_{i\perp} / 3}{T_{i0}} \right] - \frac{m_p \mu \delta B}{k_B T_{i0}} + \frac{m_p v_{\parallel} \delta u_{\parallel}}{k_B T_{i0}} \Big) - \frac{f_{i0}^0 \delta \bar{B}_R}{ik_{\parallel}} \times \\ & \frac{\Gamma + ik_{\parallel} v_{\parallel}}{\Gamma + ik_{\parallel} v_{\parallel} + \nu_i} \left[ \frac{\partial \ln \rho_0}{\partial R} - \frac{3}{2} \frac{\partial \ln T_{i0}}{\partial R} + \right. \\ & \left. \left( \frac{m_p \mu B_0}{k_B T_{i0}} + \frac{m_p v_{\parallel}^2}{2k_B T_{i0}} \right) \frac{\partial \ln T_{i0}}{\partial R} \right], \\ \delta f_e = & \frac{m_e v_{\parallel}}{k_B T_{e0}} \left( \frac{-ik_{\parallel} \mu \delta B - e \delta E_{\parallel} / m_e + v_e^2 \delta \bar{B}_R \partial \ln p_{e0} / \partial R}{\Gamma + ik_{\parallel} v_{\parallel} + \nu_e} - \right. \\ & \left. \frac{(2\Omega + \Omega' R) \Gamma \cos \chi \delta \bar{B}_R}{ik_{\parallel} (\Gamma + ik_{\parallel} v_{\parallel} + \nu_e)} \right) f_{e0}^0 + \\ & f_{e0}^0 \frac{\nu_e}{\Gamma + ik_{\parallel} v_{\parallel} + \nu_e} \left( \delta \bar{\rho} - \frac{\delta T_{e\parallel} / 2 + \delta T_{e\perp}}{T_{e0}} + \left[ \frac{m_e \mu B_0}{k_B T_{e0}} + \frac{m_e v_{\parallel}^2}{2k_B T_{e0}} \right] \times \right. \end{aligned} \quad (5.3.4)$$

$$\begin{aligned} & \left[ \frac{\delta T_{e\parallel} / 3 + 2\delta T_{e\perp} / 3}{T_{e0}} \right] - \frac{m_e \mu \delta B}{k_B T_{e0}} + \frac{m_e v_{\parallel} \delta u_{\parallel}}{k_B T_{e0}} \Big) - \frac{f_{e0}^0 \delta \bar{B}_R}{ik_{\parallel}} \times \\ & \frac{\Gamma + ik_{\parallel} v_{\parallel}}{\Gamma + ik_{\parallel} v_{\parallel} + \nu_e} \left[ \frac{\partial \ln \rho_0}{\partial R} - \frac{3}{2} \frac{\partial \ln T_{e0}}{\partial R} + \right. \\ & \left. \left( \frac{m_e \mu B_0}{k_B T_{e0}} + \frac{m_e v_{\parallel}^2}{2k_B T_{e0}} \right) \frac{\partial \ln T_{e0}}{\partial R} \right]. \end{aligned}$$

We consider negligible electron dynamics. With the perturbed ion distribution function given by Eq. (5.3.3), then  $\delta p_\perp$ ,  $\delta p_\parallel$ , and  $\delta \bar{\rho}$  for finite collisionality are,

$$\begin{aligned} \frac{\delta p_\perp}{p_{i0}} = & -2 \frac{\delta B}{B_0} \zeta_i \left( \bar{\nu}_i R(i\zeta'_i) + \frac{1}{2} i Z(i\zeta'_i) \right) + \frac{2\Omega\Gamma}{k_\parallel^2 v_i^2} R(i\zeta'_i) \delta \bar{B}_R \cos \chi - \\ & \frac{2i\delta \bar{B}_R}{k_\parallel} \left( \frac{\partial \ln p_0}{\partial R} \right) \zeta_i \left( \bar{\nu}_i R(i\zeta'_i) + \frac{1}{2} i Z(i\zeta'_i) \right) + \\ & \frac{i\delta \bar{B}_R}{k_\parallel} \left( \frac{\partial \ln T_{i0}}{\partial R} \right) \bar{\nu}_i \left( (\zeta_i - \bar{\nu}_i) R(i\zeta'_i) - \frac{1}{2} i Z(i\zeta'_i) \right) + \\ & \frac{\delta n}{\rho_0} \bar{\nu}_i \left( (\zeta_i - \nu_i) R(i\zeta'_i) - \frac{1}{2} i Z(i\zeta'_i) \right) + \\ & \frac{\delta p_\parallel/3 + 2\delta p_\perp/3}{p_{i0}} \bar{\nu}_i \left( \zeta'_i R(i\zeta'_i) - \frac{1}{2} i Z(i\zeta'_i) \right), \end{aligned} \quad (5.3.5)$$

$$\begin{aligned} \frac{\delta p_\parallel}{p_{i0}} = & 2 \frac{\delta B}{B_0} \zeta_i \left( \zeta'_i (1 + 2\zeta_i'^2) R(i\zeta'_i) - \bar{\nu}_i \right) + \frac{2\Omega\Gamma}{k_\parallel^2 v_i^2} (1 - 2\zeta_i'^2 R(i\zeta'_i)) \delta \bar{B}_R \cos \chi + \\ & \frac{2i\delta \bar{B}_R}{k_\parallel} \left( \frac{\partial \ln p_0}{\partial R} \right) \zeta_i (\zeta'_i (1 + 2\bar{\nu}_i \zeta'_i) R(i\zeta'_i) - \bar{\nu}_i) - \\ & \frac{i\delta \bar{B}_R}{k_\parallel} \bar{\nu}_i \left( \frac{\partial \ln T_{i0}}{\partial R} \right) (\zeta'_i (2\zeta_i^2 - 2\bar{\nu}_i^2 - 3) R(i\zeta'_i) + \bar{\nu}_i - \zeta_i) - \\ & \frac{\delta n}{\rho_0} \bar{\nu}_i (\zeta'_i (2\zeta_i^2 - 2\bar{\nu}_i^2 - 3) R(i\zeta'_i) + \bar{\nu}_i - \zeta_i) - \\ & 2\bar{\nu}_i \zeta_i'^2 \frac{\delta p_\parallel/3 + 2\delta p_\perp/3}{p_{i0}} \left( \zeta'_i R(i\zeta'_i) + \frac{1}{2} i Z(i\zeta'_i) \right), \end{aligned} \quad (5.3.6)$$

$$\begin{aligned} \delta \bar{\rho} = & -\frac{\delta B}{B_0} (R(i\zeta'_i) - 1 + 2\bar{\nu}_i R(i\zeta'_i)) + \frac{2\Omega\Gamma}{k_\parallel^2 v_i^2} R(i\zeta'_i) \delta \bar{B}_R \cos \chi - \\ & \frac{i\delta \bar{B}_R}{k_\parallel} \left( \frac{\partial \ln T_{i0}}{\partial R} \right) (1 - 2\bar{\nu}_i (\zeta_i - \bar{\nu}_i) R(i\zeta'_i) + 3i\bar{\nu}_i Z(i\zeta'_i)) - \\ & \frac{i\delta \bar{B}_R}{k_\parallel} \left( \frac{\partial \ln p_0}{\partial R} \right) \zeta_i (2\bar{\nu}_i R(i\zeta'_i) + i Z(i\zeta'_i)) + \\ & \delta \bar{\rho} \left( \bar{\nu}_i (\zeta_i - \bar{\nu}_i) R(i\zeta'_i) - \frac{3}{2} i \bar{\nu}_i Z(i\zeta'_i) \right), \end{aligned} \quad (5.3.7)$$

where  $\bar{\nu}_i = \nu_i / (k_{\parallel} v_i \sqrt{2})$ . In the limit of high collisionality,  $\nu_i \gtrsim \Omega \beta^{1/2}$ , the perturbed density and pressures are given by,

$$\frac{\delta p_{\perp}}{p_{i0}} \simeq \frac{\delta p_{\parallel}/3 + 2\delta p_{\perp}/3}{p_{i0}} + \nu_i^{-1} \left( \Gamma \frac{\delta p_{\parallel}/3 + 2\delta p_{\perp}/3}{p_{i0}} + \Gamma \frac{i\delta \bar{B}_R}{k_{\parallel}} \frac{\partial \ln p_0}{\partial R} + \right. \\ \left. 2\Gamma \frac{\delta B}{B_0} - \Omega' R \delta \bar{B}_R \cos \chi - ik_{\parallel} \delta u_{\parallel} \right), \quad (5.3.8)$$

$$\frac{\delta p_{\parallel}}{p_{i0}} \simeq \frac{\delta p_{\parallel}/3 + 2\delta p_{\perp}/3}{p_{i0}} + \nu_i^{-1} \left( \Gamma \frac{\delta B}{B_0} - \Gamma \frac{\delta p_{\parallel}/3 + 2\delta p_{\perp}/3}{p_{i0}} - 3ik_{\parallel} \delta u_{\parallel} + \right. \\ \left. \delta \bar{B}_R \left[ \frac{i\Gamma}{k_{\parallel}} \left( \frac{\partial \ln p_0}{\partial R} \right) - 3\Omega' R \cos \chi \right] \right). \quad (5.3.9)$$

If we employ Eq. (5.1.3) to make simplifications, Eqs. (5.3.8) and (5.3.9) can be arranged into an expression for the viscous stress,

$$\frac{\delta p_v}{p_0} = -3\nu_i^{-1} \left( ik_{\parallel} \delta u_{\parallel} + \Omega' R \cos \chi \delta \bar{B}_R - \frac{1}{3} i \mathbf{k} \cdot \delta \mathbf{u} \right) \quad (5.3.10)$$

For arbitrary normalized collisional frequency  $\hat{\nu}_i = \nu_i / \Omega$ , the pressure response is given by,

$$\begin{pmatrix} A_{11} & A_{12} \\ A_{21} & A_{22} \end{pmatrix} \begin{pmatrix} \delta p_{i\perp}/p_{i0} \\ \delta p_{i\parallel}/p_{i0} \end{pmatrix} = \begin{pmatrix} B_{11} & B_{12} & B_{13} \\ B_{21} & B_{22} & B_{23} \end{pmatrix} \begin{pmatrix} \delta \bar{B}_R \\ \delta B/B_0 \\ \delta \bar{\rho} \end{pmatrix}, \quad (5.3.11)$$

where,

$$\begin{aligned}
A_{11} &= 1 - \frac{2\nu_i}{3x\sqrt{2\beta}} \left( \frac{\hat{\nu}_i + \gamma}{x\sqrt{2\beta}} R \left( \frac{i[\hat{\nu}_i\gamma]}{x\sqrt{2\beta}} \right) - \frac{1}{2} iZ \left( \frac{i[\hat{\nu}_i + \gamma]}{x\sqrt{2\beta}} \right) \right), \\
A_{12} &= -\frac{\nu_i}{3x\sqrt{2\beta}} \left( \frac{\hat{\nu}_i + \gamma}{x\sqrt{2\beta}} R \left( \frac{i[\hat{\nu}_i\gamma]}{x\sqrt{2\beta}} \right) - \frac{1}{2} iZ \left( \frac{i[\hat{\nu}_i + \gamma]}{x\sqrt{2\beta}} \right) \right), \\
A_{21} &= \frac{\hat{\nu}_i (\hat{\nu}_i + \gamma)^2}{3x^3\beta^{3/2}\sqrt{2}} \left( \frac{\hat{\nu}_i + \gamma}{x\sqrt{2\beta}} R \left( \frac{i[\hat{\nu}_i + \gamma]}{x\sqrt{2\beta}} \right) + \frac{1}{2} iZ \left( \frac{i[\hat{\nu}_i + \gamma]}{x\sqrt{2\beta}} \right) \right), \\
A_{22} &= 1 + \frac{2\hat{\nu}_i (\hat{\nu}_i + \gamma)^2}{3x^3\beta^{3/2}\sqrt{2}} \left( \frac{\hat{\nu}_i + \gamma}{x\sqrt{2\beta}} R \left( \frac{i[\hat{\nu}_i + \gamma]}{x\sqrt{2\beta}} \right) + \frac{1}{2} iZ \left( \frac{i[\hat{\nu}_i + \gamma]}{x\sqrt{2\beta}} \right) \right),
\end{aligned} \tag{5.3.12}$$

and,

$$\begin{aligned}
B_{11} &= \frac{2\gamma}{x^2\beta} \cos \chi R \left( \frac{i[\hat{\nu}_i + \gamma]}{x\sqrt{2\beta}} \right) + \frac{i\alpha_P}{x\sqrt{\beta}} \left( \frac{\gamma}{x\sqrt{2\beta}} \right) \left( \frac{\hat{\nu}_i}{x\sqrt{2\beta}} R \left( \frac{i[\hat{\nu}_i + \gamma]}{x\sqrt{2\beta}} \right) + \right. \\
&\quad \left. \frac{1}{2} iZ \left( \frac{i[\hat{\nu}_i + \gamma]}{x\sqrt{2\beta}} \right) \right) - \frac{i\alpha_T}{x\sqrt{\beta}} \left( \frac{\hat{\nu}_i}{x\sqrt{2\beta}} \right) \left( \frac{\gamma - \hat{\nu}_i}{x\sqrt{2\beta}} R \left( \frac{i[\hat{\nu}_i + \gamma]}{x\sqrt{2\beta}} \right) - \right. \\
&\quad \left. \frac{1}{2} iZ \left( \frac{i[\hat{\nu}_i + \gamma]}{x\sqrt{2\beta}} \right) \right),
\end{aligned} \tag{5.3.13}$$

$$B_{12} = -\frac{2\gamma}{x\sqrt{2\beta}} \left( \frac{\hat{\nu}_i}{x\sqrt{2\beta}} R \left( \frac{i[\hat{\nu}_i + \gamma]}{x\sqrt{2\beta}} \right) + \frac{1}{2} iZ \left( \frac{i[\hat{\nu}_i + \gamma]}{x\sqrt{2\beta}} \right) \right), \tag{5.3.14}$$

$$B_{13} = \frac{\hat{\nu}_i}{x\sqrt{2\beta}} \left( \frac{\gamma - \hat{\nu}_i}{x\sqrt{2\beta}} R \left( \frac{i[\hat{\nu}_i + \gamma]}{x\sqrt{2\beta}} \right) - \frac{1}{2} iZ \left( \frac{i[\hat{\nu}_i + \gamma]}{x\sqrt{2\beta}} \right) \right), \tag{5.3.15}$$

$$\begin{aligned}
B_{21} &= \frac{2\gamma}{x^2\beta} \cos \chi \left( 1 - \frac{(\hat{\nu}_i + \gamma)^2}{x^2\beta} R \left( \frac{i[\hat{\nu}_i + \gamma]}{x\sqrt{2\beta}} \right) \right) - \frac{2i\alpha_P}{x\sqrt{\beta}} \left( \frac{\gamma}{x\sqrt{2\beta}} \right) \times \\
&\quad \left( \frac{\hat{\nu}_i + \gamma}{x\sqrt{2\beta}} \left( \frac{\gamma^2 - \hat{\nu}_i^2}{x^2\beta} - 3 \right) R \left( \frac{i[\hat{\nu}_i + \gamma]}{x\sqrt{2\beta}} \right) - \frac{\hat{\nu}_i}{x\sqrt{2\beta}} \right) + \\
&\quad \frac{i\alpha_T}{x\sqrt{\beta}} \left( \frac{\hat{\nu}_i}{x\sqrt{2\beta}} \right) \left( \frac{\gamma}{x\sqrt{2\beta}} \left( \frac{\gamma^2 - \hat{\nu}_i^2}{x^2\beta} - 3 \right) R \left( \frac{i[\hat{\nu}_i + \gamma]}{x\sqrt{2\beta}} \right) + \right. \\
&\quad \left. \frac{\hat{\nu}_i - \gamma}{x\sqrt{2\beta}} \right),
\end{aligned} \tag{5.3.16}$$

$$B_{22} = \frac{2\gamma}{x\sqrt{2\beta}} \left( \frac{\hat{\nu}_i + \gamma}{x\sqrt{2\beta}} \left( 1 + \frac{(\hat{\nu}_i + \gamma)^2}{x^2\beta} \right) R \left( \frac{i[\hat{\nu}_i + \gamma]}{x\sqrt{2\beta}} \right) + \frac{\hat{\nu}_i - \gamma}{x\sqrt{2\beta}} \right), \tag{5.3.17}$$

$$\begin{aligned}
B_{23} &= -\alpha_T \left( \frac{\hat{\nu}_i}{x\sqrt{2\beta}} \right) \left( \frac{\gamma}{x\sqrt{2\beta}} \left( \frac{\gamma^2 - \hat{\nu}_i^2}{x^2\beta} - 3 \right) R \left( \frac{i[\hat{\nu}_i + \gamma]}{x\sqrt{2\beta}} \right) + \right. \\
&\quad \left. \frac{\hat{\nu}_i - \gamma}{x\sqrt{2\beta}} \right).
\end{aligned} \tag{5.3.18}$$



We use the force balance equation, Eq. (5.2.3), with expressions for the perturbed pressure response given by Eq. (5.3.11), to solve for the mildly collisional MVTI dispersion relation. The MRI dispersion relation becomes that given by Sharma et al. (2003). In Fig. (5.3.1) we show the real and imaginary parts of the growth rate for a Keplerian rotation profile,  $\beta = 10^3$ ,  $\chi = \pi/4$ , radial gradients  $\alpha_P = 3/2$  and  $\alpha_T = 1$ , for various ion collisional frequencies  $\nu_i$ . For  $\nu_i > \Omega\beta^{1/2}$ , we reproduce the MVTI.

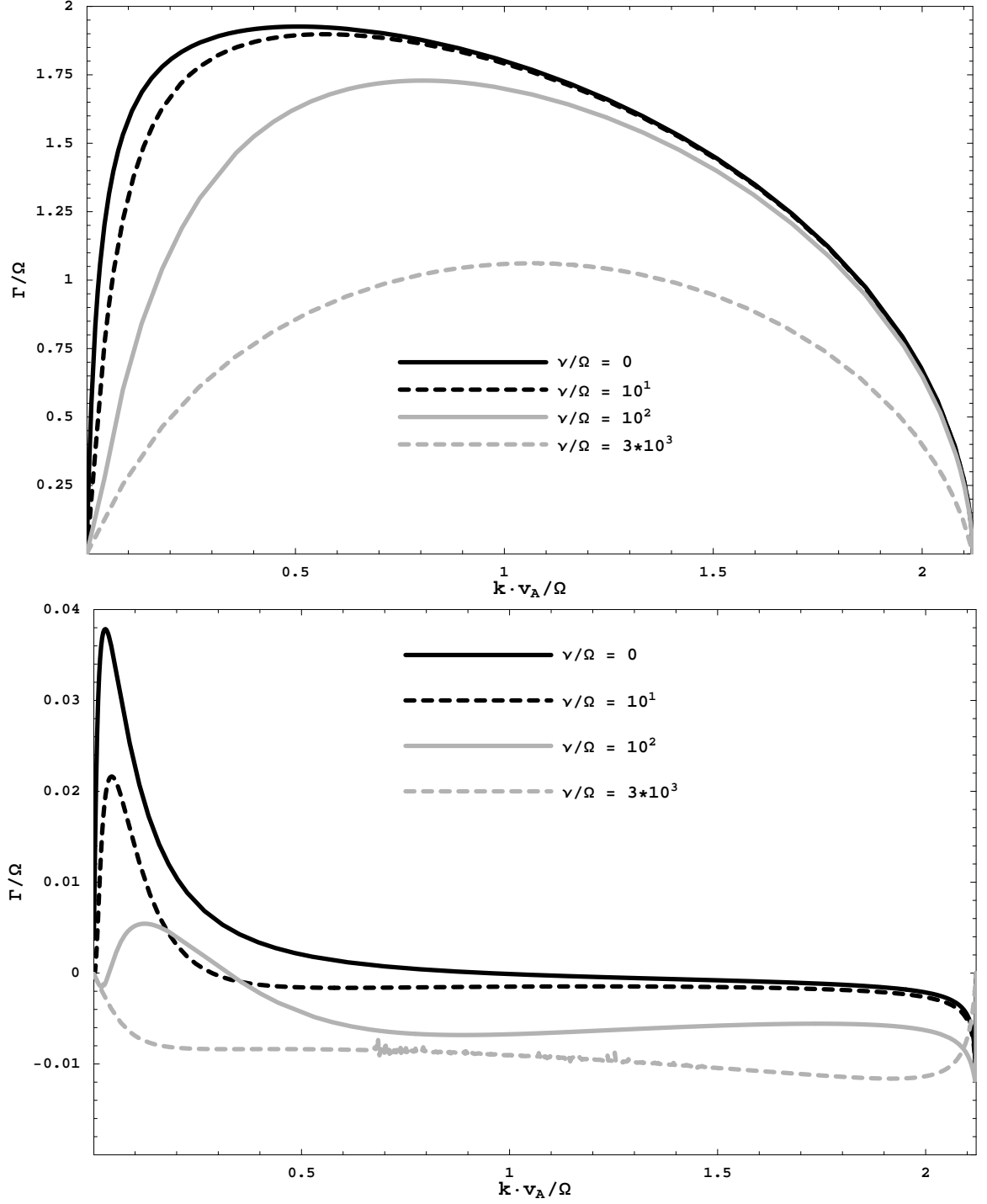


Fig. 5.3.1.— Real (top) and imaginary (bottom) parts of the growth rate of the MVTI. We reproduce the MVTI dispersion relation for  $\nu_i \geq \Omega \beta^{1/2}$ .

## 5.4 Summary of Results

We have derived the drift kinetic equation in a rotating frame with possible significant gas pressures and only mild collisionality. There is a larger range of applicable densities and temperatures, within hot, dilute, magnetized rotating plasmas, for which this collisionless treatment can be applied. We analyze the collisionless MTI at the disk midplane, analogous to the MVTI for the fluid case. We reproduce the collisionless MRI dispersion relation of Quataert et al. (2002). We demonstrate that both the collisionless MRI and MTI agree with their fluid counterparts – the MVI and MVTI, respectively. Heat and angular momentum fluxes associated with the collisionless MTI have the right sign, to drive accretion in thick dilute nonradiative rotating plasmas, and approximately match their respective fluid counterparts. We also find the collisionless MTI can transport angular momentum, even within a rigidly rotating plasma.

Although we have applied the drift-kinetic equation to a single but important class of instability in Keplerian-like rotating systems, its representation as given in Eq. (5.1.23) lends itself to much richer studies of these types of dilute rotating plasmas. Even if the equilibrium can be described by a fluid treatment, it may be unstable to shorter-wavelength collisionless MHD modes. There exists a range of collision frequencies  $\nu < \Omega\beta^{1/2}$  where the MHD dynamics are collisionless. If the wavelength of the instability, of order  $v_A/\Omega$ , is smaller than the ion mean free path, of order  $\theta_0^{1/2}/\nu_i$ , then collisionless physics applies. As  $\beta \rightarrow 1$  we reproduce compressive pure MHD modes. The effects of collisionless momentum and energy transfer effects become dynamically unimportant, and the imaginary part of the growth rate of these modes becomes larger (see §4.4 for compressible MHD in the fluid limit).

## Chapter 6

# Additional Physics: Electron and Off-Plane Dynamics

In this chapter, we discuss in more detail the collisionless MTI and the MVTI by including the effects of finite electron temperature and dynamics of the plasma away from the midplane. The plasma is dilute enough that ions and electrons are not explicitly thermally coupled (see Fig. [1.5.1]). Also, the equilibrium electron acceleration, divided by the electron thermal velocity, away from the midplane is much larger than the growth rate or the orbital angular velocity. We perform an incompressible fluid analysis of collisional plasmas and a kinetic analysis of collisionless plasmas. These analyses are detailed in Appendix D and Appendix E

### 6.1 Finite Ion and Electron Pressure Responses

We include electron dynamics by considering finite electron temperature. In a dilute plasma, the ion-electron collisional frequency is much smaller than the ion-ion and electron-electron collision frequencies. Therefore, even if ion and electrons remain collisional, the explicit thermal coupling between ions and electrons, which in a clas-

sical fluid ensures equal ion and electron temperatures, may not exist. However, if  $T_{i0} \gtrsim T_{e0}$ , the plasma dispersion relation is not substantially different from our simplified analyses. The main difference arises when  $T_{e0} \gg T_{i0}$ . For the fluid case, we find that the maximum growth rate occurs at wavenumbers  $\eta_{\kappa e} k_Z^2 \sim \Omega$  (see Fig. [6.1.1]). We do not find much difference in the dispersion relation between the collisionless and collisional plasmas (see Fig. [6.1.4]). The ion and electron temperatures are given by,

$$T_{i0} = \frac{(m_p + m_e) \theta_0}{k_B} \cos^2 \psi, \quad (6.1.1)$$

$$T_{e0} = \frac{(m_p + m_e) \theta_0}{k_B} \sin^2 \psi. \quad (6.1.2)$$

The fluid treatment of finite electron temperature is detailed in Appendix D.1. In Fig. (6.1.1), we show the normalized growth rate as a function of wavenumber for a Keplerian rotational profile,  $\alpha_P = 5$ ,  $\alpha_T = 2$ ,  $\chi = \pi/4$ ,  $\eta_{\nu 0} \Omega / v_A^2 = 10^2$ , for various ratios of  $T_{e0}$  to  $T_{i0}$ .  $\eta_{\nu 0}$  is the Braginskii viscosity where  $T_{i0} = T_{e0}$ , and is given in Eq. (D.1). For  $T_{i0} \gtrsim T_{e0}$  we reproduce the MVTI plasma response – a maximum growth rate at wavenumbers  $\eta_{\nu 0} k_Z^2 \sim \Omega$ . For  $T_{i0} \lesssim T_{e0}$ , the viscosity becomes dynamically unimportant,  $\eta_{\nu} \Omega / v_A^2 \rightarrow 0$ . The maximum growth rate occurs at wavenumbers  $101 \eta_{\nu 0} k_Z^2 \sim \Omega$  (see Eq. [D.6]). Furthermore, as  $T_{e0}/T_{i0} \rightarrow \infty$ , for dynamically important viscosity the density response over most of the unstable wavenumbers is approximately,

$$\delta \bar{\rho} \approx \frac{\delta \bar{B}_R}{i k_Z \sin \chi} \times \frac{\partial \ln T_0}{\partial R}. \quad (6.1.3)$$

The growth rate satisfies the following polynomial equation,

$$\left( \frac{k^2}{k_Z^2} \Gamma^2 + \frac{d\Omega^2}{d \ln R} + k^2 v_A^2 \sin^2 \chi - \theta_0 \frac{\partial \ln p_0}{\partial R} \frac{\partial \ln T_0}{\partial R} \right) \times \quad (6.1.4)$$

$$(\Gamma^2 + k_Z^2 v_A^2 \sin^2 \chi) + 4\Omega^2 \Gamma^2 = 0.$$

Note that for a plasma with equal ion and electron temperatures, as explained in §4, the plasma response with dynamically unimportant viscous diffusivity (see Figs. [4.2.1]) is not qualitatively similar to one in which  $\eta_{\nu 0}\Omega/v_A^2 \gtrsim 1$  but with  $T_{i0}/T_{e0} \rightarrow 0$ .

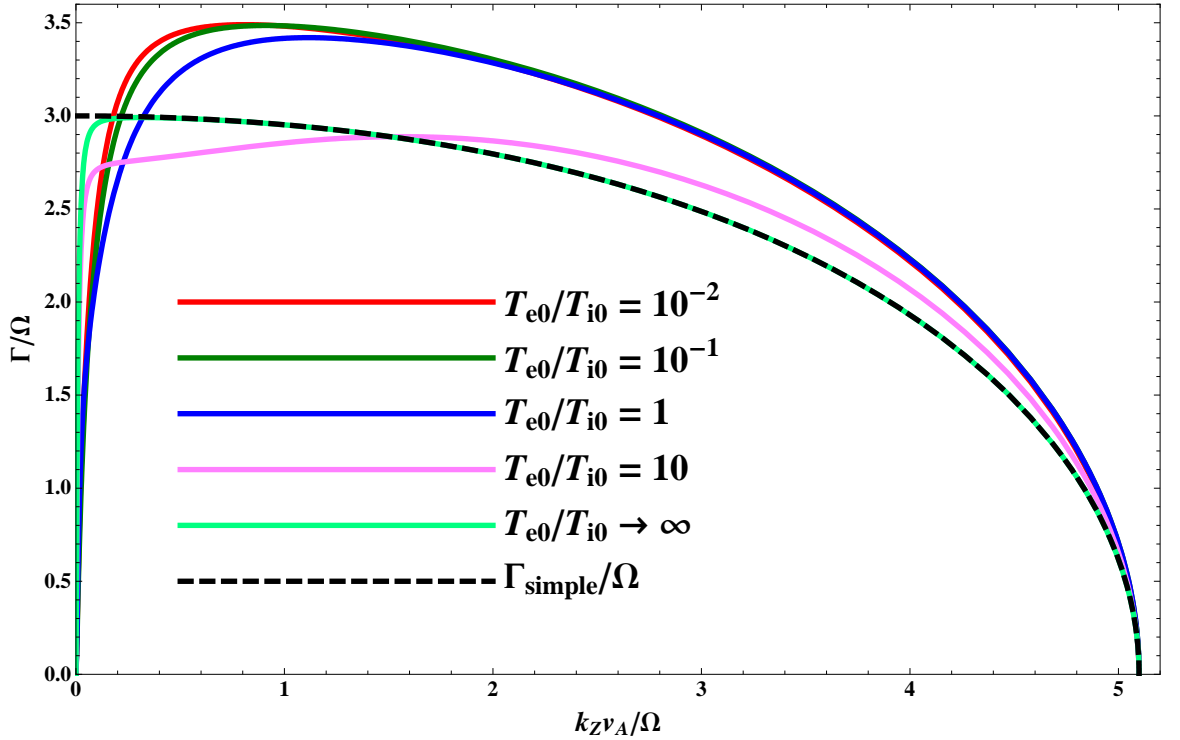


Fig. 6.1.1.— Normalized growth rate as a function of normalized nonradial wavenumber for the MVTI for various values of  $T_{e0}/T_{i0}$ . We choose a Keplerian rotational profile, with  $\alpha_P = 5$ ,  $\alpha_T = 2$ ,  $\chi = \pi/4$ , and  $\eta_{\nu 0}\Omega/v_A^2 = 10^2$ . The dashed red line refers to the simplified plasma response, whose growth rate satisfies Eq. (6.1.4).

The kinetic treatment of finite electron temperature is detailed in Appendix D.2. Figs. (6.1.2) and (6.1.3) are plots of the collisionless MRI and collisionless MTI, respectively, at various  $T_{e0}/T_{i0}$ . We take  $\beta = 10^2$ , a Keplerian-like rotation profile, and  $\chi = \pi/4$ . For the MVTI, we use a system that is Schwarzschild stable, hence  $\alpha_P = 5$  and  $\alpha_T = 1$ .

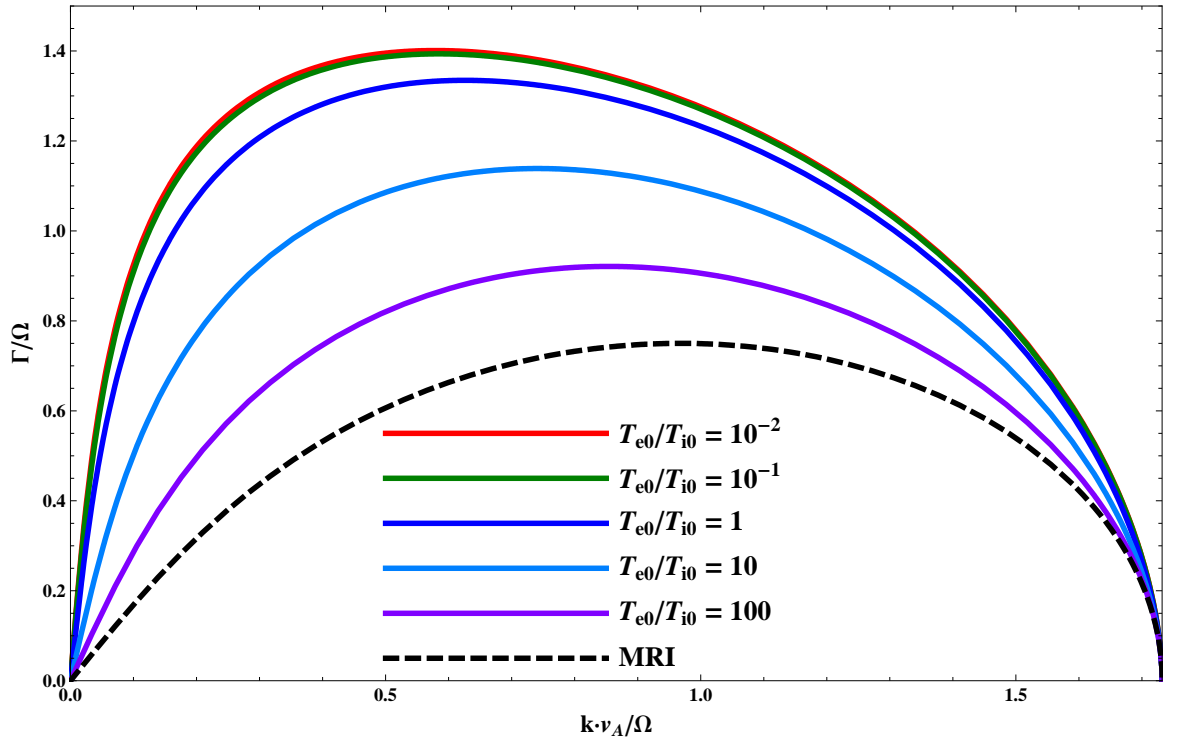


Fig. 6.1.2.— The growth rate as a function of wavenumber for the collisionless MRI for both equal and negligible ion and electron temperatures.

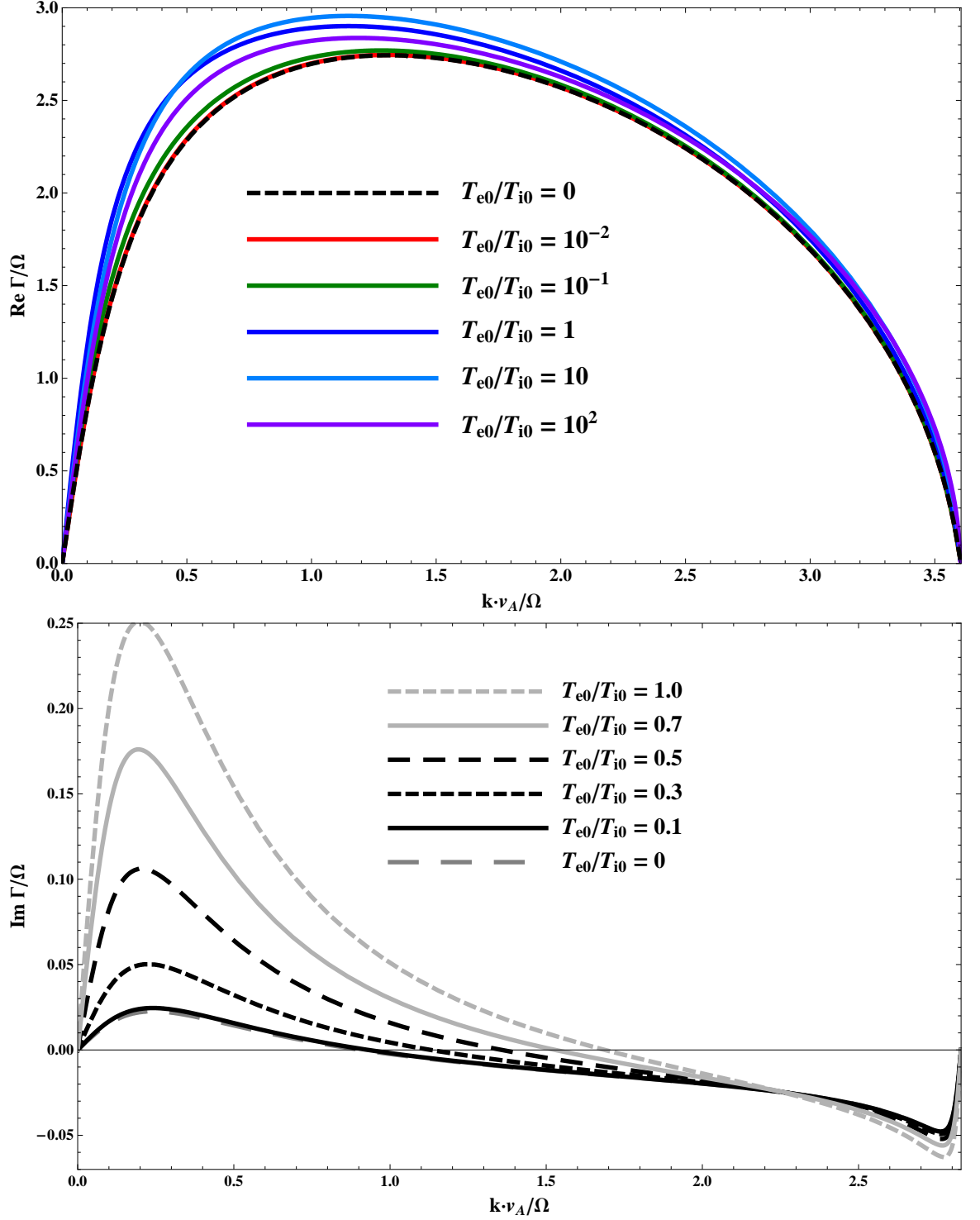


Fig. 6.1.3.— The real (top) and imaginary (bottom) parts of growth rate of the collisionless MTI. The imaginary part of the growth rates where  $T_{e0}/T_{i0} = 10^{-1}$  nearly coincide where  $T_{e0}/T_{i0} = 0$ . Maximal compressible effects are reached for wavenumbers  $k_{\parallel} \sim \Omega/\theta_0^{1/2}$ .



Furthermore, unlike the MVTI, the growth rate for the collisionless MTI reaches a maximum at wavenumbers  $k_Z\theta_0 \sim \Omega$  even when  $T_{i0}/T_{e0} \rightarrow 0$ . The “knee” at which the growth rate reaches a maximum is located at larger wavenumbers than would be expected if only electron collisionless damping was considered. In Fig. (6.1.4) we plot the real and imaginary parts, respectively, of the growth rate for the collisionless MTI with  $T_{e0}/T_{i0} = 10$  and various plasma  $\beta$ . Similar behavior is seen in Figs. (5.2.4) and (5.2.5) with a simpler treatment that does not consider the electron pressure response.

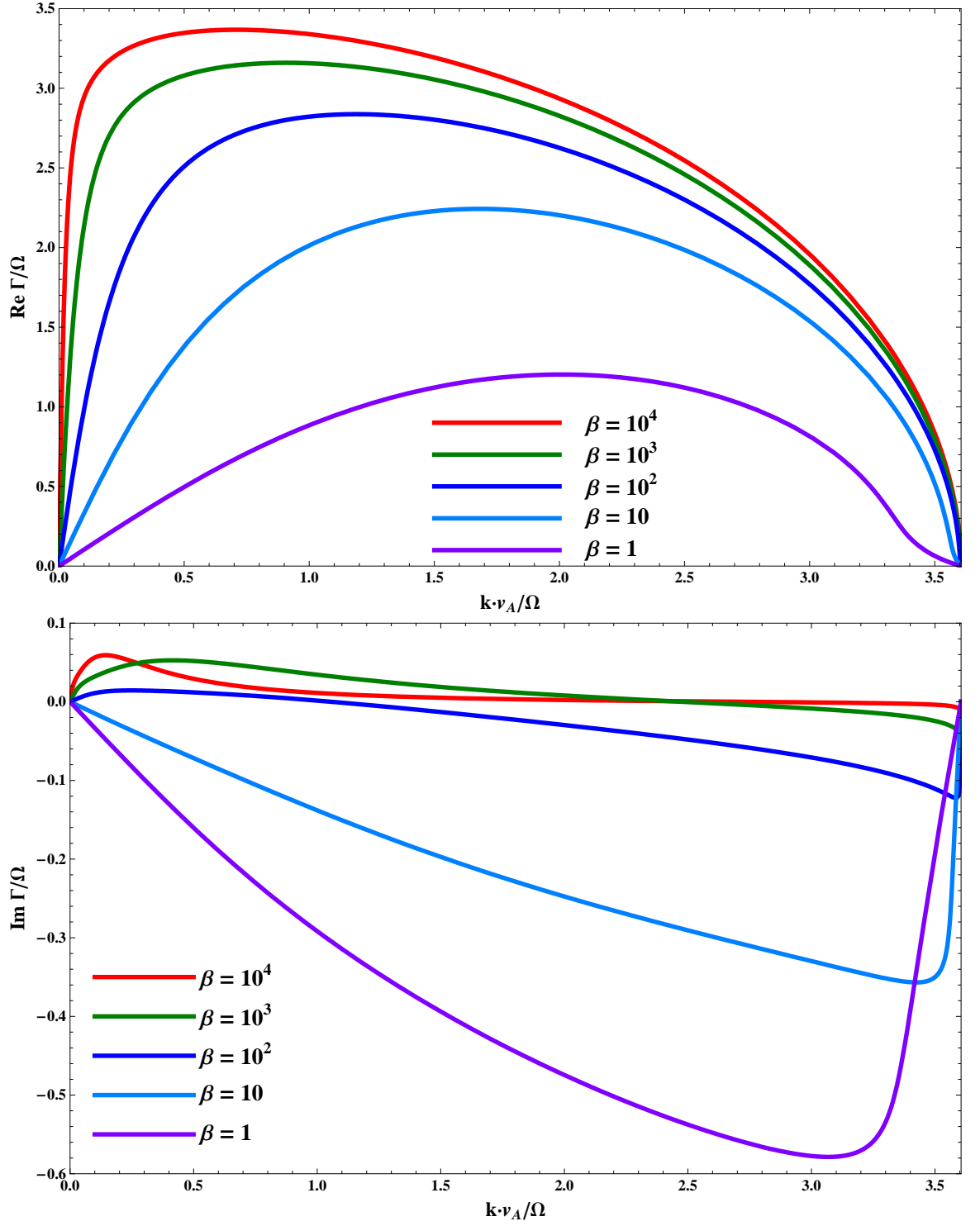


Fig. 6.1.4.— The real (top) and imaginary (bottom) parts of the normalized growth rate as a function of normalized nonradial wavenumber for  $T_{e0}/T_{i0} = 10$ , for various  $\beta \geq 1$ . We take a Keplerian rotation profile,  $\alpha_P = 5$ ,  $\alpha_T = 2$ , and  $\chi = \pi/4$ .

The discrepancy between fluid and kinetic results when  $T_{e0} \gg T_{i0}$  remains unclear. A framework for moving between the collisionless and collisional regimes, described in §5.3, may be necessary to examine this apparent inconsistency.

## 6.2 Off Plane Dynamics of the Plasma

In §3 we describe the structure of a thin dilute magnetized disk. To a good approximation only the density and pressure change significantly over the height of the disk. In the vertical direction, the magnetic field is constant and nonradial, and the orbital angular velocity and temperature are constant. This equilibrium thin dilute magnetized disk is Schwarzschild stable in the vertical direction. The entropy gradient in the vertical direction is such that,

$$\frac{\partial \ln p_0}{\partial z} \times \frac{\partial \ln p_0 \rho_0^{-5/3}}{\partial z} \approx -\frac{2}{3} \frac{z^2}{H^4} < 0 \quad (6.2.1)$$

The Alfvén speed relative to the midplane is,

$$v_A^2 = v_{A0}^2 \exp(z^2/H^2), \quad (6.2.2)$$

where  $v_{A0}$  is the Alfvén speed at the midplane. The wavenumber, and viscous and thermal diffusivities are normalized in this manner,

$$\hat{\mathbf{k}} = \mathbf{k} v_{A0} / \Omega, \quad (6.2.3)$$

$$\hat{\eta}_\nu = \eta_\nu \Omega / v_{A0}^2, \quad (6.2.4)$$

$$\hat{\eta}_\kappa = \eta_\kappa \Omega / v_{A0}^2. \quad (6.2.5)$$

Here  $\eta_{\nu 0}$  and  $\eta_{\kappa 0}$  are the viscous diffusivity and thermal diffusivity at the midplane, respectively. We find that the main difference away from the midplane is the smaller range of MVTI unstable wavenumbers.

In the collisionless plasma, we find significant accelerations experienced by electrons in the perturbed electron distribution function. We calculate the growth rate of the collisionless MRI away from the midplane. We show that the effect of finite electron acceleration alters the growth rate of the collisionless MRI away from the midplane beyond that of merely decreasing the range of unstable wavenumbers.

The growth rate goes to zero at  $\hat{\mathbf{k}} = \mathbf{0}$  and  $\hat{\mathbf{k}}$  that satisfies the following,

$$\left( \alpha_P - \frac{\hat{k}_R}{\hat{k}_Z} z/H \right) \alpha_T - 2 \frac{d \ln \Omega}{d \ln R} = \hat{k}^2 e^{z^2/(2H^2)} \sin^2 \chi \quad (6.2.6)$$

However, the maximum growth rate occurs at the midplane for  $\hat{\mathbf{k}}_{\max} = \pm \hat{k}_{\max} \hat{\mathbf{z}}$ . At points away from the midplane, the maximum growth rate goes as  $\hat{\mathbf{k}}_{\max} = \pm \hat{k}_{\max} e^{-z^2/(2H^2)} \hat{\mathbf{z}}$ . As one moves to positive  $z$ , the range of unstable wavenumbers increases. However, these changes occur at wavenumbers where  $\Gamma \ll \Omega$ . These features are demonstrated for a Keplerian rotation profile,  $\chi = \pi/4$ , and a marginally Schwarzschild stable system with  $\alpha_P = 5$  and  $\alpha_T = 2$ , in a fluid plasma (Figs. [6.2.1] - [6.2.6]).

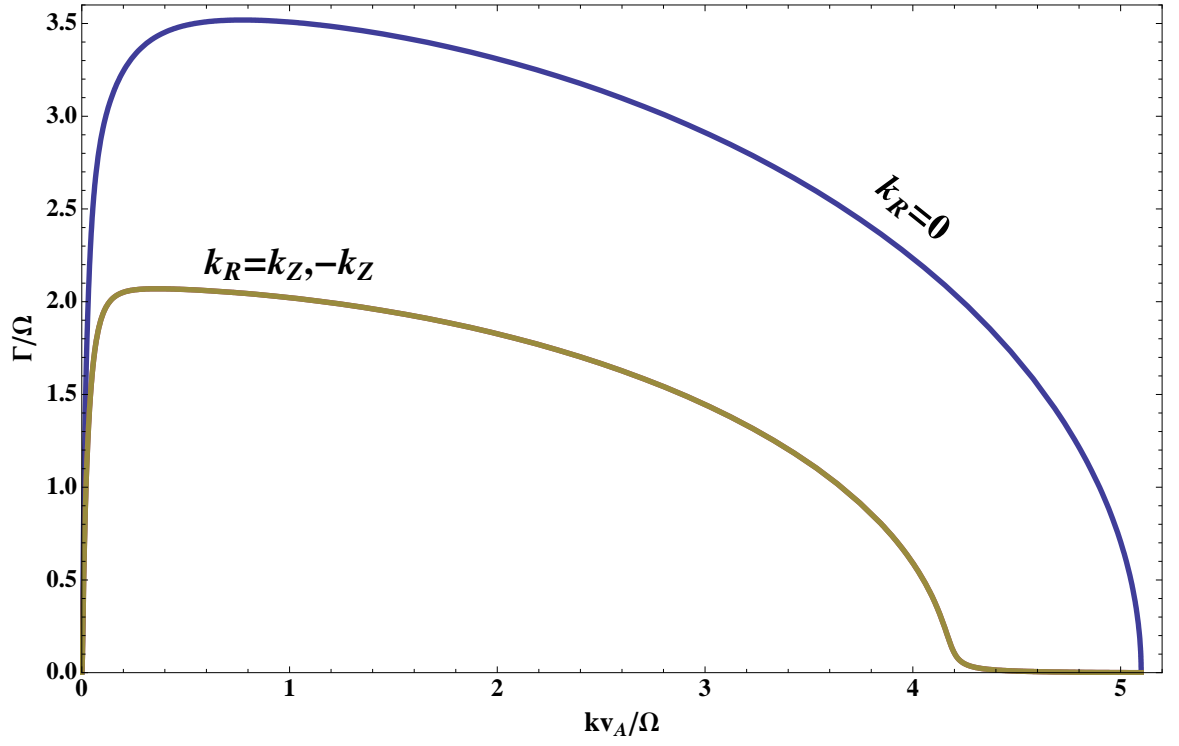


Fig. 6.2.1.— Normalized growth rate as a function of normalized wavenumber  $kv_{A0}/\Omega$  at  $z/H = 0$  for  $k_R = 0$  and  $k_R = \pm k_Z$  with  $k_Z \geq 0$ .

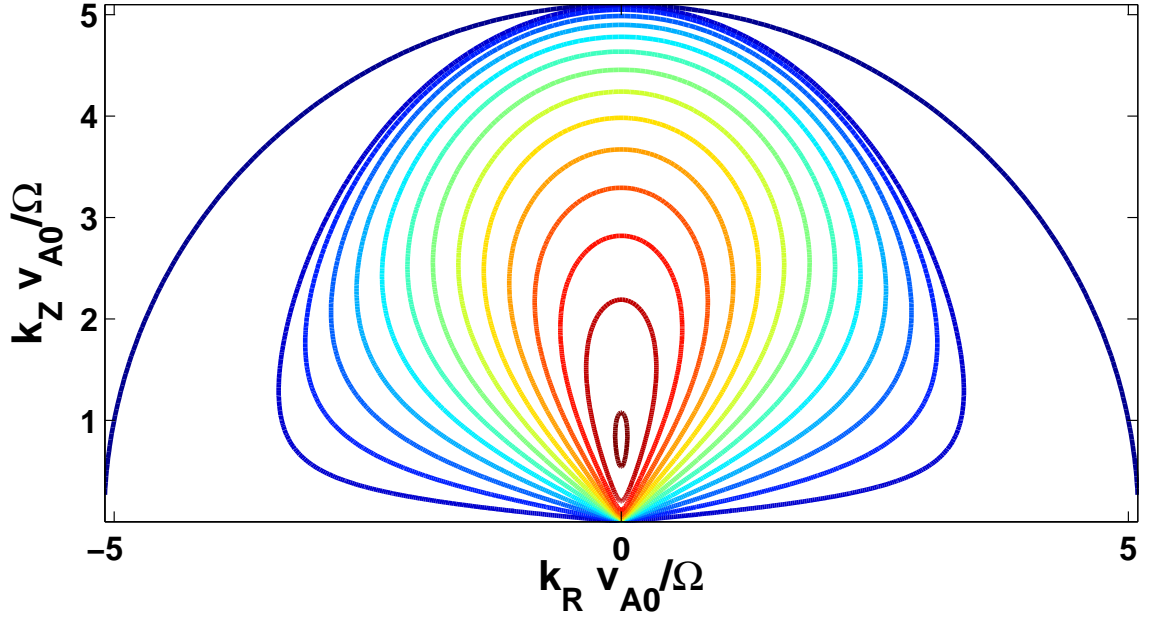


Fig. 6.2.2.— Contours of normalized growth rate  $\Gamma/\Omega$  as a function of normalized radial and vertical wavenumbers  $k_R v_{A0}/\Omega$  and  $k_Z v_{A0}/\Omega$  at  $z/H = 0$ . The outermost contour has  $\Gamma/\Omega = 0$ , the innermost contour has  $\Gamma/\Omega = 3.5$ , and adjacent contours are separated by units of  $\Delta\Gamma/\Omega = 0.25$ . The growth rate is symmetric about the  $k_R = 0$  axis.

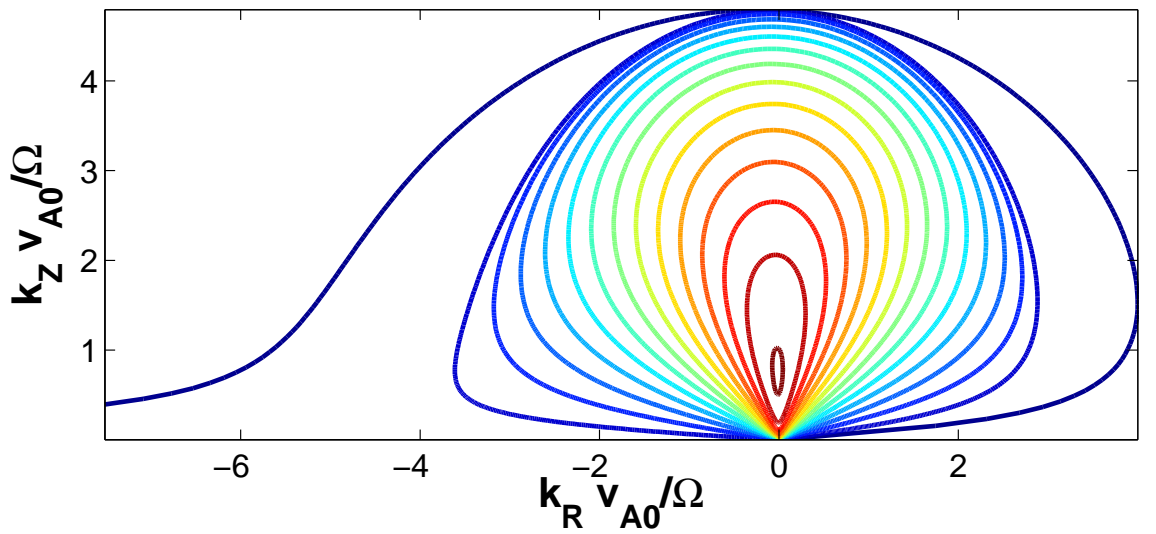


Fig. 6.2.3.— Normalized growth rate as a function of normalized wavenumber  $kv_{A0}/\Omega$  at  $z/H = 0.5$  for  $k_R = 0$  and  $k_R = \pm k_Z$  with  $k_Z \geq 0$ .

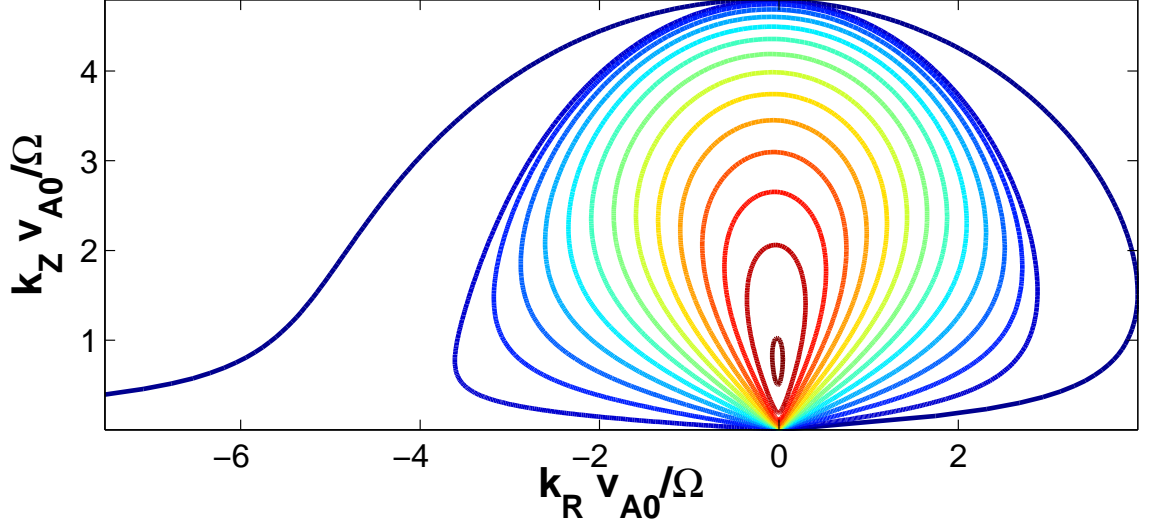


Fig. 6.2.4.— Contours of normalized growth rate  $\Gamma/\Omega$  as a function of normalized radial and vertical wavenumbers  $k_R v_{A0}/\Omega$  and  $k_Z v_{A0}/\Omega$  at  $z/H = 0.5$ . The outermost contour has  $\Gamma/\Omega = 0$ , the innermost contour has  $\Gamma/\Omega = 3.5$ , and adjacent contours are separated by units of  $\Delta\Gamma/\Omega = 0.25$ .

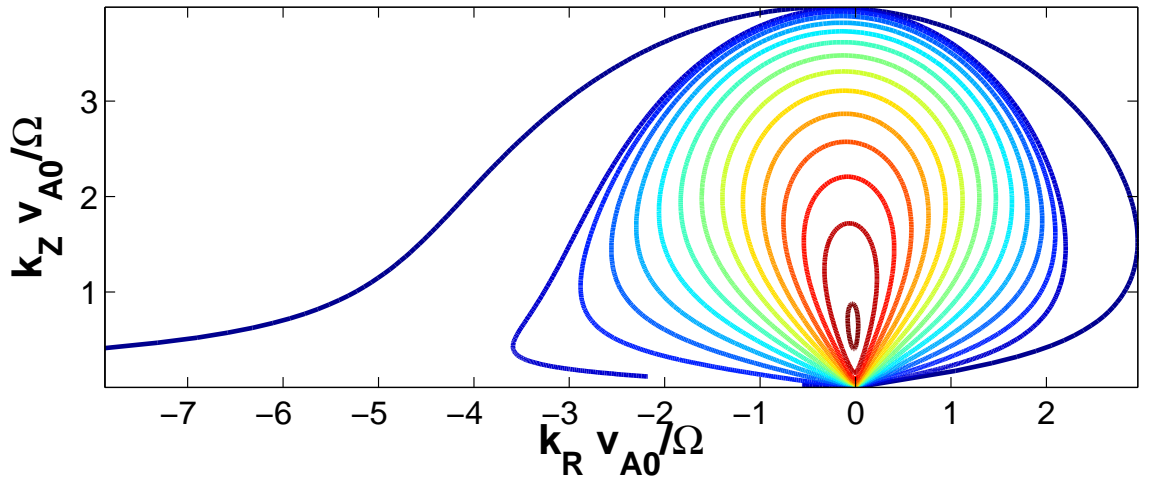


Fig. 6.2.5.— Normalized growth rate as a function of normalized wavenumber  $kv_{A0}/\Omega$  at  $z/H = 1$  for  $k_R = 0$  and  $k_R = \pm k_Z$  with  $k_Z \geq 0$ .

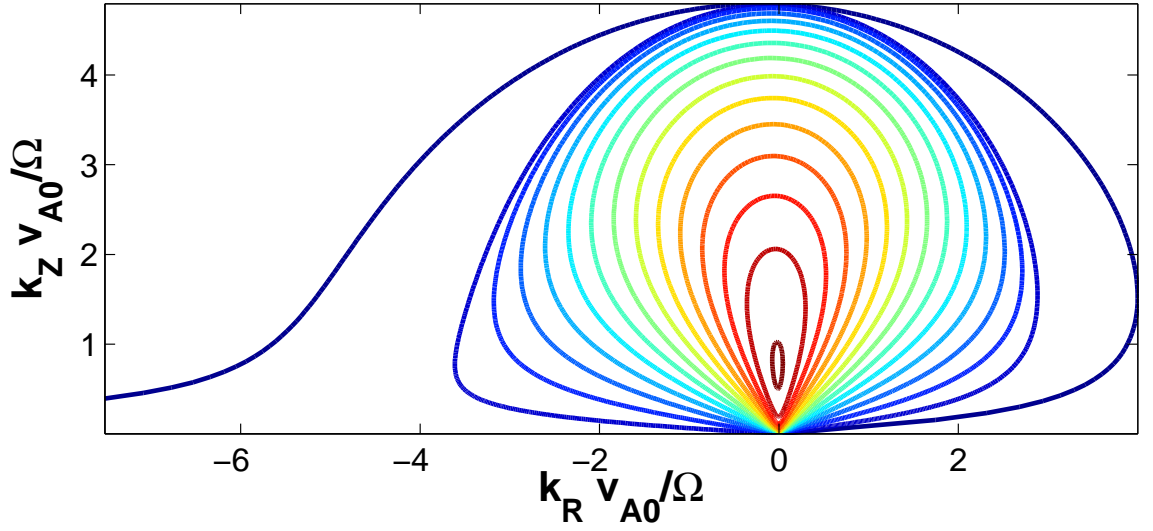


Fig. 6.2.6.— Contours of normalized growth rate  $\Gamma/\Omega$  as a function of normalized radial and vertical wavenumbers  $k_R v_{A0}/\Omega$  and  $k_Z v_{A0}/\Omega$  at  $z/H = 1$ . The outermost contour has  $\Gamma/\Omega = 0$ , the innermost contour has  $\Gamma/\Omega = 3.5$ , and adjacent contours are separated by units of  $\Delta\Gamma/\Omega = 0.25$ .



The derivation of the dispersion relation for the off-plane collisionless MTI is described in Appendix E.2. The growth rate is the solution of Eq. (E.36), with expressions for the perturbed pressures  $\delta p_{\parallel}$  and  $\delta p_{\perp}$  given by Eq. (E.29). We examine the growth rate as a function of height from the midplane for three normalized wavenumbers:  $\hat{k}_Z v_{A0}/\Omega = 10^{-1}$  (Fig. [6.2.7]),  $\hat{k}_Z v_{A0}/\Omega = 10^{-1/2}$  (Fig. [6.2.8]), and  $\hat{k}_Z v_{A0}/\Omega = 1$  (Fig. [6.2.9]). We take a Keplerian rotational profile,  $\chi = \pi/4$ , and  $\beta = 10^2$ . Here we compare the real and imaginary growth rates with  $\Gamma_s$ .  $\Gamma_s$  is also a solution of Eq. (E.36), but with  $\delta p_{\parallel}$  and  $\delta p_{\perp}$  given by their forms at  $z/H = 0$ , Eqs. (D.7) and (D.6), respectively. We find significant difference between  $\Gamma$  and  $\Gamma_s$ . The physical effects due to going away from the midplane, for the collisionless plasma, go beyond merely changing the range of unstable wavenumbers.

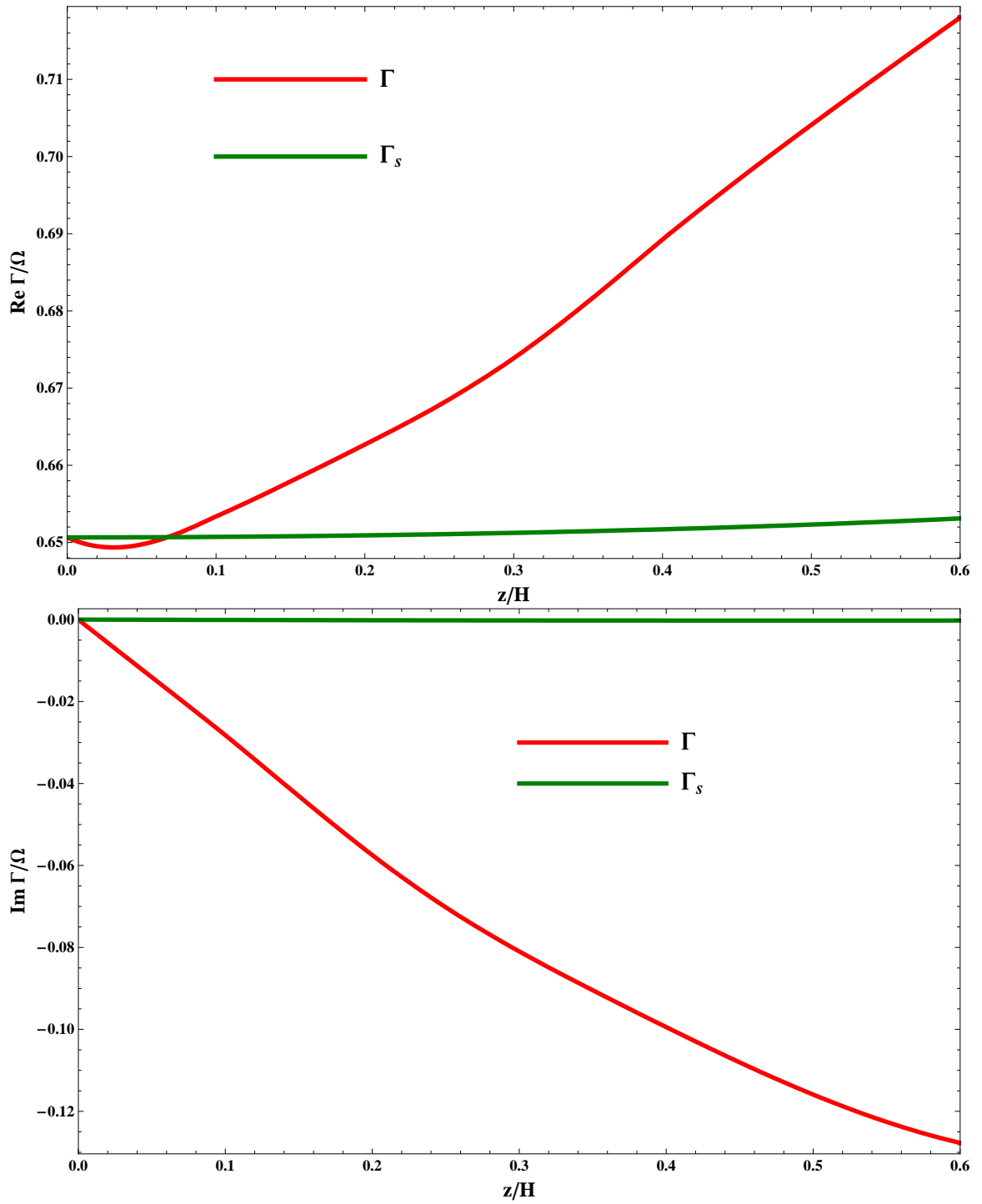


Fig. 6.2.7.— On top is the real, and on bottom is the imaginary, normalized growth rate as a function of height  $z/H$  for  $k_Z v_{A0}/\Omega = 10^{-1}$ . We compare  $\Gamma$  to  $\Gamma_s$ .

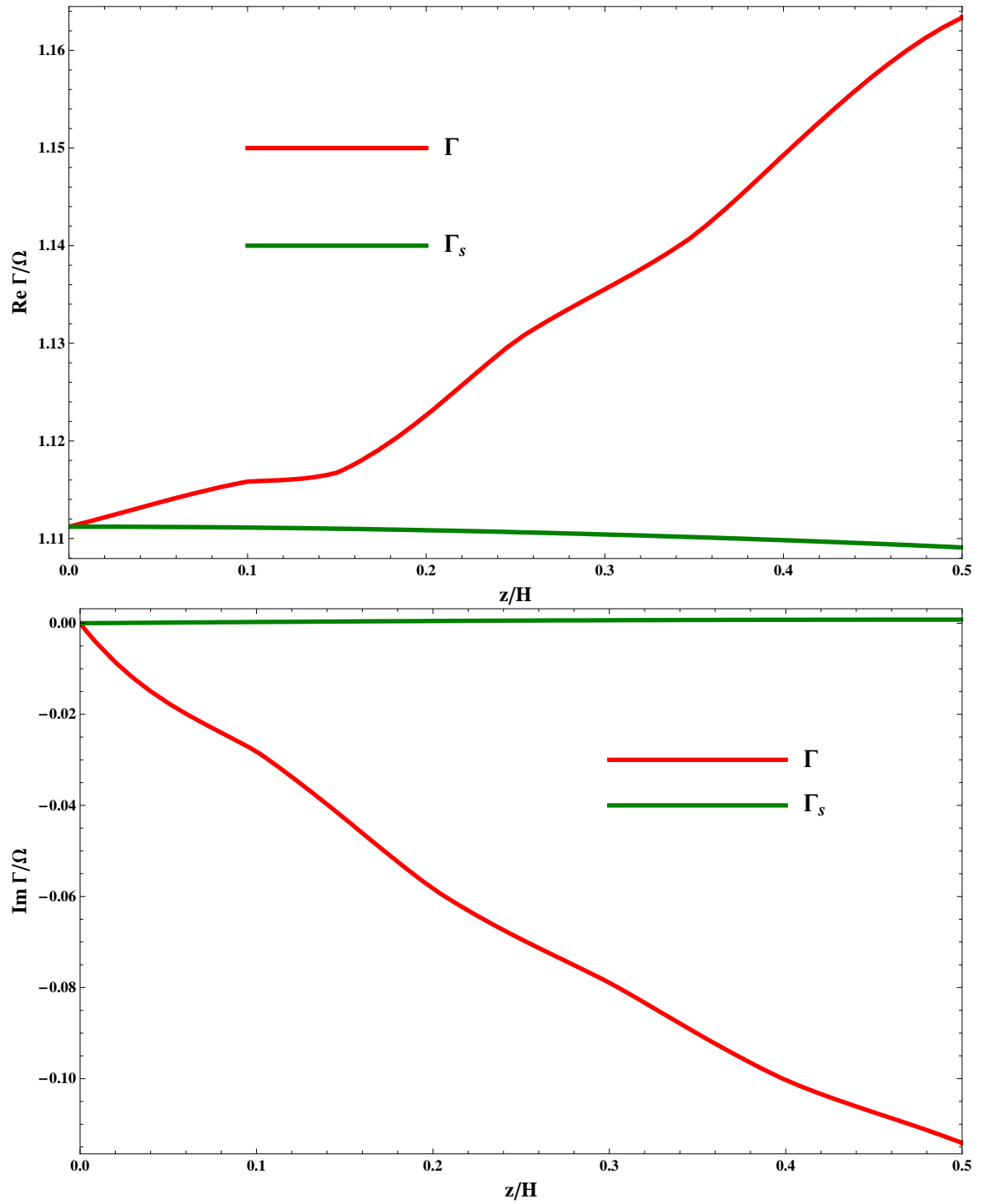


Fig. 6.2.8.— On top is the real, and on bottom is the imaginary, normalized growth rate as a function of height  $z/H$  for  $k_Z v_{A0}/\Omega = 10^{-1/2}$ . We compare  $\Gamma$  to  $\Gamma_s$ .

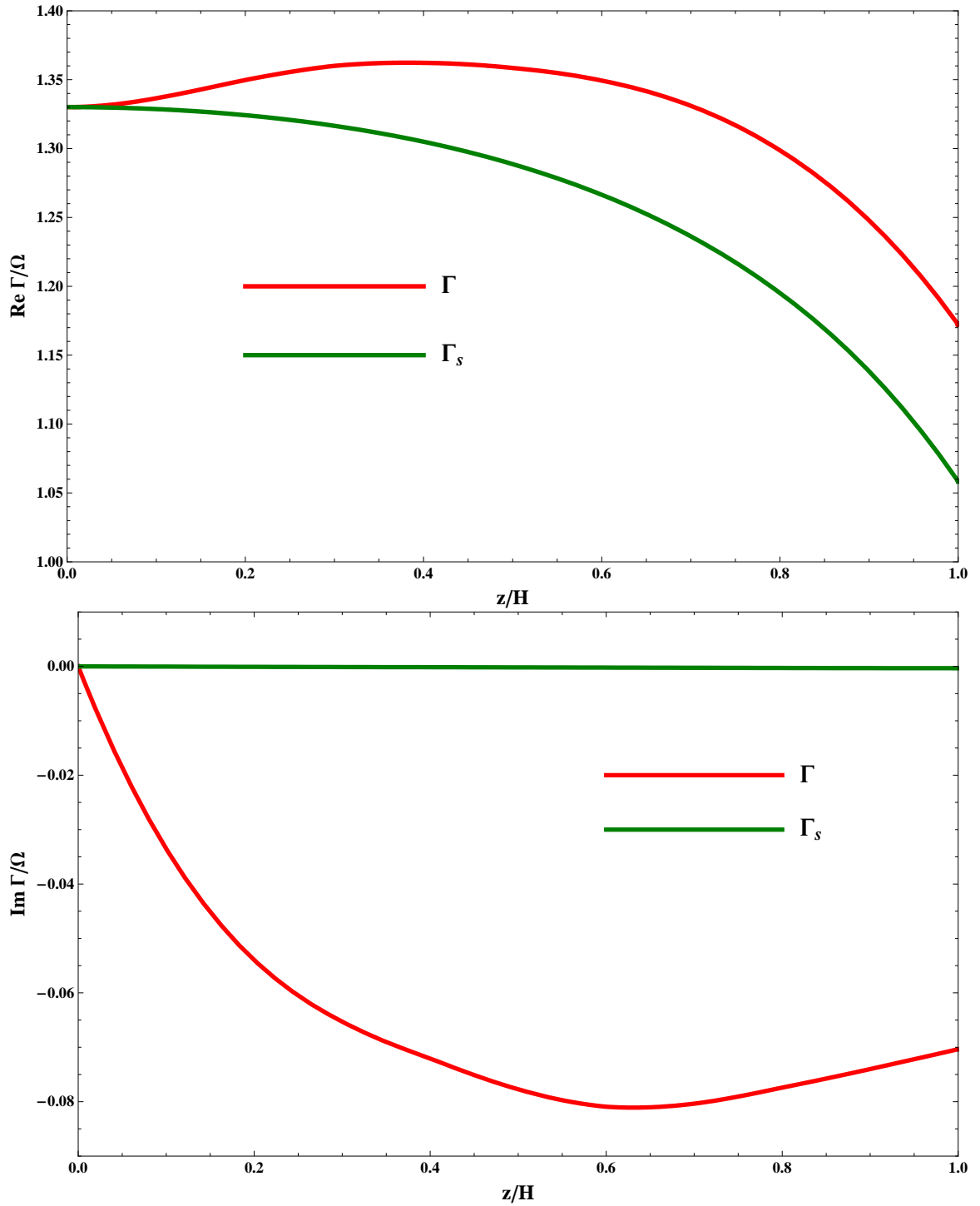


Fig. 6.2.9.— On top is the real, and on bottom is the imaginary, normalized growth rate as a function of height  $z/H$  for  $k_Z v_{A0}/\Omega = 1$ . We compare  $\Gamma$  to  $\Gamma_s$ .

# Chapter 7

## Conclusions

The focus of our research is on those MHD modes that can transport angular momentum and thermal energy outwards in mildly collisional and collisionless radiatively inefficient accretion flows. We summarize the main thesis research, from §4 - §6, in §7.1. In §7.2 we discuss local numerical simulations of astrophysical systems unstable to the collisionless MTI or MVTI. We formulate parallel and perpendicular heat fluxes appropriate to the study of collisionless plasmas with equilibrium gradients, and explain issues associated with gyrokinetic (phenomena on the length scales of ion Larmor radius) instabilities that force the plasma to have a maximal pressure anisotropy. Finally, in §7.3 we describe analytic and numerical work that can arise from our research into collisionless and mildly collisional MHD phenomena in rotationally supported dilute magnetized plasmas.

### 7.1 Summary of Results

We have identified local modes in dilute magnetized accretion flows that can transport angular momentum and thermal energy outwards. We have demonstrated the parameter regimes for which the viscosity or thermal conductivity can play a dynami-

cally important role, and shown that these instabilities are not qualitatively modified when going into the collisionless regime. The dispersion relations, quadratic angular momentum and heat fluxes for the collisionless MTI are qualitatively similar to the MVTI. In the collisionless MTI, transit-time (or Barnes) damping of modes with phase velocities much smaller than the ion sound speed provides a sort of “collisionless” transport of momentum and thermal energy that behaves as a viscosity and thermal conductivity, respectively. Next, as shown in §4.4, if we include the effects of finite compressibility in the MVTI, the viscosity and thermal conductivity become dynamically unimportant as the magnetic pressure increases; as  $\beta \rightarrow 1$  from infinity, the MVTI reduces to the MRI. Finally, when we include the effects of finite collisionality we notice that the collisionless MTI reduces to the MVTI when the wavelength of the fastest growing modes (wavelength of order  $v_A/\Omega$ ) becomes larger than the ion mean free path. This result has been confirmed by Sharma et al. (2003) for the collisionless MRI.

In §6 we justify and explore the effects of considering both ion and electron dynamics, and the effects of finite equilibrium vertical forces away from the disk midplane. We validate our *a posteriori* assumption that we need consider only ion dynamics in the collisionless plasma and only electron thermal conductivity and ion viscosity in the collisional plasma. We also demonstrate new features on the growth rate of the collisionless offplane MRI beyond that of increasing Alfvén velocity (see Figs. [6.2.7], [6.2.8], and [6.2.9]).

## 7.2 Numerical Simulations

Here we describe the setup and initial issues for preliminary numerical simulations of radiatively inefficient magnetized flows. The features of numerical simulations of

the collisionless MTI or MVTI are the following: 1) there are momentum and thermal fluxes directed along magnetic fields in the collisional and collisionless plasmas; and 2) dilute plasmas are easily susceptible to gyrokinetic instabilities that keep the plasma pressure from becoming too anisotropic (Gary et al. 1994). Sharma et al. (2006); Sharma (2006) have simulated the nonlinear collisionless MRI with the ZEUS (Stone & Norman 1992a,b) 3D MHD parallel algorithm with modifications of anisotropic viscosity and isotropizing instabilities. Sharma et al. (2006); Sharma (2006) have employed closed-form expressions for the parallel and perpendicular heat fluxes that approximate, for small fluctuations, the linear behavior of the collisionless MRI. These are referred to as Landau fluid closures as they “close” the fluid equations, allowing for numerical codes that evolve magnetofluid quantities (e.g., pressure, density, magnetic field) with position and time rather than evolving the full six-dimensional (3 in space + 3 in velocity) particle distribution function.

In §7.2.1 we consider fluid closures of heat flux that can model systems that are unstable to the collisionless MTI. We solve the fluid equations up to third order in velocity moments of the drift-kinetic equation. We demonstrate that a closure expression for heat flux in terms of lower-order fluid quantities (perturbed density, pressure) and magnetic fields appropriate for collisionless MHD is that of Snyder et al. (1997), but modified to include finite equilibrium gradients of pressure and temperature. We then show the limits of this fluid closure of heat fluxes at large magnetic field strengths, by demonstrating the discrepancy between the collisionless MTI and the Landau-closed collisionless MTI.

In §7.2.2 we discuss the issue of pressure anisotropy in dilute MHD plasmas. We demonstrate that pressure anisotropy at any level can destabilize a differentially rotating plasma via MHD modes; this implies that even via MHD phenomena, a plasma with no pressure anisotropy becomes destabilized. We then discuss the theoretical

underpinnings and observational evidence of gyrokinetic instabilities that ensure a maximum pressure anisotropy. We finish with a discussion of issues associated with numerical simulations whose pressure anisotropies are constrained by these gyrokinetic modes.

### 7.2.1 Landau Fluid Closures Appropriate to Collisionless MTI

Landau fluid closures of higher order moments of the distribution function, which are typically expressions for the heat fluxes, are employed to model the appropriate physics of a collisionless plasma using a fluid formalism. The fluid closure heat fluxes  $q_{\parallel}$  and  $q_{\perp}$  match the collisionless heat fluxes  $q_{\parallel}$  and  $q_{\perp}$  to various orders in the growth rate  $\Gamma$ . These closures are chosen to satisfy conservation laws, such as density, particle momentum, and energy. They have been used in the study of ion-temperature gradient modes (Lee & Diamond 1986; Waltz 1988; Hammett & Perkins 1990), gyrokinetic plasmas (Hammett et al. 1992; Dorland 1993), and collisionless MHD plasmas (Snyder et al. 1997).

We employ linearized forms of the continuity equation Eq. (5.1.27), the parallel force balance equation Eq. (5.1.28), and parallel and perpendicular pressures in Eqs. (5.1.29) and (5.1.30):

$$\Gamma \delta \bar{\rho} + (i\mathbf{k} \cdot \delta \mathbf{u}) + \delta u_R \frac{\partial \ln \rho_0}{\partial R} = 0, \quad (7.2.1)$$

$$\Gamma \delta u_{\parallel} + (2\Omega + \Omega' R) \delta u_R \cos \chi = -ik_{\parallel} \frac{\delta p_{\parallel}}{\rho}, \quad (7.2.2)$$

$$\Gamma \delta p_{\parallel} + p_0 (i\mathbf{k} \cdot \delta \mathbf{u}) + \delta u_R \frac{\partial p_{i0}}{\partial R} + 2p_0 (ik_{\parallel} \delta u_{\parallel} + \Omega' R \delta \bar{B}_R \cos \chi) + \quad (7.2.3)$$

$$ik_{\parallel} \delta q_{\parallel} = 0,$$

$$\Gamma \delta p_{\perp} + p_0 (2i\mathbf{k} \cdot \delta \mathbf{u} - ik_{\parallel} \delta u_{\parallel} - \Omega' R \delta \bar{B}_R \cos \chi) + \quad (7.2.4)$$

$$\delta u_R \frac{\partial p_{i0}}{\partial R} + ik_{\parallel} \delta q_{\perp} = 0.$$



These reduce to the following,

$$\begin{aligned}
& \gamma \delta \bar{\rho} + ix \left( \frac{\delta u_{\parallel}}{v_A} \right) + \left( \frac{d \ln \Omega}{d \ln R} \cos \chi - \frac{\gamma}{ix \beta^{1/2}} [\alpha_P - \alpha_T] \right) \delta \bar{B}_R - \gamma \delta \bar{B} = 0, \\
& \gamma \left( \frac{\delta u_{\parallel}}{v_A} \right) + \left( 2 + \frac{d \ln \Omega}{d \ln R} \right) \frac{\gamma \cos \chi}{ix} \delta \bar{B}_R = -ix \beta \left( \frac{\delta p_{\parallel}}{p_{i0}} \right), \\
& \gamma \left( \frac{\delta p_{\parallel}}{p_{i0}} \right) + \left[ 3ix \frac{\delta u_{\parallel}}{v_A} + 3 \frac{d \ln \Omega}{d \ln R} \delta \bar{B}_R \cos \chi - \gamma \delta \bar{B} \right] - \alpha_P \frac{\gamma}{ix \beta^{1/2}} \delta \bar{B}_R + ix \beta^{1/2} \frac{\delta q_{\parallel}}{p_{i0} v_i} = 0, \\
& \gamma \left( \frac{\delta p_{\perp}}{p_{i0}} \right) + \left[ ix \frac{\delta u_{\parallel}}{v_A} + \frac{d \ln \Omega}{d \ln R} \delta \bar{B}_R \cos \chi - 2\gamma \delta \bar{B} \right] - \alpha_P \frac{\gamma}{ix \beta^{1/2}} \delta \bar{B}_R + ix \beta^{1/2} \frac{\delta p_{\perp}}{p_{i0} v_i} = 0.
\end{aligned} \tag{7.2.5}$$

We choose forms of  $\delta q_{\parallel}$  and  $\delta q_{\perp}$  that are linear combinations of the magnetic fields and lower order moments of the Boltzmann equation,

$$\begin{aligned}
\delta q_{\parallel} &= \alpha_{\parallel} (v_i^3 \delta \rho) + \gamma_{\parallel} (\delta p_{\parallel} v_i) + \epsilon_{\parallel} (p_{i0} v_i \delta \bar{B}_R) + \zeta_{\parallel} (p_{i0} v_i \delta \bar{B}) \\
\delta q_{\perp} &= \alpha_{\perp} (v_i^3 \delta \rho) + \delta_{\perp} (\delta p_{\perp} v_i) + \epsilon_{\perp} (p_{i0} v_i \delta \bar{B}_R) + \zeta_{\perp} (p_{i0} v_i \delta \bar{B}).
\end{aligned} \tag{7.2.6}$$

The following closures for parallel and perpendicular heat flux results in a  $\delta p_{\parallel}$  that matches Eq. (5.2.8) up to order  $\gamma^3$  in  $\delta B/B$  and  $\delta \bar{B}_R$ , and results in  $\delta p_{\perp}$  that matches Eq. (5.2.7) up to order  $\gamma$  in  $\delta B/B$  and  $\delta \bar{B}_R$ .

$$\frac{\delta q_{\parallel}}{p_{i0} v_i} = 2i \sqrt{\frac{2}{\pi}} \left( \delta \bar{\rho} - \frac{\delta p_{\parallel}}{p_{i0}} \right) - 2 \left( \frac{1}{k_{\parallel}} \frac{\partial \ln T_{i0}}{\partial R} \right) \sqrt{\frac{2}{\pi}} \delta \bar{B}_R, \tag{7.2.7}$$

$$\frac{\delta q_{\perp}}{p_{i0} v_i} = i \sqrt{\frac{2}{\pi}} \left( \delta \bar{\rho} - \frac{\delta p_{\perp}}{p_{i0}} \right) - \left( \frac{1}{k_{\parallel}} \frac{\partial \ln T_{i0}}{\partial R} \right) \sqrt{\frac{2}{\pi}} \delta \bar{B}_R. \tag{7.2.8}$$

Eqs. (7.2.7) and (7.2.8) consists of expressions for the heat flux of parallel and perpendicular pressure as given in Snyder et al. (1997), but modified to include finite equilibrium gradients of temperature and pressure. We consider modes only with vertical wavenumbers. We solve the following equations for  $\delta \bar{B}_R$  and  $\delta \bar{B}_{\phi}$  – the radial and azimuthal force balance equations represented in terms of the magnetic field. We then use the radial and azimuthal force balance equations, Eqs. (5.2.4) and (5.2.5).

Divergence from the exact expression occurs at wavenumbers for which the modes become supersonic, i.e. at  $k \lesssim \Omega/v_i$ .

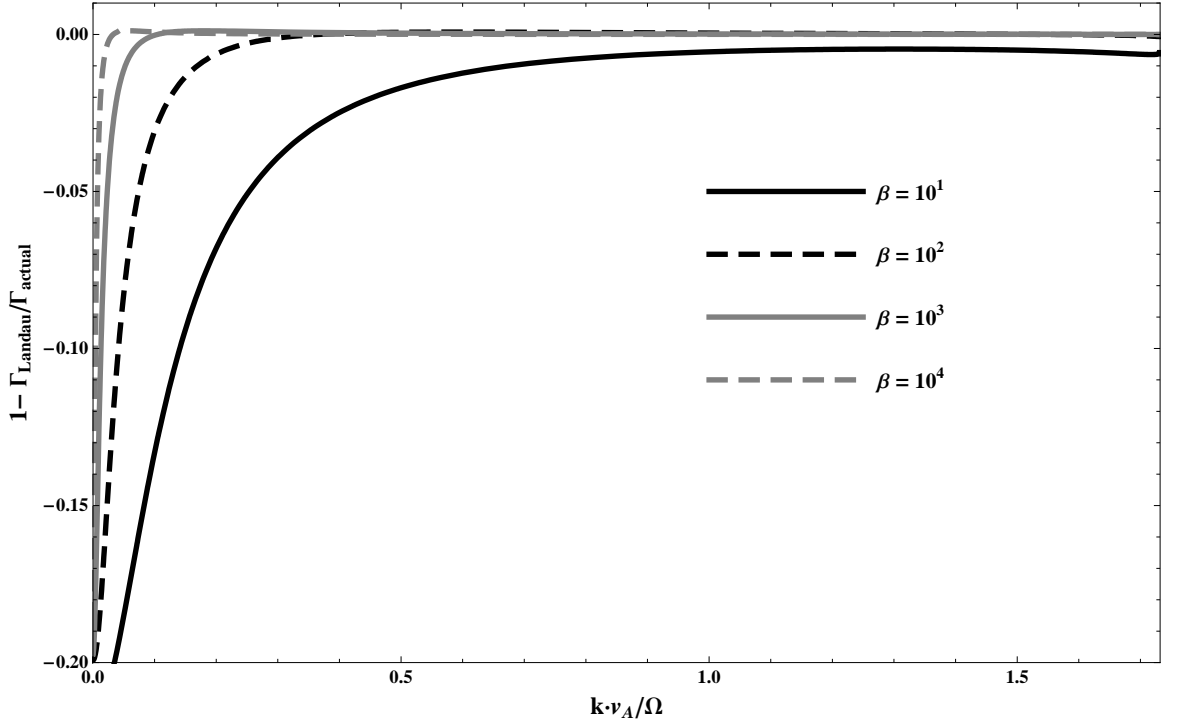


Fig. 7.2.1.— Plot of the relative difference between the growth rates between the Landau approximation and the “exact” expressions, given as  $1 - \Gamma_{\text{Landau}}/\Gamma_{\text{exact}}$ , for the collisionless MRI.

The largest discrepancy in the Landau approximation to the heat fluxes appears at wavenumbers for which the phase velocity is of the order sound speed, at wavenumbers  $k \lesssim \Omega/\theta_0^{1/2}$ . However, when putting in a system that is unstable to free thermal energy gradients, i.e.  $\alpha_P \alpha_T > 0$  and yet is convectively stable  $\alpha_S < 0$ , we find that the Landau approximation does not accurately model the imaginary part of the growth rate. This is not a severe issue as, for a plasma with subthermal magnetic fields, the imaginary part of the growth rate goes as  $\beta^{-1/2}$  that of the real part. These aspects of the Landau fluid approximation with finite equilibrium gradients are demonstrated in Figs. (7.2.2) and (7.2.3). In these figures we choose a Schwarzschild stable system with  $\alpha_P = 5$  and  $\alpha_T = 1$ . In Fig. (7.2.2), for all  $\beta_i = v_i^2/v_A^2$ , we find that the sign

of the imaginary component of the Landau growth rate differs from that of the exact growth rate. Furthermore, in Fig. (7.2.3), we see that the magnitude of the “Landau” growth rate is not substantially different from the “exact” growth rate.

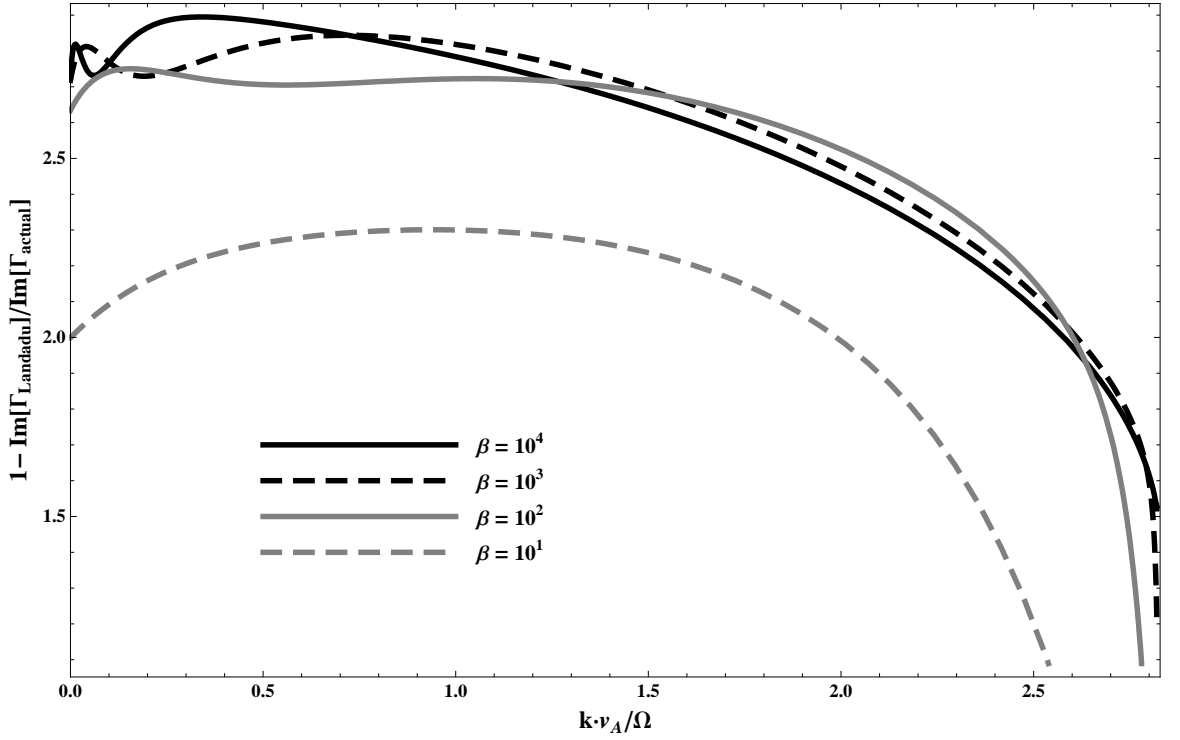


Fig. 7.2.2.— Comparison of the relative difference between the imaginary portion of the “Landau” and “exact” expressions, defined as  $1 - \text{Im}(\Gamma_{\text{Landau}})/\text{Im}(\Gamma_{\text{exact}})$ .

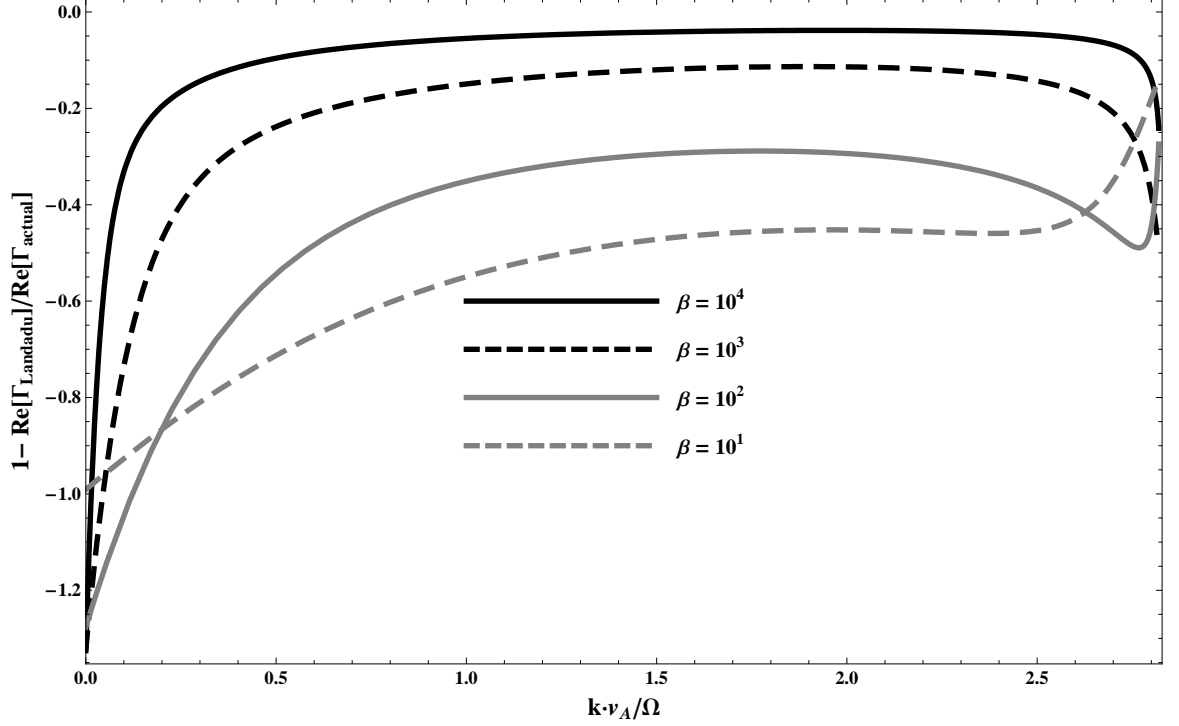


Fig. 7.2.3.— Comparison of the relative difference between the real part of the “Landau” and “exact” expressions for the growth rate, defined as  $1 - \text{Re}(\Gamma_{\text{Landau}}) / \text{Re}(\Gamma_{\text{exact}})$ .

## 7.2.2 Pressure Anisotropy in Collisionless Plasmas

A collisionless or mildly collisional plasma can easily support equilibrium pressure anisotropy, and instabilities can lead to anisotropic pressures. If one looks at physical processes whose phase velocity is much faster than the sound speed, the energy balance equations are given by Chew et al. (1956):

$$\frac{d}{dt} \left( \frac{p_{\perp}}{\rho B} \right) = 0, \quad (7.2.9)$$

$$\frac{d}{dt} \left( \frac{p_{\parallel} B^2}{\rho^3} \right) = 0. \quad (7.2.10)$$

Increasing the magnetic field, while keeping the density constant, leads to an increase in perpendicular pressure while a decrease in parallel pressure. Likewise, in the oppo-

site limit of modes far slower than the sound speed, the evolution equations of parallel and perpendicular pressure are given in Eqs. (5.2.14) and (5.2.15). If  $\delta B/B_0 > 0$ , then  $\delta p_\perp/p_0 > 0$  and  $\delta p_\parallel/p_0 < 0$ .

### MHD Unstable Modes in Anisotropic Plasma

We consider a Bimaxwellian plasma,  $p_\parallel \neq p_\perp$ . The force balance equations can be represented in the following form useful in studies of solar wind physics (Parker 1958a). Terms in **purple** denoting anisotropic pressure forces that drive **mirror modes**, and terms in **blue** drive **firehose modes**.

$$\rho \frac{\partial \mathbf{V}}{\partial t} = -\nabla \left( p + \frac{B^2}{8\pi} \right) + \frac{\mathbf{B} \cdot \nabla \mathbf{B}}{4\pi} + \frac{1}{3} \nabla (p_\parallel - p_\perp) - \frac{\mathbf{B} \cdot \nabla \mathbf{B}}{4\pi} \times \frac{p_\parallel - p_\perp}{B^2}. \quad (7.2.11)$$

If  $p_\parallel > p_\perp$  becomes sufficiently large, the magnetic tension coefficient associated with  $\mathbf{B} \cdot \nabla \mathbf{B}$  becomes negative leading to *firehose* instability. Likewise, if  $p_\perp > p_\parallel$  becomes sufficiently large then the pressure response  $\nabla p$  is no longer restoring leading to *mirror* instabilities.

Here we derive the ion density and pressure response, where  $T_{i\perp 0}$  and  $T_{i\parallel 0}$  are the ion perpendicular and parallel temperatures, respectively. The equilibrium pressure tensor is given by,

$$\mathbb{P}_0 = p_{\perp 0} \mathbb{I} + \mathbf{b}_0 \mathbf{b}_0 (p_{\parallel 0} - p_{\perp 0}). \quad (7.2.12)$$

The radial component of the divergence of the equilibrium pressure tensor is given by,

$$(\nabla \cdot \mathbb{P}_0)_R = \frac{\partial p_{\perp 0}}{\partial R} + \frac{\partial b_{R0}}{\partial z} b_{z0} (p_{\parallel 0} - p_{\perp 0}) - \frac{\cos^2 \chi}{R} (p_{\parallel 0} - p_{\perp 0}). \quad (7.2.13)$$

The perturbed distribution function is given by,

$$\begin{aligned} \delta f_i = & \frac{m_p u_{\parallel}}{k_B T_{i\parallel}} \left( \frac{-ik_{\parallel} \mu \delta B + e \delta E_{\parallel} / m_p + [k_B T_{i\perp} / m_p] \bar{B}_R \partial \ln p_{i\perp 0} / \partial R}{\Gamma + ik_{\parallel} u_{\parallel}} - \right. \\ & \left. \frac{2\Omega\Gamma \cos \chi \bar{B}_R}{ik_{\parallel} (\Gamma + ik_{\parallel} u_{\parallel})} - \frac{\Omega' R \cos \chi \bar{B}_R}{ik_{\parallel}} \right) f_{i0}^0 - \frac{\bar{B}_R}{ik_{\parallel}} \left( \frac{\partial \ln n_0}{\partial R} - \frac{\partial \ln T_{i\perp}}{\partial R} - \right. \\ & \left. \frac{1}{2} \frac{\partial \ln T_{i\parallel}}{\partial R} + \left[ \frac{m_p \mu B_0}{k_B T_{i\perp}} \times \frac{\partial \ln T_{i\perp}}{\partial R} + \frac{m_p u_{\parallel}^2}{2k_B T_{i\parallel}} \times \frac{\partial \ln T_{i\parallel}}{\partial R} \right] \right) f_{i0}^0. \end{aligned} \quad (7.2.14)$$

This implies the forms of  $\delta\rho$ ,  $\delta p_{i\perp}$ , and  $\delta p_{i\parallel}$ ,

$$\begin{aligned} \delta \bar{\rho} = & \frac{\delta B}{B} \left( 1 - \frac{T_{i\perp}}{T_{i\parallel}} R(i\zeta_{i\parallel}) \right) + \frac{i\bar{B}_R}{k_{\parallel}} \left( \frac{\partial \ln \rho}{\partial R} \right) - \\ & \frac{i\bar{B}_R}{k_{\parallel}} \left( \frac{T_{i\perp}}{T_{i\parallel}} \right) \frac{\partial \ln p_{i\perp 0}}{\partial R} R(i\zeta_{i\parallel}) + \frac{2\Omega\Gamma}{k_{\parallel}^2 v_{i\parallel}^2} R(i\zeta_{i\parallel}) \bar{B}_R \cos \chi, \end{aligned} \quad (7.2.15)$$

$$\begin{aligned} \frac{\delta p_{i\perp}}{p_{i\perp 0}} = & 2 \frac{\delta B}{B} \left( 1 - \frac{T_{i\perp}}{T_{i\parallel}} R(i\zeta_{i\parallel}) \right) + \frac{i\bar{B}_R}{k_{\parallel}} \left( \frac{\partial \ln p_{i\perp 0}}{\partial R} \right) \times \\ & \left( 1 - \frac{T_{i\perp}}{T_{i\parallel}} R(i\zeta_{i\parallel}) \right) + \frac{2\Omega\Gamma}{k_{\parallel}^2 v_{i\parallel}^2} R(i\zeta_{i\parallel}) \bar{B}_R \cos \chi, \end{aligned} \quad (7.2.16)$$

$$\begin{aligned} \frac{\delta p_{i\parallel}}{p_{i\parallel 0}} = & \frac{\delta B}{B} \left( 1 - \frac{T_{i\perp}}{T_{i\parallel}} [1 - 2\zeta_{i\parallel}^2 R(i\zeta_{i\parallel})] \right) + \\ & \frac{i\bar{B}_R}{k_{\parallel}} \left( \frac{T_{i\perp}}{T_{i\parallel}} \right) \frac{\partial \ln p_{i\perp 0}}{\partial R} \left( 1 - \frac{T_{i\perp}}{T_{i\parallel}} [1 - 2\zeta_{i\parallel}^2 R(i\zeta_{i\parallel})] \right) + \\ & \frac{2\Omega\Gamma}{k_{\parallel}^2 v_{i\parallel}^2} (1 - 2\zeta_{i\parallel}^2 R(i\zeta_{i\parallel})) \bar{B}_R \cos \chi. \end{aligned} \quad (7.2.17)$$

In this case,

$$\zeta_{i\parallel} = \frac{\Gamma}{k_{\parallel} v_{i\parallel} \sqrt{2}}. \quad (7.2.18)$$

When  $T_{i\perp} = T_{i\parallel}$  we reproduce  $\delta p_{\perp}$ ,  $\delta p_{\parallel}$ , and  $\delta\rho$  given by Eqs. (5.2.7), (5.2.8), and (5.2.9), respectively. The force balance equation for an equilibrium anisotropic plasma

is,

$$\begin{aligned}
& \rho \left( \left[ \frac{\partial}{\partial t} + \Omega \frac{\partial}{\partial \phi} \right] \mathbf{u} + \mathbf{u} \cdot \nabla \mathbf{u} - 2\Omega \hat{\mathbf{z}} \times \mathbf{u} + \Omega' R u_R \hat{\phi} \right) + \\
& \nabla \cdot (p_{\perp} + \mathbf{b}\mathbf{b} [p_{\parallel} - p_{\perp}]) = \frac{1}{c} \mathbf{J} \times \mathbf{B} + \\
& \frac{\rho}{\rho_0} (\nabla p_{\perp 0} + \nabla \cdot [\mathbf{b}_0 \mathbf{b}_0 (p_{\parallel 0} - p_{\perp 0})]) ,
\end{aligned} \tag{7.2.19}$$

so that we have the following expression for the perturbed force balance equation,

$$\begin{aligned}
& \gamma^2 \bar{\mathbf{B}} - \gamma^2 \left( \delta \bar{\rho} - \frac{\alpha_P - \alpha_T}{ix\beta_{\parallel}^{1/2}} \bar{B}_R \right) \mathbf{b} + 2\gamma \hat{\mathbf{z}} \times \bar{\mathbf{B}} + 2 \frac{d \ln \Omega}{d \ln R} \bar{B}_R \hat{\mathbf{R}} - \\
& 2\gamma \hat{\mathbf{z}} \times \mathbf{b} \left( \delta \bar{\rho} - \frac{\alpha_P - \alpha_T}{ix\beta_{\parallel}^{1/2}} \bar{B}_R \right) = \hat{\mathbf{k}} x \beta_{\parallel} \Delta_i \frac{\delta p_{\perp}}{p_{\perp 0}} + x^2 \beta_{\parallel} (\delta p_{\parallel} / p_{\parallel 0} - \\
& \Delta_i \delta p_{\perp} / p_{\perp 0}) \mathbf{b} + x^2 \beta_{\parallel} \left( \bar{\mathbf{B}} - 2 \frac{\delta B}{B} \mathbf{b} \right) (1 - \Delta_i) + \\
& ix\beta_{\parallel}^{1/2} \alpha_P (1 - \Delta_i) \bar{B}_R \mathbf{b} - ix\beta_{\parallel}^{1/2} \alpha_P \Delta_i \delta \bar{\rho} \hat{\mathbf{R}} - x^2 \bar{\mathbf{B}} + \hat{\mathbf{k}} x \frac{\delta B}{B},
\end{aligned} \tag{7.2.20}$$

where  $\Delta_i = p_{i\perp 0} / p_{i\parallel 0}$  is the anisotropy parameter and  $\beta_{\parallel} = 4\pi p_{\parallel 0} / B_0^2$ . The equations of radial, azimuthal, and magnetic-field directed components of the force balance

equation are,

$$\begin{aligned} \bar{B}_R \left( \gamma^2 + x^2 \left[ 1 + \frac{k_R^2}{k_Z^2} \right] + 2 \frac{d \ln \Omega}{d \ln R} - 2 \gamma \cos \chi \frac{\alpha_P - \alpha_T}{ix \beta_{\parallel}^{1/2}} - \right. \\ \left. x^2 \beta_{\parallel} [1 - \Delta_i] \right) - 2 \gamma \bar{B}_{\phi} + \delta \bar{\rho} \left( 2 \gamma \cos \chi + ix \beta_{\parallel}^{1/2} \alpha_P \Delta_i \right) = \end{aligned} \quad (7.2.21)$$

$$\begin{aligned} \frac{k_R}{k_Z \sin \chi} x^2 \beta_{\parallel} \Delta_i \delta p_{\perp} / p_{\perp}, \\ \bar{B}_R \left( \gamma^2 \cos \chi \frac{\alpha_P - \alpha_T}{ix \beta_{\parallel}^{1/2}} + 2 \gamma - ix \beta_{\parallel}^{1/2} \cos \chi [1 - \Delta_i] \alpha_P - \right. \\ \left. 2 x^2 \beta_{\parallel} \frac{k_R \cos \chi}{k_Z \sin \chi} \right) + (\gamma^2 + x^2 - x^2 \beta_{\parallel} [1 - \Delta_i] [1 - 2 \cos^2 \chi]) \bar{B}_{\phi} - \end{aligned} \quad (7.2.22)$$

$$\begin{aligned} \gamma^2 \cos \chi \delta \bar{\rho} = x^2 \cos \chi \beta_{\parallel} (\delta p_{\parallel} / p_{\parallel} - \Delta_i \delta p_{\perp} / p_{\perp}), \\ \bar{B}_R \left( \gamma^2 \frac{\alpha_P - \alpha_T}{ix \beta_{\parallel}^{1/2}} - \gamma^2 \frac{k_R}{k_Z} \sin \chi + 2 \gamma \cos \chi - ix \beta_{\parallel}^{1/2} \alpha_P (1 - \Delta_i) - \right. \\ \left. x^2 \beta_{\parallel} \frac{k_R}{k_Z} \sin \chi (1 - \Delta_i) \right) + (\gamma^2 + x^2 \beta_{\parallel} (1 - \Delta_i)) \cos \chi \bar{B}_{\phi} - \end{aligned} \quad (7.2.23)$$

$$\gamma^2 \delta \bar{\rho} = x^2 \beta_{\parallel} \delta p_{\parallel} / p_{\parallel}$$

The growth rate as a function of anisotropy parameter  $\Delta_i - 1$  is shown below, for the collisionless MRI, in Fig. (7.2.4). This leads to the following complicated branches of solution arising from MHD pressure anisotropy. In **red** we denote the equilibrium magnetic field being purely vertical. In this instance, for zero equilibrium pressure anisotropy  $p_{\perp 0} = p_{\parallel 0}$ , there exist no viscous forces and the MRI dispersion relation is reproduced. In this instance, the primary upper solution “(U)” becomes MHD stabilized at finite pressure anisotropies  $|p_{\perp 0} / p_{\parallel 0} - 1| \sim \beta^{-1}$ . In **blue** we denote a  $\chi = \pi/3$  magnetic field equilibrium. The “(U)” branch refers to the MRI solution destabilized in the regime  $p_{\perp 0} < p_{\parallel 0}$  but stabilized for  $p_{\perp 0} / p_{\parallel 0} - 1 \sim \beta^{-1}$ . The “(L)” branch refers to slower MHD firehose modes that are excited at a threshold  $p_{\perp 0} < p_{\parallel 0}$ . At a critical level of anisotropy the “(U)” and “(L)” branches join to a



“(C)” (complex) branch of this solution at smaller  $p_{\perp 0}/p_{\parallel 0}$ . In green we denote that  $\chi = \pi/4$  equilibrium magnetic field, with its corresponding “(U)” and “(L)” branches.

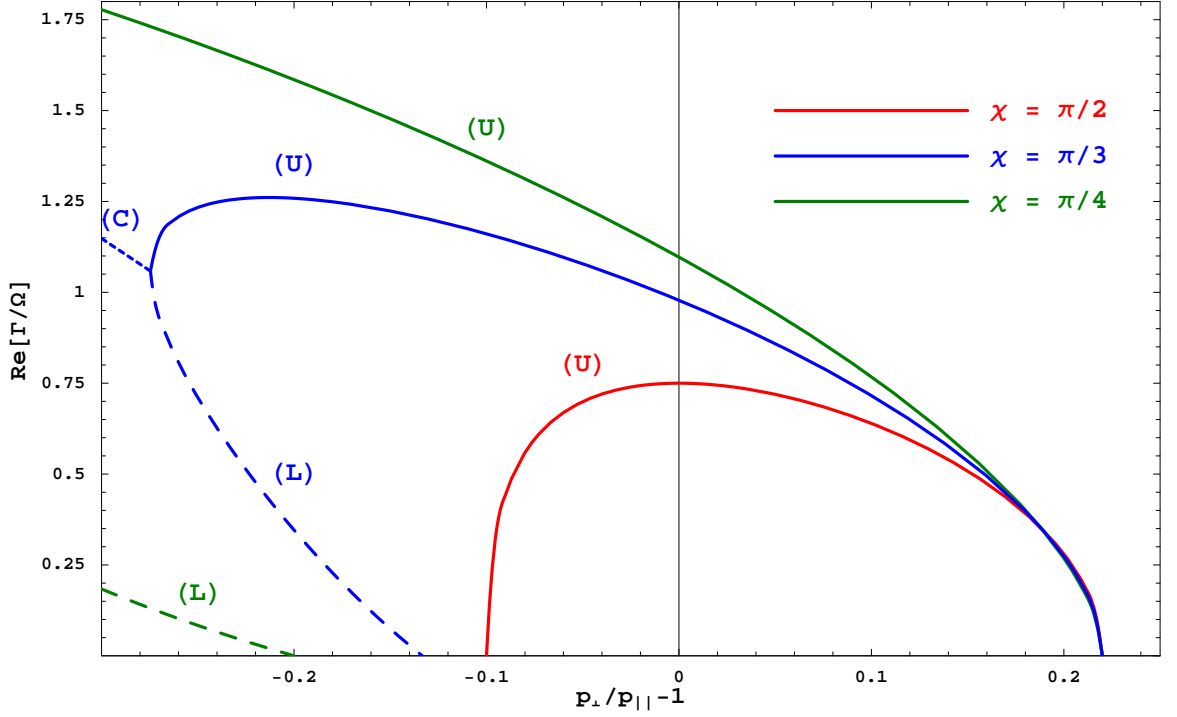


Fig. 7.2.4.— Demonstration of additional instabilities arising from pressure anisotropy. We take  $\beta = 10$  and  $k_{\parallel} v_A / \Omega = \sqrt{15/16}$ , with wavenumber being purely vertical, and plot the real part of the growth rate,  $\text{Re}(\Gamma/\Omega)$ . Note that for the MRI, all solutions of equilibrium magnetic fields that are not purely vertical  $\chi < \pi/2$  become stabilized at  $p_{\perp 0}/p_{\parallel 0} - 1 \sim \beta^{-1}$ .

### Gyrokinetic Instabilities in Anisotropic Plasmas

Although a differentially rotating plasma is unstable to anisotropizing MHD instabilities, if  $|p_{\perp}/p_{\parallel} - 1|$  then we can excite gyrokinetic instabilities, with growth rates of order the ion gyrofrequency, that can isotropize the plasma. For plasmas in which  $p_{i\perp 0}/p_{i\parallel 0} > 1$ , the gyrokinetic proton cyclotron (Gary et al. 1994) or mirror (Southwood & Kivelson 1993) instabilities may operate. For  $p_{\parallel 0}/p_{\perp 0} > 1$  the gyroki-

netic firehose instability (Kennel & Sagdeev 1967) or the oblique firehose instability (Hellinger & Matsumoto 2000) may operate. Furthermore, as well as operating within collisionless plasmas, these instabilities may operate in high- $\beta$  magnetized but collisional astrophysical plasmas, such as within galactic clusters (Schekochihin et al. 2005a,b).

Numerical 2D kinetic simulations of anisotropic magnetized plasmas (Gary et al. 1996, 1997) demonstrate the threshold pressure anisotropies that can drive fast ion cyclotron instabilities, in which the growth rate is of order the ion cyclotron frequency. They have found thresholds for fast growth where  $p_{i\perp 0}/p_{i\parallel 0} - 1 \geq S_{\parallel}/\beta_{i\parallel}^{\alpha_{\parallel}}$ , where  $\beta_{i\parallel} = 8\pi p_{i\parallel 0}/B_0^2$ ,  $S_{\parallel}$  and  $\alpha_{\parallel}$  are fitting parameters, and  $0.4 \lesssim \alpha_{\parallel} \lesssim 0.5$ . These same simulations demonstrate instability to the fast mirror instability where  $p_{i\perp 0}/p_{i\parallel 0} - 1 \geq S_{\perp}/\beta_{i\perp}^{\alpha_{\perp}}$ , where  $\beta_{i\perp} = 8\pi p_{i\perp 0}/B_0^2$ , and  $S_{\perp}$  and  $\alpha_{\perp}$  are fitting parameters. These simulations also demonstrate that relatively little energy from the pressure anisotropy goes into magnetic energy. Numerical simulations of the gyrokinetic and oblique firehose instability (Gary et al. 1998) also show a lower threshold to firehose instabilities, of the form  $p_{i\parallel 0}/p_{i\perp 0} - 1 < S_p/\beta_{i\parallel}^{\alpha_P}$ , where  $S_p$  and  $\alpha_P$  are fitting parameters, and with relatively weak magnetic fields excited by these instabilities. This implies that numerical simulations of collisionless MHD can treat the effect of these instabilities as a “hard wall” on pressure anisotropy.

There is also strong evidence that, for example, the solar wind is kept marginally stable to these fast gyrokinetic instabilities, as demonstrated by Hellinger et al. (2006) in Fig. (7.2.5). Research of collisionless and mildly collisional MHD turbulence within an astrophysical context have been constructed (Schekochihin & Cowley 2005, 2006; Schekochihin et al. 2007; Howes et al. 2007a,b), that build upon previous treatments of weak (Sridhar & Goldreich 1994) and strong (Goldreich & Sridhar 1995) MHD turbulence. However, these treatments of MHD turbulence in collisionless plasmas

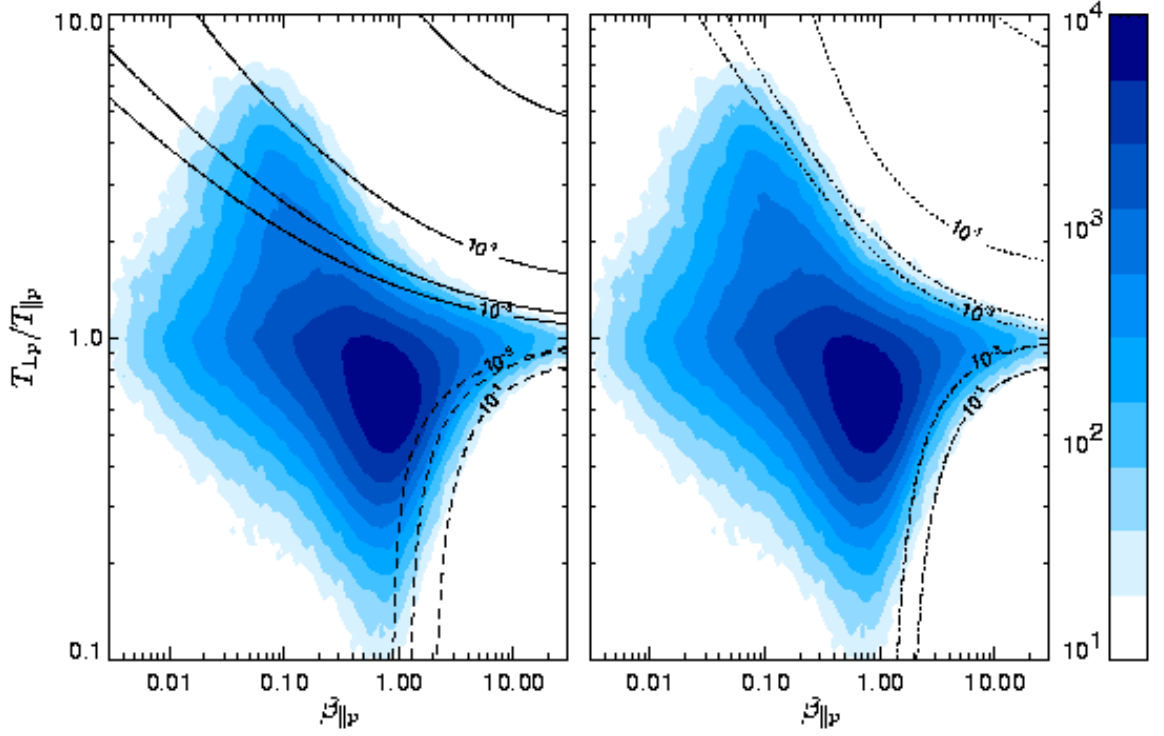


Fig. 7.2.5.— Relative frequency of measured proton parallel plasma  $\beta_{\parallel p} = 8\pi p/B_{\parallel}^2$  and relative proton temperature anisotropy  $T_{\perp p}/T_{\parallel p}$  from the WIND/SWE data (1995-2001) for the slow solar wind ( $v < 600 \text{ km s}^{-1}$ ). The solar wind remains marginally stable to gyrokinetic instabilities – for the case  $T_{\perp p} > T_{\parallel p}$  it is the oblique firehose instability (on right), and for the case that an observed  $T_{\perp p} < T_{\parallel p}$  it may be the proton cyclotron or mirror instabilities (left and right). This figure is taken from Hellinger et al. (2006).

consider weak turbulence supporting a power-law cascade of turbulent spectrum, cut off on the shortest length scales by dissipative gyrokinetic modes. These theoretical models treat the effects of fast gyrokinetic instabilities that isotropize the particle distribution as either a source of enhanced effective scattering by short-wavelength magnetic field structure (Schekochihin & Cowley 2006; Schekochihin et al. 2007) or posit secondary roles that do not qualitatively alter a picture of weak power-law turbulence (Howes et al. 2007a,b). Schekochihin et al. (2005b) has proposed physical effects that these gyrokinetic isotropic instabilities might play if the turbulence is either strong or weak. Further work should focus on the possibly important role

that the mirror/ion cyclotron and parallel/gyrokinetic firehose might play in, for instance, the spectrum of turbulence and critical anisotropy seen in the solar wind (Kasper et al. 2002; Hellinger et al. 2006).

## 7.3 Further Work

The research described in this thesis lies clearly on the path for further studies of underluminous accretion. We now describe directions for further work that will help to make predictive models of underluminous accretion. We describe further analytic models of local instabilities in accretion flows, which allows for more physics to be explored, but not with great depth. We then describe further numerical work, which allows for the detailed behavior of specific physical processes.

### Further Analytic Work

In §6 we demonstrated additional physics that may occur when studying dilute rotationally supported plasmas. We may explore in what manner the collisional regime connects to the collisionless regime where the electron thermal energy is dominant, . We can also explore in more detail the effects of the collisionless MRI and MTI away from the midplane. In order to be analyzed more thoroughly, we need a more efficient method to calculate modified plasma response functions  $Z_n(\zeta, \hat{z})$  and  $Z_{nc}(\zeta, \hat{z})$ . Second, recent work by Ferraro & Jardin (2006) demonstrates the gyroviscous stabilization, due to off-diagonal components of the Braginskii viscous stress tensor, of the Rayleigh-Taylor instability at relatively small values of the ion cyclotron frequency and small magnetic field strength. Off diagonal components of the viscous stress tensor may allow for new instabilities to operate in the physical parameter space of RIAFs, and may modify the collisionless MTI and MVTI. Finally, some

short-time-scale variability of fully ionized astrophysical plasmas may be due to the abrupt reconnection of magnetic fields as evidenced by sawteeth modes in magnetically confined plasmas. Whereas sawteeth instabilities are localized among the tokamak field's rational surfaces, in astrophysical disks these would be located at the sonic and magnetosonic resonances of corotating modes (Coppi & Coppi 1997, 1998). Unfortunately, nonlinear isotropic thermal, magnetic, and viscous diffusive operators, whose form and existence were hard to justify, were required to excite these modes (Coppi & Coppi 1997, 2001a,b). It may be possible, however, that an anisotropic viscous stress or collisionless viscous and thermal transport can excite these modes.

### Further Numerical Work

First, we can consider phenomenological local models of the MVTI and collisionless MTI, in order to explore the role this type of turbulence plays in the transport of angular momentum. For instance, Fig. (4.3.5) demonstrates that the MVTI, and presumably the collisionless MTI, are able to transport angular momentum outwards or inwards, depending on wavenumber, for a rigidly rotating plasma. Balbus et al. (1996) and Lesur & Longaretti (2005) have analyzed the nature of turbulence and angular momentum transport in local numerical simulations of differentially rotating hydrodynamic flows, for rotational profiles near marginal hydrodynamic stability. Similar work may be done for the MVTI or collisionless MTI for rigidly rotating flows; this may begin to resolve the question of whether there naturally exists angular momentum transport in an MVTI-unstable, rigidly rotating fluid.

Second, for the nonlinear development of the collisionless MTI or the MVTI in an accreting system, one cannot extract the necessary physics within a local simulation. Local simulations, through terms associated with energy generation via a (quasi-steady) azimuthal stress  $(-\partial\Omega/\partial\ln R)T_{R\phi})$  lead to a secular increase in

thermal energy within the computational domain (see Fig. [7.3.1]). Global simulations using the ZEUS 3D MHD algorithms only approximately conserve total energy (De Villiers & Hawley 2003). For simulations of nonradiative accretion, we require numerical MHD codes that automatically conserve mechanical, magnetic, and ther-

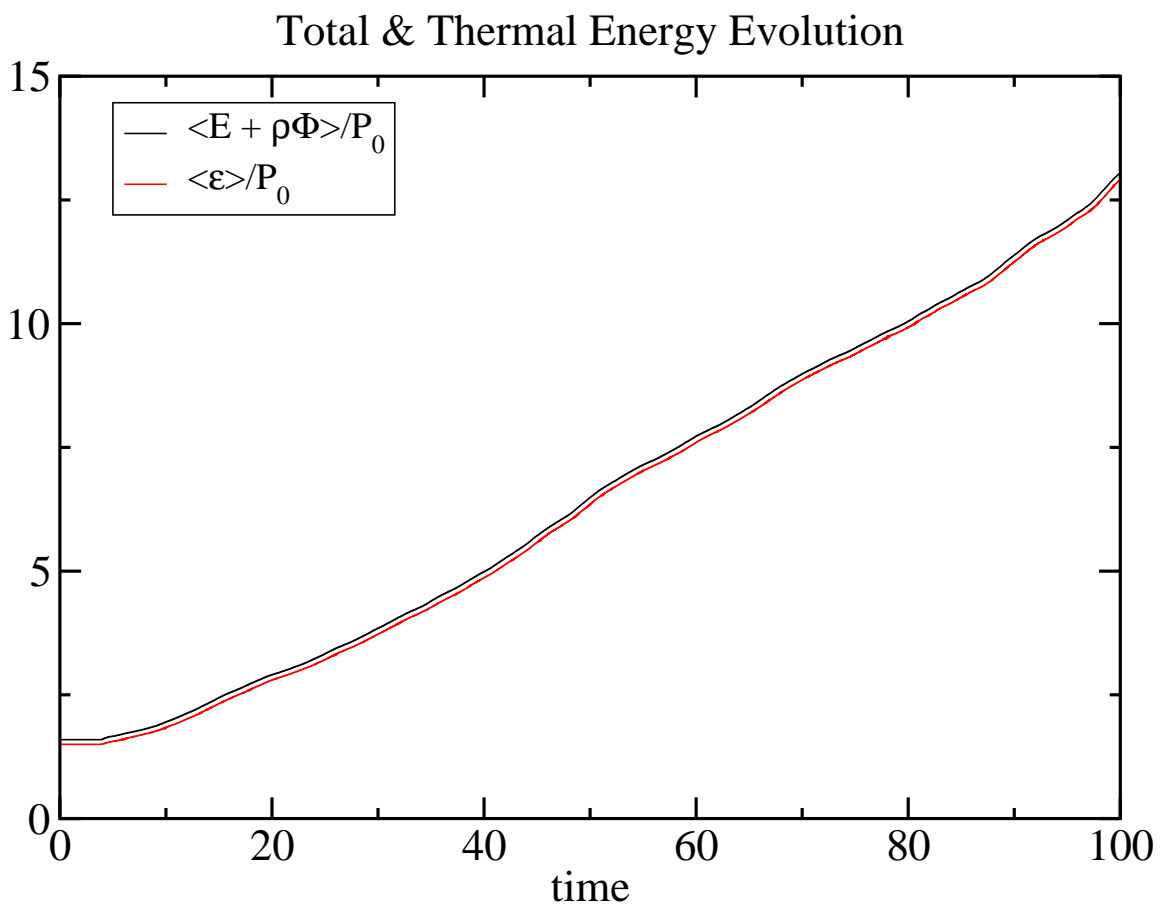


Fig. 7.3.1.— Evolution of the total energy within a local MRI simulation, using the Athena 3D MHD numerical algorithm. Total energy is accounted for naturally with Athena, and the box is “heated” due to the energy injected by the average positive azimuthal stress  $T_{R\phi}$ . This figure is taken from Gardiner & Stone (2005).

However, Sharma et al. (2006); Sharma (2006) show that the levels of saturated magnetic and gas turbulence, and fluxes of angular momentum, in a local simulation of the collisionless MRI is not qualitatively different from numerical simulations of

the MRI. Therefore it is plausible that global simulations of the collisionless MRI and MTI using the Athena 3D MHD code will not differ from global simulations of the MRI as done by De Villiers & Hawley (2003).

Finally, even the most computationally expensive global numerical simulations of radiatively inefficient flows will have a spatial range of at most a few hundred Schwarzschild radii and a temporal range of at most a few weeks for radiatively inefficient supermassive black hole accretion. Therefore, local simulations of radiatively inefficient flows may be necessary in order to characterize “local” rates of at least angular momentum flux carried by the turbulence, despite the fact that in local simulations the energy within the computational domain increases in time. Numerical results of the local MRI by Pessah et al. (2006a,b); Pessah (2007); Pessah et al. (2007), have demonstrated a nonlinear relation between turbulent angular momentum flux and gas pressure. The issue of energy transport in local simulations of RIAFs may therefore be ignored by including dissipation of the accretion energy, or by setting boundary conditions on the flux of heat or temperature as done by Parrish & Stone (2005); Parrish & Stone (2006).

## Timescales and Lengthscales in Accretion Disks

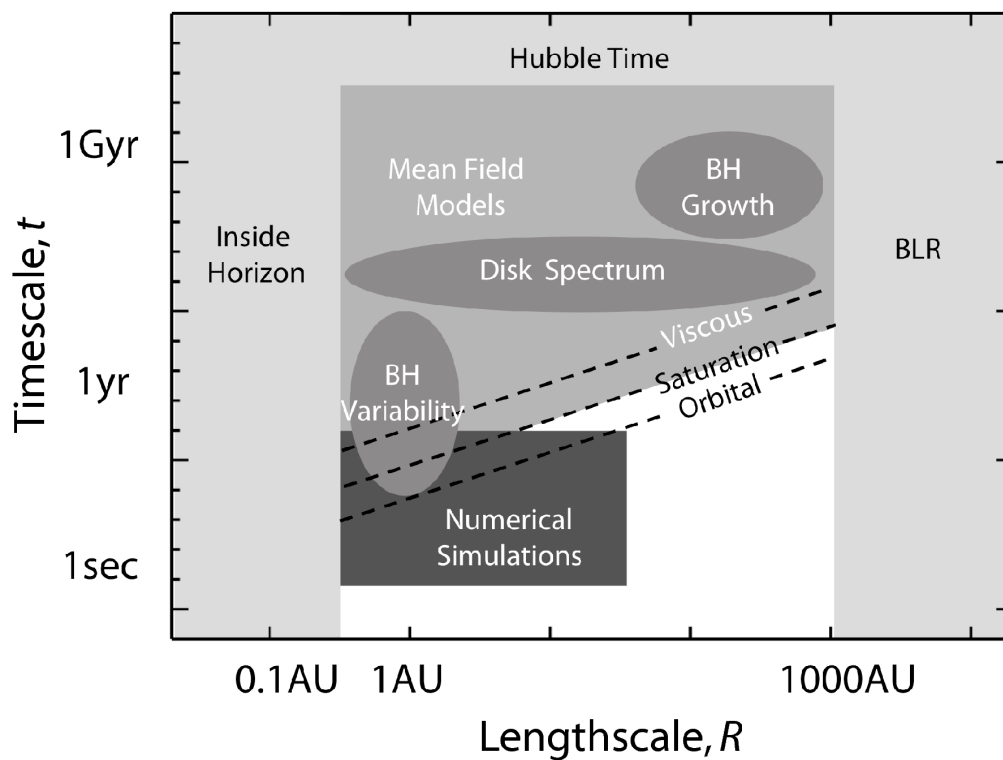


Fig. 7.3.2.— The dynamic spatial and temporal ranges of observations and numerical simulations of central galactic supermassive black hole accretion processes. Even with state-of-the-art computational facilities, there is significant disjoint between phenomena that can be explored through global numerical simulations and those that can be observed. This requires that the nature of local turbulence in RIAFs be explored in detail, in order to characterize the nature of angular momentum and heat flux due to turbulence due to the collisionless MTI and MVTI. This figure is taken from Pessah (2007).



# Appendix A

## Variables

Here we define the vocabulary of the variables, the convenient variable simplifications and normalizations, and convenient physical parameters used in the body of the thesis.

Table A.1:: Table of Variables

Name	Variable
$M$	mass of central object
$\dot{M}$	mass accretion rate
$L$	luminosity of accreting source
$\Phi = -GM/\sqrt{R^2 + z^2}$	central object gravitational potential
$R_{\text{schw}} = 2GM/c^2$	black hole Schwarzschild radius – radius of event horizon
$T_{i/e}$	ion/electron temperature
$p_{i/e}$	ion/electron pressure
$q_{i/e}$	ion/electron heat flux along magnetic field lines
$q = q_i + q_e$	total heat flux along magnetic field lines
$p = p_i + p_e$	total pressure

$\sigma$	viscous stress tensor
$n$	(ion/electron) number density
$\rho = (m_p + m_e) n$	mass density
$v_i = \sqrt{k_B T_{i0}/m_p}$	ion isothermal sound speed
$v_e = \sqrt{k_B T_{e0}/m_e}$	electron isothermal sound speed
$\theta_0 = k_B (T_{i0} + T_{e0}) / (m_p + m_e)$	isothermal sound speed squared
$\beta = \theta_0/v_A^2$	plasma ratio of thermal speed to sound speed <sup>1</sup>
$\tau_{i,e}$	ion/electron collisional time scale <sup>2</sup>
$\lambda_i = v_i/\tau_i, \lambda_e = v_e/\tau_e$	ion/electron collisional mean free paths <sup>2</sup>
$\eta_\kappa$	(electron) thermal diffusivity <sup>2</sup>
$\eta_\nu$	(ion) viscous diffusivity <sup>2</sup>
$\hat{\Omega}(R, z)$	orbital angular velocity
$\Omega_K = \sqrt{GM/R^3}$	Keplerian orbital angular velocity
$H = \theta_0^{1/2}/\Omega_K$	phenomenological disk height
$\mathbf{B}$	magnetic field
$\mathbf{E}$	electric field
$\mathbf{J}$	current density
$\mathbf{V}$	flow velocity
$\mathbf{k}$	wavenumber of unstable mode
$\Gamma$	growth rate of unstable mode (imaginary terms correspond to oscillations)
$\mathbf{u} = \mathbf{V} - R\Omega(R, z)\hat{\phi}$	net flow velocity
$B = \sqrt{\mathbf{B} \cdot \mathbf{B}}$	magnetic field magnitude

---

<sup>1</sup>In the plasma physics literature,  $\beta_{\text{lit}} = 8\pi p/B^2$  is the ratio of gas pressure to magnetic pressure. Our definition is one in which our  $\beta = \beta_{\text{lit}}/2$ .

<sup>2</sup>Fluid expressions are valid only if the mean free paths are smaller than the system scale, and if the wavelength of instability is smaller than the mean free path. This treatment is described in Chap. (4).

$\mathbf{b} = \mathbf{B}/B$	magnetic field unit vector
$v_A = B/\sqrt{4\pi\rho}$	Alfvén speed
$\omega_{pi} = \sqrt{4\pi e^2 n/m_p}$	ion plasma frequency
$\Omega_{ci} = eB/(m_p c)$	ion gyrofrequency
$\rho_i = v_i/\Omega_{ci}$	ion gyroradius
$p_{\parallel/\perp}$	pressure component parallel/perpendicular to the magnetic field <sup>3</sup>
$q_{\parallel/\perp}$	heat flux of parallel/perpendicular pressure field <sup>3</sup>
$r_{\parallel,\times,\perp}$	fourth-order velocity moments of distribution function, parallel/cross/perpendicular fluxes of heat <sup>3</sup>

---

Table A.2:: Table of Normalized and Simplified Variables

$\gamma = \Gamma/\Omega$	normalized growth rate
$a_{\parallel} = \mathbf{a} \cdot \mathbf{b}$	component of vector quantity $\mathbf{a}$ (for example, wavenumber $\mathbf{k}$ or electric field $\mathbf{E}$ ) along the magnetic field
$\hat{\mathbf{k}} = \mathbf{k}v_A/\Omega$	normalized wavenumber
$x = \mathbf{k} \cdot \mathbf{b}_0 v_A/\Omega$	normalized parallel wavenumber
$\alpha_P = -H \frac{\partial \ln p_0}{\partial R} > 0$	pressure normalized scale height
$\alpha_T = -H \frac{\partial \ln T_0}{\partial R} > 0$	temperature normalized scale height
$\alpha_S = -H \frac{\partial \ln p_0 \rho_0^{-5/3}}{\partial R}$	entropy normalized scale height
$= \frac{5}{3}\alpha_T - \frac{2}{3}\alpha_P$	normalized entropy scale height <sup>4</sup>

<sup>3</sup>See Chap. (5), which enumerates a kinetic description of a dilute plasma, for the form of these  $p_{\parallel,\perp}$ ,  $q_{\parallel,\perp}$ , and  $r_{\parallel,\times,\perp}$ . Furthermore, the expression for equilibrium parallel ion pressure is given by  $p_{0\parallel i}$ .

<sup>4</sup>Convective stability in the absence of rotation requires that  $\alpha_S < 0$

---

$\hat{\eta}_\nu = \eta_\nu \Omega / v_A^2$	normalized viscosity
$\hat{\eta}_\kappa = \eta_\kappa \Omega / v_A^2$	normalized thermal conductivity

---

Table A.3:: Physical Parameters Associated With Black  
Hole Accretion

---



---

mass of black holes	$10^6 - 10^{10} M_\odot$
Scwharzchild radius	$3 \times 10^5 (M/M_\odot) \text{ cm} = 3 \times 10^{11} - 3 \times 10^{15} \text{ cm}$
ion number density of ambient gas	$1 - 100 \text{ cm}^{-3}$
temperature of ambient gas	$10^6 - 10^8 \text{ K}$
ion temperature in flow	$10^6 - 10^{12} \text{ K}$
electron temperature in flow	$10^6 - 10^{10} \text{ K}$

---

## Appendix B

### Plasma Equilibrium Disk

Here we calculate the equilibrium profile of a slender magnetized rotating plasma disk. We consider an axisymmetric equilibrium in which the magnetic thermal energy is highly subthermal, hence Lorentz forces do not play a role in describing the equilibrium. In the MHD limit strong radial and vertical electric fields are induced that lead to quasineutrality and single flow velocity in the plasma. For simplicity, we consider an electron-ion plasma, where the ratio of ion to electron temperatures is kept constant. We define the temperature  $T$  as the sum of ion and electron temperatures,  $T = T_i + T_e$ . We express the  $z$ -dependence of equilibrium angular velocity, density, temperature, and magnetic field by,

$$\Omega(R, z) = \Omega(R, 0) + \Delta\Omega(z), \quad (\text{B.1})$$

$$\rho_0(R, z) = \rho_0(R, 0) + \Delta\rho_0(z), \quad (\text{B.2})$$

$$T_0(R, z) = T_0(R, 0) + \Delta T_0(z), \quad (\text{B.3})$$

$$\mathbf{B}_0(R, z) = \mathbf{B}_0(R, 0) + \Delta\mathbf{B}_0(z). \quad (\text{B.4})$$

The equilibrium temperatures  $T_0(R, z) = T_{i0}(R, z) + T_{e0}(R, z)$ . To get the solution of the vertical disk profile, we must solve the leading-order polynomial expansions in  $z$  of  $\Delta\Omega(z)$ ,  $\Delta\rho_0(z)$ ,  $\Delta\mathbf{B}_0(z)$ , and  $\Delta T_0(z)$ . At the disk midplane,  $\Delta\Omega(z=0)/\Omega(R) = 0$ ,  $\Delta\rho_0(z=0)/\rho_0(R) = 0$ ,  $\Delta T_0(z=0)/T_0(R) = 0$ , and  $|\Delta\mathbf{B}_0(z=0)|/B_0(R) = 0$ . The total electric field is defined as,

$$\mathbf{E} = -\frac{1}{c}R\Omega\hat{\boldsymbol{\phi}} \times \mathbf{B} - \frac{1}{c}\delta\mathbf{u} \times \mathbf{B} + E_{\parallel}\mathbf{b} + E_{R,ES}\hat{\mathbf{R}} + E_{Z,ES}\hat{\mathbf{z}}, \quad (\text{B.5})$$

where  $E_{R,ES}$  and  $E_{Z,ES}$  are the radial and vertical components of the electrostatic field, respectively, and  $E_{\parallel}$  is a component of electric field parallel to the magnetic field ( $E_{\parallel} = 0$  in equilibrium). The equilibrium electric field is given by,

$$\mathbf{E}_0 = -\frac{1}{c}R\Omega(R, z)\hat{\boldsymbol{\phi}} \times \mathbf{B}_0 + \hat{E}_{0R,ES}\hat{\mathbf{R}} + \hat{E}_{0Z,ES}\hat{\mathbf{z}}, \quad (\text{B.6})$$

where  $\hat{E}_{0R,ES}$  and  $\hat{E}_{0Z,ES}$  are equilibrium electrostatic fields that ensure quasineutrality. The magnitude of these electrostatic fields is roughly of order  $\Omega/\Omega_i$  ( $\ll 1$ ) relative to that of the primary electric field  $-c^{-1}R\Omega\hat{\boldsymbol{\phi}} \times \mathbf{B}_0$ , where  $\Omega_i = eB/(m_p c)$  is the ion cyclotron frequency. Equivalently, the  $\mathbf{E} \times \mathbf{B}$  plasma drift velocity associated with the electrostatic field is of order  $\Omega/\Omega_i \ll 1$  relative to the orbital velocity.

To lowest order in  $z$ , the equilibrium nonradial magnetic field is constant. To next-lowest order in  $z$ , it has the following form:

$$\hat{B}_{0Z} = B_{0Z} + \frac{1}{2}\alpha''_{B0Z}z^2, \quad (\text{B.7})$$

$$\hat{B}_{0\phi} = B_{0\phi}. \quad (\text{B.8})$$

The gravitational acceleration experienced by species  $s$ , to second order in  $z$ , is,

$$\frac{\mathbf{F}_s}{m_s} = -\Omega_K^2 \left( 1 - \frac{3z^2}{2R^2} \right) \hat{\mathbf{R}} - \Omega_K^2 z \hat{\mathbf{z}}, \quad (\text{B.9})$$

where  $\Omega_K^2 = GM/R^3$  is the Keplerian orbital angular velocity. Eq. (B.9) implies that the angular velocity has the form:

$$\Omega(R, z) = \Omega(R) - \frac{1}{2} \alpha_\Omega z^2. \quad (\text{B.10})$$

Since  $\nabla \times \mathbf{E}_0 = 0$ , the radial magnetic field is,

$$\hat{B}_{0R} = \frac{\alpha_\Omega z}{\partial \Omega / \partial R} B_{0Z}. \quad (\text{B.11})$$

In equilibrium the magnetic field line must lie along isotherms, i.e.  $\mathbf{B}_0 \cdot \nabla T_0 = 0$ , therefore:

$$T_0(R, z) = T_0(R) \left( 1 - \frac{\alpha_\Omega z^2 / 2}{\partial \Omega / \partial R} \left( \frac{\partial \ln T_0}{\partial R} \right) \right), \quad (\text{B.12})$$

The vertical force balance condition,

$$-\frac{\partial \hat{p}_0}{\partial z} - (m_p + m_e) \hat{n}_0 \Omega_K^2 z = 0, \quad (\text{B.13})$$

implies that pressure and density profiles, up to second order in  $z$ , are,

$$\hat{p}_0(R, z) = p_0(R) - \frac{1}{2} (m_p + m_e) n_0(R) \Omega_K^2 z^2, \quad (\text{B.14})$$

$$\hat{n}_0(R, z) = n_0(R) \left( 1 - \frac{\Omega_K^2 z^2}{2\theta} + \frac{\alpha_\Omega z^2 / 2}{\partial \Omega / \partial R} \left( \frac{\partial \ln T_0}{\partial R} \right) \right). \quad (\text{B.15})$$

The radial force balance condition is given by,

$$(\Omega^2 - \Omega\alpha_\Omega z^2) R - \Omega_K^2 \left(1 - \frac{3z^2}{2R^2}\right) R = \frac{1}{\hat{n}_0 (m_p + m_e)} \frac{\partial \hat{p}_0}{\partial R}. \quad (\text{B.16})$$

Using Eqs. (B.14), (B.15), and (B.16), we solve for  $\Omega$  and  $\alpha_\Omega$  to arrive at,

$$\Omega = \sqrt{\Omega_K^2 + \frac{\theta}{R^2} \left( \frac{\partial \ln p_0}{\partial \ln R} \right)}, \quad (\text{B.17})$$

$$\alpha_\Omega = \frac{\Omega_K^2}{2R^2\Omega} \times \frac{\frac{\partial \ln p_0}{\partial \ln R} + \frac{\partial \ln n_0}{\partial \ln R}}{1 + \frac{\theta}{R^2} \left( \frac{\partial \ln p_0}{\partial \ln R} \right) \left( \frac{\partial \ln T_0}{\partial \ln R} \right) \left( \frac{\partial \Omega^2}{\partial \ln R} \right)^{-1}}. \quad (\text{B.18})$$

Now let us assume that midplane temperature and pressures are power laws of radius  $R$ , so that  $\partial \ln p_0 / \partial \ln R$  and  $\partial \ln T_0 / \partial \ln R$  are constants. Using Eqs. (B.17) and (B.18), the equilibrium radial magnetic field, Eq. (B.11), is written as,

$$\hat{B}_{0R} = -\frac{H}{R} \left( \frac{z}{H} \right) \frac{2 \frac{\partial \ln p_0}{\partial \ln R} - \frac{\partial \ln T_0}{\partial \ln R}}{3 + 2H^2/R^2 \left( 1 - \frac{\partial \ln T_0}{\partial \ln R} \right) \frac{\partial \ln p_0}{\partial \ln R}} B_{0Z}. \quad (\text{B.19})$$

The disk scale height is  $H = \theta^{1/2} / \Omega_K$ . Since  $\nabla \cdot \mathbf{B}_0 = 0$  the vertical magnetic field, given in Eq. (B.7), is,

$$\hat{B}_{0Z} = B_{0Z} \left( 1 - \frac{\frac{\partial \ln p_0}{\partial \ln R} \left( 2 \frac{\partial \ln p_0}{\partial \ln R} - \frac{\partial \ln T_0}{\partial \ln R} \right) \left( 1 - \frac{\partial \ln T_0}{\partial \ln R} \right) \left( 2 - \frac{\partial \ln T_0}{\partial \ln R} \right)}{\left( 3 + 2H^2/R^2 \frac{\partial \ln p_0}{\partial \ln R} \left( 1 - \frac{\partial \ln T_0}{\partial \ln R} \right) \right)^2} \left( \frac{H}{R} \right)^4 \left( \frac{z}{H} \right)^2 \right). \quad (\text{B.20})$$



Likewise, the equilibrium pressure, density, and angular velocity profiles are,

$$\hat{p}_0 = p_0 \left( 1 - \frac{z^2}{2H^2} \right), \quad (\text{B.21})$$

$$\rho_0 = \rho_0 \left( 1 - \frac{3 + 2H^2/R^2 \left( \frac{\partial \ln p_0}{\partial \ln R} \left( 2 - \frac{\partial \ln T_0}{\partial \ln R} \right) - \frac{1}{2} \frac{\partial \ln T_0}{\partial \ln R} \right)}{6 + 4H^2/R^2 \frac{\partial \ln p_0}{\partial \ln R} \left( 1 - \frac{\partial \ln T_0}{\partial \ln R} \right)} \left( \frac{z}{H} \right)^2 \right), \quad (\text{B.22})$$

$$T_0 = T_0 \left( 1 + \frac{\frac{\partial \ln T_0}{\partial \ln R} \left( \frac{\partial \ln p_0}{\partial \ln R} - \frac{1}{2} \frac{\partial \ln T_0}{\partial \ln R} \right)}{3 + 2H^2/R^2 \frac{\partial \ln p_0}{\partial \ln R} \left( 1 - \frac{\partial \ln T_0}{\partial \ln R} \right)} \left( \frac{H}{R} \right)^2 \left( \frac{z}{H} \right)^2 \right), \quad (\text{B.23})$$

$$\Omega = \Omega_K \sqrt{1 + H^2/R^2 \frac{\partial \ln p_0}{\partial \ln R} \left( 1 - \left( \frac{H}{R} \right)^2 \left( \frac{z}{H} \right)^2 \times \right.} \\ \left. \frac{\frac{\partial \ln p_0}{\partial \ln R} - \frac{1}{2} \frac{\partial \ln T_0}{\partial \ln R}}{2 \left( 1 + H^2/R^2 \frac{\partial \ln p_0}{\partial \ln R} \right) \left( 1 - \frac{H^2/R^2 \left( \frac{\partial \ln p_0}{\partial \ln R} \right) \left( \frac{\partial \ln T_0}{\partial \ln R} \right)}{9 + H^2/R^2 \left( 2 - \frac{\partial \ln T_0}{\partial \ln R} \right) \frac{\partial \ln p_0}{\partial \ln R}} \right)} \right). \quad (\text{B.24})$$

Expressions for  $\hat{E}_{0R,\text{ES}}$  and  $\hat{E}_{0Z,\text{ES}}$  can be derived from the following radial and vertical force balance equations for the ions and electrons,

$$\frac{e}{m_p} E_{0R,\text{ES}} - \Omega_K^2 R \left( 1 - \frac{3z^2}{2R^2} \right) = \frac{1}{m_p \hat{n}_0} \frac{\partial \hat{p}_{i0}}{\partial R} - \Omega^2 R, \quad (\text{B.25})$$

$$-\frac{e}{m_e} E_{0R,\text{ES}} - \Omega_K^2 R \left( 1 - \frac{3z^2}{2R^2} \right) = \frac{1}{m_e \hat{n}_0} \frac{\partial \hat{p}_{e0}}{\partial R} - \Omega^2 R, \quad (\text{B.26})$$

$$\frac{e}{m_p} E_{0Z,\text{ES}} - \Omega_K^2 z = \frac{1}{m_p \hat{n}_0} \frac{\partial \hat{p}_{i0}}{\partial z}, \quad (\text{B.27})$$

$$-\frac{e}{m_e} E_{0Z,\text{ES}} - \Omega_K^2 z = \frac{1}{m_e \hat{n}_0} \frac{\partial \hat{p}_{e0}}{\partial z}. \quad (\text{B.28})$$

The entropy gradient in the vertical direction is,

$$\frac{\partial \ln \hat{p}_0}{\partial z} \frac{\partial \ln \hat{p}_0 \rho_0^{-5/3}}{\partial z} \approx -\frac{2}{3} \frac{z^2}{H^4} < 0 \quad (\text{B.29})$$

Hence this equilibrium disk is Schwarzschild stable.

Since equilibrium radial gradients have scale heights  $\sim R$ , we conclude that from

Eqs. (B.19), (B.23), and (B.24) for thin disks, the orbital velocity  $\Omega \approx \Omega_K$ , the radial magnetic field is negligible, and isotherms to a good approximation lie along surfaces of constant  $R$ . For thick disks,  $H \lesssim R$  or equivalently  $\theta \lesssim \Omega_K^2 R^2$  hold. Therefore, the orbital angular velocity is significantly sub-Keplerian, there is a significant radial magnetic field, and isotherms no longer lie along surfaces of constant  $R$ .

For a thin disk, from Eqs. (B.19) - (B.24), the equilibrium densities, magnetic fields, and pressures, are modified as,

$$\begin{aligned}\rho_0 &\approx \rho_0(R) \left(1 - \frac{z^2}{2H^2}\right), \\ \hat{p}_0 &\approx p_0(R) \left(1 - \frac{z^2}{2H^2}\right), \\ \Omega &\approx \Omega_K, \\ \mathbf{B}_0 &\approx B_{0\phi} \hat{\phi} + B_{0Z} \hat{z}.\end{aligned}\tag{B.30}$$

In addition, isothermality in  $z$  implies  $T_{i0}(R, z) = T_{i0}(R)$ , and  $T_{e0}(R, z) = T_{e0}(R)$ . In a thin disk, from Eqs. (B.25) - (B.28), the electrostatic radial  $\hat{E}_{0R,ES}$  and vertical  $\hat{E}_{0Z,ES}$  fields are,

$$\hat{E}_{0Z,ES} \approx -\Omega_K^2 z \frac{m_p T_{e0} - m_e T_{i0}}{T_{e0} + T_{i0}},\tag{B.31}$$

$$\hat{E}_{0R,ES} \approx -\frac{1}{n_0} \left( \frac{m_p T_{e0} - m_e T_{i0}}{m_p + m_e} \right) \frac{\partial \ln p_0}{\partial R}.\tag{B.32}$$

Ion and electron force balance, in the radial and vertical directions, is shown in Fig. (B.1).  $\mathbf{F}_e = F_{eR} \hat{\mathbf{R}} + F_{eZ} \hat{\mathbf{z}}$  and  $\mathbf{F}_i = F_{iR} \hat{\mathbf{R}} + F_{iZ} \hat{\mathbf{z}}$  are the electron and ion gravitational forces, respectively;  $\mathbf{F}_e^{\text{ES}} = F_{eR}^{\text{ES}} \hat{\mathbf{R}} + F_{eZ}^{\text{ES}} \hat{\mathbf{z}}$  and  $\mathbf{F}_i^{\text{ES}} = F_{iR}^{\text{ES}} \hat{\mathbf{R}} + F_{iZ}^{\text{ES}} \hat{\mathbf{z}}$  are the electron and ion electrostatic forces, respectively; and  $\mathbf{F}_e^p = F_{eR}^p \hat{\mathbf{R}} + F_{eZ}^p \hat{\mathbf{z}}$  and  $\mathbf{F}_i^p = F_{iR}^p \hat{\mathbf{R}} + F_{iZ}^p \hat{\mathbf{z}}$  are the electron and ion pressure forces, respectively.

We next demonstrate that an inviscid, insulating, nonmagnetized, and incom-

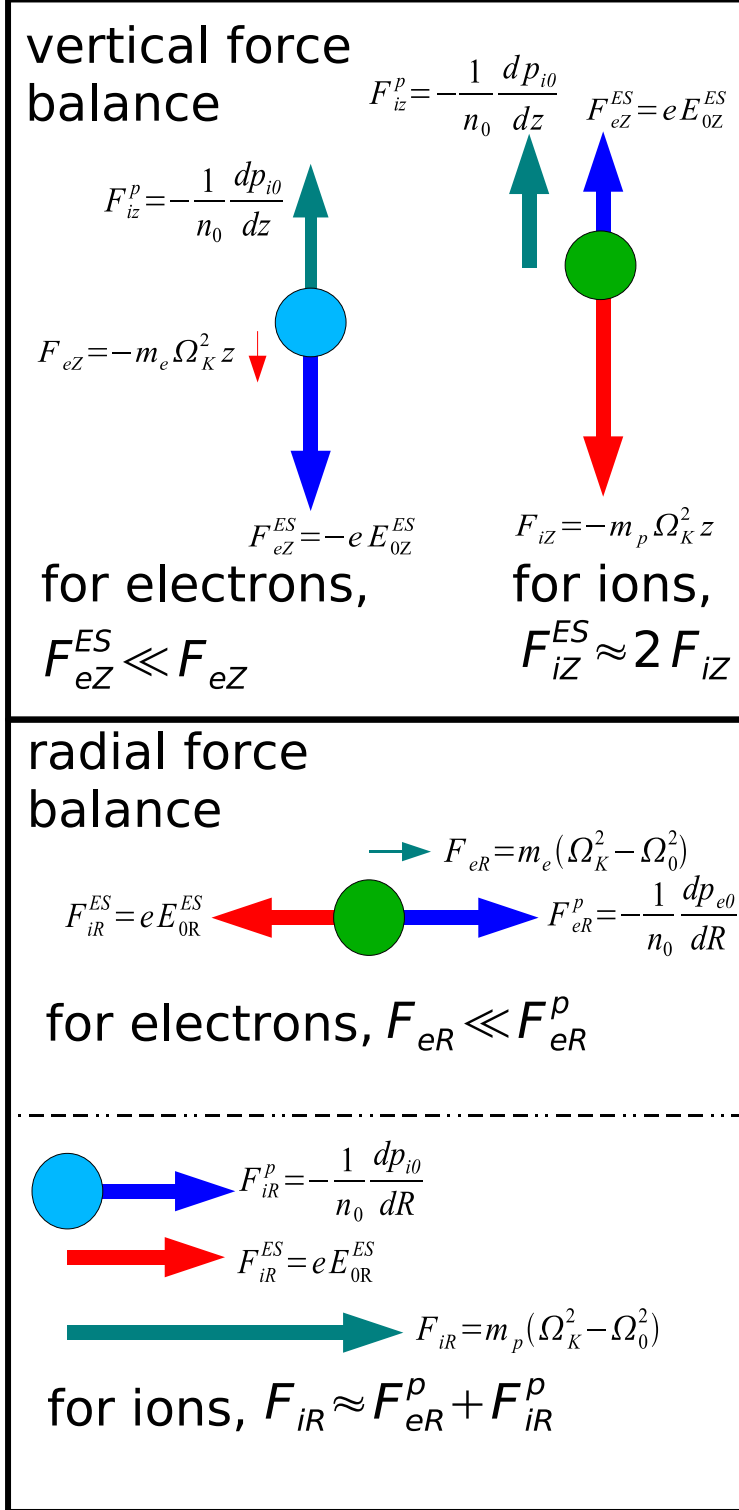


Fig. B.1.— MHD equilibrium in a thin disk  $H/R \ll 1$ , mediated by electrostatic and pressure forces. In considering vertical force balance (see top), electrons experience a large electrostatic force downwards and a very small gravitational force, while the ions experience an electrostatic force upwards that is approximately half as strong as the gravitational force.

pressible fluid with  $\partial\Omega/\partial z \neq 0$ , and with outwardly increasing specific angular momentum (Chandrasekhar 1961), is hydrodynamically stable within the plane of the disk. For thin disks, the pressure and density vary significantly over a vertical scale height. However, over the disk scale height the vertical angular velocity gradient is subdominant to the radial gradient of angular velocity,

$$\left| \frac{\partial\Omega/\partial z}{\partial\Omega/\partial R} \right| \sim H/R. \quad (\text{B.33})$$

The comoving MHD equations of force balance, Eq. (1.2.2), reduce to,

$$\frac{\partial \mathbf{u}}{\partial t} + 2\Omega \hat{\mathbf{z}} \times \mathbf{u} + \Omega' R u_R \hat{\boldsymbol{\phi}} + R \frac{\partial \Omega}{\partial z} \hat{\boldsymbol{\phi}} = -\nabla p, \quad (\text{B.34})$$

We examine axisymmetric modes of the form  $\delta a \propto \exp(\Gamma t + i k_R R + i k_Z z)$ . Eq. (B.34) and the incompressibility condition,  $\nabla \cdot \mathbf{u} = 0$ , in perturbed, component form are given by,

$$\Gamma \delta u_R - 2\Omega \delta u_\phi = -i k_R \theta_0 \frac{\delta p}{p_0}, \quad (\text{B.35})$$

$$\Gamma \delta u_\phi + (2\Omega + \Omega' R) \delta u_R + R \frac{\partial \Omega}{\partial z} \delta u_Z = 0, \quad (\text{B.36})$$

$$\Gamma \delta u_Z = -i k_Z \theta_0 \frac{\delta p}{p_0}, \quad (\text{B.37})$$

$$i k_R \delta u_R + i k_Z \delta u_Z = 0. \quad (\text{B.38})$$

Eqs. (B.35) - (B.38) can be solved to yield the dispersion relation,

$$\Gamma^2 + \kappa^2 - \frac{k_R/k_Z}{1 + k_R^2/k_Z^2} 2\Omega R \frac{\partial \Omega}{\partial z} = 0 \quad (\text{B.39})$$

For  $z > 0$ , then  $\partial\Omega/\partial z > 0$ . At  $k_R = k_Z$ ,  $\Gamma^2$  is a maximum given by,

$$\Gamma_{\max}^2 = -\kappa^2 + R\Omega\frac{\partial\Omega}{\partial z} \quad (\text{B.40})$$

For a Keplerian disk,  $\kappa^2 = \Omega^2$ , and from Eq. (B.33),  $\left|R\Omega\frac{\partial\Omega}{\partial z}\right| \sim \Omega^2 H/R$  within the disk. This results in  $\Gamma_{\max}^2 < 0$  and so the disk remains hydrodynamically stable.

## Appendix C

# Full Perturbed Axisymmetric Distribution Function

Here we calculate out the perturbed ion and electron axisymmetric distribution function. We take our dilute, magnetized disk to be thin, therefore its structure is described in §3. The equilibrium parallel and perpendicular temperatures of each species are equal,  $T_{s\parallel 0} = T_{s\perp 0} = T_{s0}$ . We employ the perturbed collisional operator, Eq. (5.3.2). We begin with Eq. (5.1.23). If we employ Eq. (5.1.20), then we derive the Boltzmann equation in non-covariant form,

$$\begin{aligned}
& \left( \frac{\partial}{\partial t} + \Omega \frac{\partial}{\partial \phi} \right) f_s^0 + (v_{\parallel} \mathbf{b} + \mathbf{u}_{\perp}) \cdot \nabla f_s^0 + \frac{\partial f_s^0}{\partial v_{\parallel}} \left( \frac{Z_s e}{m_s} E_{\parallel} + \frac{1}{n_{s0} m_s} \mathbf{b} \cdot \nabla p_{s0} \right) + \\
& \frac{\partial f_s^0}{\partial v_{\parallel}} \left( -\mathbf{b} \cdot \left( \left[ \frac{\partial}{\partial t} + \Omega \frac{\partial}{\partial \phi} \right] \mathbf{u}_{\perp} + [v_{\parallel} \mathbf{b} + \mathbf{u}_{\perp}] \cdot \nabla \mathbf{u}_{\perp} \right) + \right. \\
& \left. \mu B \nabla \cdot \mathbf{b} + 2\Omega \hat{\mathbf{z}} \cdot (\mathbf{b} \times \mathbf{u}) - b_{\phi} R \nabla \Omega \cdot (\mathbf{u}_{\perp} + v_{\parallel} \mathbf{b}) \right) = \\
& -\nu_s (f_s^0 - \langle f_s^0 \rangle)
\end{aligned} \tag{C.1}$$

To lowest order in small perturbed quantities, Eq. (C.1) for each species is,

$$\begin{aligned}
& (\Gamma + ik_{\parallel}v_{\parallel} + \nu_i) \delta f_i - \frac{\partial \delta f_i}{\partial v_{\parallel}} \left( \frac{k_B T_{i0}}{m_p} \times \frac{z}{H^2} \sin \chi \right) = \frac{m_p v_{\parallel}}{k_B T_{i0}} \left( -ik_{\parallel} \mu \delta B + \frac{e \delta E_{\parallel}}{m_p} - \right. \\
& \left. \frac{z}{H^2} v_i^2 v_{\parallel} \delta b_Z + v_i^2 \frac{\partial \ln p_{i0}}{\partial R} \delta \bar{B}_R - \frac{\cos \chi \delta \bar{B}_R}{ik_{\parallel}} (\Omega' R [\Gamma + ik_{\parallel}v_{\parallel}] + 2\Omega \Gamma) \right) f_{i0}^0 + \\
& \nu_i f_{i0}^0 \left( \delta \bar{\rho} - \frac{\delta T_{i\parallel}/2 + \delta T_{i\perp}}{T_{i0}} + \left[ \frac{m_p \mu B_0}{k_B T_{i0}} + \frac{m_p v_{\parallel}^2}{2k_B T_{i0}} \right] \left[ \frac{\delta T_{i\parallel}/3 + 2\delta T_{i\perp}/3}{T_{i0}} \right] - \right. \quad (C.2) \\
& \left. \frac{m_p \mu \delta B}{k_B T_{i0}} + \frac{m_p v_{\parallel} \delta u_{\parallel}}{k_B T_{i0}} \right) - f_{i0}^0 (v_{\parallel} \delta \mathbf{b} + \delta \mathbf{u}_{\perp}) \cdot \left( \frac{\partial \ln \rho_0}{\partial R} \hat{\mathbf{R}} - \frac{z \hat{\mathbf{z}}}{H^2} - \frac{3}{2} \frac{\partial \ln T_{i0}}{\partial R} \hat{\mathbf{R}} + \right. \\
& \left. \left( \frac{m_p \mu B_0}{k_B T_{i0}} + \frac{m_p v_{\parallel}^2}{2k_B T_{i0}} \right) \frac{\partial \ln T_{i0}}{\partial R} \hat{\mathbf{R}} \right),
\end{aligned}$$

$$\begin{aligned}
& (\Gamma + ik_{\parallel}v_{\parallel} + \nu_e) \delta f_e - \frac{\partial \delta f_e}{\partial v_{\parallel}} \left( \frac{k_B T_{e0}}{m_e} \times \frac{z}{H^2} \sin \chi \right) = \frac{m_e v_{\parallel}}{k_B T_{e0}} \left( -ik_{\parallel} \mu \delta B - \frac{e \delta E_{\parallel}}{m_e} - \right. \\
& \left. \frac{z}{H^2} v_e^2 v_{\parallel} \delta b_Z + v_e^2 \frac{\partial \ln p_{e0}}{\partial R} \delta \bar{B}_R - \frac{\cos \chi \delta \bar{B}_R}{ik_{\parallel}} (\Omega' R [\Gamma + ik_{\parallel}v_{\parallel}] + 2\Omega \Gamma) \right) f_{e0}^0 + \\
& \nu_e f_{e0}^0 \left( \delta \bar{\rho} - \frac{\delta T_{e\parallel}/2 + \delta T_{e\perp}}{T_{e0}} + \left[ \frac{m_e \mu B_0}{k_B T_{e0}} + \frac{m_e v_{\parallel}^2}{2k_B T_{e0}} \right] \left[ \frac{\delta T_{e\parallel}/3 + 2\delta T_{e\perp}/3}{T_{e0}} \right] - \right. \quad (C.3) \\
& \left. \frac{m_e \mu \delta B}{k_B T_{e0}} + \frac{m_e v_{\parallel} \delta u_{\parallel}}{k_B T_{e0}} \right) - f_{e0}^0 (v_{\parallel} \delta \mathbf{b} + \delta \mathbf{u}_{\perp}) \cdot \left( \frac{\partial \ln \rho_0}{\partial R} \hat{\mathbf{R}} - \frac{z \hat{\mathbf{z}}}{H^2} - \frac{3}{2} \frac{\partial \ln T_{e0}}{\partial R} \hat{\mathbf{R}} + \right. \\
& \left. \left( \frac{m_e \mu B_0}{k_B T_{e0}} + \frac{m_e v_{\parallel}^2}{2k_B T_{e0}} \right) \frac{\partial \ln T_{e0}}{\partial R} \hat{\mathbf{R}} \right).
\end{aligned}$$

Here, we denote terms in **dark red** with **finite collisionality**; terms in **dark green** with **points away from the midplane**; terms in **purple** with **differential rotation**; and terms in **dark blue** with **radial equilibrium gradients in pressure and temperature**. If we employ Eq. (5.1.3), then,

$$\delta u_{R\perp} = \frac{\Gamma}{ik_{\parallel}} \delta \bar{B}_R, \quad (C.4)$$

$$\delta u_{Z\perp} = -\frac{\Gamma}{ik_{\parallel}} \cos \chi \left( \delta \bar{B}_{\phi} \sin \chi + \frac{k_R}{k_Z} \delta \bar{B}_R \cos \chi \right) - \frac{\Omega' R \delta \bar{B}_R}{ik_{\parallel}} \sin \chi \cos \chi. \quad (C.5)$$

If we substitute Eqs. (C.4) and (C.5) into Eqs. (C.2) and (C.3), then we have,

$$\begin{aligned}
& (\Gamma + ik_{\parallel}v_{\parallel} + \nu_i) \delta f_i - \frac{\partial \delta f_i}{\partial v_{\parallel}} \left( \frac{k_B T_{i0}}{m_p} \times \frac{z}{H^2} \sin \chi \right) = \frac{m_p v_{\parallel}}{k_B T_{i0}} \left( -ik_{\parallel} \mu \delta B + \frac{e \delta E_{\parallel}}{m_p} + \right. \\
& \left. v_i^2 \frac{\partial \ln p_{i0}}{\partial R} \delta \bar{B}_R - \frac{\cos \chi \delta \bar{B}_R}{ik_{\parallel}} (\Omega' R [\Gamma + ik_{\parallel}v_{\parallel}] + 2\Omega \Gamma) \right) f_{i0}^0 + \\
& \nu_i f_{i0}^0 \left( \delta \bar{\rho} - \frac{\delta T_{i\parallel}/2 + \delta T_{i\perp}}{T_{i0}} + \left[ \frac{m_p \mu B_0}{k_B T_{i0}} + \frac{m_p v_{\parallel}^2}{2k_B T_{i0}} \right] \left[ \frac{\delta T_{i\parallel}/3 + 2\delta T_{i\perp}/3}{T_{i0}} \right] - \right. \\
& \left. \frac{m_p \mu \delta B}{k_B T_{i0}} + \frac{m_p v_{\parallel} \delta u_{\parallel}}{k_B T_{i0}} \right) - f_{i0}^0 \frac{\Gamma + ik_{\parallel}v_{\parallel}}{ik_{\parallel}} \left( \frac{\partial \ln \rho_0}{\partial R} - \frac{3}{2} \frac{\partial \ln T_{i0}}{\partial R} + \right. \\
& \left. \left( \frac{m_p \mu B_0}{k_B T_{i0}} + \frac{m_p v_{\parallel}^2}{2k_B T_{i0}} \right) \frac{\partial \ln T_{i0}}{\partial R} \right) - \\
& f_{i0}^0 \frac{z}{H^2} \frac{\cos \chi}{ik_{\parallel}} \left( \Gamma \left[ \delta \bar{B}_{\phi} \sin \chi + \frac{k_R}{k_Z} \delta \bar{B}_R \cos \chi \right] + \Omega' R \delta \bar{B}_R \sin \chi \right).
\end{aligned} \tag{C.6}$$

$$\begin{aligned}
& (\Gamma + ik_{\parallel}v_{\parallel} + \nu_e) \delta f_e - \frac{\partial \delta f_e}{\partial v_{\parallel}} \left( \frac{k_B T_{e0}}{m_e} \times \frac{z}{H^2} \sin \chi \right) = \frac{m_e v_{\parallel}}{k_B T_{e0}} \left( -ik_{\parallel} \mu \delta B - \frac{e \delta E_{\parallel}}{m_e} + \right. \\
& \left. v_e^2 \frac{\partial \ln p_{e0}}{\partial R} \delta \bar{B}_R - \frac{\cos \chi \delta \bar{B}_R}{ik_{\parallel}} (\Omega' R [\Gamma + ik_{\parallel}v_{\parallel}] + 2\Omega \Gamma) \right) f_{e0}^0 + \\
& \nu_e f_{e0}^0 \left( \delta \bar{\rho} - \frac{\delta T_{e\parallel}/2 + \delta T_{e\perp}}{T_{e0}} + \left[ \frac{m_e \mu B_0}{k_B T_{e0}} + \frac{m_e v_{\parallel}^2}{2k_B T_{e0}} \right] \left[ \frac{\delta T_{e\parallel}/3 + 2\delta T_{e\perp}/3}{T_{e0}} \right] - \right. \\
& \left. \frac{m_e \mu \delta B}{k_B T_{e0}} + \frac{m_e v_{\parallel} \delta u_{\parallel}}{k_B T_{e0}} \right) - f_{e0}^0 \frac{\Gamma + ik_{\parallel}v_{\parallel}}{ik_{\parallel}} \left( \frac{\partial \ln \rho_0}{\partial R} - \frac{3}{2} \frac{\partial \ln T_{e0}}{\partial R} + \right. \\
& \left. \left( \frac{m_e \mu B_0}{k_B T_{e0}} + \frac{m_e v_{\parallel}^2}{2k_B T_{e0}} \right) \frac{\partial \ln T_{e0}}{\partial R} \right) - \\
& f_{e0}^0 \frac{z}{H^2} \frac{\cos \chi}{ik_{\parallel}} \left( \Gamma \left[ \delta \bar{B}_{\phi} \sin \chi + \frac{k_R}{k_Z} \delta \bar{B}_R \cos \chi \right] + \Omega' R \delta \bar{B}_R \sin \chi \right).
\end{aligned} \tag{C.7}$$

In §5.2 we consider only **differential rotation** and equilibrium gradients in pressure and temperature. In §5.3 we consider **differential rotation**, radial equilibrium gradients in pressure and temperature, and **dark red**. In Appendix E.2, we consider **differential rotation**, radial equilibrium gradients in pressure and temperature, and **points away from the midplane**. Finally, in Appendix D.2, we consider **differential rotation** and radial equilibrium gradients in pressure and temperature but do not ignore electron



dynamics.

## Appendix D

# Finite Ion and Electron Pressure Responses

In this appendix we detail the fluid and collisionless plasma response when including finite electron temperature. The ion and electron temperatures are given by Eqs. (6.1.1) and (6.1.2), respectively.

### D.1 Fluid Treatment

From Braginskii (1965), the (ion) viscosity and ion and electron thermal diffusivities are,

$$\eta_\nu = \eta_{\nu 0} (T_{i0}/T_0)^{5/2}, \quad (\text{D.1})$$

$$\eta_{\kappa i} = \eta_{\kappa 0} (T_{e0}/T_0)^{5/2}, \quad (\text{D.2})$$

$$\eta_{\kappa e} = 1.22 (m_e/m_i)^{1/2} \eta_{\kappa 0} (T_{i0}/T_0)^{5/2}. \quad (\text{D.3})$$

Here,  $\eta_{\nu 0}$  and  $\eta_{\kappa 0}$  are the viscous and thermal diffusivities, respectively, for  $T_{i0} = T_{e0} = T_0$ .  $\eta_{\nu 0}$  is given in Eq. (4.1.26), and  $\eta_{\kappa 0} = 101\eta_{\nu 0}$  (see Eq. [4.1.18]). If we

substitute in Eqs. (6.1.1) and (6.1.2), the viscous and thermal diffusivities are,

$$\eta_\nu = \eta_{\nu 0} \left( \sqrt{2} \cos \psi \right)^5, \quad (\text{D.4})$$

$$\eta_{\kappa e} = 101 \eta_{\nu 0} \left( \sqrt{2} \sin \psi \right)^5, \quad (\text{D.5})$$

$$\eta_{\kappa i} = 2.88 \eta_{\nu 0} \left( \sqrt{2} \cos \psi \right)^5. \quad (\text{D.6})$$

Equations for the perturbed ion and electron comoving internal energy balance are,

$$\Gamma \left( \frac{\delta p_i}{p_{i0}} - \frac{5}{3} \delta \bar{\rho} \right) + \delta u_R \frac{\partial \ln p_0 \rho_0^{-5/3}}{\partial R} = \frac{2}{3} \eta_{\kappa i} \left( i k_Z \sin \chi \left( \delta \bar{B}_R \frac{\partial \ln T_0}{\partial R} \right) - k_Z^2 \sin^2 \chi \frac{\delta T_i}{T_{i0}} \right), \quad (\text{D.7})$$

$$\Gamma \left( \frac{\delta p_e}{p_{e0}} - \frac{5}{3} \delta \bar{\rho} \right) + \delta u_R \frac{\partial \ln p_0 \rho_0^{-5/3}}{\partial R} = \frac{2}{3} \eta_{\kappa e} \left( i k_Z \sin \chi \left( \delta \bar{B}_R \frac{\partial \ln T_0}{\partial R} \right) - k_Z^2 \sin^2 \chi \frac{\delta T_e}{T_{e0}} \right). \quad (\text{D.8})$$

If we use the perturbed comoving induction equation, Eq. (4.1.3), and use Eqs. (D.5) and (D.6) for ion and electron thermal diffusivities, respectively, the ion and electron pressures are related to  $\delta \bar{\rho}$  and  $\delta \bar{B}_R$  by,

$$\delta \bar{\rho} = \frac{3 \delta \bar{B}_R}{5 i k_Z \sin \chi} \times \frac{\Gamma \partial \ln p_0 \rho_0^{-5/3} / \partial R + 1.92 \eta_{\nu 0} \left( \sqrt{2} \cos \psi \right)^5 k_Z^2 \sin^2 \chi \partial \ln T_0 / \partial R}{\Gamma + 1.15 \eta_{\nu 0} \left( \sqrt{2} \cos \psi \right)^5 k_Z^2 \sin^2 \chi} + \quad (\text{D.9})$$

$$\frac{3 \delta p_i}{5 p_{i0}} \times \frac{\Gamma + 1.92 \eta_{\nu 0} \left( \sqrt{2} \cos \psi \right)^5 k_Z^2 \sin^2 \chi}{\Gamma + 1.15 \eta_{\nu 0} \left( \sqrt{2} \cos \psi \right)^5 k_Z^2 \sin^2 \chi}$$

$$\delta \bar{\rho} = \frac{3 \delta \bar{B}_R}{5 i k_Z \sin \chi} \times \frac{\Gamma \partial \ln p_0 \rho_0^{-5/3} / \partial R + 67.3 \eta_{\nu 0} \left( \sqrt{2} \sin \psi \right)^5 k_Z^2 \sin^2 \chi \partial \ln T_0 / \partial R}{\Gamma + 40.4 \eta_{\nu 0} \left( \sqrt{2} \sin \psi \right)^5 k_Z^2 \sin^2 \chi} + \quad (\text{D.10})$$

$$\frac{3 \delta p_e}{5 p_{e0}} \times \frac{\Gamma + 67.3 \eta_{\nu 0} \left( \sqrt{2} \sin \psi \right)^5 k_Z^2 \sin^2 \chi}{\Gamma + 40.4 \eta_{\nu 0} \left( \sqrt{2} \sin \psi \right)^5 k_Z^2 \sin^2 \chi}$$

In the Boussinesq limit, perturbations are nearly isobaric,  $(\delta p_i + \delta p_e)/p_0 \ll \delta \rho/\rho_0$ .

Using Eqs. (D.9) and (D.10),  $\delta \bar{\rho}$  is given by,

$$\begin{aligned} \delta \bar{\rho} = & \frac{3\delta \bar{B}_R}{5ik_Z \sin \chi} \times \\ & \left( \frac{\Gamma \partial \ln p_0 \rho_0^{-5/3} / \partial R + 1.92\eta_{\nu 0} (\sqrt{2} \cos \psi)^5 k_Z^2 \sin^2 \chi \partial \ln T_0 / \partial R}{\Gamma + 1.92\eta_{\nu 0} (\sqrt{2} \cos \psi)^5 k_Z^2 \sin^2 \chi} \cos^2 \psi + \right. \\ & \left. \frac{\Gamma \partial \ln p_0 \rho_0^{-5/3} / \partial R + 67.3\eta_{\nu 0} (\sqrt{2} \sin \psi)^5 k_Z^2 \sin^2 \chi \partial \ln T_0 / \partial R}{\Gamma + 67.3\eta_{\nu 0} (\sqrt{2} \sin \psi)^5 k_Z^2 \sin^2 \chi} \sin^2 \psi \right) / (D.11) \\ & \left( \frac{\Gamma + 1.15\eta_{\nu 0} (\sqrt{2} \cos \psi)^5 k_Z^2 \sin^2 \chi}{\Gamma + 1.92\eta_{\nu 0} (\sqrt{2} \cos \psi)^5 k_Z^2 \sin^2 \chi} \cos^2 \psi + \right. \\ & \left. \frac{\Gamma + 67.3\eta_{\nu 0} (\sqrt{2} \sin \psi)^5 k_Z^2 \sin^2 \chi}{\Gamma + 40.4\eta_{\nu 0} (\sqrt{2} \sin \psi)^5 k_Z^2 \sin^2 \chi} \sin^2 \psi \right). \end{aligned}$$

From Eq. (4.1.17), the dispersion relation with finite electron temperatures is given by,

$$\begin{aligned} & \left( \frac{k^2}{k_Z^2} \Gamma^2 + \frac{d\Omega^2}{d \ln R} + 3\eta_{\nu 0} (\sqrt{2} \cos \psi)^5 k_R^2 \Gamma \sin^4 \chi + k^2 v_A^2 \sin^2 \chi - \theta_0 \frac{\partial \ln p_0}{\partial R} \mathcal{A}_\rho \right) \times \\ & \left( \Gamma^2 + k_Z^2 v_A^2 \sin^2 \chi + 3\eta_{\nu 0} (\sqrt{2} \cos \psi)^5 k_Z^2 \Gamma \sin^2 \chi \cos^2 \chi \right) + \\ & \Gamma^2 \left( 4\Omega^2 - 9\eta_{\nu 0}^2 (2 \cos^2 \psi)^5 k_R^2 k_Z^2 \sin^6 \chi \cos^2 \chi \right) = 0, \end{aligned} \quad (D.12)$$

where,

$$\begin{aligned} \mathcal{A}_\rho = & \frac{3}{5} \left( \frac{\Gamma \partial \ln p_0 \rho_0^{-5/3} / \partial R + 1.92 \eta_{\nu 0} (\sqrt{2} \cos \psi)^5 k_Z^2 \sin^2 \chi \partial \ln T_0 / \partial R}{\Gamma + 1.92 \eta_{\nu 0} (\sqrt{2} \cos \psi)^5 k_Z^2 \sin^2 \chi} \cos^2 \psi + \right. \\ & \left. \frac{\Gamma \partial \ln p_0 \rho_0^{-5/3} / \partial R + 67.3 \eta_{\nu 0} (\sqrt{2} \sin \psi)^5 k_Z^2 \sin^2 \chi \partial \ln T_0 / \partial R}{\Gamma + 67.3 \eta_{\nu 0} (\sqrt{2} \sin \psi)^5 k_Z^2 \sin^2 \chi} \sin^2 \psi \right) / \\ & \left( \frac{\Gamma + 1.15 \eta_{\nu 0} (\sqrt{2} \cos \psi)^5 k_Z^2 \sin^2 \chi}{\Gamma + 1.92 \eta_{\nu 0} (\sqrt{2} \cos \psi)^5 k_Z^2 \sin^2 \chi} \cos^2 \psi + \right. \\ & \left. \frac{\Gamma + 40.4 \eta_{\nu 0} (\sqrt{2} \sin \psi)^5 k_Z^2 \sin^2 \chi}{\Gamma + 67.3 \eta_{\nu 0} (\sqrt{2} \sin \psi)^5 k_Z^2 \sin^2 \chi} \sin^2 \psi \right). \end{aligned} \quad (\text{D.13})$$

## D.2 Kinetic Treatment

Here we examine the response of a collisionless plasma when considering the dynamics of both ions and electrons. One can demonstrate that the ion and electron perturbed density are given by,

$$\begin{aligned} \frac{\delta n_i}{n_0} = & 2\pi n_0^{-1} \int \delta f_i B d\mu du_{\parallel} + \frac{\delta B}{B} = -\frac{ie\delta E_{\parallel}}{k_{\parallel} k_B T_{i0}} R(i\zeta_i) - \frac{\delta B}{B} (R(i\zeta_i) - 1) + \\ & \frac{2\Omega\Gamma}{k_{\parallel}^2 v_i^2} R(i\zeta_i) \cos \chi \delta \bar{B}_R + \frac{i\delta \bar{B}_R}{k_{\parallel}} \left( \frac{\partial \ln n_0}{\partial R} \right) - \frac{i\delta \bar{B}_R}{k_{\parallel}} \left( \frac{\partial \ln p_i^0}{\partial R} \right) R(i\zeta_i), \end{aligned} \quad (\text{D.1})$$

$$\begin{aligned} \frac{\delta n_e}{n_0} = & 2\pi n_0^{-1} \int \delta f_e B d\mu du_{\parallel} + \frac{\delta B}{B} = \frac{ie\delta E_{\parallel}}{k_{\parallel} k_B T_{e0}} R(i\zeta_e) - \frac{\delta B}{B} (R(i\zeta_e) - 1) + \\ & \frac{2\Omega\Gamma}{k_{\parallel}^2 v_e^2} R(i\zeta_e) \cos \chi \delta \bar{B}_R + \frac{i\delta \bar{B}_R}{k_{\parallel}} \left( \frac{\partial \ln n_0}{\partial R} \right) - \frac{i\delta \bar{B}_R}{k_{\parallel}} \left( \frac{\partial \ln p_e^0}{\partial R} \right) R(i\zeta_e), \end{aligned} \quad (\text{D.2})$$

From Tab. (A.2), Eqs. (6.1.1) and (6.1.2), expressions for  $\zeta_i$  and  $\zeta_e$  are,

$$\zeta_i = \frac{\gamma}{x\sqrt{2\beta}} \sec \psi \left( \frac{m_p}{m_p + m_e} \right)^{1/2}, \quad (\text{D.3})$$

$$\zeta_e = \frac{\gamma}{x\sqrt{2\beta}} \csc \psi \left( \frac{m_e}{m_p + m_e} \right)^{1/2}, \quad (\text{D.4})$$

With quasineutrality  $\delta n_i = \delta n_e$  one can demonstrate that the electric field is given by the following:

$$\begin{aligned} \frac{ie\delta E_{\parallel}}{k_{\parallel}(m_p + m_e)\theta_0} = & -\frac{\delta B}{B} \sin^2 \psi \cos^2 \psi \frac{R(i\zeta_i) - R(i\zeta_e)}{R(i\zeta_i) \sin^2 \psi + R(i\zeta_e) \cos^2 \psi} - \\ & \frac{\delta \bar{B}_R}{ik_{\parallel}} \sin^2 \psi \cos^2 \psi \frac{\alpha_P (R(i\zeta_i) - R(i\zeta_e))}{R(i\zeta_i) \sin^2 \psi + R(i\zeta_e) \cos^2 \psi} + \\ & \frac{2\Omega\Gamma}{k_{\parallel}^2\theta_0} \delta \bar{B}_R \frac{R(i\zeta_i) \frac{m_p}{m_p+m_e} \sin^2 \psi - R(i\zeta_e) \frac{m_e}{m_p+m_e} \cos^2 \psi}{R(i\zeta_i) \sin^2 \psi + R(i\zeta_e) \cos^2 \psi}, \end{aligned} \quad (\text{D.5})$$

The total perturbed parallel and perpendicular pressures are then,

$$\begin{aligned} \frac{\delta p_{\perp}}{p_0} = & \frac{i\delta \bar{B}_R}{x\beta^{1/2}} \alpha_P (R(i\zeta_i) \cos^2 \psi + R(i\zeta_e) \sin^2 \psi - 1) - \\ & \frac{2\delta B}{B} (R(i\zeta_i) \cos^2 \psi + R(i\zeta_e) \sin^2 \psi - 1) + \\ & \frac{2\gamma}{x^2\beta} \delta \bar{B}_R \cos \chi \frac{m_p R(i\zeta_i) + m_e R(i\zeta_e)}{m_p + m_e} + \frac{2ie\delta E_{\parallel}}{k_{\parallel}(m_p + m_e)\theta_0} (R(i\zeta_i) - R(i\zeta_e)), \end{aligned} \quad (\text{D.6})$$

$$\begin{aligned} \frac{\delta p_{\parallel}}{p_0} = & -\frac{2i\delta \bar{B}_R}{x\beta^{1/2}} \alpha_P (\zeta_i^2 R(i\zeta_i) \cos^2 \psi + \zeta_e^2 R(i\zeta_e) \sin^2 \psi) + \\ & \frac{2\delta B}{B} (\zeta_i^2 R(i\zeta_i) \cos^2 \psi + \zeta_e^2 R(i\zeta_e) \sin^2 \psi) + \\ & \frac{2\gamma}{x^2\beta} \delta \bar{B}_R \cos \chi \left( 1 - \frac{2\zeta_i^2 m_p R(i\zeta_i) + 2\zeta_e^2 m_e R(i\zeta_e)}{m_p + m_e} \right) + \\ & \frac{2ie\delta E_{\parallel}}{k_{\parallel}(m_p + m_e)\theta_0} (\zeta_i^2 R(i\zeta_i) - \zeta_e^2 R(i\zeta_e)). \end{aligned} \quad (\text{D.7})$$

## Appendix E

### Off Plane Plasma Dynamics

In this appendix, we detail the derivation of the dispersion relation for the MVTI and collisionless MTI away from the disk midplane. Most of our analysis will focus on the kinetic treatment of a collisionless plasma. We consider a plasma with  $T_{i0} = T_{e0}$  and  $\partial T_{i0}/\partial R = \partial T_{e0}/\partial R$ . We explore the parallel and perpendicular pressure responses of the plasma, as a function of perturbed radial and azimuthal magnetic fields, away from the midplane at a specific growth rate and vertical wavenumber. The parallel and perpendicular pressure responses are shown in Figs. (E.1) - (E.4).

#### E.1 Fluid Treatment

We follow a treatment of dilute magnetized disk stability away from the midplane that is given by Balbus (2001). The perturbed viscous stress  $\delta\sigma$  is given by Eq. (4.1.1). The perturbed heat flux  $\delta q$  away from the midplane is given by Eq. (4.1.2). The

perturbed comoving internal energy balance, Eq. (1.2.7), away from the midplane,

$$\Gamma \left( \frac{\delta p}{p_0} - \frac{5}{3} \frac{\delta \rho}{\rho_0} \right) + \delta u_R \left( \frac{\partial \ln p_0 \rho_0^{-5/3}}{\partial R} - \frac{k_R}{k_Z} \frac{\partial \ln p_0 \rho_0^{-5/3}}{\partial z} \right) = \frac{2}{3} \eta_\kappa \left( i k_Z \sin \chi \left( \delta \bar{B}_R \frac{\partial \ln T_0}{\partial R} \right) - k_Z^2 \sin^2 \chi \frac{\delta \theta_0}{\theta_0} \right), \quad (\text{E.1})$$

In the Boussinesq limit, terms with  $\delta p/p_0$  are dynamically unimportant. Eq. (E.1) can be solved to yield an equation for  $\delta \bar{\rho}$ ,

$$\frac{\delta \rho}{\rho_0} = \frac{3}{5} \times \frac{\delta u_R \left( \frac{\partial \ln p_0 \rho_0^{-5/3}}{\partial R} - \frac{k_R}{k_Z} \frac{\partial \ln p_0 \rho_0^{-5/3}}{\partial z} \right) - \frac{2}{3} i \eta_\kappa k_Z \sin \chi \frac{\partial \ln T_0}{\partial R} \delta \bar{B}_R}{\Gamma + \frac{2}{5} \eta_\kappa k_Z^2 \sin^2 \chi}. \quad (\text{E.2})$$

The perturbed form of the comoving MHD force balance equations, Eq. (1.2.6), can be rewritten as,

$$\Gamma \delta \mathbf{u} + 2\Omega \hat{\mathbf{z}} \times \delta \mathbf{u} + \Omega' R \delta u_R \hat{\boldsymbol{\phi}} = \frac{\delta \rho}{\rho_0} \theta_0 \left( \frac{\partial \ln p_0}{\partial R} \hat{\mathbf{R}} + \frac{\partial \ln p_0}{\partial z} \hat{\mathbf{z}} \right) - \frac{i \mathbf{k}}{\rho_0} \left( \delta p + \frac{\mathbf{B}_0 \cdot \delta \mathbf{B}}{4\pi} \right) + i k_Z \sin \chi v_A^2 \delta \bar{\mathbf{B}} - \nabla \cdot \delta \boldsymbol{\sigma}, \quad (\text{E.3})$$

If we substitute in Eqs. (4.1.3) and (4.1.7), then the vertical component of Eq. (E.3) can be represented as,

$$\frac{\delta p}{\rho_0} + v_A^2 \cos \chi \delta \bar{B}_\phi = \eta_\nu \Gamma (3 \sin^2 \chi - 1) \left( \delta \bar{B}_\phi \cos \chi - \frac{k_R}{k_Z} \delta \bar{B}_R \sin \chi \right) - \frac{i k_R}{k_Z^2} \Gamma \delta u_R + \theta_0 \frac{1}{i k_Z} \frac{\partial \ln p_0}{\partial z} \frac{\delta \rho}{\rho_0}. \quad (\text{E.4})$$



If we employ Eqs. (4.1.3), (4.1.7), and (E.4), then the radial and azimuthal components of Eq. (E.3) reduce to,

$$\begin{aligned}
& \left(1 + \frac{k_R^2}{k_Z^2}\right) \Gamma^2 \delta \bar{B}_R - 2\Omega \left(\Gamma \delta \bar{B}_\phi - \Omega' R \delta \bar{B}_R\right) = \\
& 3\eta_\nu \Gamma k_R k_Z \sin^3 \chi \left(\delta \bar{B}_\phi \cos \chi - \frac{k_R}{k_Z} \delta \bar{B}_R \sin \chi\right) - \\
& (k_R^2 + k_Z^2) v_A^2 \sin^2 \chi \delta \bar{B}_R + \frac{3}{5} \theta_0 \left(\frac{\partial \ln p_0}{\partial R} - \frac{k_R}{k_Z} \frac{\partial \ln p_0}{\partial z}\right) \times \\
& \Gamma \left(\frac{\partial \ln p_0 \rho_0^{-5/3}}{\partial R} - \frac{k_R}{k_Z} \frac{\partial \ln p_0 \rho_0^{-5/3}}{\partial z}\right) + \frac{2}{3} \eta_\kappa k_Z^2 \sin^2 \chi \partial \ln T_0 / \partial R \\
& \frac{\delta \bar{B}_R}{\Gamma + \frac{2}{5} \eta_\kappa k_Z^2 \sin^2 \chi},
\end{aligned} \tag{E.5}$$

$$\begin{aligned}
& \Gamma^2 \delta \bar{B}_\phi + 2\Omega \Gamma \delta \bar{B}_R = -3\eta_\nu \Gamma k_Z^2 \sin^2 \chi \cos \chi \times \\
& \left(\delta \bar{B}_\phi \cos \chi - \frac{k_R}{k_Z} \delta \bar{B}_R \sin \chi\right) - k_Z^2 v_A^2 \sin^2 \chi \delta \bar{B}_\phi.
\end{aligned} \tag{E.6}$$

Terms explicitly due to the vertical structure of the disk appear only with nonzero  $k_R$ . Eqs. (E.5) and (E.6) can be rearranged into this dispersion relation,

$$\begin{aligned}
& \left(\frac{k^2}{k_Z^2} \Gamma^2 + \frac{d\Omega^2}{d \ln R} + 3\eta_\nu k_R^2 \Gamma \sin^4 \chi + k^2 v_A^2 \sin^2 \chi - \frac{3}{5} \theta_0 \left(\frac{\partial \ln p_0}{\partial R} - \frac{k_R}{k_Z} \frac{\partial \ln p_0}{\partial z}\right) \times \right. \\
& \left. \Gamma \left(\frac{\partial \ln p_0 \rho_0^{-5/3}}{\partial R} - \frac{k_R}{k_Z} \frac{\partial \ln p_0 \rho_0^{-5/3}}{\partial z}\right) + \frac{2}{3} \eta_\kappa k_Z^2 \sin^2 \chi \partial \ln T_0 / \partial R \right) \times \\
& \frac{\delta \bar{B}_R}{\Gamma + \frac{2}{5} \eta_\kappa k_Z^2 \sin^2 \chi} \tag{E.7}
\end{aligned}$$

$$\begin{aligned}
& (\Gamma^2 + k_Z^2 v_A^2 \sin^2 \chi + 3\eta_\nu k_Z^2 \Gamma \sin^2 \chi \cos^2 \chi) + \\
& \Gamma^2 (4\Omega^2 - 9\eta_\nu^2 k_R^2 k_Z^2 \sin^6 \chi \cos^2 \chi) = 0,
\end{aligned}$$

From Eqs. (1.3.9) and (1.3.10),  $\eta_\nu \propto T^{5/2} n^{-1}$  and  $\eta_\kappa \propto T^{5/2} n^{-1}$ . For our disk,

$$\eta_\nu = \eta_{\nu 0} e^{z^2/(2H^2)}, \tag{E.8}$$

$$\eta_\kappa = \eta_{\kappa 0} e^{z^2/(2H^2)}. \tag{E.9}$$

This implies,

$$\hat{\eta}_\nu = \hat{\eta}_{\nu 0} e^{z^2/(2H^2)}, \quad (\text{E.10})$$

$$\hat{\eta}_\kappa = \text{Pr}^{-1} \hat{\eta}_{\nu 0} e^{z^2/(2H^2)}. \quad (\text{E.11})$$

If we apply the normalizations given by Tab. (A.2), and employ Eqs. (6.2.2) - (E.11), then Eq. (E.7) reduces to,

$$\begin{aligned} & \left( \frac{\hat{k}^2}{\hat{k}_Z^2} \gamma^2 + 2 \frac{d \ln \Omega}{d \ln R} + 3 \hat{\eta}_{\nu 0} \hat{k}_R^2 \gamma e^{z^2/(2H^2)} \sin^4 \chi + \hat{k}^2 e^{z^2/(2H^2)} \sin^2 \chi - \right. \\ & \left. \frac{3}{5} \left( \alpha_P - \frac{\hat{k}_R}{\hat{k}_Z} z/H \right) \frac{\left[ \alpha_S + \frac{2\hat{k}_R}{3\hat{k}_Z} z/H \right] \gamma + \frac{2}{3} \alpha_T \text{Pr}^{-1} \hat{\eta}_{\nu 0} e^{z^2/(2H^2)} \hat{k}_Z^2 \sin^2 \chi}{\gamma + \frac{2}{5} \text{Pr}^{-1} \hat{\eta}_{\nu 0} e^{z^2/(2H^2)} \hat{k}_Z^2 \sin^2 \chi} \right) (\text{E.12}) \\ & \left( \gamma^2 + \hat{k}_Z^2 e^{z^2/(2H^2)} \sin^2 \chi + 3 \hat{\eta}_{\nu 0} e^{z^2/(2H^2)} \hat{k}_Z^2 \gamma \sin^2 \chi \cos^2 \chi \right) + \\ & \gamma^2 \left( 4 - 9 \hat{\eta}_{\nu 0}^2 e^{z^2/H^2} \hat{k}_R^2 \hat{k}_Z^2 \sin^6 \chi \cos^2 \chi \right) = 0. \end{aligned}$$

## E.2 Kinetic Treatment

The perturbed distribution function for ions and electrons away from the midplane is given by,

$$\begin{aligned}
 & (\Gamma + ik_{\parallel}v_{\parallel}) \delta f_i - \frac{\partial \delta f_i}{\partial v_{\parallel}} \left( \frac{k_B T_0}{m_p} \times \frac{z}{H^2} \sin \chi \right) = \frac{m_p v_{\parallel}}{k_B T_0} (-ik_{\parallel} \mu \delta B + \\
 & \frac{e \delta E_{\parallel}}{m_p} + v_i^2 \frac{\partial \ln p_{i0}}{\partial R} \delta \bar{B}_R - \frac{\cos \chi \delta \bar{B}_R}{ik_{\parallel}} (\Omega' R [\Gamma + ik_{\parallel}v_{\parallel}] + 2\Omega \Gamma) \Big) f_{i0}^0 - \\
 & f_{i0}^0 \frac{\Gamma + ik_{\parallel}v_{\parallel}}{ik_{\parallel}} \left( \frac{\partial \ln \rho_0}{\partial R} - \frac{3}{2} \frac{\partial \ln T_0}{\partial R} + \left( \frac{m_p \mu B_0}{k_B T_0} + \frac{m_p v_{\parallel}^2}{2k_B T_0} \right) \frac{\partial \ln T_0}{\partial R} \right) - \\
 & f_{i0}^0 \frac{z}{H^2} \frac{\cos \chi}{ik_{\parallel}} \left( \Gamma \left[ \delta \bar{B}_{\phi} \sin \chi + \frac{k_R}{k_Z} \delta \bar{B}_R \cos \chi \right] + \Omega' R \delta \bar{B}_R \sin \chi \right). \tag{E.1}
 \end{aligned}$$

$$\begin{aligned}
 & (\Gamma + ik_{\parallel}v_{\parallel}) \delta f_e - \frac{\partial \delta f_e}{\partial v_{\parallel}} \left( \frac{k_B T_0}{m_e} \times \frac{z}{H^2} \sin \chi \right) = \frac{m_e v_{\parallel}}{k_B T_0} (-ik_{\parallel} \mu \delta B - \\
 & \frac{e \delta E_{\parallel}}{m_e} + v_e^2 \frac{\partial \ln p_{e0}}{\partial R} \delta \bar{B}_R - \frac{\cos \chi \delta \bar{B}_R}{ik_{\parallel}} (\Omega' R [\Gamma + ik_{\parallel}v_{\parallel}] + 2\Omega \Gamma) \Big) f_{e0}^0 - \\
 & f_{e0}^0 \frac{\Gamma + ik_{\parallel}v_{\parallel}}{ik_{\parallel}} \left( \frac{\partial \ln \rho_0}{\partial R} - \frac{3}{2} \frac{\partial \ln T_0}{\partial R} + \left( \frac{m_e \mu B_0}{k_B T_0} + \frac{m_e v_{\parallel}^2}{2k_B T_0} \right) \frac{\partial \ln T_0}{\partial R} \right) - \\
 & f_{e0}^0 \frac{z}{H^2} \frac{\cos \chi}{ik_{\parallel}} \left( \Gamma \left[ \delta \bar{B}_{\phi} \sin \chi + \frac{k_R}{k_Z} \delta \bar{B}_R \cos \chi \right] + \Omega' R \delta \bar{B}_R \sin \chi \right). \tag{E.2}
 \end{aligned}$$

If we make the following normalizations we then have that the ion and electron perturbed velocity profiles in terms  $\delta E_{\parallel}$ ,  $\delta \bar{B}_{\phi}$ , and  $\delta \bar{B}_R$  are given by the following:

$$\begin{aligned}
& (y - i\zeta_i) \delta f_i(y, \mu) + \frac{iz/H \sin \chi}{2x\beta^{1/2}} \frac{\partial \delta f_i}{\partial y} = y \left( -\frac{\mu B_0}{v_i^2} \left[ \delta \bar{B}_{\phi} \cos \chi - \frac{k_R}{k_Z} \delta \bar{B}_R \sin \chi \right] - \right. \\
& \left. \frac{ie\delta E_{\parallel}}{k_{\parallel} k_B T_0} - \frac{1}{ix\beta^{1/2}} \alpha_P \delta \bar{B}_R - \cos \chi \frac{2\delta \bar{B}_R}{ix\beta^{1/2}} \sqrt{\frac{m_p}{m_p + m_e}} \left[ \frac{d \ln \Omega}{d \ln R} (y - i\zeta_i) - 2i\zeta_i \right] \right) \times \\
& \frac{n_0}{(2\pi)^{3/2} v_i^3} \exp \left( -y^2 - \frac{\mu B_0}{v_i^2} \right) + \frac{\delta \bar{B}_R}{ix\beta^{1/2}} (y - i\zeta_i) \left( \alpha_P - \frac{5}{2} \alpha_T + \right. \\
& \left. \left[ y^2 + \frac{\mu B_0}{v_i^2} \right] \alpha_T \right) \frac{n_0}{(2\pi)^{3/2} v_i^3} \exp \left( -y^2 - \frac{\mu B_0}{v_i^2} \right) + \\
& \left( \left[ \zeta_i \delta \bar{B}_{\phi} + \frac{d \ln \Omega}{d \ln R} \frac{1}{x\beta^{1/2}} \sqrt{\frac{m_p}{m_p + m_e}} \delta \bar{B}_R \right] \sin \chi + \frac{k_R}{k_Z} \zeta_i \delta \bar{B}_R \cos \chi \right) \frac{z/H \cos \chi}{x\beta^{1/2}} \times \\
& \frac{n_0}{(2\pi)^{3/2} v_i^3} \exp \left( -y^2 - \frac{\mu B_0}{v_i^2} \right), \tag{E.3}
\end{aligned}$$

$$\begin{aligned}
& (y - i\zeta_e) \delta f_e(y, \mu) + \frac{iz/H \sin \chi}{2x\beta^{1/2}} \frac{\partial \delta f_e}{\partial y} = y \left( -\frac{\mu B_0}{v_e^2} \left[ \delta \bar{B}_{\phi} \cos \chi - \frac{k_R}{k_Z} \delta \bar{B}_R \sin \chi \right] + \right. \\
& \left. \frac{ie\delta E_{\parallel}}{k_{\parallel} k_B T_0} - \frac{1}{ix\beta^{1/2}} \alpha_P \delta \bar{B}_R - \cos \chi \frac{2\delta \bar{B}_R}{ix\beta^{1/2}} \sqrt{\frac{m_e}{m_p + m_e}} \left[ \frac{d \ln \Omega}{d \ln R} (y - i\zeta_e) - 2i\zeta_e \right] \right) \times \\
& \frac{n_0}{(2\pi)^{3/2} v_e^3} \exp \left( -y^2 - \frac{\mu B_0}{v_e^2} \right) + \frac{\delta \bar{B}_R}{ix\beta^{1/2}} (y - i\zeta_e) \left( \alpha_P - \frac{5}{2} \alpha_T + \right. \\
& \left. \left[ y^2 + \frac{\mu B_0}{v_e^2} \right] \alpha_T \right) \frac{n_0}{(2\pi)^{3/2} v_e^3} \exp \left( -y^2 - \frac{\mu B_0}{v_e^2} \right) + \\
& \left( \left[ \zeta_e \delta \bar{B}_{\phi} + \frac{d \ln \Omega}{d \ln R} \frac{1}{x\beta^{1/2}} \sqrt{\frac{m_e}{m_p + m_e}} \delta \bar{B}_R \right] \sin \chi + \frac{k_R}{k_Z} \zeta_e \delta \bar{B}_R \cos \chi \right) \frac{z/H \cos \chi}{x\beta^{1/2}} \times \\
& \frac{n_0}{(2\pi)^{3/2} v_e^3} \exp \left( -y^2 - \frac{\mu B_0}{v_e^2} \right), \tag{E.4}
\end{aligned}$$

where  $y = v_{\parallel} / (v_s \sqrt{2})$ . Although the WKB approximation implies  $k_{\parallel} H > 1$ , one can have situations under which  $\zeta_i < (k_{\parallel} H)^{-1}$  and  $\zeta_e < (k_{\parallel} H)^{-1}$ . Therefore, we need to consider electron dynamics and cannot ignore  $\delta E_{\parallel}$ . To calculate moments of the perturbed ion and electron particle distribution function, we introduce new functions

given by,

$$(y - i\zeta) f_n + i\hat{z} \frac{df_n}{dy} = \pi^{-1/2} y^n e^{-y^2}, \quad (\text{E.5})$$

$$(y - i\zeta) f_{nc} + i\hat{z} \frac{df_n}{dy} = \pi^{-1/2} y^n (y - i\zeta) y^n e^{-y^2}. \quad (\text{E.6})$$

$f_n$  and  $f_{nc}$  have the asymptotic behavior for large  $y$ ,

$$\lim_{|y| \rightarrow \infty} f_n = \pi^{-1/2} \frac{y^n}{y - i\zeta} e^{-y^2}, \quad (\text{E.7})$$

$$\lim_{|y| \rightarrow \infty} f_{nc} = \pi^{-1/2} y^n e^{-y^2}. \quad (\text{E.8})$$

Plasma moment functions  $Z_n$  and  $Z_{nc}$  are given by,

$$Z_n(\zeta, \hat{z}) = \int_{-\infty}^{\infty} f_n(y, \zeta, \hat{z}) dy, \quad (\text{E.9})$$

$$Z_{nc}(\zeta, \hat{z}) = \int_{-\infty}^{\infty} f_{nc}(y, \zeta, \hat{z}) dy. \quad (\text{E.10})$$

The limits of  $Z_n$  and  $Z_{nc}$  at  $\hat{z} = 0$  up to  $n = 4$ , for  $\text{Re}(\zeta) > 0$ , are given in Eqs. (E.11) - (E.20).

$$Z_0(\zeta, 0) = i\pi^{1/2} \exp(\zeta^2) \text{Erfc}(\zeta), \quad (\text{E.11})$$

$$Z_{0c}(\zeta, 0) = 1, \quad (\text{E.12})$$

$$Z_1(\zeta, 0) = 1 - \pi^{1/2} \zeta \exp(\zeta^2) \text{Erfc}(\zeta), \quad (\text{E.13})$$

$$Z_{1c}(\zeta, 0) = 0, \quad (\text{E.14})$$

$$Z_2(\zeta, 0) = i\zeta (1 - \pi^{1/2} \exp(\zeta^2) \text{Erfc}(\zeta)), \quad (\text{E.15})$$

$$Z_{2c}(\zeta, 0) = \frac{1}{2}, \quad (\text{E.16})$$

$$Z_3(\zeta, 0) = \frac{1}{2} - \zeta^2 (1 - \pi^{1/2} \zeta \exp(\zeta^2) \text{Erfc}(\zeta)), \quad (\text{E.17})$$

$$Z_{3c}(\zeta, 0) = 0, \quad (\text{E.18})$$

$$Z_4(\zeta, 0) = i\zeta \left( \frac{1}{2} - \zeta^2 [1 - \pi^{1/2} \zeta \exp(\zeta^2) \text{Erfc}(\zeta)] \right), \quad (\text{E.19})$$

$$Z_{4c}(\zeta, 0) = \frac{3}{4}. \quad (\text{E.20})$$

From Eq. (E.3) and (E.4), the ion and electron density responses in terms of  $\delta\bar{B}_R$ ,  $\delta\bar{B}_\phi$ , and  $\delta E_\parallel$  are,

$$\begin{aligned} \frac{\delta n_i}{n_0} = & \left( \delta\bar{B}_\phi \cos \chi - \frac{k_R}{k_Z} \delta\bar{B}_R \sin \chi \right) \left( 1 - Z_1 \left( \zeta_i, \frac{z/H \sin \chi}{2x\beta^{1/2}} \right) \right) - \\ & \frac{ie\delta E_\parallel}{k_\parallel k_B T_0} Z_1 \left( \zeta_i, \frac{z/H \sin \chi}{2x\beta^{1/2}} \right) - \frac{\alpha_P}{ix\beta^{1/2}} Z_1 \left( \zeta_i, \frac{z/H \sin \chi}{2x\beta^{1/2}} \right) \delta\bar{B}_R - \\ & \frac{2 \cos \chi}{ix\beta^{1/2}} \sqrt{\frac{m_p}{m_p + m_e}} \left( \frac{d \ln \Omega}{d \ln R} Z_{1c} \left[ \zeta_i, \frac{z/H \sin \chi}{2x\beta^{1/2}} \right] - 2i\zeta_i Z_1 \left[ \zeta_i, \frac{z/H \sin \chi}{2x\beta^{1/2}} \right] \right) \delta\bar{B}_R + \\ & \frac{\delta\bar{B}_R}{ix\beta^{1/2}} \left( \left[ \alpha_P - \frac{3}{2}\alpha_T \right] Z_{0c} \left[ \zeta_i, \frac{z/H \sin \chi}{2x\beta^{1/2}} \right] + \alpha_T Z_{2c} \left[ \zeta_i, \frac{z/H \sin \chi}{2x\beta^{1/2}} \right] \right) + \\ & \left( \left[ \zeta_i \delta\bar{B}_\phi + \frac{d \ln \Omega}{d \ln R} \frac{1}{x\beta^{1/2}} \sqrt{\frac{m_p}{m_p + m_e}} \delta\bar{B}_R \right] \sin \chi + \frac{k_R}{k_Z} \zeta_i \delta\bar{B}_R \cos \chi \right) \frac{z/H \cos \chi}{x\beta^{1/2}} \times \\ & Z_0 \left( \zeta_i, \frac{z/H \sin \chi}{2x\beta^{1/2}} \right), \end{aligned} \quad (\text{E.21})$$

$$\begin{aligned} \frac{\delta n_e}{n_0} = & \left( \delta\bar{B}_\phi \cos \chi - \frac{k_R}{k_Z} \delta\bar{B}_R \sin \chi \right) \left( 1 - Z_1 \left( \zeta_e, \frac{z/H \sin \chi}{2x\beta^{1/2}} \right) \right) + \\ & \frac{ie\delta E_\parallel}{k_\parallel k_B T_0} Z_1 \left( \zeta_e, \frac{z/H \sin \chi}{2x\beta^{1/2}} \right) - \frac{\alpha_P}{ix\beta^{1/2}} Z_1 \left( \zeta_e, \frac{z/H \sin \chi}{2x\beta^{1/2}} \right) \delta\bar{B}_R - \\ & \frac{2 \cos \chi}{ix\beta^{1/2}} \sqrt{\frac{m_e}{m_p + m_e}} \left( \frac{d \ln \Omega}{d \ln R} Z_{1c} \left[ \zeta_e, \frac{z/H \sin \chi}{2x\beta^{1/2}} \right] - 2i\zeta_e Z_1 \left[ \zeta_e, \frac{z/H \sin \chi}{2x\beta^{1/2}} \right] \right) \delta\bar{B}_R + \\ & \frac{\delta\bar{B}_R}{ix\beta^{1/2}} \left( \left[ \alpha_P - \frac{3}{2}\alpha_T \right] Z_{0c} \left[ \zeta_e, \frac{z/H \sin \chi}{2x\beta^{1/2}} \right] + \alpha_T Z_{2c} \left[ \zeta_e, \frac{z/H \sin \chi}{2x\beta^{1/2}} \right] \right) + \\ & \left( \left[ \zeta_e \delta\bar{B}_\phi + \frac{d \ln \Omega}{d \ln R} \frac{1}{x\beta^{1/2}} \sqrt{\frac{m_e}{m_p + m_e}} \delta\bar{B}_R \right] \sin \chi + \frac{k_R}{k_Z} \zeta_e \delta\bar{B}_R \cos \chi \right) \frac{z/H \cos \chi}{x\beta^{1/2}} \times \\ & Z_0 \left( \zeta_e, \frac{z/H \sin \chi}{2x\beta^{1/2}} \right). \end{aligned} \quad (\text{E.22})$$

Here  $\beta = \theta_0/v_{A0}^2$ . Furthermore, recall that,

$$\zeta_i = \frac{\Gamma}{k_\parallel v_i \sqrt{2}} = \frac{\gamma}{x\beta^{1/2}} \sqrt{\frac{m_p}{m_p + m_e}}, \quad (\text{E.23})$$

$$\zeta_e = \frac{\Gamma}{k_\parallel v_e \sqrt{2}} = \frac{\gamma}{x\beta^{1/2}} \sqrt{\frac{m_e}{m_p + m_e}}. \quad (\text{E.24})$$

We solve for  $\delta E_{\parallel}$  by noting  $\delta n_i = \delta n_e$ . From Eq. (5.1.25), the parallel ion and electron pressures are,

$$\begin{aligned}
\frac{\delta p_{i\parallel}}{p_{i0}} = & \left( \delta \bar{B}_{\phi} \cos \chi - \frac{k_R}{k_Z} \delta \bar{B}_R \sin \chi \right) \left( 1 - 2Z_3 \left( \zeta_i, \frac{z/H \sin \chi}{2x\beta^{1/2}} \right) \right) - \\
& \frac{ie\delta E_{\parallel}}{k_{\parallel} k_B T_0} 2Z_3 \left( \zeta_i, \frac{z \sin \chi}{2k_{\parallel} H^2} \right) - \frac{2\alpha_P}{ix\beta^{1/2}} Z_3 \left( \zeta_i, \frac{z/H \sin \chi}{2x\beta^{1/2}} \right) \delta \bar{B}_R - \\
& \frac{4 \cos \chi}{ix\beta^{1/2}} \sqrt{\frac{m_p}{m_p + m_e}} \left( \frac{d \ln \Omega}{d \ln R} Z_{3c} \left[ \zeta_i, \frac{z/H \sin \chi}{2x\beta^{1/2}} \right] - 2i\zeta_i Z_3 \left[ \zeta_i, \frac{z/H \sin \chi}{2x\beta^{1/2}} \right] \right) \delta \bar{B}_R + \\
& \frac{\delta \bar{B}_R}{ix\beta^{1/2}} \left( [2\alpha_P - 3\alpha_T] Z_{2c} \left[ \zeta_i, \frac{z/H \sin \chi}{2x\beta^{1/2}} \right] + 2\alpha_T Z_{4c} \left[ \zeta_i, \frac{z/H \sin \chi}{2x\beta^{1/2}} \right] \right) + \\
& 2 \left( \left[ \zeta_i \delta \bar{B}_{\phi} + \frac{d \ln \Omega}{d \ln R} \frac{1}{x\beta^{1/2}} \sqrt{\frac{m_p}{m_p + m_e}} \delta \bar{B}_R \right] \sin \chi + \frac{k_R}{k_Z} \zeta_i \delta \bar{B}_R \cos \chi \right) \frac{z/H \cos \chi}{x\beta^{1/2}} \times \\
& Z_2 \left( \zeta_i, \frac{z/H \sin \chi}{2x\beta^{1/2}} \right), \tag{E.25}
\end{aligned}$$

$$\begin{aligned}
\frac{\delta p_{e\parallel}}{p_{e0}} = & \left( \delta \bar{B}_{\phi} \cos \chi - \frac{k_R}{k_Z} \delta \bar{B}_R \sin \chi \right) \left( 1 - 2Z_3 \left( \zeta_e, \frac{z/H \sin \chi}{2x\beta^{1/2}} \right) \right) + \\
& \frac{ie\delta E_{\parallel}}{k_{\parallel} k_B T_0} 2Z_3 \left( \zeta_e, \frac{z \sin \chi}{2k_{\parallel} H^2} \right) - \frac{2\alpha_P}{ix\beta^{1/2}} Z_3 \left( \zeta_e, \frac{z/H \sin \chi}{2x\beta^{1/2}} \right) \delta \bar{B}_R - \\
& \frac{4 \cos \chi}{ix\beta^{1/2}} \sqrt{\frac{m_e}{m_p + m_e}} \left( \frac{d \ln \Omega}{d \ln R} Z_{3c} \left[ \zeta_e, \frac{z/H \sin \chi}{2x\beta^{1/2}} \right] - 2i\zeta_e Z_3 \left[ \zeta_e, \frac{z/H \sin \chi}{2x\beta^{1/2}} \right] \right) \delta \bar{B}_R + \\
& \frac{\delta \bar{B}_R}{ix\beta^{1/2}} \left( [2\alpha_P - 3\alpha_T] Z_{2c} \left[ \zeta_e, \frac{z/H \sin \chi}{2x\beta^{1/2}} \right] + 2\alpha_T Z_{4c} \left[ \zeta_e, \frac{z/H \sin \chi}{2x\beta^{1/2}} \right] \right) + \\
& 2 \left( \left[ \zeta_e \delta \bar{B}_{\phi} + \frac{d \ln \Omega}{d \ln R} \frac{1}{x\beta^{1/2}} \sqrt{\frac{m_e}{m_p + m_e}} \delta \bar{B}_R \right] \sin \chi + \frac{k_R}{k_Z} \zeta_e \delta \bar{B}_R \cos \chi \right) \frac{z/H \cos \chi}{x\beta^{1/2}} \times \\
& Z_2 \left( \zeta_e, \frac{z/H \sin \chi}{2x\beta^{1/2}} \right), \tag{E.26}
\end{aligned}$$



and the ion and electron perpendicular pressures are,

$$\begin{aligned}
\frac{\delta p_{i\perp}}{p_{i0}} = & 2 \left( \delta \bar{B}_\phi \cos \chi - \frac{k_R}{k_Z} \delta \bar{B}_R \sin \chi \right) \left( 1 - Z_1 \left( \zeta_i, \frac{z/H \sin \chi}{2x\beta^{1/2}} \right) \right) - \\
& \frac{ie\delta E_\parallel}{k_\parallel k_B T_0} Z_1 \left( \zeta_i, \frac{z \sin \chi}{2k_\parallel H^2} \right) - \frac{\alpha_P}{ix\beta^{1/2}} Z_1 \left( \zeta_i, \frac{z/H \sin \chi}{2x\beta^{1/2}} \right) \delta \bar{B}_R - \\
& \frac{2 \cos \chi}{ix\beta^{1/2}} \sqrt{\frac{m_p}{m_p + m_e}} \left( \frac{d \ln \Omega}{d \ln R} Z_{1c} \left[ \zeta_i, \frac{z/H \sin \chi}{2x\beta^{1/2}} \right] - 2i\zeta_i Z_1 \left[ \zeta_i, \frac{z/H \sin \chi}{2x\beta^{1/2}} \right] \right) \delta \bar{B}_R + \\
& \frac{\delta \bar{B}_R}{ix\beta^{1/2}} \left( \left[ \alpha_P - \frac{1}{2} \alpha_T \right] Z_{0c} \left[ \zeta_i, \frac{z/H \sin \chi}{2x\beta^{1/2}} \right] + \alpha_T Z_{2c} \left[ \zeta_i, \frac{z/H \sin \chi}{2x\beta^{1/2}} \right] \right) + \\
& \left( \left[ \zeta_i \delta \bar{B}_\phi + \frac{d \ln \Omega}{d \ln R} \frac{1}{x\beta^{1/2}} \sqrt{\frac{m_p}{m_p + m_e}} \delta \bar{B}_R \right] \sin \chi + \frac{k_R}{k_Z} \zeta_i \delta \bar{B}_R \cos \chi \right) \frac{z/H \cos \chi}{x\beta^{1/2}} \times \\
& Z_0 \left( \zeta_i, \frac{z/H \sin \chi}{2x\beta^{1/2}} \right), \tag{E.27}
\end{aligned}$$

$$\begin{aligned}
\frac{\delta p_{e\perp}}{p_{e0}} = & 2 \left( \delta \bar{B}_\phi \cos \chi - \frac{k_R}{k_Z} \delta \bar{B}_R \sin \chi \right) \left( 1 - Z_1 \left( \zeta_e, \frac{z/H \sin \chi}{2x\beta^{1/2}} \right) \right) + \\
& \frac{ie\delta E_\parallel}{k_\parallel k_B T_0} Z_1 \left( \zeta_e, \frac{z \sin \chi}{2k_\parallel H^2} \right) - \frac{\alpha_P}{ix\beta^{1/2}} Z_1 \left( \zeta_e, \frac{z/H \sin \chi}{2x\beta^{1/2}} \right) \delta \bar{B}_R - \\
& \frac{2 \cos \chi}{ix\beta^{1/2}} \sqrt{\frac{m_e}{m_p + m_e}} \left( \frac{d \ln \Omega}{d \ln R} Z_{1c} \left[ \zeta_e, \frac{z/H \sin \chi}{2x\beta^{1/2}} \right] - 2i\zeta_e Z_1 \left[ \zeta_e, \frac{z/H \sin \chi}{2x\beta^{1/2}} \right] \right) \delta \bar{B}_R + \\
& \frac{\delta \bar{B}_R}{ix\beta^{1/2}} \left( \left[ \alpha_P - \frac{1}{2} \alpha_T \right] Z_{0c} \left[ \zeta_e, \frac{z/H \sin \chi}{2x\beta^{1/2}} \right] + \alpha_T Z_{2c} \left[ \zeta_e, \frac{z/H \sin \chi}{2x\beta^{1/2}} \right] \right) + \\
& \left( \left[ \zeta_e \delta \bar{B}_\phi + \frac{d \ln \Omega}{d \ln R} \frac{1}{x\beta^{1/2}} \sqrt{\frac{m_e}{m_p + m_e}} \delta \bar{B}_R \right] \sin \chi + \frac{k_R}{k_Z} \zeta_e \delta \bar{B}_R \cos \chi \right) \frac{z/H \cos \chi}{x\beta^{1/2}} \times \\
& Z_0 \left( \zeta_e, \frac{z/H \sin \chi}{2x\beta^{1/2}} \right). \tag{E.28}
\end{aligned}$$

Therefore, the parallel and perpendicular pressures are defined in this manner,

$$\begin{pmatrix} \delta p_\perp / p_0 \\ \delta p_\parallel / p_0 \end{pmatrix} = \begin{pmatrix} \mathcal{A}_{R\perp} & \mathcal{A}_{\phi\perp} \\ \mathcal{A}_{\phi\perp} & \mathcal{A}_{\phi\parallel} \end{pmatrix} \begin{pmatrix} \delta \bar{B}_R \\ \delta \bar{B}_\phi \end{pmatrix}. \tag{E.29}$$

Recall that  $p_{i0} = p_{e0}$ , therefore  $p_0 = 2p_{i0} = 2p_{e0}$ . We plot the normalized pressure response functions –  $\mathcal{A}_{R\perp}$ ,  $\mathcal{A}_{\phi\perp}$ ,  $\mathcal{A}_{R\parallel}$ , and  $\mathcal{A}_{\phi\parallel}$  – given in Eq. (E.29) as a function of normalized height  $z/H$  for various  $\beta \geq 1$ , in Figs. (E.1) - (E.4). We choose a

Keplerian rotational profile,  $\alpha_P = \alpha_T = 0$ ,  $\chi = \pi/4$ ,  $\Gamma/\Omega = 1$ , and  $k_Z v_{A0}/\Omega = 1$ . The real and imaginary parts of the normalized  $\mathcal{A}_{R\perp}$  are shown in Fig. (E.1). The real and imaginary parts of the normalized  $\mathcal{A}_{\phi\perp}$  are shown in Fig. (E.2). The real and imaginary parts of the normalized  $\mathcal{A}_{R\parallel}$  are shown in Fig. (E.3). The real and imaginary parts of the normalized  $\mathcal{A}_{\phi\parallel}$  are shown in Fig. (E.4). The pressure response values at the midplane for various  $\beta \geq 1$  are shown in Tab. (E.1),

Table E.1: Pressure Response Functions at Midplane For Various  $\beta$

function	$\beta = 10^{2.5}$	$\beta = 10^2$	$\beta = 10^{1.5}$	$\beta = 10^1$	$\beta = 10^{0.5}$
$\mathcal{A}_{R\perp}(z=0)$	$8.314 \times 10^{-3}$	$2.481 \times 10^{-2}$	$7.065 \times 10^{-2}$	$1.848 \times 10^{-1}$	$4.183 \times 10^{-1}$
$\mathcal{A}_{\phi\perp}(z=0)$	$9.663 \times 10^{-2}$	$1.650 \times 10^{-1}$	$2.735 \times 10^{-1}$	$4.319 \times 10^{-1}$	$6.324 \times 10^{-1}$
$\mathcal{A}_{R\parallel}(z=0)$	$8.892 \times 10^{-3}$	$2.779 \times 10^{-2}$	$8.497 \times 10^{-2}$	$2.459 \times 10^{-1}$	$6.299 \times 10^{-1}$
$\mathcal{A}_{\phi\parallel}(z=0)$	$4.157 \times 10^{-3}$	$1.241 \times 10^{-2}$	$3.532 \times 10^{-2}$	$9.242 \times 10^{-2}$	$2.092 \times 10^{-1}$

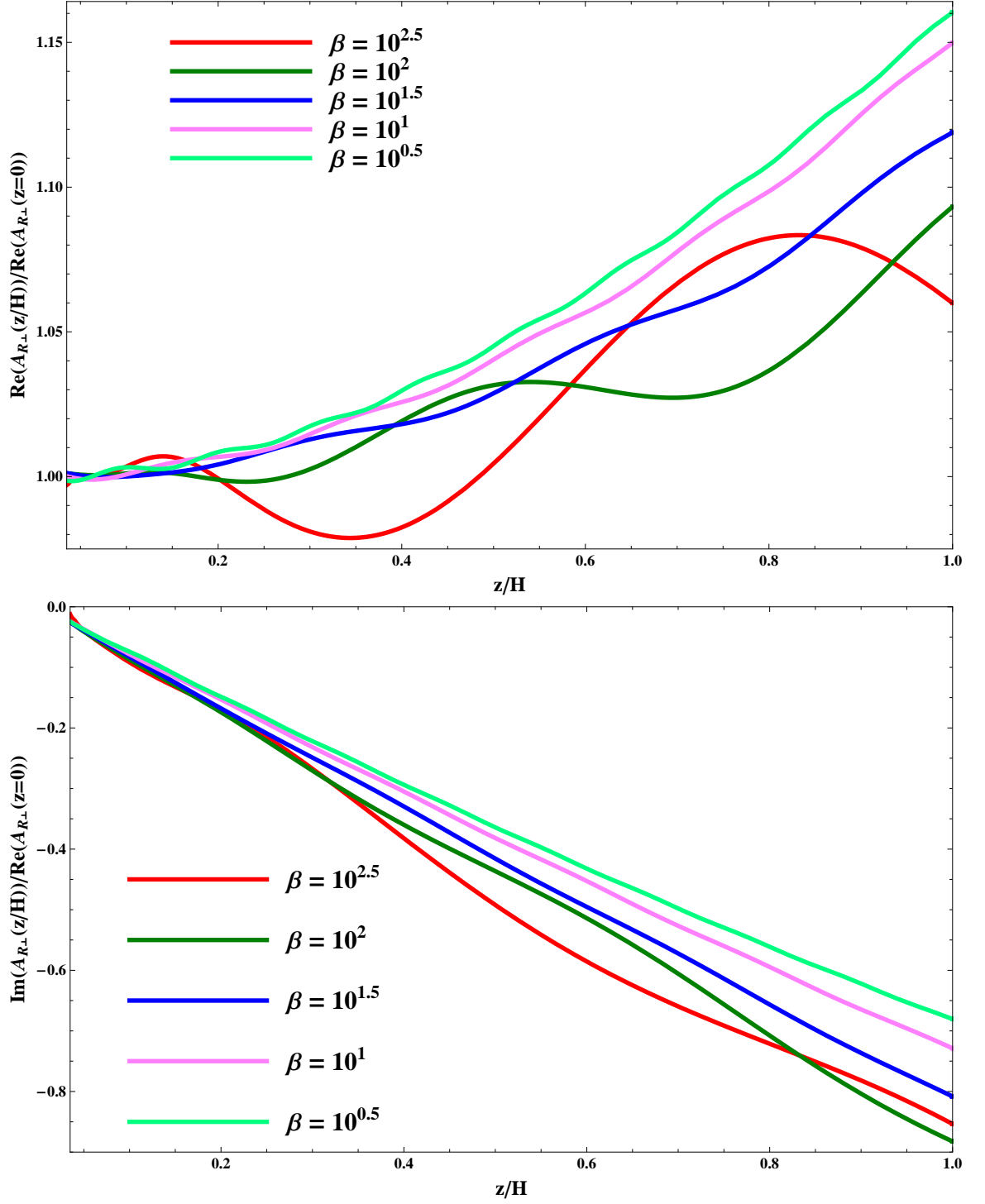


Fig. E.1.— Offplane normalized perpendicular pressure response function  $\text{Re}(\mathcal{A}_{R\perp}(z/H))/\text{Re}(\mathcal{A}_{R\perp}(z=0))$  (on top) and  $\text{Im}(\mathcal{A}_{R\perp})/\text{Re}(\mathcal{A}_{R\perp}(z=0))$  (on bottom) for the collisionless MRI as a function of  $z/H$ , for various  $\beta \geq 1$ .

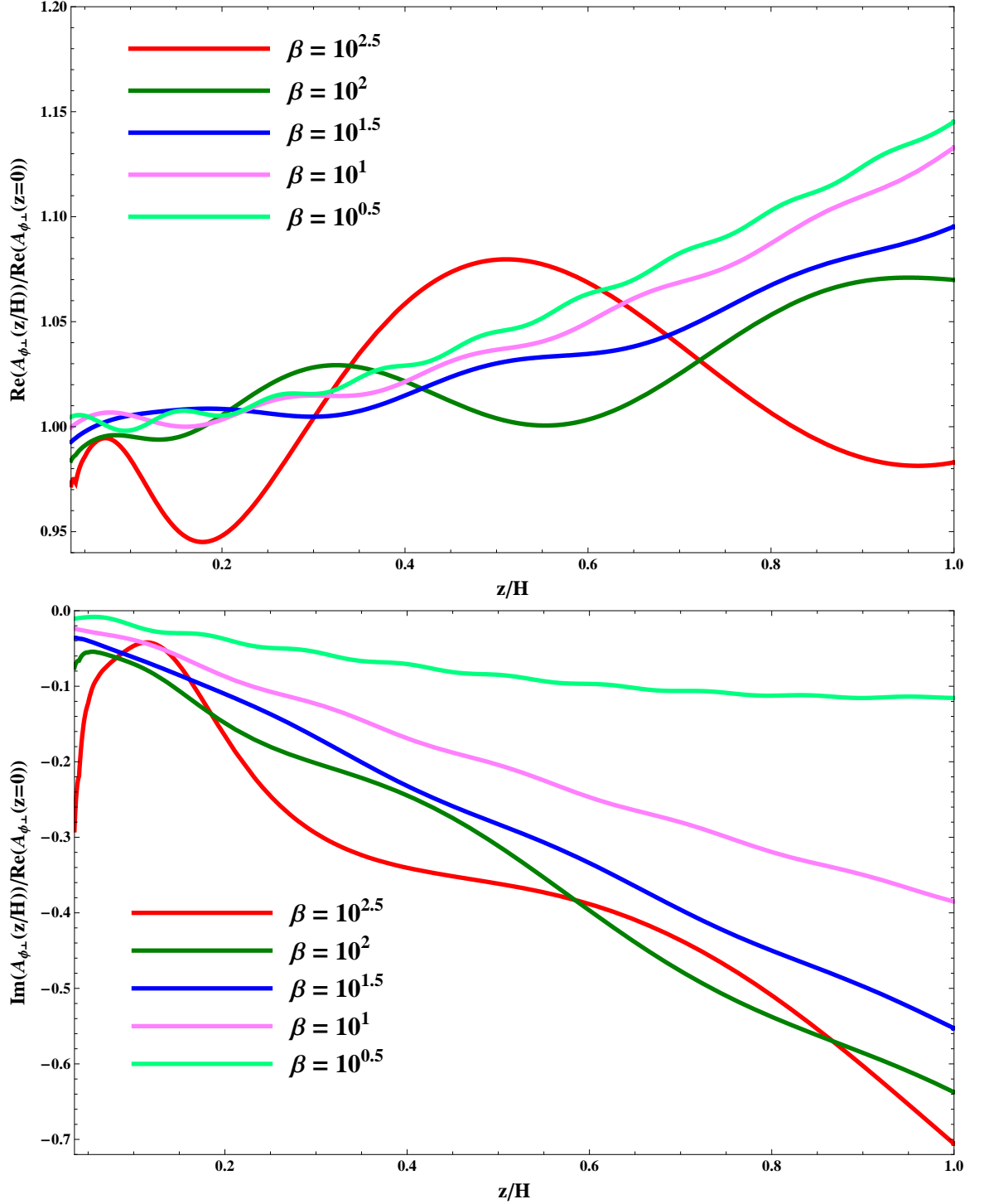


Fig. E.2.— Offplane normalized perpendicular pressure  $\text{Re}(\mathcal{A}_{\phi\perp}(z/H))/\text{Re}(\mathcal{A}_{\phi\perp}(z=0))$  (on top) and  $\text{Im}(\mathcal{A}_{\phi\perp}(z/H))/\text{Re}(\mathcal{A}_{\phi\perp}(z=0))$  (on bottom) for the collisionless MRI as a function of  $z/H$ , for various  $\beta \geq 1$ .

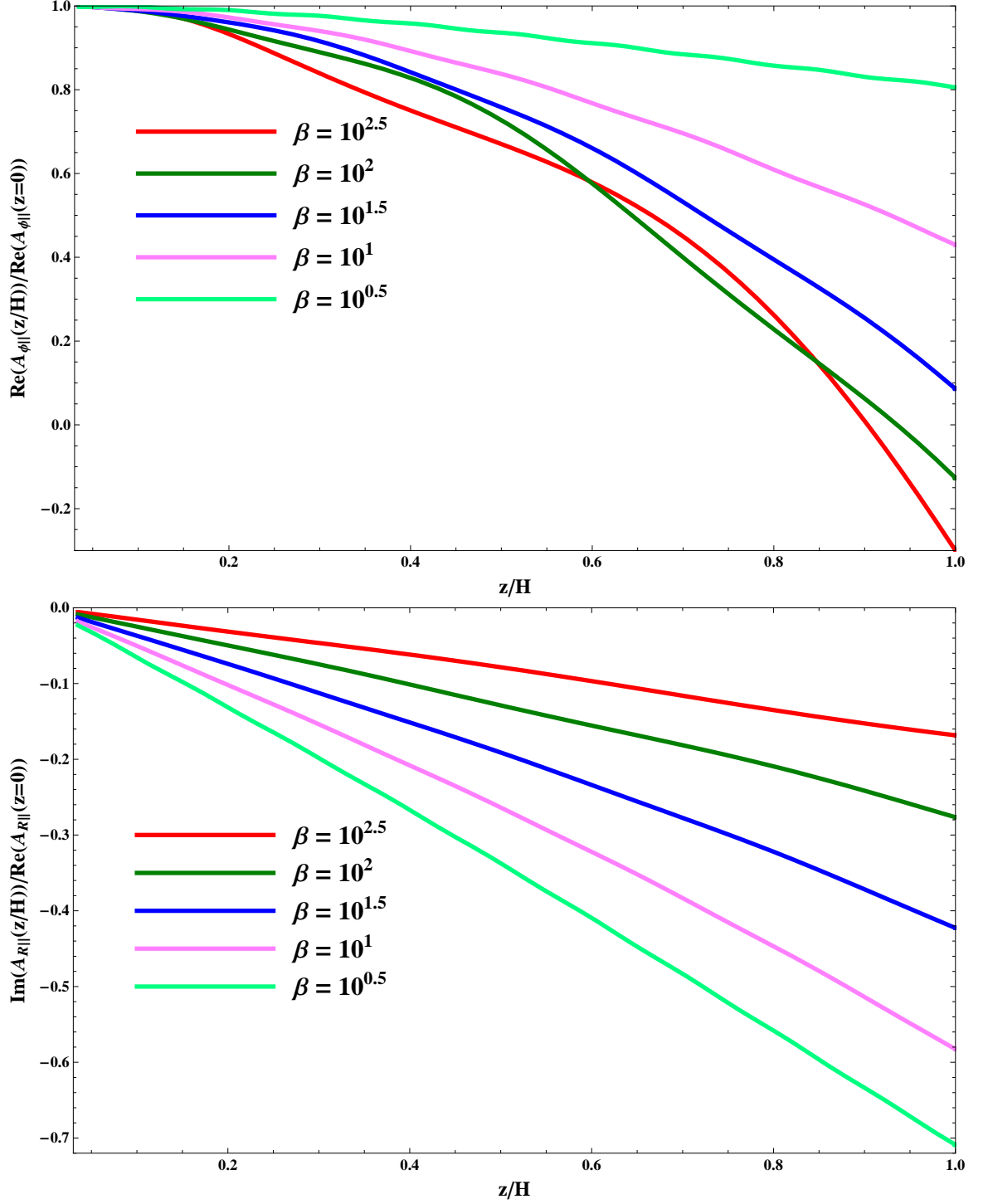


Fig. E.3.— Offplane normalized parallel pressure response function  $\text{Re}(\mathcal{A}_{R\parallel}(z/H))/\text{Re}(\mathcal{A}_{R\parallel}(z=0))$  (on top) and  $\text{Im}(\mathcal{A}_{R\parallel})/\text{Re}(\mathcal{A}_{R\parallel}(z=0))$  (on bottom) for the collisionless MRI as a function of  $z/H$ , for various  $\beta \geq 1$ .

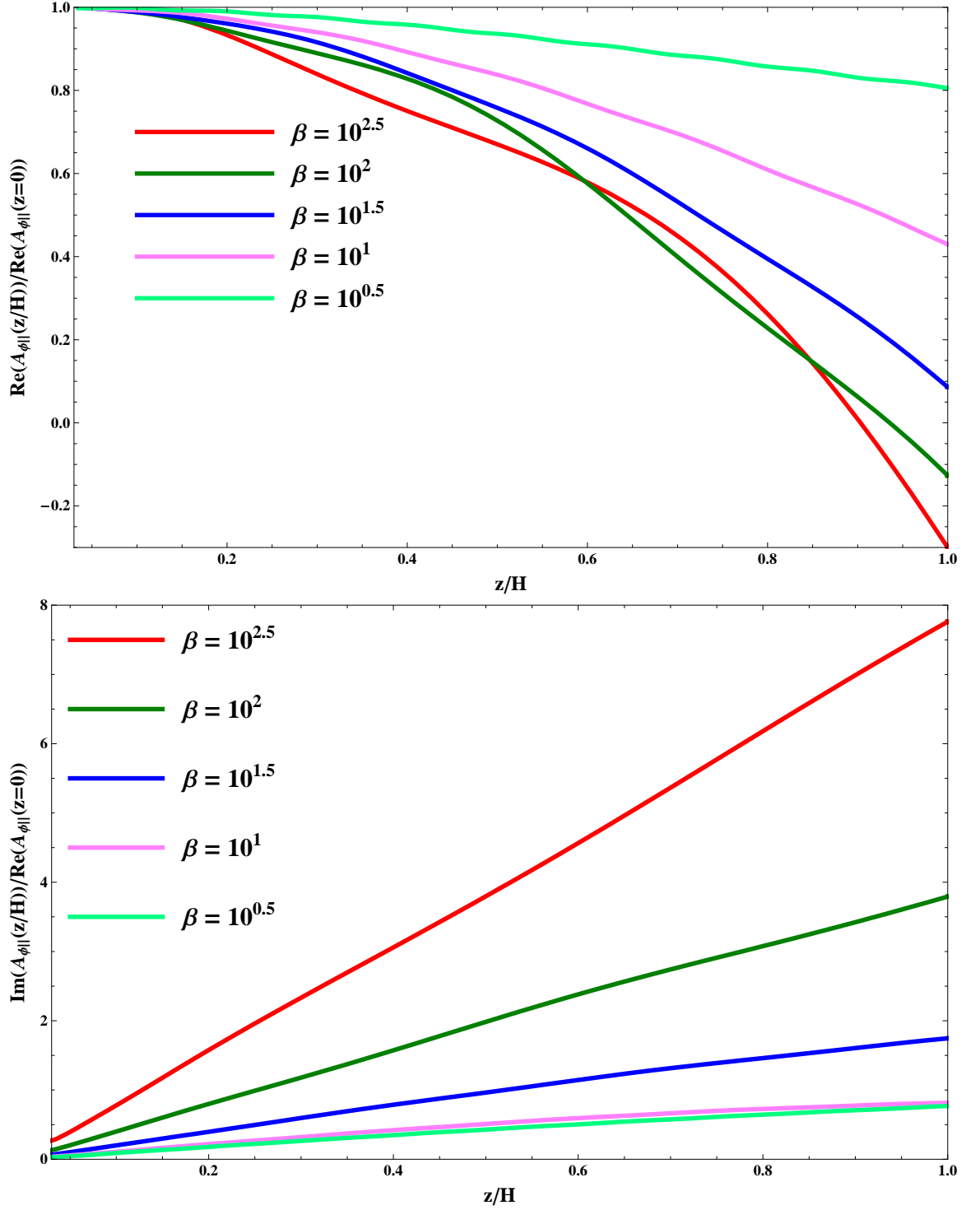


Fig. E.4.— Offplane normalized parallel pressure  $\text{Re}(\mathcal{A}_{\phi\perp}(z/H))/\text{Re}(\mathcal{A}_{\phi\perp}(z=0))$  (on top) and  $\text{Im}(\mathcal{A}_{\phi\perp}(z/H))/\text{Re}(\mathcal{A}_{\phi\perp}(z=0))$  (on bottom) for the collisionless MRI as a function of  $z/H$ , for various  $\beta \geq 1$ .

If we employ Eqs. (1.2.6), the perturbed equation of force balance away from the midplane is given by,

$$\begin{aligned} \Gamma \delta \mathbf{u} + 2\Omega \hat{\mathbf{z}} \times \delta \mathbf{u} + \Omega' R \delta u_R \hat{\boldsymbol{\phi}} = & \delta \bar{\rho} \theta_0 \left( -\alpha_P H^{-1} \hat{\mathbf{R}} - \frac{z}{H^2} \hat{\mathbf{z}} \right) - \\ & i\mathbf{k} \left( \frac{\delta p_{\perp}}{p_0} \theta_0 + \mathbf{b}_0 \cdot \delta \bar{\mathbf{B}} v_{A0}^2 e^{z^2/H^2} \right) + i k_{\parallel} v_{A0}^2 e^{z^2/H^2} \delta \bar{\mathbf{B}} - \\ & i k_{\parallel} \mathbf{b}_0 \theta_0 \frac{\delta p_{\parallel} - \delta p_{\perp}}{p_0}, \end{aligned} \quad (\text{E.30})$$

The MHD continuity equation away from the midplane, Eq. (1.2.5), yields,

$$i\mathbf{k} \cdot \delta \mathbf{u} = -\Gamma \delta \bar{\rho} + \frac{\Gamma \delta \bar{B}_R}{ix\beta^{1/2}} \left( \alpha_P - \alpha_T - \frac{k_R}{k_Z} z/H \right) \quad (\text{E.31})$$

Therefore, Eq. (5.1.3) results in the MHD induction equation away from the midplane,

$$\begin{aligned} i k_{\parallel} \delta \mathbf{u} = & \Gamma \delta \bar{\mathbf{B}} - \Omega' R \delta \bar{B}_R \hat{\boldsymbol{\phi}} - \\ & \Gamma \left( \delta \bar{\rho} - \frac{\alpha_P - \alpha_T - k_R/k_Z \times z/H}{ix\beta^{1/2}} \delta \bar{B}_R \right) \mathbf{b}_0. \end{aligned} \quad (\text{E.32})$$

If we substitute Eq. (E.32) into Eq. (E.30), we then have,

$$\begin{aligned} \Gamma^2 \delta \bar{\mathbf{B}} + 2\Omega \Gamma \cos \chi \left( \delta \bar{\rho} - \frac{\alpha_P - \alpha_T - k_R/k_Z \times z/H}{ix\beta^{1/2}} \delta \bar{B}_R \right) \hat{\mathbf{R}} + \\ 2\Omega \Omega' R \delta \bar{B}_R \hat{\mathbf{R}} - \Gamma^2 \left( \delta \bar{\rho} - \frac{\alpha_P - \alpha_T - k_R/k_Z \times z/H}{ix\beta^{1/2}} \delta \bar{B}_R \right) \mathbf{b}_0 + \\ 2\Omega \Gamma \hat{\mathbf{z}} \times \delta \bar{\mathbf{B}} = -ix\beta^{1/2} \Omega^2 \left( \alpha_P \hat{\mathbf{R}} + \frac{z}{H} \hat{\mathbf{z}} \right) \delta \bar{\rho} + \\ \mathbf{k} k_{\parallel} \left( \frac{\delta p_{\perp}}{p_0} \theta_0 + \mathbf{b}_0 \cdot \delta \bar{\mathbf{B}} v_{A0}^2 e^{z^2/H^2} \right) - k_{\parallel}^2 v_{A0}^2 e^{z^2/H^2} \delta \bar{\mathbf{B}} + k_{\parallel}^2 \theta_0 \mathbf{b}_0 \frac{\delta p_{\parallel} - \delta p_{\perp}}{p_0}. \end{aligned} \quad (\text{E.33})$$

In terms of normalized variables, the radial, azimuthal, and equilibrium magnetic-

field-directed components of Eq. (E.33) are,

$$\left( \gamma^2 + x^2 \left[ 1 + \frac{\hat{k}_R^2}{\hat{k}_Z^2} \right] e^{z^2/H^2} + 2 \frac{d \ln \Omega}{d \ln R} - 2 \gamma \cos \chi \frac{\alpha_P - \alpha_T - \hat{k}_R/\hat{k}_Z \times z/H}{ix\beta^{1/2}} \right) \delta \bar{B}_R - \quad (E.34)$$

$$\left( 2 \gamma + x^2 \cot \chi \frac{\hat{k}_R}{\hat{k}_Z} \right) \delta \bar{B}_\phi + \delta \bar{\rho} (2 \gamma \cos \chi + ix\beta^{1/2} \alpha_P) = \hat{k}_R x \beta \frac{\delta p_\perp}{p_0},$$

$$\left( \gamma^2 \cos \chi \frac{\alpha_P - \alpha_T - \hat{k}_R/\hat{k}_Z \times z/H}{ix\beta^{1/2}} + 2 \gamma \right) \delta \bar{B}_R + \left( \gamma^2 + x^2 e^{z^2/H^2} \right) \delta \bar{B}_\phi - \quad (E.35)$$

$$\gamma^2 \delta \bar{\rho} = x^2 \beta \cos \chi \frac{\delta p_\parallel - \delta p_\perp}{p_0},$$

$$\delta \bar{B}_R \left( \gamma^2 \frac{\alpha_P - \alpha_T - \hat{k}_R/\hat{k}_Z \times z/H}{ix\beta^{1/2}} - \frac{\hat{k}_R}{\hat{k}_Z} \gamma^2 \sin \chi + 2 \gamma \cos \chi \right) + \gamma^2 \cos \chi \delta \bar{B}_\phi + \quad (E.36)$$

$$\left( ix\beta^{1/2} \sin \chi \frac{z}{H} - \gamma^2 \right) \delta \bar{\rho} = x^2 \beta \frac{\delta p_\parallel}{p_0}.$$



# References

- Abramowicz, M. A., Czerny, B., Lasota, J. P., & Szuszkiewicz, E. 1988, *ApJ*, 332, 646
- Adams, F. C., Ruden, S. P., & Shu, F. H. 1989, *ApJ*, 347, 959
- Aitken, D. K., Greaves, J., Chrysostomou, A., Jenness, T., Holland, W., Hough, J. H., Pierce-Price, D., & Richer, J. 2000, *apjl*, 534, L173
- Arons, J. 1992, *ApJ*, 388, 561
- Baganoff, F. K., Maeda, Y., Morris, M., Bautz, M. W., Brandt, W. N., Cui, W., Doty, J. P., Feigelson, E. D., Garmire, G. P., Pravdo, S. H., Ricker, G. R., & Townsley, L. K. 2003, *ApJ*, 591, 891
- Balbus, S. & Hawley, J. 2002, *ApJ*, 573, 749
- Balbus, S. A. 1995, *ApJ*, 453, 380
- . 2001, *ApJ*, 562, 909
- . 2004a, *ApJ*, 600, 865
- . 2004b, *ApJ*, 616, 857

- Balbus, S. A. 2005, in *Astronomical Society of the Pacific Conference Series*, Vol. 330, *The Astrophysics of Cataclysmic Variables and Related Objects*, ed. J.-M. Hameury & J.-P. Lasota, 185–+
- Balbus, S. A., Gammie, C. F., & Hawley, J. F. 1994, *MNRAS*, 271, 197
- Balbus, S. A. & Hawley, J. F. 1991, *ApJ*, 376, 214
- . 1998, *Rev. Mod. Phys.*, 70, 1
- Balbus, S. A., Hawley, J. F., & Stone, J. M. 1996, *ApJ*, 467, 76
- Batchelor, G. K. 1967, *An Introduction to Fluid Dynamics* (Cambridge: Cambridge University Press)
- Bayly, B. J., Orszag, S. A., & Herbert, T. 1988, *Annual Review of Fluid Mechanics*, 20, 359
- Begelman, M. C. 1978, *MNRAS*, 184, 53
- . 2006a, *ApJ*, 636, 995
- . 2006b, *ApJ*, 643, 1065
- Bhatnager, P., Gross, E., & Krook, M. 1954, *Phys. Rev.*, 94, 511
- Blaes, O. M. & Socrates, A. 2001, *ApJ*, 553, 987
- Blandford, R. D. & Begelman, M. C. 1999, *MNRAS*, 303, L1
- Bondi, H. 1952, *MNRAS*, 112, 195
- Bower, G. C., Wright, M. C. H., Falcke, H., & Backer, D. C. 2003, *ApJ*, 588, 331
- Braginskii, S. I. *Reviews of Plasma Physics*, Vol. 1 (New York: Consultants Bureau), 205–311

- Brandenburg, A., Nordlund, A., Stein, R. F., & Torkelsson, U. 1995, *ApJ*, 446, 741
- Chandrasekhar, S. 1960, *Proceedings of the National Academy of Science*, 46, 253
- . 1961, *Hydrodynamic and hydromagnetic stability* (International Series of Monographs on Physics, Oxford: Clarendon, 1961)
- Chang, Z. & Callen, J. 1992, *Phys. Fluids*, B, 4, 1167
- Chew, G. F., Goldberger, M. L., & Low, F. E. 1956, *Proc. R. Soc. London A*, 236, 112
- Coppi, B. & Coppi, P. S. 1997, *Physics Letters A*, 237, 58
- . 1998, *Physics Letters A*, 239, 261
- . 2001a, *Physical Review Letters*, 87, 051101
- . 2001b, *Annals of Physics*, 291, 134
- Cowie, L. L. & McKee, C. F. 1977, *ApJ*, 211, 135
- De Villiers, J.-P. & Hawley, J. 2003, *ApJ*, 592, 1060
- De Villiers, J.-P., Hawley, J. F., & Krolik, J. H. 2003, *ApJ*, 599, 1238
- Di Matteo, T., Allen, S. W., Fabian, A. C., Wilson, A. S., & Young, A. J. 2003, *ApJ*, 582, 133
- Dorland, W. 1993, PhD thesis, Princeton University
- Drazin, P. G. & Reid, W. H. 1981, *Hydrodynamical Stability* (Cambridge: Cambridge University Press)
- Esin, A. A., McClintock, J. E., & Narayan, R. 1997, *ApJ*, 489, 865

- Ferraro, N. M. & Jardin, S. C. 2006, *Physics of Plasmas*, 13, 2101
- Frank, J., King, A., & Raine, D. 2002, *Accretion Power in Astrophysics* (Cambridge: Cambridge University Press), 93
- Fromang, S., Balbus, S. A., & De Villiers, J.-P. 2004a, *ApJ*, 616, 357
- Fromang, S., Balbus, S. A., Terquem, C., & De Villiers, J.-P. 2004b, *ApJ*, 616, 364
- Fromang, S., de Villiers, J. P., & Balbus, S. A. 2004c, *Ap&SS*, 292, 439
- Gammie, C. F. 1998, *MNRAS*, 297, 929
- Gardiner, T. & Stone, J. 2005, *J. Comp. Phys.*, 205, 509
- Gardiner, T. A. & Stone, J. M. 2006, in *Astronomical Society of the Pacific Conference Series*, Vol. 359, *Numerical Modeling of Space Plasma Flows*, ed. G. P. Zank & N. V. Pogorelov, 143–+
- Gary, S. P., Li, H., O'Rourke, S., & Winske, D. 1998, *J. Geophys. Res.*, 103, 14567
- Gary, S. P., McKean, M. E., & Winske, D. 1996, *Geophys. Res. Lett.*, 23, 2887
- Gary, S. P., McKean, M. E., Winske, D., Anderson, B. J., Denton, R. E., & Fuselier, S. A. 1994, *J. Geophys. Res.*, 99, 5903
- Gary, S. P., Wang, J., Winske, D., & Fuselier, S. A. 1997, *J. Geophys. Res.*, 102, 27159
- Ghez, A. M., Becklin, E., Duchjné, G., Hornstein, S., Morris, M., Salim, S., & Tanner, A. 2003, *Astronomische Nachrichten Supplement*, 324, 527
- Goldreich, P., Goodman, J., & Narayan, R. 1986, *MNRAS*, 221, 339
- Goldreich, P. & Lynden-Bell, D. 1965, *MNRAS*, 130, 135

- Goldreich, P. & Sridhar, S. 1995, *ApJ*, 438, 763
- Hammett, G. W., Dorland, W., & Perkins, F. W. 1992, *Phys. Fluids*, B, 4, 2952
- Hammett, G. W. & Perkins, F. W. 1990, *Phys. Rev. Lett.*, 64, 3019
- Hawley, J. F. 2001, *ApJ*, 554, 534
- Hawley, J. F. & Balbus, S. A. 2002, *ApJ*, 573, 738
- Hawley, J. F., Balbus, S. A., & Stone, J. M. 2001, *ApJ*, 552, L49
- Hawley, J. F., Balbus, S. A., & Winters, W. F. 1998, *ApJ*, 440, 372
- Hawley, J. F., Gammie, C. F., & Balbus, S. A. 1995, *ApJ*, 440, 742
- . 1996, *ApJ*, 464, 690
- Hawley, J. F. & Stone, J. M. 1998, *ApJ*, 501, 758
- Hellinger, P. & Matsumoto, H. 2000, *J. Geophys. Res.*, 105, 10519
- Hellinger, P., Trávníček, P., Kasper, J. C., & Lazarus, A. J. 2006, *Geophys. Res. Lett.*, 33, 9101
- Ho, L. C., Terashima, Y., & Ulvestad, J. S. 2003, *ApJ*, 589, 783
- Howes, G. G., Cowley, S. C., Dorland, W., Hammett, G., Quataert, E., & Schekochihin, A. A. 2007a, in *American Astronomical Society Meeting Abstracts*, Vol. 210, American Astronomical Society Meeting Abstracts
- Howes, G. G., Cowley, S. C., Dorland, W., Hammett, G. W., Quataert, E., & Schekochihin, A. A. 2007b, *ArXiv e-prints*, 707
- Ichimaru, S. 1977, *ApJ*, 214, 840

- Igumenshchev, I. V. & Abramowicz, M. A. 1999, MNRAS, 303, 309
- Igumenshchev, I. V., Narayan, R., & Abramowicz, M. A. 2003, ApJ, 592, 1042
- Islam, T. S. & Balbus, S. A. 2005, ApJ, 633, 328
- Ji, H., Burin, M., Scharfman, E., & Goodman, J. 2006, Nature, 444, 343
- Johnson, B. M. & Quataert, E. 2007, ApJ, 660, 1273
- Julian, W. & Toomre, A. 1966, ApJ, 146, 810
- Kasper, J. C., Lazarus, A. J., & Gary, S. P. 2002, Geophys. Res. Lett., 29, 20
- Kennel, C. F. & Sagdeev, R. Z. 1967, J. Geophys. Res., 72, 3303
- Krolik, J. H., Hawley, J. F., & Hirose, S. 2005, ApJ, 622, 1008
- Kulsrud, R. M. 1983, in Basic Plasma Physics: Selected Chapters, Handbook of Plasma Physics, Volume 1, ed. A. A. Galeev & R. N. Sudan, 1–115
- Kulsrud, R. M. 2005, Plasma Physics for Astrophysics (Princeton, N.J.: Princeton University Press)
- Laughlin, G., Korchagin, V., & Adams, F. C. 1997, ApJ, 477, 410
- Lee, G. S. & Diamond, P. H. 1986, Phys. Fluids, 29, 3291
- Lesur, G. & Longaretti, P.-Y. 2005, A&A, 444, 25
- Loewenstein, M., Mushotzky, R. F., Angelini, L., Arnaud, K. A., & Quataert, E. 2001, apjl, 555, L21
- Lynden-Bell, D. 1969, Nature, 223, 690
- Marrone, D. P., Moran, J. M., Zhao, J.-H., & Rao, R. 2006, ApJ, 640, 308

- Menou, K. 2005, in KITP Program: Physics of Astrophysical Outflows and Accretion Disks
- Mestel, L. 1954, MNRAS, 114, 437
- Miller, K. A. & Stone, J. M. 2000, ApJ, 534, 398
- Narayan, R. 2002, in Lighthouses of the Universe: The Most Luminous Celestial Objects and Their Use for Cosmology Proceedings of the MPA/ESO, 405
- Narayan, R., Mahadevan, R., & Quataert, E. 1998, in Theory of Black Hole Accretion Disks, ed. M. Abramowicz, G. Bjornsson, & J. E. Pringle (Cambridge: Cambridge University Press), 148
- Narayan, R. & Yi, I. 1994, ApJL, 428, 13
- . 1995, ApJ, 452, 710
- Narayan, R., Yi, I., & Mahadevan, R. 1995, Nature, 374, 623
- Orszag, S. A. & Kells, L. C. 1980, Journal of Fluid Mechanics, 96, 159
- Papaloizou, J. C. B. & Pringle, J. E. 1984, MNRAS, 208, 721
- . 1985, MNRAS, 213, 799
- Parker, E. N. 1958a, Phys. Rev. Lett., 109, 1874
- . 1958b, ApJ, 128, 664
- Parrish, I. J. & Stone, J. 2005, ApJ, 633, 334
- Parrish, I. J. & Stone, J. M. 2006, ArXiv Astrophysics e-prints
- Pessah, M. E. 2007, PhD thesis, The University of Arizona

- Pessah, M. E., Chan, C.-K., & Psaltis, D. 2006a, *Physical Review Letters*, 97, 221103
- . 2006b, *MNRAS*, 372, 183
- Pessah, M. E., Chan, C.-k., & Psaltis, D. 2007, *ArXiv e-prints*, 705
- Piran, T. 1978, *ApJ*, 221, 652
- Pringle, J. E. 1981, *Ann. Rev. Astron. Astrophys.*, 19, 137
- Proga, D. & Begelman, M. C. 2003, *ApJ*, 592, 767
- Quataert, E. 2003, *Astronomische Nachrichten Supplement*, 324, 435
- Quataert, E. 2004, *ApJ*, 613, 322
- Quataert, E., Dorland, W., & Hammett, G. W. 2002, *ApJ*, 577, 524
- Rees, M. J., Phinney, E. S., Begelman, M. C., & Blandford, R. D. 1982, *Nature*, 295, 17
- Richard, D. 2001, PhD thesis, Université Paris 7 Denis Diderot
- Richards, G. T., Strauss, M. A., Fan, X., Hall, P. B., Jester, S., Schneider, D. P., Vanden Berk, D. E., Stoughton, C., Anderson, S. F., Brunner, R. J., Gray, J., Gunn, J. E., Ivezić, Ž., Kirkland, M. K., Knapp, G. R., Loveday, J., Meiksin, A., Pope, A., Szalay, A. S., Thakar, A. R., Yanny, B., York, D. G., Barentine, J. C., Brewington, H. J., Brinkmann, J., Fukugita, M., Harvanek, M., Kent, S. M., Kleinman, S. J., Krzesiński, J., Long, D. C., Lupton, R. H., Nash, T., Neilsen, Jr., E. H., Nitta, A., Schlegel, D. J., & Snedden, S. A. 2006, *AJ*, 131, 2766
- Richstone, D., Ajhar, E. A., Bender, R., Bower, G., Dressler, A., Faber, S. M., Filippenko, A. V., Gebhardt, K., Green, R., Ho, L. C., Kormendy, J., Lauer, T. R., Magorrian, J., & Tremaine, S. 1998, *Nature*, 395, A14+



- Sano, T. & Stone, J. M. 2002, *ApJ*, 570, 314
- Schekochihin, A., Cowley, S., Kulsrud, R., Hammett, G., & Sharma, P. 2005a, in *The Magnetized Plasma in Galaxy Evolution*, ed. K. T. Chyzy, K. Otmianowska-Mazur, M. Soida, & R.-J. Dettmar, 86–92
- Schekochihin, A. A. & Cowley, S. C. 2005, *ArXiv Astrophysics e-prints*
- . 2006, *Physics of Plasmas*, 13, 6501
- Schekochihin, A. A., Cowley, S. C., Dorland, W., Hammett, G. W., Howes, G. G., Quataert, E., & Tatsuno, T. 2007, *ArXiv e-prints*, 704
- Schekochihin, A. A., Cowley, S. C., Kulsrud, R. M., Hammett, G. W., & Sharma, P. 2005b, *ApJ*, 629, 139
- Schödel, R., Ott, T., Genzel, R., Hofmann, R., Lehnert, M., Eckart, A., Mouawad, N., Alexander, T., Reid, M. J., Lenzen, R., Hartung, M., Lacombe, F., Rouan, D., Gendron, E., Rousset, G., Lagrange, A.-M., Brandner, W., Ageorges, N., Lidman, C., Moorwood, A. F. M., Spyromilio, J., Hubin, N., & Menten, K. M. 2002, *Nature*, 419, 694
- Shakura, N. I. & Sunyaev, R. A. 1973, *A&A*, 24, 337
- Shapiro, S. I., Lightman, A. P., & Eardley, D. M. 1976, *ApJ*, 204, 187
- Sharma, P. 2006, PhD thesis, Princeton University
- Sharma, P., Hammett, G. W., & Quataert, E. 2003, *ApJ*, 596, 1121
- Sharma, P., Hammett, G. W., Quataert, E., & Stone, J. 2006, *ApJ*, 637, 952
- Simon, J. S. 2007

- Snyder, P. B., Hammett, G. W., & Dorland, W. 1997, *Phys. Plasmas*, 4, 11
- Southwood, D. J. & Kivelson, M. G. 1993, *J. Geophys. Res.*, 98, 9181
- Spitzer, L. 1962, *Physics of Fully Ionized Gases* (New York: John Wiley & Sons)
- Sridhar, S. & Goldreich, P. 1994, *ApJ*, 432, 612
- Stepney, S. & Guilbert, P. W. 1983, *MNRAS*, 204, 1269
- Stone, J. M., Hawley, J. F., Gammie, C. F., & Balbus, S. A. 1996, *ApJ*, 463, 656
- Stone, J. M. & Norman, M. 1992, *ApJS*, 80, 753
- Stone, J. M. & Norman, M. L. 1992a, *ApJS*, 80, 753
- . 1992b, *ApJS*, 80, 791
- Tanaka, T. & Menou, K. 2006, *ApJ*, 649, 345
- Toomre, A. 1977, *ARA&A*, 15, 437
- Turner, N. J., Blaes, O. M., Socrates, A., Begelman, M. C., & Davis, S. W. 2005, *ApJ*, 624, 267
- Velikhov, E. P. 1959, *Sov. Phys. JETP*, 9, 995
- von Weizsäcker, C. F. 1948, *Zeitschrift für Astrophysik*, 24, 181
- Waltz, R. E. 1988, *Phys. Fluids*, 31, 1962
- Wardle, M. & Ng, C. 1999, *MNRAS*, 303, 239
- Wisdom, J. & Tremaine, S. 1988, *AJ*, 95, 925